# Surface Engineering of Metal Oxides and Sulphides for Photocatalysis




**Wentian Niu**

Inorganic Chemistry Laboratory
Department of Chemistry
Pembroke College

A thesis submitted for the degree of
*Doctor of Philosophy in Inorganic Chemistry*

Trinity Term 2024

# Table of Contents

**Table of Contents** ..... I

**Declaration** ..... IV

**Acknowledgements** ..... V

**Abstract** ..... VIII

**List of Abbreviations** ..... X

**List of Publications** ..... XII

**Chapter 1 Introduction** ..... 1

**1.1 Motivation** ..... 1

**1.2 Principles of Photocatalytic Water-Splitting** ..... 2

**1.3 Efficiency Evaluation and Industrial Prospects** ..... 8

**1.4 Surface Engineering Strategies for Aiding Photocatalysis** ..... 10

**1.4.1 Single-Atom Engineering** ..... 10

**1.4.2 Heterojunction Engineering** ..... 17

**1.4.3 Facet Engineering** ..... 24

**1.5 Aims and Objectives** ..... 29

**1.6 Thesis Overview** ..... 30

**1.7 References** ..... 32

**Chapter 2 Characterisation Techniques and Experimental Methods** ..... 42

**2.1 Introduction** ..... 42

**2.2 Characterisation Techniques** ..... 42

**2.2.1 Powder X-ray Diffraction (PXRD)** ..... 42

**2.2.2 Transmission Electron Microscopy (TEM)** ..... 45

**2.2.3 X-ray Photoelectron Spectroscopy (XPS)** ..... 48

**2.2.4 X-ray Absorption Spectroscopy (XAS)** ..... 52

**2.2.5 Electron Paramagnetic Resonance (EPR) Spectroscopy** ..... 55

**2.2.6 Gas Chromatography (GC)** ..... 57

**2.2.7 Time-Resolved Photoluminescence (TRPL)** ..... 58

**2.2.8 Ultraviolet-Visible Diffuse Reflectance Spectroscopy (UV-Vis DRS)** ..... 60

**2.2.9 Electrochemical Impedance Spectroscopy (EIS)** ..... 62
**2.2.10 Atomic Force Microscopy (AFM)** ..... 63
**2.3 Experimental Methods** ..... 65
**2.3.1 Chemicals** ..... 65
**2.3.2 Synthesis of Few-Layer $WS_2$ (FL-$WS_2$) and Metal-Doped $WS_2$** ..... 67
**2.3.3 Synthesis of $TiO_2$ Flake (f-$TiO_2$)** ..... 67
**2.3.4 Synthesis of $WS_2$-$TiO_2$ and W-$TiO_2$** ..... 68
**2.3.5 Synthesis of Faceted $CeO_2$ Samples** ..... 68
**2.3.6 Synthesis of Faceted $TiO_2$ Samples** ..... 69
**2.3.7 Synthesis of Faceted ZnO Samples** ..... 70
**2.3.8 Photocatalytic Testing** ..... 70
**2.4 Conclusion** ..... 71
**2.5 References** ..... 72
**Chapter 3 Surface Engineering of Ultrathin $WS_2$ as Photocatalysts** ..... 75
**3.1 Introduction** ..... 75
**3.2 Results and Discussion** ..... 77
**3.2.1 Bulk $WS_2$ Exfoliation to FL-$WS_2$** ..... 77
**3.2.2 FL-$WS_2$ Modification by d-Block Metal Doping** ..... 79
**3.2.3 Structural Characterisation on Ru-$WS_2$** ..... 81
**3.2.4 $WS_2$ -$TiO_2$ Assembly for 2D-2D Heterojunctions** ..... 86
**3.2.5 $WS_2$ -$TiO_2$ Heterojunctions for Photocatalytic HER** ..... 90
**3.3 Conclusion** ..... 93
**3.4 References** ..... 94
**Chapter 4 $WS_2$ to W Single-Atom Transformation on $TiO_2$** ..... 98
**4.1 Introduction** ..... 98
**4.2 Results and Discussion** ..... 102
**4.2.1 Transformation from $WS_2$ to W Single Atoms on $TiO_2$ Support** ..... 102
**4.2.2 Structural Characterisations and Analysis of $WS_2$ Decomposition** ..... 106
**4.2.3 Electronic Properties and Photocatalytic Performance** ..... 114

**4.3 Conclusion** ..... 120
**4.4 References** ..... 120
**Chapter 5 Surface Charge Probing on Faceted Metal Oxides under Illumination** ..... 124
**5.1 Introduction** ..... 124
**5.2 Results and Discussion** ..... 127
**5.2.1 $CeO_2$: Tuning the Number of Exposed Facets** ..... 127
**5.2.2 $TiO_2$ and ZnO: Tuning the Ratio of Exposed Facets** ..... 136
**5.2.3 Photocatalytic Study: Effect of Facet-Dependent Charge Accumulation** 148
**5.2.4 Application of Ammonia as a Surface Probe** ..... 150
**5.2.5 Influence of X-ray Photon Energy on Binding Energy Shifting** ..... 152
**5.3 Conclusion** ..... 157
**5.4 References** ..... 158
**Chapter 6 Conclusions and Outlook** ..... 162
**6.1 Conclusions** ..... 162
**6.2 Outlook** ..... 165
**6.3 References** ..... 167
**Appendix** ..... 169
**References** ..... 170

# Declaration

All research works reported in this thesis have not previously been accepted in substance for any degree and are not being concurrently submitted in candidature for any degree. This thesis is conducted by the author unless stated otherwise. All Materials from other sources have been properly and fully acknowledged.

Wentian Niu

## Acknowledgements

Firstly, I would like to thank my supervisor Prof. Shik Chi Edman Tsang, for his guidance and support over the past four years. His insights into scientific topics have inspired me in many ways, for which I am deeply grateful. Furthermore, Prof. Tsang has provided me with numerous opportunities to collaborate with researchers worldwide, which enabled me to complete my research using cutting-edge characterisation techniques. Additionally, I have received tremendous help from Dr. Yiyang (Bruce) Li, who has helped and inspired me both in the lab and in life throughout my DPhil studies and offered me the opportunity to work with him on the NAP-XPS project under Prof. Tsang's supervision. Special thanks go to Prof. Michail Stamatakis and Prof. Xin Tu for the fruitful discussions during my viva and their valuable suggestions regarding this thesis and future work.

I also would like to thank the Tsang group members and my friends, without whose support this DPhil journey would not have been possible. Particularly, I would like to express my gratitude to the following individuals: Prof. Jianwei Zheng, Dr. Yiyang Li, Dr. Yanjie Wang, Dr. Hangjuan Ren, Prof. Huihuang Fang, Prof. Guangchao Li and Dr. Yifei Wang for their advice and support on my DPhil project; Dr. Simson Wu, Dr. Xuelei Pan, Dr. Bryan Ng and Dr. Karen Chan for their assistance on XAS; Dr. Ping-Luen Ho, Dr. Yanjie Wang, Dr. Tianyi Chen, Prof. Huihuang Fang, Mengqi Duan, Zhiyang Zhong, Zhaoyue Weng and Xinyang Li for their help with electron microscopy; Dr. Yiyang Li, Prof. Jianwei Zheng and Dr. Kwan Chee Leung for reactor assembly; Dr. Yifei Wang, Dr. Xuelei Pan and Dr. Hangjuan Ren for their guidance on electrochemistry; Dr. Yiyang Li and Mengqi Duan for conducting NAP-XPS measurements and characterisations of the photocatalysts; Prof. Pu Zhao, Dr. Tugce

Ayvali, Dr. Tatchamapan Yoskamtorn, Dr. Jiaying Mo, Dr. Kwan Chee Leung, Dr. Xuelan Hou, Yuancheng Sun, Haokun Wang, Xiang Li, Cherie Wong, Renzo Leeflang, Jiasi Li and Ziyu Lu for their lab support; Amy Radford and Dori Szalay for organising group events; Dr. Yiyang Li, Dr. Yifei Wang, Mengqi Duan, Cherie Wong, Dongpei Ye and Haozhe Zhang for involving me in their research projects.

Throughout my DPhil studies, I really appreciate the countless support that I received from Prof. Tsang, all our group members and collaborators. Results are properly acknowledged under each figure, and the data analysis was conducted by the author, unless otherwise specified. The data included in this thesis are acknowledged as the following list:

Dr. Weiran Zheng for the AFM measurement on $WS_2$ in Chapter 3.

Dr. Ping-Luen Ho and Prof Huihuang Fang for acquiring TEM images of $WS_2$ and $TiO_2$ in Chapter 3.

Dr. Tai-Sing Wu for performing the XAS measurements on Ru-$WS_2$ in Chapter 3.

Dr. Shaoliang Guan for the XPS measurement on $WS_2$ and $TiO_2$ in Chapter 3 & 4.

Prof. Ye Zhu and Dr. Zhihang Xu for the TEM, EDX and EELS measurements on W-$TiO_2$ in Chapter 4.

Dr. Xuelei Pan for performing Raman and XAS measurements and analysis on W-$TiO_2$ and $WS_2$-$TiO_2$ in Chapter 3 & 4.

Dr. Yifei Wang for conducting EIS measurements in Chapter 3 & 4.

Dr. William Myers and Dr. Yiyang Li for the EPR measurements and tutorial.

Prof. Songhua Cai for the TEM images of faceted metal oxide in Chapter 5.

Prof. Georg Held and Dr. Alex Large for assisting NAP-XPS experiments in Chapter 5.

Dr. Yiyang Li for conducting TRPL and NAP-XPS experiments and analysing the $TiO_2$ and $CeO_2$ NAP-XPS data in Chapter 5.

Last but not the least, I am more than grateful to my beloved parents, grandparents and my family for their unconditional love and support throughout my life. Finally, I would like to express my deepest gratitude to Yifei for her unwavering love, patience, and companionship, which have made my time in Oxford precious, meaningful, and irreplaceable.

# Abstract

Converting solar energy into solar fuels, such as hydrogen, is important to build a sustainable society. However, the current efficiency is still low and makes it challenging for industrial applications. This thesis focuses on applying various surface-engineering strategies on materials in the class of transitional metal oxides and dichalcogenides to improve the photocatalytic performance, which may provide further understanding on the structure-reactivity correlation.

Surface modifications including single-atom doping and heterojunction fabrication on exfoliated few-layer $WS_2$ were first investigated. To explore the possibility of using exfoliated $WS_2$ alone as a photocatalyst, various transitional metals were used as dopants on the $WS_2$ nanosheets. It was found that ruthenium single atoms could be doped into the interlayer region, which might contribute to the reduced charge transfer resistance between layers and the enhanced photocatalytic performance.

Then a $TiO_2$ flake was used as a support of $WS_2$ nanosheets for fabrication of 2D-2D heterojunction, where $WS_2$ played a role as a cocatalyst. The strong internal electric field at the interface promoted the charge transfer process which led to boosted photocatalytic hydrogen evolution rate. Subsequently, due to the instability of $WS_2$, its structural variation on the $TiO_2$ support was investigated. Microscopy and spectroscopy-based characterisation techniques confirmed that the $WS_2$ nanosheets were transformed into W single atoms anchored on the $TiO_2$ surface. The W atoms could functionalise the surface as dopants, achieving promising photocatalytic hydrogen evolution rate comparable to $WS_2$-$TiO_2$.

Lastly, as the exposed facets could also contribute to the catalytic performance, a novel probe-assisted XPS technique was developed for detecting the photo-generated surface charge carriers on facet-engineered metal oxides to study the contribution from exposed facets on the photocatalytic performance. It has been found that charge migration behaviour was highly dependent on the number of exposed facets, which further influenced the photocatalytic activity. These findings could potentially be used for the design of the next generation photocatalysts.

# List of Abbreviations

| | |
|---|---|
| 2D | Two Dimensional |
| AFM | Atomic Force Microscopy |
| AQY | Apparent Quantum Yield |
| BE | Binding Energy |
| CBM | Conduction Band Minimum |
| DFT | Density Functional Theory |
| DI | Deionised |
| EDX | Energy Dispersive X-Ray Spectrometry |
| EELS | Electron Energy Loss Spectrometry |
| EPR | Electron Paramagnetic Resonance |
| EXAFS | Extended X-Ray Absorption Fine Structure |
| FT | Fourier Transform |
| GC | Gas Chromatography |
| HER | Hydrogen Evolution Reaction |
| TEM | Transmission Electron Microscopy |
| n-BuLi | n-Butyllithium |
| NHE | Normal Hydrogen Electrode |
| NMR | Nuclear Magnetic Resonance |
| OER | Oxygen Evolution Reaction |
| PEC | Photoelectrochemical |
| SPV | Surface Photovoltage |
| STH | Solar To Hydrogen |

| | |
|---|---|
| TEOA | Triethanolamine |
| TMP | Trimethylphosphine |
| TRPL | Time-Resolved Photoluminescence |
| UV-Vis DRS | Ultraviolet-Visible Diffuse Reflectance Spectroscopy |
| $O_v$ | Oxygen Vacancy |
| VBM | Valence Band Maximum |
| XANES | X-Ray Absorption Near-Edge Structure |
| XAS | X-Ray Absorption Spectroscopy |
| XPS | X-Ray Photoelectron Spectroscopy |
| XRD | X-Ray Diffraction |
| Z | Impedance |

# List of Publications

### Journal Articles

1. **W. Niu**, Y. Li, Y. Wang, X. Pan, S. C. E. Tsang *et al.*, 2D/2D to 0D/2D Heterostructure Transformation through $WS_2$ Oxidation on $TiO_2$ Support, *In preparation*.

2. **W. Niu**, Y. Li, Y. Wang, D. Duan, S. C. E. Tsang *et al.*, Trimethylphosphine-Assisted Charge Carriers Fingerprinting on Facet-Engineered Metal Oxides by *In-situ* Near Ambient Pressure XPS, 2024, *In preparation*.

3. Y. Li, **W. Niu**, S. C. E. Tsang *et al.*, Integrated Photocatalytic-Photothermal Water Splitting for Quantum Efficiency Exceeding 100%, *Submitted*.

4. Y. Li, H. Zhou, S. Cai, D. Prabhakaran, **W. Niu**, A. Large, G. Held, R. Taylor, X. Wu and S. C. E. Tsang, Electrolyte-assisted polarization leading to enhanced charge separation and solar-to-hydrogen conversion efficiency of seawater splitting, *Nat. Catal.*, 2024, **7**, 77-88.

5. D. Ye, K. Leung, **W. Niu**, M. Duan, J. Li, P. Ho, D. Szalay, T. Wu, Y. Soo, S. Wu, S. C. E. Tsang, Active nitrogen sites on nitrogen doped carbon for highly efficient associative ammonia decomposition, *iScience,* 2024, DOI: https://doi.org/10.1016/j.isci.2024.110571.

6. H. Zhang, Y. Wang, **W. Niu**, T. Yoskamtorn, M. Luo, X. Pan, R. Tayler, S. Day, S. C. E. Tsang, Tuning 2D Perovskite-Graphene Layered Composite for Photocatalysis, 2024, *Sustainable Energy Fuels*, 2024, **8**, 3362-3371.

7. B. Ng, C. Wong, **W. Niu**, H. Garcia, Y. Li, P. Ho, W. Kuo, R. Taylor, K. Taniya, Q. Wei, M. Li, M. Stamatakis and S. C. E. Tsang, Molecular layer-by-layer re-stacking of $MoS_2$–$In_2Se_3$ by electrostatic means: assembly of a new layered photocatalyst, *Mater. Chem. Front.*, 2023, **7**, 937-945.

**Conferences**

Oral Presentation, Probe-Assisted NAP-XPS for Mapping Charge Distribution on Facet-Engineered Photocatalysts, 18$^{th}$ International Congress on Catalysis, 2024.

# Chapter 1 Introduction

## 1.1 Motivation

The high dependence on fossil fuels for modern energy production has raised concerns in recent years. Researchers have reported a 1.7% increase in annual energy consumption and this value is predicted to be further increased in the next few years.[1] Notably, almost 80% of consumed energy was produced from fossil fuels.[2, 3] Accompanying the combustion of fossil fuels, the greenhouse gas emissions and environmental pollution do not meet the requirements for developing a sustainable and environmentally friendly society.[4] To replace fossil fuels, one of the approaches in green chemistry is to reduce the energy input in industrial-scale chemical production by reducing the energy barrier required for chemical reactions, which has been addressed by the application of thermal catalysts in chemical industry.[1, 5, 6] Although progress has been made in decreasing activation energies and selectivity improvements, traditional thermal catalysis requires energy input from non-renewable resources and may still cause environmental issues in the long term.[7] Consequently, the usage of solar energy as a renewable energy resource for photocatalysis has been attracting more attention recently.[8-10]

Despite the sustainability, inexhaustibility, and abundance of solar energy, the process of harvesting it must achieve a certain level of efficiency to convert sunlight into usable and storable chemical fuels.[11] Motivated by these requirements, artificial photosynthetic systems have been developed to imitate the natural photosynthesis process, in which water ($H_2O$) and carbon dioxide ($CO_2$) are used to generate green fuels.[12, 13] Hydrogen ($H_2$) is believed to be one of the most promising solar fuels from artificial photosynthesis, as it is carbon-free, has a

high energy density, and produces water as the only product after combustion.[14] More importantly, since water is one of the most abundant resources on earth, if it can be utilised as the source for $H_2$ production, it will create an ultimate circle for sustainable development with neither greenhouse gas nor environmental pollutant emissions.[15, 16] A schematic illustration of a sustainable cycle using solar energy is shown in **Fig. 1.1**, in which water was converted into $H_2$ in a photocatalytic water-splitting reactor to supply energy for fuel cells and engines.[17] Additionally, the produced $H_2$ can also be used as raw materials together with greenhouse gases (*e.g.* $CO_2$) captured from the atmosphere and industrial waste gases emitted by traditional chemical plants for liquid fuel production.[18]

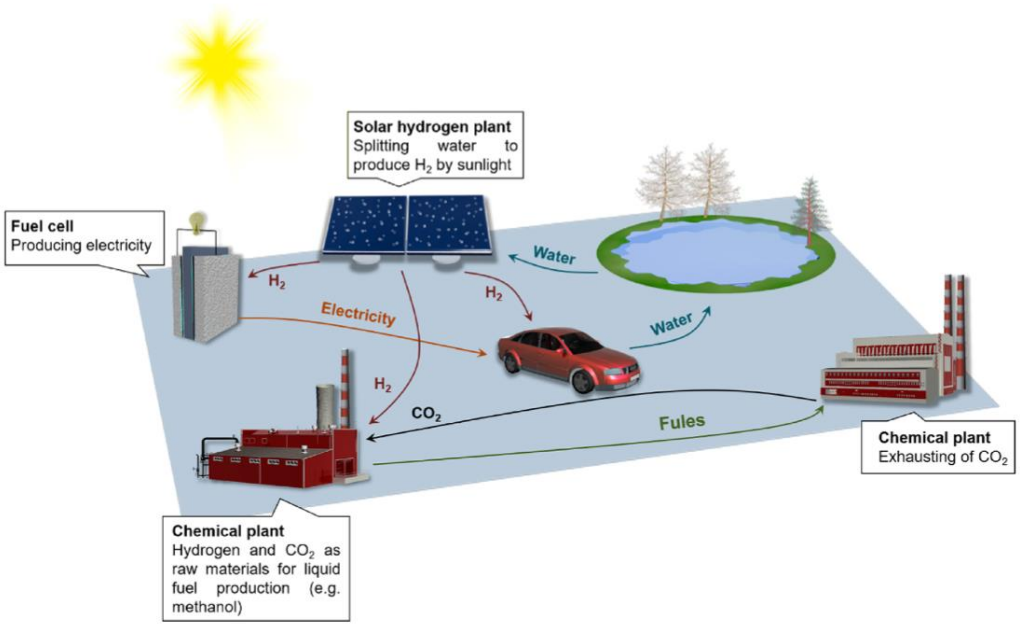



**Figure 1.1** A schematic illustration of potential hydrogen fuel cycle from photocatalytic water-splitting reaction systems for future applications. Reproduced from ref. 17. Copyright 2019 American Chemical Society.

## 1.2 Principles of Photocatalytic Water-Splitting

Catalytic water-splitting into hydrogen ($H_2$) and oxygen ($O_2$) with a ratio of 2 : 1 is an uphill

reaction with the large positive Gibbs free energy of 237 kJ $mol^{-1}$.[19] The overall reaction and half reactions are as the following chemical equations:

Overall reaction:

$2H_2O \rightarrow 2H_2 + O_2$

Hydrogen evolution reaction (HER):

In acidic aqueous solutions: $2H^+ + 2e^- \rightarrow H_2$

In alkaline aqueous solutions: $2H_2O + 2e^- \rightarrow H_2 + 2OH^-$

Oxygen evolution reaction (OER):

In acidic aqueous solutions: $2H_2O \rightarrow O_2 + 4H^+ + 4e^-$

In alkaline aqueous solutions: $4OH^- \rightarrow O_2 + 2H_2O + 4e^-$

The pioneering work on photocatalytic water-splitting was conducted by Fujishima and Honda where a titanium oxide ($TiO_2$) single-crystal photoanode was fabricated for photoelectrochemical (PEC) water oxidation and the experimental set-up is shown in **Fig. 1.2a**.[20, 21] When illuminated with energy greater than the band gap, electron-hole pairs are generated in rutile $TiO_2$ (an n-type semiconductor) after light absorption. Subsequently, the photo-generated electrons can migrate to the Pt counter electrode through an applied external circuit, leaving the photo-generated holes in $TiO_2$. Then the water molecules can be reduced to $H_2$ (HER) at the Pt electrode and oxidised into $O_2$ (OER) at the $TiO_2$ surface, achieving overall water-splitting, which is known as the Honda-Fujishima effect. The Honda-Fujishima effect demonstrates the possibility of using semiconductor materials for solar energy conversion into chemical fuels, and various PEC cells have been developed to optimise the reaction conditions and achieve higher efficiency.[22, 23]

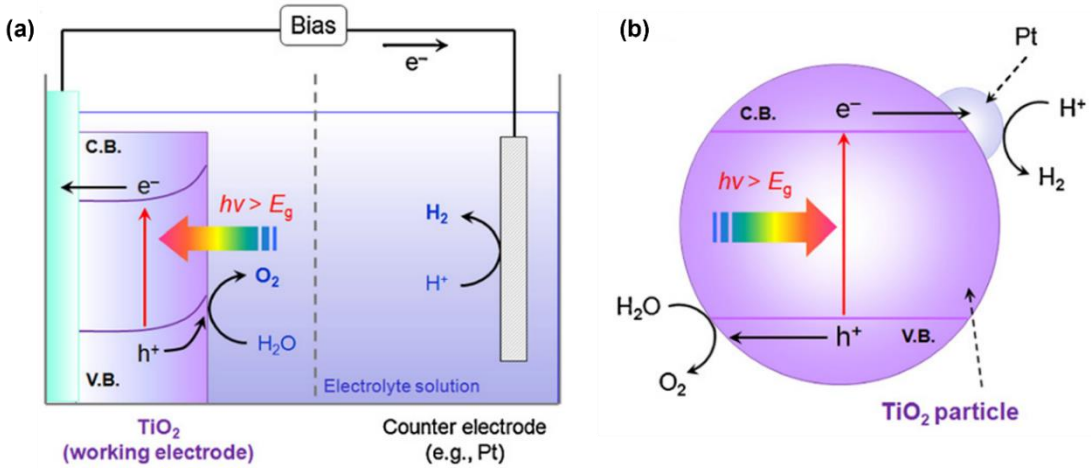



**Figure 1.2 (a)** PEC cell with external bias using rutile $TiO_2$ and Pt as the working and counter electrode; **(b)** General illustration of particulate photocatalysts comparing to the PEC cell. Reproduced from ref. 21. Copyright 2011 Elsevier.

However, as this system still requires energy input from the external bias, it poses challenges in constructing large PEC cells for industrial purposes, especially in areas where electricity is not easily accessible. Additionally, the structural complexity of industrial PEC cells can make the design and fabrication process highly costly compared to laboratory-based PEC cells. Consequently, particulate photocatalyst systems have recently been considered as promising alternatives to the PEC cells. The structure of a particulate photocatalyst can be considered directly coupling the cathode and the anode into a single semiconductor particle (photocatalyst) with metal (cocatalyst)-modified surface, as shown in **Fig. 1.2b**.[21] Using powder catalysts eliminates the need for external bias and wires, which potentially simplifies the structure of photoreactors and significantly reduces the cost of cell production. As a result, the system is believed to be more scalable and feasible to meet the industrial requirements compared to the PEC cells.

The basic principles of overall water-splitting on a semiconductor photocatalyst are shown in

**Fig. 1.3a**. As mentioned previously, the electrons in the valence band of a semiconductor can be excited to the conduction band by the photons that have equivalent or higher energy than the band gap, with holes simultaneously created in the valence band. These photo-generated electrons and holes are commonly referred to as charge carriers or electron-hole pairs, which can subsequently induce reduction and oxidation reactions, respectively. Importantly, the conduction band minimum (CBM) and valence band maximum (VBM) must straddle the relevant potentials to initiate the corresponding chemical reactions as illustrated in **Fig. 1.3b**. Achieving overall water-splitting reactions requires a semiconductor with a CBM more negative than $H^+$ to $H_2$ reduction potential (0 V relative to the normal hydrogen electrode (NHE) at pH = 0) and a VBM more positive than $H_2O$ to $O_2$ oxidation potential (+1.23 V relative to NHE at pH = 0). Therefore, a minimum band gap of 1.23 eV must be reached for a semiconductor photocatalyst which corresponds to around 1000 nm in wavelength (near-infrared region) for the light source. With the additional kinetic overpotentials for the migration of charge carriers and the reaction barriers taken into consideration, a band gap larger than 1.6 eV is typically expected from an ideal semiconductor photocatalyst to effectively utilise the visible light spectrum (400 nm to 800 nm) from the sunlight and to be reactive for generating both $H_2$ and $O_2$ from water.[24, 25] Moreover, the photocatalyst must be resistant to photo-corrosion to ensure stable photocatalytic performance, and the backward reaction should be suppressed to enhance overall efficiency.[26, 27]

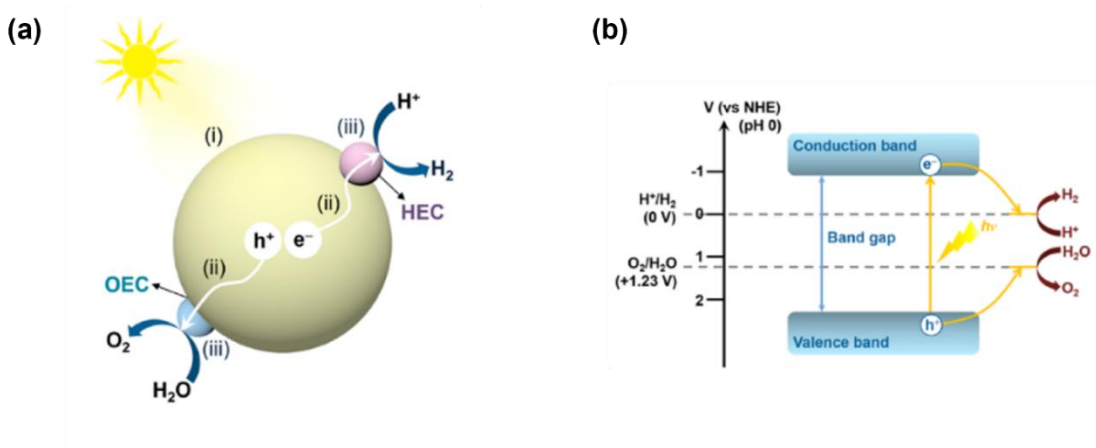



**Figure 1.3 (a)** Illustration of fundamental steps for photocatalytic water-splitting and redox potentials; **(b)** Diagram for photocatalytic water-splitting with potentials required for each half-reaction. Reproduced from ref. 17. Copyright 2019 American Chemical Society.

In light of this, it is well established that there are three fundamental steps for the photocatalytic water-splitting reaction (**Fig. 1.3a**): (i) absorption of photons possessing higher energy compared to the band gap of a semiconductor photocatalyst to create electrons and holes in the valence band and conduction band respectively; (ii) migration of the photo-generated charge carriers to the catalytically active surface sites, which is typically hampered by charge recombination due to inefficient charge separation strategies; (iii) initiation of reduction and oxidation reactions of adsorbed water molecules on reactive sites into $H_2$ and $O_2$ gases, where backward reactions may also occur simultaneously during this process. The structural and electronic properties of a semiconductor photocatalyst can significantly affect the first (photon absorption) and second (charge migration) steps. For instance, synthesising the catalysts with smaller particle sizes can potentially increase the number of reactive sites and reduce the diffusion length of charge carriers, thereby decreasing the possibility of charge recombination. However, when reducing the particle size, the band gap normally becomes larger and the particle crystallinity also becomes poorer.[21] Given that 43% of total solar

energy lies in the visible light regime, the large band gap with insufficient visible light absorption can lead to low efficiency. Additionally, besides reduced light absorption, the loss of crystallinity normally leads to more defect sites which may act as recombination centres for photo-generated electrons and holes, further reducing reaction efficiency.[28] Despite these negative effects, reducing the particle sizes may also provide an additional driving force for photocatalytic HER/OER due to the band-edge potential change.[17] As for the third step, although cocatalysts such as Pt are normally used to accelerate the water-splitting process by providing reactive sites, the reverse reaction in some cases may also be accelerated in some cases, lowering the effectiveness of light utilisation.[29] Consequently, to maximise efficiency of a photocatalyst, multiple factors in this trade-off process need to be carefully considered when designing a novel material for advanced applications.

Due to the complexity of experimental factors affecting both HER and OER, and the difficulty of achieving overall water-splitting with novel photocatalysts, most of the previous works have mainly focused on half-reactions (HER or OER) by adding sacrificial reagents into the reaction system functioning as hole/electron scavengers.[30, 31] For photocatalytic HER, organic reagents such as methanol, lactic acid and triethanolamine are extensively used as HER sacrificial reagents to accelerate the hole depletion and facilitate $H_2$ production, as the organic molecules are prone to be oxidised compared to water molecules.[32] As for photocatalytic OER, since this four-electron transfer process is considered much more challenging than photocatalytic HER, it is generally regarded as the bottleneck for achieving overall water-splitting with high efficiency.[33] To eliminate the effect from the $H_2$ evolution, numerous studies used inorganic reagents such as $KIO_3$, $AgNO_3$ and $FeCl_3$ as electron

acceptors for consumption of photo-generated electrons in the conduction band.[34, 35] Notably, photocatalysts exhibiting activity in both photocatalytic HER and OER with sacrificial reagents may not achieve overall water-splitting once these sacrificial reagents are removed.[21] From the HER perspective, one reason is that the $H_2$ produced may originate from reduction of organic reagents instead of water.[36] In this case, the photocatalyst may not be reactive to water molecules for $H_2$ evolution and removal of the sacrificial reagents may result in significant deactivation. In terms of OER investigation, as different metal ions are introduced in the reaction system, the reduction of metal cations may form nanoparticles on the photocatalyst's surface, which can potentially affect the catalytic performance by serving as an additional cocatalyst or blocking the surface reactive sites. Consequently, it is still challenging to design and fabricate a highly reactive photocatalyst for achieving overall water-splitting.

### 1.3 Efficiency Evaluation and Industrial Prospects

The catalytic performance of a photocatalyst for overall water-splitting can be typically evaluated in various indexes, such as photocatalytic $H_2$ evolution rate for HER ($O_2$ for OER), apparent quantum yield (AQY) and solar-to-hydrogen (STH) conversion efficiency. The $H_2$ evolution rate indicates the speed of the HER reaction for the tested photocatalysts. As for the AQY, it reflects efficiency of photon utilisation at a specific wavelength for $H_2$ evolution, assuming all incident photons are absorbed for photoexcitation neglecting light scattering and reflection, and is expressed by the following equation:

$$AQY\ (\%) = \frac{Number\ of\ H_2\ molecules\ produced\ \times 2}{Number\ of\ incident\ photons} \times 100\% \qquad \textbf{Equation 1.1}$$

Similarly, STH efficiency also indicates how effectively light energy is utilised for $H_2$

production, but instead of considering photons at a certain wavelength, it calculates the fraction of the output energy of produced $H_2$ from the total energy of the sunlight to obtain overall conversion efficiency, which is defined by:

$$STH\ (\%) = \frac{output\ energy\ as\ H_2}{input\ energy\ as\ solar\ incident\ light} \times 100\%$$
$$= \frac{H_2\ production\ rate\ (mol\ s^{-1}) \times 237000\ (J\ mol^{-1})}{100\ (mW\ cm^{-2}) \times Area\ (cm^2)} \times 100\% \quad \textbf{Equation 1.2}$$

From previous studies, to meet the industrial requirements for $H_2$ production in industrial scale, STH efficiency of a photocatalytic reaction system should reach around 10%.[1] However, in most of the previous studies, STH efficiency has only reached around 1%, which is far from satisfactory.[37] Therefore, further fundamental studies are needed on the photoreactor design and the fabrication of effective, stable photocatalysts to enhance overall efficiency.

Despite the aforementioned efficiency indexes, to illustrate the effects of the three established steps of photocatalysis, overall solar energy conversion efficiency ($\eta_{total}$) can be defined as:

$$\eta_{total} = \eta_{absorption} \times \eta_{separation} \times \eta_{reaction} \quad \textbf{Equation 1.3}$$

where $\eta_{absorption}$ is the efficiency of absorbed photons creating electron-hole pairs; $\eta_{separation}$ is the fraction of photo-generated charge carriers being separated and migrating to the reactive sites at the liquid-solid interface without recombination; $\eta_{reaction}$ is the efficiency of charge carriers being consumed for the desired chemical reactions.[17] Optimising any of these three factors can enhance overall efficiency. Specifically, the band structure should be optimised for efficient solar light absorption; charge carrier recombination should be minimised to prevent energy loss as heat; and the catalyst surface should be designed for high activity while inhibiting reverse reactions, resisting poisoning and preventing photo-corrosion.

Unfortunately, current characterisation techniques can only provide qualitative information, and it is still challenging to obtain the exact value of these three factors. Consequently, this equation is not as commonly used as AQY and STH efficiency for evaluating photocatalysts. Nevertheless, it can serve as a general guideline when designing new photocatalysts.

Various strategies have been developed in laboratories to achieve the industrial goals of photocatalytic reaction systems.[38] Among these strategies, surface engineering of photocatalysts is one of the most widely applied methodologies.[38-40] In addition to accelerating the chemical reactions by introducing surface reactive sites, research has shown that the electronic properties of a photocatalyst for light absorption and charge separation efficiency can be optimised through proper surface modification techniques, including but not limited to introducing single-atom sites as dopants, forming heterojunctions with other materials, and tailoring exposed facets during synthesis, which will be discussed in detail in the next section.

## 1.4 Surface Engineering Strategies for Aiding Photocatalysis

### 1.4.1 Single-Atom Engineering

Loading nanoscale metal particles as cocatalysts on the photocatalyst surface has been widely studied in the past few years.[41-45] Tremendous progress has been made in terms of identifying reactive sites, understanding the reaction mechanism and enhancing the catalytic performance. However, from an atomistic perspective, only the few exposed atoms on the topmost surface of the cocatalysts can be involved in the chemical reactions. As the exposed atoms only count small proportions in the loaded nanoparticle, atom-utilisation efficiency is still very low. Leaving the majority of atoms unused for chemical reactions potentially increases cost

unnecessarily, hindering practical applications (**Fig. 1.4a**).[46] Moreover, from the charge transfer view, only the atoms at the interface between the cocatalyst and the support can determine the actual rate of charge migration and insufficient interface contact can lead to relatively low charge migration efficiency.[46] With low atom-utilisation efficiency and poor charge transfer rate, a long average migration distance is expected for photo-generated charge carriers before initiating chemical reactions, resulting in severe charge recombination and low STH efficiency.[47]

Emerging single-atom photocatalysts provide potential solutions for this issue. Zhang *et al.* were the first to propose the terminology of single-atom catalysts where they successfully loaded isolated atoms as cocatalysts on the catalyst support.[48] It is believed that one of the most important advantages of decreasing the size of the cocatalysts to the atomic scale is the optimisation of activity and selectivity by increasing the number of unsaturated coordination sites and achieving 100% atom-utilisation efficiency compared to the traditional nano-sized cocatalysts (**Fig. 1.4b**).[49] The increased reactive sites can further reduce the average travel distance for the charge carriers to initiate chemical reactions, inhibiting the possibility of charge recombination. Additionally, the metal-support interaction is also maximised as all the introduced atoms bind to the surface atoms on the catalyst support, normally by covalent or ionic interactions.[50] From the theoretical perspective, since the reaction centres at single-atom sites are relatively well-defined compared to traditional nanoparticle cocatalysts, a single-atom catalyst is considered to be an ideal platform for studying the reaction mechanisms and understanding the structure-activity relationships.[51] Consequently, various studies have been conducted in this research field to explore the contribution and advantages of applying the

single-atom cocatalysts in catalytic processes. Recent progress in single-atom catalyst applications for photocatalytic HER is summarised in **Table A1**.

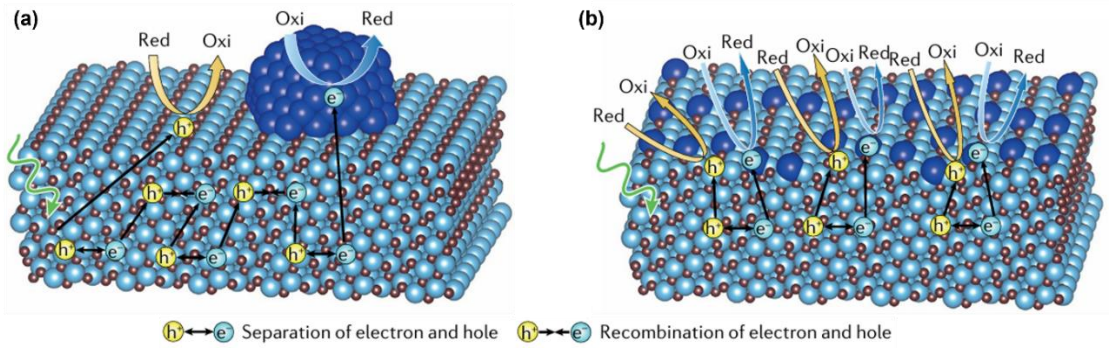



**Figure 1.4** Structural comparison between loading **(a)** traditional nanoparticle cocatalysts and **(b)** single-atom cocatalysts on the catalyst support. Loading single-atom cocatalysts potentially increases the reactive sites and reduces the average travel distance of the photo-generated charge carriers. Reproduced from ref. 46. Copyright 2022 Springer Nature.

More specifically, based on the three fundamental steps of photocatalysis, the effect of introducing single atoms into a photocatalyst can be investigated in terms of light harvesting efficiency, the charge transfer dynamics, and the surface reaction mechanisms. For the first step, it can influence light harvesting efficiency of particulate photocatalysts by modifying their band structure.[52] The modification is normally caused by introducing extra energy levels with an increased density of states.[53] As a result, red shifts are typically observed in the ultraviolet-visible (UV-Vis) absorption spectra due to single-atom modification.[54] For instance, Li *et al.* reported that the presence of Pt single-atom sites in graphitic carbon nitride ($g\text{-}C_3N_4$) could provide additional energy states in the mid gap region for light absorption ranging from 460-900 nm (**Fig. 1.5**).[55] This was verified by the photocatalytic tests under 420 nm and 550 nm light source, where increased concentration of Pt in $g\text{-}C_3N_4$ showed higher performance under 550 nm irradiation, while all the samples exhibited similar activity under

420 nm irradiation in contrast. Detailed density functional theory (DFT) studies conducted by Tong *et al.* illustrated changes in the electronic structure of g-$C_3N_4$ after loading different metal single-atom cocatalysts.[56] Besides the observation of increased photocatalytic activity, the band gaps of g-$C_3N_4$ were found to be decreased from 2.48 eV to 1.54 eV, 1.48 eV and 0.96 eV with Pt, Pd and Au single atom loaded on the g-$C_3N_4$ surface. A smaller band gap broadens the light absorption range, particularly in the visible light region, which can potentially increase solar energy utilisation efficiency.

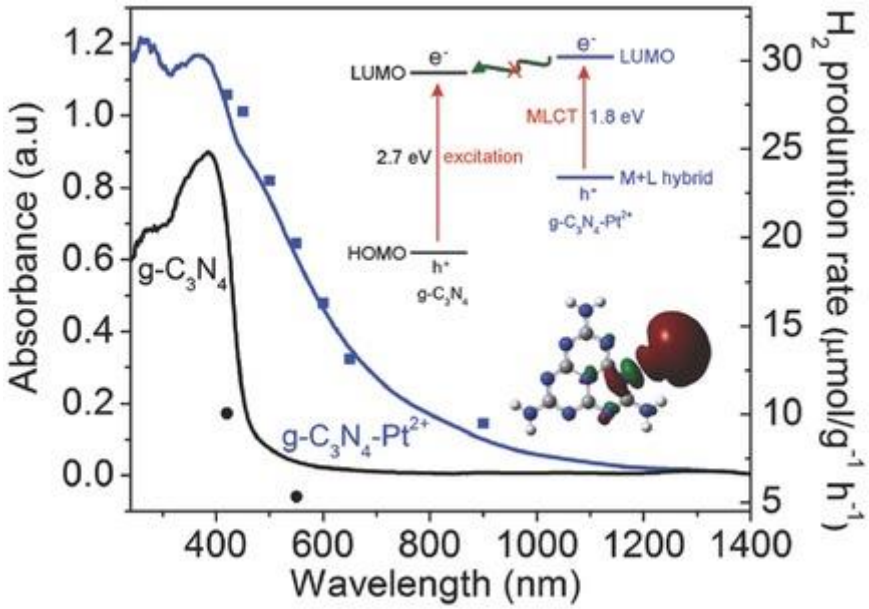



**Figure 1.5** UV-Vis absorption spectra difference after introducing Pt single-atom sites in g-$C_3N_4$. The band gap of g-$C_3N_4$ was significantly reduced after loading Pt single atoms. Reproduced from ref. 55. Copyright 2016 John Wiley and Sons.

In terms of charge separation, besides light absorption efficiency, energy states in the mid-gap region created by single-atom loading can also locally trap photo-generated charges, suppressing charge recombination.[47] For instance, Liu *et al.* observed that the average lifetimes of photo-generated charge carriers in open-circuit voltage decay were extended after Co single atom loading on g-$C_3N_4$.[57] The following experimental and theoretical studies

showed that extra energy states were formed at the presence of $Co_1$-$P_4$ sites on g-$C_3N_4$, which could accommodate electrons, separating them from holes for suppressing charge recombination as shown in **Fig. 1.6**. Besides the modification on the band structure of photocatalysts, the introduced metal single atoms can also serve as a charge transfer channel for interlayer electron migration in layered two-dimensional (2D) materials. Specifically, the weak van der Waals interaction between stacked layers in 2D materials makes it challenging for interlaminar charge migration and the photo-generated electrons and holes are mostly confined in the same layer, resulting in insufficient charge separation. With single-atom sites inserted in the interlay region, it can significantly lower the charge transfer resistance, allowing electrons and holes to separate onto different layers to achieve efficient charge separation. For instance, Cao *et al.* successfully inserted Pd single atoms into the interlayer region of g-$C_3N_4$ (Pd/g-CN) to facilitate the charge transfer between layers (**Fig. 1.7a**).[58] The reduced radii in the Nyquist plot of Pd/g-CN compared to the pristine g-$C_3N_4$ nanosheets (CN-NS) as illustrated in **Fig. 1.7b**, indicate the decease of charge resistance at the solid/liquid interface, which may be attributed to inserted Pd single atoms acting as charge transfer bridges of photo-generated electrons and holes, leading to increased charge transfer efficiency. As a result, the $H_2$ production rate could be boosted from nearly zero in CN-NS to 6688 μmol $h^{-1}$ $g^{-1}$, which was also 1.8 times higher than Pt/g-CN.

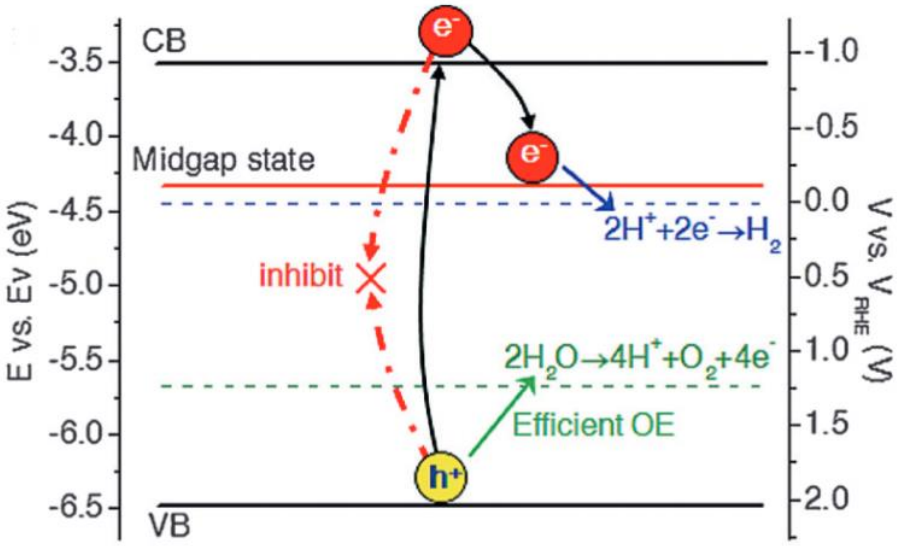



**Figure 1.6** Mid-gap energy level formation with Co single-atom doped g-$C_3N_4$, facilitating the charge separation. Reproduced from ref. 57. Copyright 2017 John Wiley and Sons.

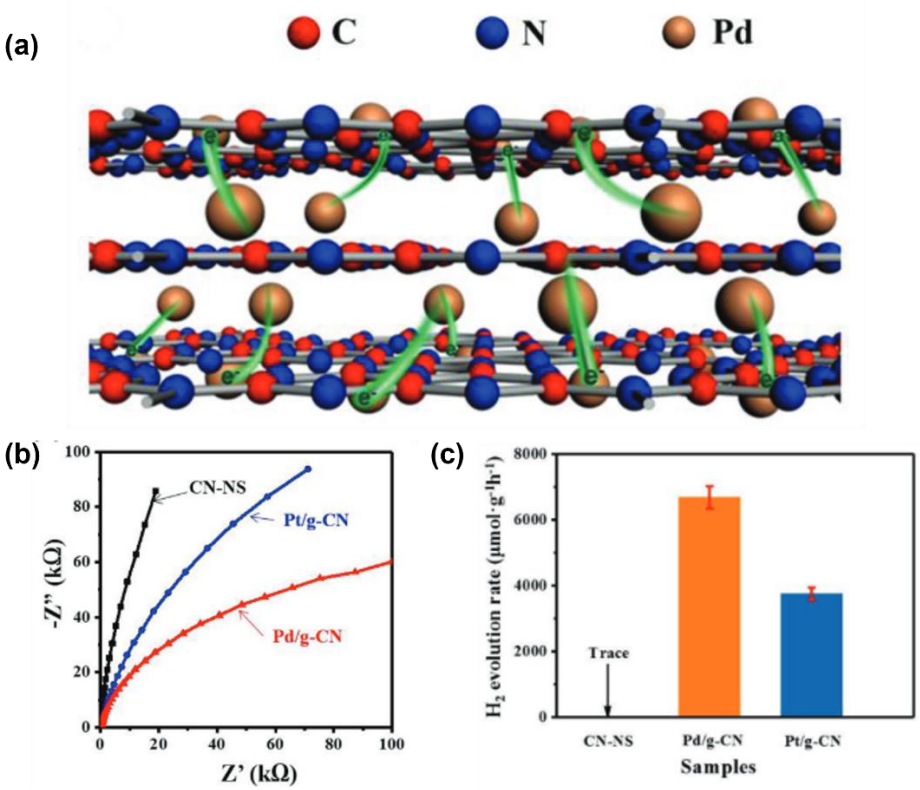



**Figure 1.7 (a)** Structural illustration of Pd single-atom intercalation between g-$C_3N_4$ layers with enhanced interlayer charge transport efficiency; **(b)** Nyquist plot generated from electrochemical impedance spectroscopy (EIS) testing, where Pd/g-CN showed the lowest charge transfer resistance; **(c)** Photocatalytic HER rate of different g-$C_3N_4$ samples. Reproduced from ref. 58. Copyright 2018 John Wiley and Sons.

As for the surface reactions, the activity and selectivity of photocatalysis are highly dependent on the geometric and electronic structure of the photocatalysts.[59, 60] By tuning the surface features for creating a different coordination environment of the single-atom dopant, it is possible to alter the adsorption strength of the reactants and the reaction pathways for different products. For example, Ban *et al.* reported a single-atom Ag catalyst loaded on $TiO_2$ supports for photocatalytic $CO_2$ reduction with high selectivity to $CH_4$.[61] The introduced Ag single-atom sites could facilitate the adsorption of $CO_2$ molecules for initiating the catalytic reactions, and the synergetic effect between Ag and adjacent Ti sites could stabilise *CO and *CHO intermediate while activating $H_2O$ for $CH_4$ production revealed by theoretical studies (**Fig. 1.8)**. A similar effect can be seen from the work conducted by Di *et al.*, where Co single-atom sites loaded on $Bi_3O_4Br$ could benefit the $CO_2$ adsorption with lowered activation energy barrier by stabilising the *COOH intermediates at the adsorption sites for producing CO, and altering the rate determine step to *CO desorption.[62] Apart from the surface geometric structure, selectivity could also be tuned from the electronic structure modification originating from band structure variation.[50] Besides enhancing light harvesting and facilitating charge separation as previously discussed, the mid gap states introduced by single-atom doping can also alter the band-edge potential for different redox reactions, thus modulating selectivity for specific reactions with suitable redox potentials.[57]

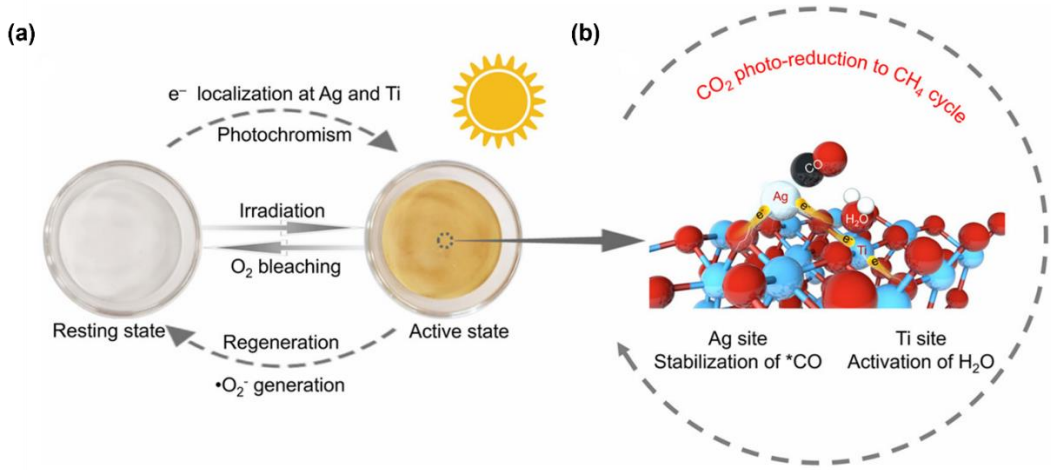



**Figure 1.8** A schematic illustration of $TiO_2$ with Ag single-atom modified surface for the **(a)** photochromic cycle and **(b)** $CO_2$-to-$CH_4$ conversion cycle. Reproduced from ref. 61. Copyright 2024 The Royal Society of Chemistry.

### 1.4.2 Heterojunction Engineering

In the second step of the photocatalytic process, most of the photo-generated electrons and holes suffer from recombination if ineffective charge separation strategies are applied, leading to dissipation of solar energy in the form of heat release. Mimicking the natural photosynthesis mechanism (known as Z-scheme) offers a potential solution to this issue where the light-generated charge carriers are separated by using two distinct photosystems with an effective electron transfer chain (**Fig. 1.9**).[63] By artificially creating intimate contact between two materials with band alignments similar to the natural photosynthesis system, it is possible to achieve more effective charge separation with efficient interfacial charge transfer channels and driving forces to separate charge carriers from one component to the other, which is widely known as heterojunctions. Heterojunction engineering is believed to be the one of most powerful methods for spatially separating the electron-hole pairs. In such systems, the experimentally measured lifetimes of photo-generated charge carriers can be

normally prolonged compared to single-component systems, and a positive correlation between the extended lifetime and the enhanced photocatalytic performance can be observed.[64] In general, based on the band structure of the involved materials, heterojunctions can be classified into two categories: semiconductor-semiconductor heterojunctions and semiconductor-conductor heterojunctions. For semiconductor-conductor heterojunctions, the conductor can be both metal particles and metallic materials such as 1T-$MoS_2$, graphene and carbon nanotubes. Recent advances in heterojunctions for photocatalytic HER are summarised in **Table A2**.

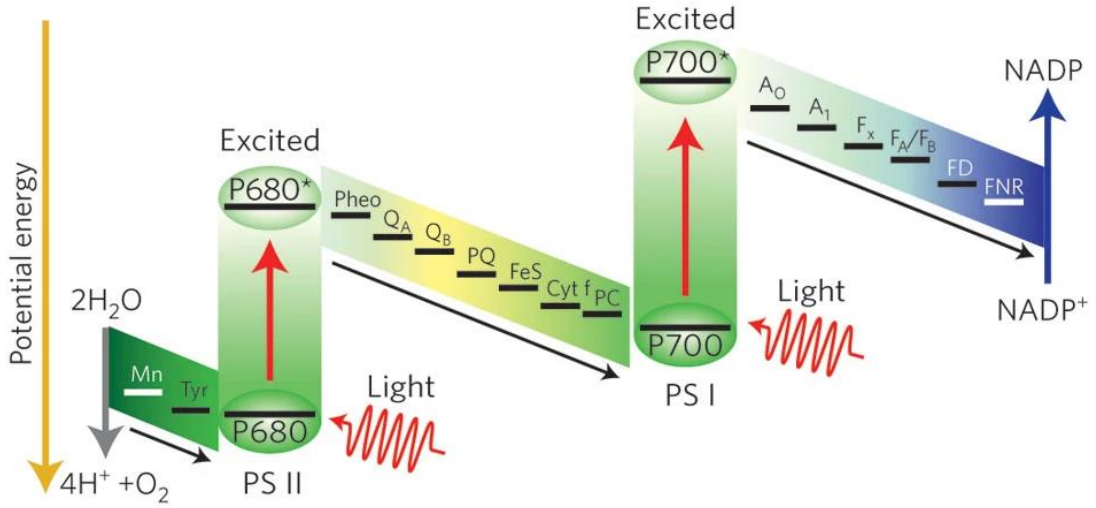



**Figure 1.9** A schematic illustration of charge-separation in natural photosynthesis process. The two different photosynthesis systems are connected by an effective electron transferring channel. Reproduced from ref. 63. Copyright 2012 Springer Nature.

Semiconductor-semiconductor heterojunction engineering normally involves two semiconductors with different band structures. Based on the band alignments, there are three possibilities of semiconductor-semiconductor heterojunctions originating from the band alignments, which are classified as type-I, type-II and type-III heterojunctions as shown in **Fig. 1.10**.[65, 66] For type-I (straddling gap) heterojunctions, the VBM and CBM of one

semiconductor is more negative and positive than the other. With this alignment, photo-generated electrons and holes cannot be separated effectively, as the charge carriers will accumulate on the semiconductor with lower redox potential under this band alignment. In type-III (broken gap) heterojunctions, the band gaps of two materials do not overlap and the charge transfer between two components is restricted with this structure. Consequently, it is similarly ineffective for achieving spatial charge separation as in type-I heterojunctions. As for type-II (staggered gap) heterojunctions, with the VBM and CBM of one semiconductor having less positive VBM and more negative CBM compared to the other semiconductor, this band alignment allows photo-excited electrons to migrate from one semiconductor to the other for reduction reactions, while driving photo-generated holes to migrate to the opposite direction simultaneously for oxidation reactions. In this way, the electrons and holes are spatially separated to different semiconductors as shown in **Fig.1.10b** and prolonged lifetime of charge carriers can be normally achieved. This charge transfer mechanism under this band alignment is normally known as conventional type-II heterojunctions, where numerous studies have been conducted applying this strategy for enhancement of overall photocatalytic activity.[66] For example, Hong *et al.* constructed a $BiVO_4/WO_3$ heterojunction photocatalyst for water oxidation, where efficient charge separation resulted in higher photocurrent and the activity could be enhanced up to 7.3 times higher than bare $BiVO_4$.[67]

Moreover, under the type-II heterojunction alignment, the charge separation can be further optimised when a p-type semiconductor with more negative CBM and a n-type semiconductor with more positive VBM are involved for the heterojunction fabrication. It is well-established that the Fermi level of a n-type semiconductor is closer to the CBM while

for a p-type semiconductor, it is closer to VBM. The difference in Fermi levels leads to the formation of a p-n junction at the interface between two materials accompanied by band realignment, providing an additional internal electric field with electrons transferred from the n-type to the p-type semiconductor, making the n-type semiconductor more positively charged and the p-type semiconductor more negatively charged.[68] Upon illumination, the internal electric field provides extra driving forces for charge separation, driving the photo-generated electrons to the n-type semiconductor, and holes to p-type semiconductor to achieve longer charge carriers' lifetime.[69]

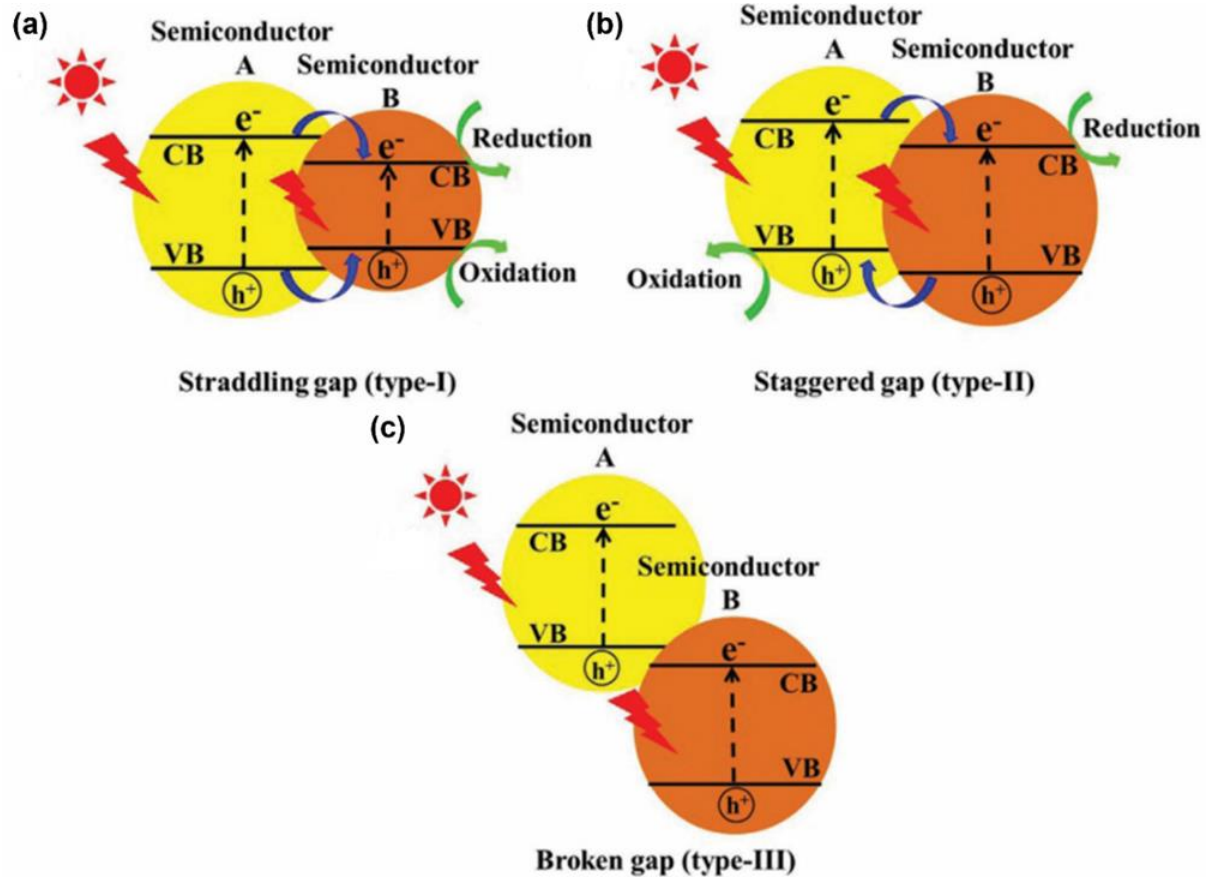



**Figure 1.10** Three possibilities of heterojunctions based on band alignments of **(a)** type-I, **(b)** type-II and **(c)** type-III semiconductor-semiconductor heterojunctions. Reproduced from ref. 66. Copyright 2017 John Wiley and Sons.

Notably, even with the same band alignment, experimental evidence suggests that the

mechanism of charge transfer could be different from conventional type II heterojunctions and p-n junctions. It is known as direct Z-scheme (or S-scheme) reported by Yu's research group in 2013.[70] This charge transfer process is similar to the natural Z-scheme photocatalytic system, but the electron mediator is not required (**Fig. 1.11**).[71] In this case, opposite to p-n junctions, the semiconductor with a more negative CBM also possesses a higher Fermi level compared to the other semiconductor, which can be noted as the reduction photocatalyst (RP) and the oxidation photocatalyst (OP), respectively. Consequently, an internal electric field at the interface is formed after the contact between two semiconductors, where the OP, with a more positive VBM, becomes negatively charged, and the RP, with a more negative CBM, becomes positively charged. Under this internal electric field, the photo-generated electrons from the conduction band of OP are preferably transferred to the valence band of RP, where the migration of electrons is further driven by the Coulombic attraction from the holes in the valence band of RP. Simultaneously, electron transfer from the conduction band of RP to the conduction band of OP, and hole transfer from the valence band of OP to the valence band of RP are both prohibited due to the electric field, Coulombic repulsion and band bending. With this charge transfer mechanism, not only the electrons and holes are spatially separated with the direct Z-scheme heterojunction, but also the redox potentials are maximised for accelerating the catalytic reaction rate.[72]

To investigate the charge transfer mechanism for a given heterojunction photocatalyst, several experimental methodologies have been established. For instance, due to the redox potential difference between conventional type-II heterojunctions and direct Z-scheme heterojunctions, radical experiment results can be significantly different, where some

characteristically active species can be trapped and detected by the electron spin resonance (EPR) spectroscopy.[73] By comparing the EPR signal differences and combining with the experimentally verified band structure of each components, this allows differentiation between the two charge transfer mechanisms. Additionally, if internal electric field has been constructed after forming the heterojunction, *in-situ* X-ray photoelectron spectroscopy (XPS) can also be applied to study the electron density difference under light and dark conditions. As the charge migration mechanism is opposite in conventional type-II heterojunctions compared to the direct Z-scheme, it is possible to differentiate them by combining the XPS peak shift under illumination with the original band structure of two materials forming heterojuntions.[74]

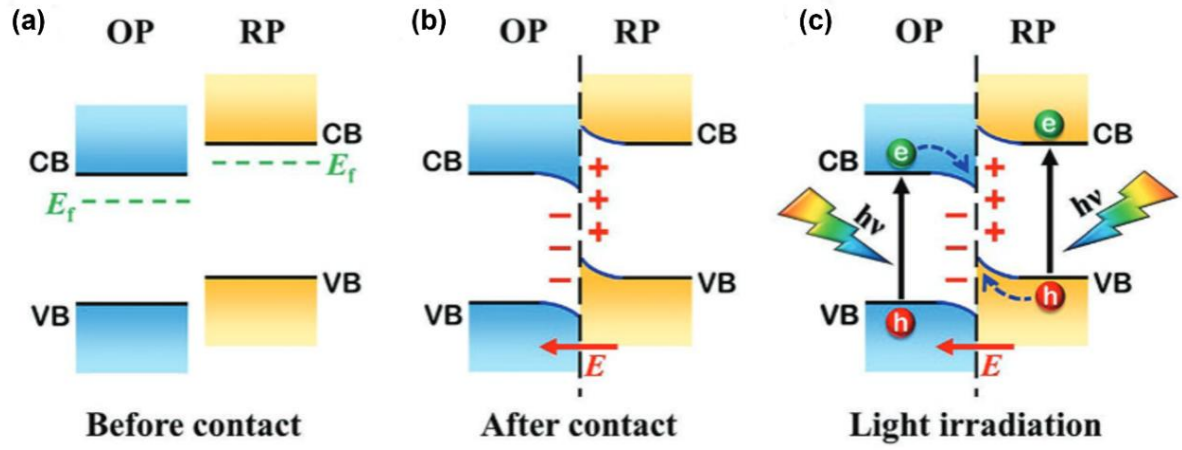



**Figure 1.11 (a, b)** Band structure before and after contact of two semiconductors; **(c)** Charge transfer mechanism for direct Z-scheme heterojunctions under light irradiation. Reproduced from ref. 71. Copyright 2022 John Wiley and Sons.

Fabrication of semiconductor-conductor heterojunctions is another important strategy for improving the performance of heterogeneous photocatalysts. The contact between a semiconductor (normally n-type semiconductor) and a conductor (metal/metallic materials)

will also lead to realignment of Fermi energy levels, similar to semiconductor-semiconductor heterojunctions.[75] Ideally, when a conductor with a higher work function is in contact with a semiconductor, the electrons will migrate from the semiconductor to the conductor due to the Fermi level realignment, which makes conductors more negatively charged and semiconductors more positively charged. This potential energy barrier helps to prevent electrons transferring from the conductor to semiconductor which is known as Schottky barrier (**Fig. 1.12**).[75] At excitation state, the Schottky barrier can trap the photo-excited electrons in the conductor which in turn prevents the charge recombination.[76] This partially explains the reason that loading noble metals including Au, Ag and Pt as cocatalysts can significantly increase the photocatalytic activity, besides providing surface reactive sites. Another important class of conductors for semiconductor-conductor heterojunctions includes metallic materials such as graphene and carbon nanotubes. These materials normally have a large surface area and high conductivity, which can greatly improve the photocatalytic performance by effectively promoting electron migration.[77, 78]

Recently, transition metal dichalcogenides (TMDs) such as $MoS_2$ and $WS_2$ have been extensively studied as promising candidates for hydrogen evolution in both photocatalysis and electrochemical catalysis.[79, 80] Their metallic 1T phase can be applied as reactive cocatalysts when forming the heterojunction with wide range of photocatalysts. It has lower cost compared to noble metals, and owing to its highly active edge sites for HER, it can exhibit even higher activity compared to other metallic materials like graphene.[81] For instance, Li *et al.* used ultrathin $Bi_{12}O_{17}Cl_2$ nanosheets to form a 2D Janus bilayer junction with $MoS_2$ monolayers for highly efficient hydrogen evolution under visible illumination.[82] It

was found that an internal electric field inside the $Bi_{12}O_{17}Cl_2$ could drive photo-generated electrons transferring to the $MoS_2$ monolayers through Bi-S bonds, which could facilitate the charge migration and separation. Following that, as the edge of $MoS_2$ layers could serve as highly active sites for HER, the fabricated 2D-2D heterojunction photocatalysts exhibited 38 times higher activity than pristine $Bi_{12}O_{17}Cl_2$.

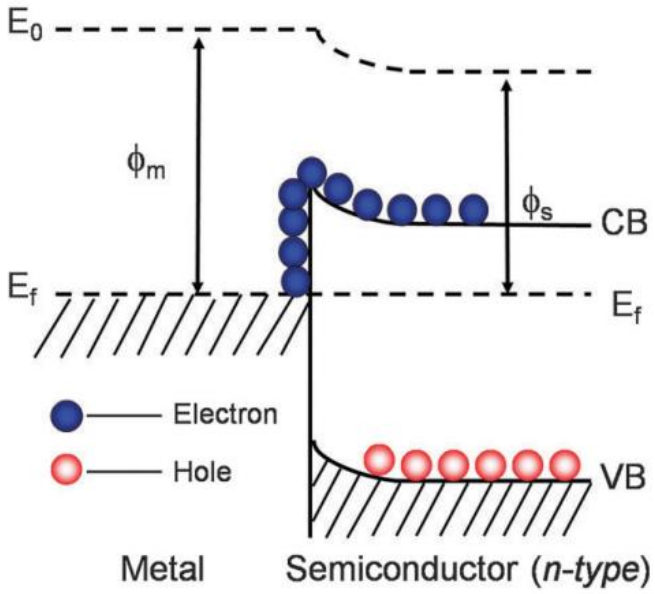



**Figure 1.12** Schottky contact between semiconductor and metal/metallic materials. Reproduced from ref. 75. Copyright 2014 The Royal Society of Chemistry.

### 1.4.3 Facet Engineering

It is well established that modifying the exposed facets of a heterogeneous catalyst significantly impacts catalytic performance.[83] Due to the difference in atomic arrangements, changing the exposed facets can lead to variation in surface energies and catalytic reactivities.[84] In traditional thermal catalysis, for instance, doping the high energy (111) facet of MgO with Ru could result in 4.5 times higher catalytic activity for ammonia synthesis compared to conventional MgO catalysts.[85] This enhancement in activity could be attributed

to the high affinity of the exposed (111) facet for hydrogen species, which prevents hydrogen poisoning at reactive Ru sites. Similar surface-dependent characteristics can also be observed in photocatalysis and recent developments of facet-engineered photocatalysts have been listed in **Table A3**. It has been shown by previous DFT studies that the activity of water-splitting reactions is highly dependent on the exposed facet of anatase $TiO_2$ nanoparticles, following the order of (001) > (100) > (110) > (101).[86] Furthermore, it should be noted that the surface structure not only affects the surface activities, but also has a significant impact on the electronic structures of the catalyst, which can determine the redox potentials and driving forces for different chemical reactions.[87] For instance, Xu *et al.* conducted a detailed study on the effect of the electronic structure of $TiO_2$ facets on the photocatalytic HER performance.[88] The band structures of $TiO_2$ samples with different dominant exposed facets were carefully studied (**Fig. 1.13a**), and the CBMs were found in the order of (111) > (010) > (101) > (001) (**Fig. 1.13b**). The more negative CBMs could offer higher reduction potentials (*i.e.* greater driving forces) for $H_2$ revolution, thus the sample with the (111) facet exposed exhibited the highest activity among all the samples.

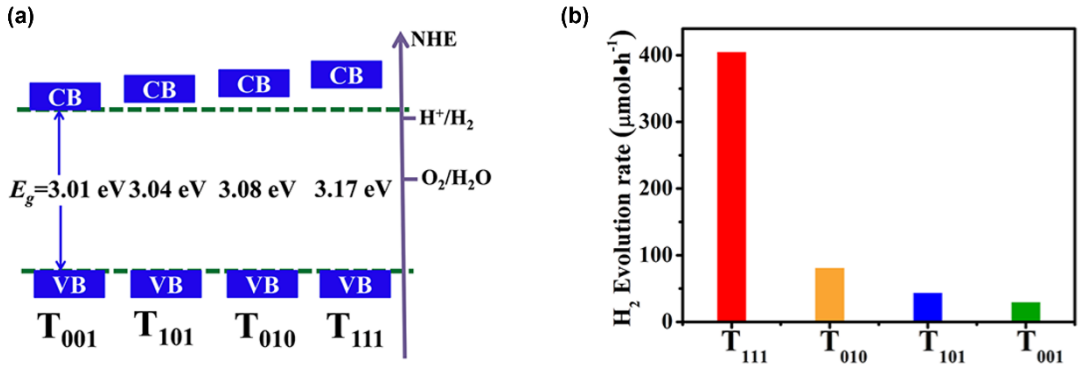



**Figure 1.13 (a)** Band structures of anatase $TiO_2$ samples with varied exposed facets and **(b)** the corresponding photocatalytic HER performance. Reproduced from ref. 88. Copyright 2013 American Chemical Society.

From the surface activity perspective, it seems that the percentage of the most reactive facet exposed on the surface should be maximised to achieve the highest overall catalytic performance. However, previous research showed that the reactivities were optimised when the two exposed facets were balanced, instead of maximising the most reactive one.[89] Due to differences in the electronic structures of facets, a band alignment like type-II heterojunctions can be formed with two types of facets exposed on the catalysts' surface.[90] As mentioned in heterojunction engineering, this band alignment can facilitate the spatial charge migration, inhibiting the possibility of charge recombination. In this case, one facet is positively charged while the other is negatively charged under light, enabling reduction and oxidation reactions to occur on different sites. The evidence of this facet-dependent charge accumulation was firstly established by Ohno *et al.*, who found that photoreduction and photooxidation products were deposited on distinct facets of $TiO_2$ particles based on scanning electron microscopy (SEM) images.[91] More specifically, the $Pt^{4+}$ ions could be selectively reduced onto the (110) facet of rutile $TiO_2$ and the (011) facet of anatase $TiO_2$, while $Pb^{2+}$ ions were oxidised onto the (011) facet of rutile $TiO_2$ and the (001) facet of anatase $TiO_2$ (**Fig. 1.14**). Following this study, similar results were observed on numerous faceted materials, and different techniques were applied to verify facet-dependent charge accumulation. For instance, single-molecule fluorescence spectroscopy was applied to directly visualise the distribution of photo-generated charge carriers under illumination (**Fig. 1.15**).[92, 93] The probe molecules (redox-responsive fluorogenic dyes) were first adsorbed to different facets of the synthesised crystals. Under illumination, the probe molecules could become highly fluorescent when interacting with the photo-generated charge carriers. Consequently, the distribution of surface-

accumulated charge carriers could be mapped using the fluorescence signal from the image (**Fig. 1.15b**).

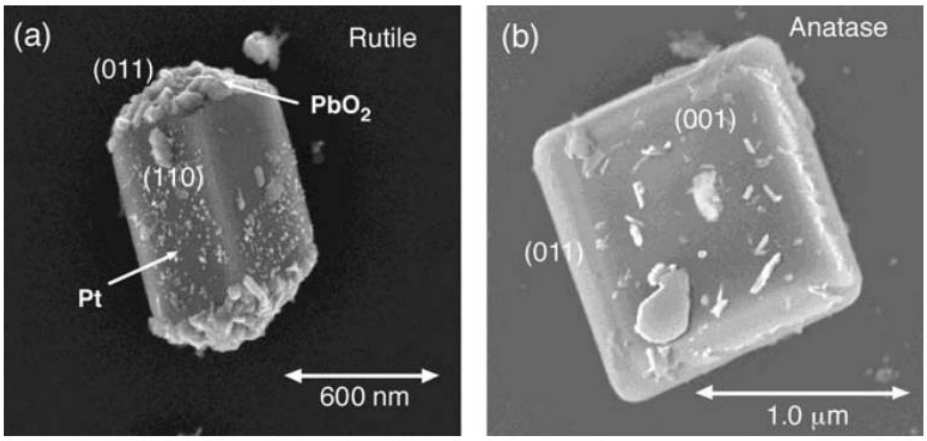



**Figure 1.14** Facet-selective photo-deposition of Pt and $PbO_2$ on **(a)** rutile $TiO_2$ and **(b)** anatase $TiO_2$. Reproduced from ref. 91. Copyright 2002 The Royal Society of Chemistry.

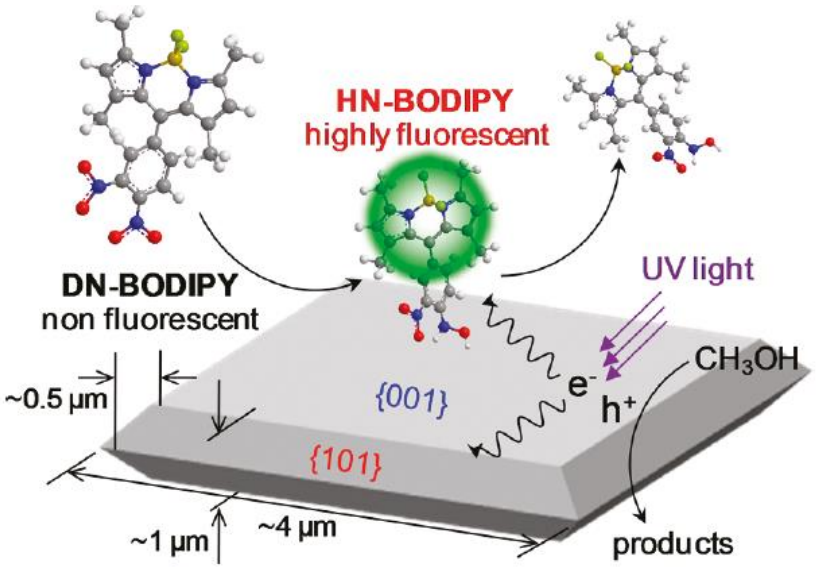



**Figure 1.15** Generation of highly fluorescent species from probe molecules adsorbed on the faceted photocatalyst under illumination. Reproduced from ref. 93. Copyright 2011 American Chemical Society.

Detailed studies on the contributions of facet-dependent charge accumulation on

photocatalysts were conducted by Yu's group in 2014.[94] The percentage of exposed (001) and (101) facets of anatase $TiO_2$ was systematically tuned to investigate the photocatalytic activity for $CO_2$ reduction, where the term 'surface junction' was proposed to describe this phenomenon. Recently, the first industrial attempt of facet-engineered photocatalysts was developed by Domen's group in Japan, where they successfully synthesised a faceted $SrTiO_3$:Al photocatalyst to achieve overall water-splitting with 96% quantum efficiency under 350 nm and 360 nm light sources.[95] Then this photocatalyst was used for constructing a 100 $m^2$ photoreactor for solar hydrogen production from water, which successfully set an example to demonstrate the possibility for large scale photocatalytic water-splitting in a safe and feasible way.[96]

The mechanism has been extensively studied by Li's group, where a Kelvin probe was applied to measure the surface photovoltage (SPV) potential of various faceted semiconductors under different experimental conditions.[97-100] By comparing the SPV results from different facets, they proposed a surface band bending model where various exposed facets induced a built-in electric field, providing an additional driving force for charge migration to distinct surface sites. Moreover, loading cocatalysts such as Au and $MnO_x$ on the surface was proved to further facilitate the band bending, strengthening the built-in electric field, and improving the photocatalytic activity.[101] Recently, another breakthrough was made by Li's group where they successfully illustrated an increase in electric field by enhancing the isotropic effects through higher surface defect density to drive photo-generated holes to the surface for catalytic reactions (**Fig. 1.16a**).[102] A positive correlation between driving force of anisotropic charge transfer and photocatalytic HER performance was identified which

provides insights for the future design of novel photocatalysts (**Fig. 1.16b**).

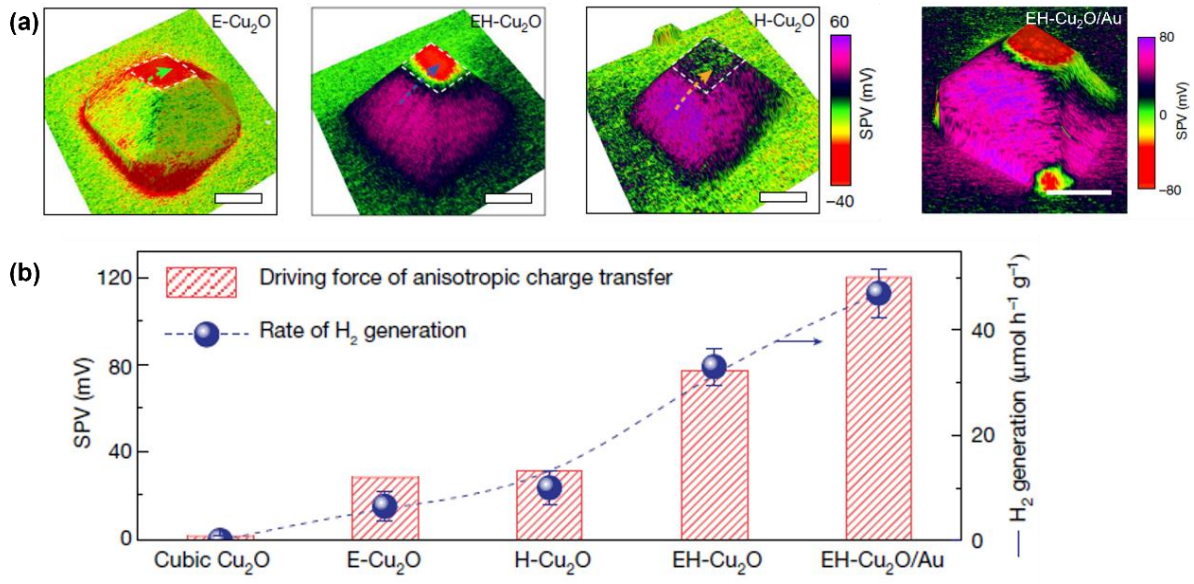



**Figure 1.16 (a)** Facet-dependent surface charge accumulation mapping by Kelvin probe on $Cu_2O$ samples under illumination; **(b)** Photocatalytic HER performance and its correlation with SPV. Reproduced from ref. 102. Copyright 2022 Springer Nature.

## 1.5 Aims and Objectives

The aims of this thesis can be classified into three main aspects: applying surface engineering strategies including single-atom doping, fabricating heterojunctions and facet engineering on two categories of materials - emerging 2D TMDs and traditional metal oxides. As discussed in section 1.4.2, TMDs, particularly $MoS_2$, have been widely used in various research fields. However, comparatively few studies have explored the application of $WS_2$ in photocatalysis, especially in comparison to $MoS_2$ and other 2D materials (*e.g.* g-$C_3N_4$). Theoretically, $WS_2$ has higher conduction band potential than $MoS_2$, making it a promising candidate for photocatalytic HER. Consequently, this thesis first investigates the potential of $WS_2$-based materials as photocatalysts. To achieve this goal, surface engineering techniques were applied to $WS_2$ including the introduction of single-atom sites and the formation of heterojunctions

with other materials. For single-atom doping, the main objective was to use different d-block metals as dopants to increase the catalytic performance using $WS_2$ alone for photocatalysis. Then the effect of using $WS_2$ as a cocatalyst on photocatalysis was studied, together with a detailed investigation on the structure change of $WS_2$ following the heterojunction formation.

The second main aim of this thesis was to use the facet-engineered metal oxides as model systems to study surface junctions and their effects on photocatalysis. It has been shown that different characterisation techniques can be applied to measure the facet-dependent charge separation. However, only micron-sized particles can be used in these methods due to the resolution limitations, while nanoparticle photocatalysts are more commonly used in previous studies. Consequently, it is essential to develop a feasible characterisation method to measure the surface charges under illumination. Trimethylphosphine molecules were applied as a surface probe for faceted nanoparticles. By monitoring the binding energy difference with and without illumination via *in-situ* XPS technique, the surface-accumulated electrons and holes on different facets were detected.

### 1.6 Thesis Overview

This thesis comprises 6 chapters, starting with a literature review (Chapter 1) of developments and challenges of heterogeneous photocatalysis along with surface engineering techniques to enhance the photocatalytic performance. Experimental details are presented in Chapter 2, followed by the results of the DPhil research projects in Chapters 3 to 5. Chapter 6 concludes the thesis with a summary and a discussion of future research avenues.

In detail, Chapter 1 outlines the rationale for utilising solar energy and the necessity of developing effective photocatalytic systems for energy conversion into solar fuels. Then

fundamental principles of photocatalysis are discussed together with current challenges. Following that, three surface engineering methods including single-atom doping, heterojunction engineering and facet tailoring are reviewed as promising approaches for enhancing photocatalytic performance.

Chapter 2 focuses on the synthesis methodologies of materials used in this research and describes the experimental protocols. The theories and principles of characterisation techniques employed in this research are also introduced.

Chapter 3 investigates the potential of modified ultrathin $WS_2$ layers as photocatalysts. Different d-block metals were doped into ultrathin $WS_2$ nanosheets in the form of single-atom dopants. Following that, ultrathin $WS_2$ nanosheets were applied as cocatalysts to $TiO_2$ flakes to form 2D-2D heterojunctions, maximising contact between the two materials. The photocatalytic activity and structure were analysed to establish the structure-activity correlations.

Chapter 4 continues the investigation into $WS_2$-$TiO_2$ heterojunctions. It revealed that the $WS_2$ layers decomposed into W single atoms on the $TiO_2$ support, creating significant amount of oxygen vacancies on the $TiO_2$ surface. The 2D-2D to 0D-2D structural transformation is carefully investigated and discussed. Then the catalytic performance is studied to understand the contribution of W single-atom sites on the overall photocatalytic performance.

Chapter 5 demonstrates a novel characterisation method for measuring facet-dependent charge accumulation in metal oxides nanocrystals. Facet-engineered $CeO_2$, $TiO_2$ and ZnO are applied as models to understand the charge distribution under illumination. Trimethylphosphine was applied as a surface probe, combined with near-ambient pressure

XPS to detect surface-accumulated charges under UV light. It was found that the facet-dependant charge migration could be detected by measuring the P 2p peak shift under illumination and its contribution to photocatalysis was also investigated.

Chapter 6 summarises the main findings of the thesis and provides perspectives for the future developments of photocatalysts.

## 1.7 References


1. T. Hisatomi and K. Domen, Reaction systems for solar hydrogen production via water splitting with particulate semiconductor photocatalysts, *Nat. Catal.*, 2019, **2**, 387-399.
2. N. Abas, A. Kalair and N. Khan, Review of fossil fuels and future energy technologies, *Futures*, 2015, **69**, 31-49.
3. B. Parkinson, Advantages of Solar Hydrogen Compared to Direct Carbon Dioxide Reduction for Solar Fuel Production, *ACS Energy Lett.*, 2016, **1**, 1057-1059.
4. G. Semieniuk, L. Taylor, A. Rezai and D. K. Foley, Plausible energy demand patterns in a growing global economy with climate policy, *Nat. Clim. Change*, 2021, **11**, 313-318.
5. J. Zheng, L. Huang, C.-H. Cui, Z.-C. Chen, X.-F. Liu, X. Duan, X.-Y. Cao, T.-Z. Yang, H. Zhu, K. Shi, P. Du, S.-W. Ying, C.-F. Zhu, Y.-G. Yao, G.-C. Guo, Y. Yuan, S.-Y. Xie and L.-S. Zheng, Ambient-pressure synthesis of ethylene glycol catalyzed by $C_{60}$-buffered $Cu/SiO_2$, *Science*, 2022, **376**, 288-292.
6. C. Vogt and B. M. Weckhuysen, The concept of active site in heterogeneous catalysis, *Nat. Rev. Chem.*, 2022, **6**, 89-111.
7. E. A. Abdelaziz, R. Saidur and S. Mekhilef, A review on energy saving strategies in industrial sector, *Renew. Sustain. Energy Rev.*, 2011, **15**, 150-168.
8. S. Fang, M. Rahaman, J. Bharti, E. Reisner, M. Robert, G. A. Ozin and Y. H. Hu, Photocatalytic $CO_2$ reduction, *Nat. Rev. Methods Primers*, 2023, **3**, 61.
9. C. Xu, P. Ravi Anusuyadevi, C. Aymonier, R. Luque and S. Marre, Nanostructured materials for photocatalysis, *Chem. Soc. Rev.*, 2019, **48**, 3868-3902.

10. J. Ran, J. Zhang, J. Yu, M. Jaroniec and S. Z. Qiao, Earth-abundant cocatalysts for semiconductor-based photocatalytic water splitting, *Chem. Soc. Rev.*, 2014, **43**, 7787-7812.
11. R. J. Detz, J. N. H. Reek and B. C. C. van der Zwaan, The future of solar fuels: when could they become competitive?, *Energy Environ. Sci.*, 2018, **11**, 1653-1669.
12. J. Ran, M. Jaroniec and S.-Z. Qiao, Cocatalysts in Semiconductor-based Photocatalytic $CO_2$ Reduction: Achievements, Challenges, and Opportunities, *Adv. Mater.*, 2018, **30**, 1704649.
13. X. Chen, S. Shen, L. Guo and S. S. Mao, Semiconductor-based Photocatalytic Hydrogen Generation, *Chem. Rev.*, 2010, **110**, 6503-6570.
14. Z. Li, S. Fang, H. Sun, R.-J. Chung, X. Fang and J.-H. He, Solar Hydrogen, *Adv. Energy Mater.*, 2023, **13**, 2203019.
15. Z. Zou, J. Ye, K. Sayama and H. Arakawa, Direct splitting of water under visible light irradiation with an oxide semiconductor photocatalyst, *Nature*, 2001, **414**, 625-627.
16. A. T. Hoang, A. Pandey, W.-H. Chen, S. F. Ahmed, S. Nižetić, K. H. Ng, Z. Said, X. Q. Duong, U. Ağbulut, H. Hadiyanto and X. P. Nguyen, Hydrogen Production by Water Splitting with Support of Metal and Carbon-Based Photocatalysts, *ACS Sustain. Chem. Eng.*, 2023, **11**, 1221-1252.
17. Q. Wang and K. Domen, Particulate Photocatalysts for Light-Driven Water Splitting: Mechanisms, Challenges, and Design Strategies, *Chem. Rev.*, 2020, **120**, 919-985.
18. Z. W. Seh, J. Kibsgaard, C. F. Dickens, I. Chorkendorff, J. K. Nørskov and T. F. Jaramillo, Combining theory and experiment in electrocatalysis: Insights into materials design, *Science*, 2017, **355**, eaad4998.
19. S. Nishioka, F. E. Osterloh, X. Wang, T. E. Mallouk and K. Maeda, Photocatalytic water splitting, *Nat. Rev. Methods Primers*, 2023, **3**, 42.
20. A. Fujishima and K. Honda, Electrochemical Photolysis of Water at a Semiconductor Electrode, *Nature*, 1972, **238**, 37-38.
21. K. Maeda, Photocatalytic water splitting using semiconductor particles: History and recent developments, *J. Photochem. Photobiol. C Photochem. Rev.*, 2011, **12**, 237-268.

22. M. Grätzel, Photoelectrochemical cells, *Nature*, 2001, **414**, 338-344.
23. Z. Li, W. Luo, M. Zhang, J. Feng and Z. Zou, Photoelectrochemical cells for solar hydrogen production: current state of promising photoelectrodes, methods to improve their properties, and outlook, *Energy Environ. Sci.*, 2013, **6**, 347-370.
24. S. Zhu and D. Wang, Photocatalysis: Basic Principles, Diverse Forms of Implementations and Emerging Scientific Opportunities, *Adv. Energy Mater.*, 2017, **7**, 1700841.
25. J. R. Bolton, S. J. Strickler and J. S. Connolly, Limiting and realizable efficiencies of solar photolysis of water, *Nature*, 1985, **316**, 495-500.
26. B. Weng, M.-Y. Qi, C. Han, Z.-R. Tang and Y.-J. Xu, Photocorrosion Inhibition of Semiconductor-Based Photocatalysts: Basic Principle, Current Development, and Future Perspective, *ACS Catal.*, 2019, **9**, 4642-4687.
27. Z. Li, R. Li, H. Jing, J. Xiao, H. Xie, F. Hong, N. Ta, X. Zhang, J. Zhu and C. Li, Blocking the reverse reactions of overall water splitting on a Rh/GaN–ZnO photocatalyst modified with $Al_2O_3$, *Nat. Catal.*, 2023, **6**, 80-88.
28. L. Li and E. A. Carter, Defect-Mediated Charge-Carrier Trapping and Nonradiative Recombination in $WSe_2$ Monolayers, *J. Am. Chem. Soc.*, 2019, **141**, 10451-10461.
29. Y. Ma, L. Lin, T. Takata, T. Hisatomi and K. Domen, A perspective on two pathways of photocatalytic water splitting and their practical application systems, *Phys. Chem. Chem. Phys.*, 2023, **25**, 6586-6601.
30. S. Wang, W. Liao, H. Su, S. Pang, C. Yang, Y. Fu and Y. Zhang, Review on the Application of Semiconductor Heterostructures in Photocatalytic Hydrogen Evolution: State-of-the-Art and Outlook, *Energy Fuels*, 2023, **37**, 1633-1656.
31. S. Lin, H. Huang, T. Ma and Y. Zhang, Photocatalytic Oxygen Evolution from Water Splitting, *Adv. Sci.*, 2021, **8**, 2002458.
32. J. Schneider and D. W. Bahnemann, Undesired Role of Sacrificial Reagents in Photocatalysis, *J. Phys. Chem. Lett.*, 2013, **4**, 3479-3483.
33. J. Song, C. Wei, Z.-F. Huang, C. Liu, L. Zeng, X. Wang and Z. J. Xu, A review on fundamentals for designing oxygen evolution electrocatalysts, *Chem. Soc. Rev.*, 2020,

**49**, 2196-2214.

34. M. Shi, G. Li, J. Li, X. Jin, X. Tao, B. Zeng, E. A. Pidko, R. Li and C. Li, Intrinsic Facet-Dependent Reactivity of Well-Defined BiOBr Nanosheets on Photocatalytic Water Splitting, *Angew. Chem. Int. Ed.*, 2020, **59**, 6590-6595.
35. H. A. Vignolo-González, S. Laha, A. Jiménez-Solano, T. Oshima, V. Duppel, P. Schützendübe and B. V. Lotsch, Toward Standardized Photocatalytic Oxygen Evolution Rates Using $RuO_2$@$TiO_2$ as a Benchmark, *Matter*, 2020, **3**, 464-486.
36. B. Han and Y. H. Hu, Highly Efficient Temperature-Induced Visible Light Photocatalytic Hydrogen Production from Water, *J. Phys. Chem. C*, 2015, **119**, 18927-18934.
37. Q. Wang, T. Hisatomi, Q. Jia, H. Tokudome, M. Zhong, C. Wang, Z. Pan, T. Takata, M. Nakabayashi, N. Shibata, Y. Li, I. D. Sharp, A. Kudo, T. Yamada and K. Domen, Scalable water splitting on particulate photocatalyst sheets with a solar-to-hydrogen energy conversion efficiency exceeding 1%, *Nat. Mater.*, 2016, **15**, 611-615.
38. Z. Wang, C. Li and K. Domen, Recent developments in heterogeneous photocatalysts for solar-driven overall water splitting, *Chem. Soc. Rev.*, 2019, **48**, 2109-2125.
39. B. Yao, J. Zhang, X. Fan, J. He and Y. Li, Surface Engineering of Nanomaterials for Photo-Electrochemical Water Splitting, *Small*, 2019, **15**, 1803746.
40. M. Batzill, Fundamental aspects of surface engineering of transition metal oxide photocatalysts, *Energy Environ. Sci.*, 2011, **4**, 3275-3286.
41. A. Meng, L. Zhang, B. Cheng and J. Yu, Dual Cocatalysts in $TiO_2$ Photocatalysis, *Adv. Mater.*, 2019, **31**, 1807660.
42. Y. Nakibli, Y. Mazal, Y. Dubi, M. Wächtler and L. Amirav, Size Matters: Cocatalyst Size Effect on Charge Transfer and Photocatalytic Activity, *Nano Lett.*, 2018, **18**, 357-364.
43. Y. Liu, Z. Sun and Y. H. Hu, Bimetallic cocatalysts for photocatalytic hydrogen production from water, *Chem. Eng. J.*, 2021, **409**, 128250.
44. D. Wang and X.-Q. Gong, Function-oriented design of robust metal cocatalyst for photocatalytic hydrogen evolution on metal/titania composites, *Nat. Commun.*, 2021,

**12**, 158.

45. H. Zhao, L. Jian, M. Gong, M. Jing, H. Li, Q. Mao, T. Lu, Y. Guo, R. Ji, W. Chi, Y. Dong and Y. Zhu, Transition-Metal-Based Cocatalysts for Photocatalytic Water Splitting, *Small Struct.*, 2022, **3**, 2100229.
46. P. Zhou, M. Luo and S. Guo, Optimizing the semiconductor–metal-single-atom interaction for photocatalytic reactivity, *Nat. Rev. Chem.*, 2022, **6**, 823-838.
47. Z.-H. Xue, D. Luan, H. Zhang and X. W. Lou, Single-atom catalysts for photocatalytic energy conversion, *Joule*, 2022, **6**, 92-133.
48. B. Qiao, A. Wang, X. Yang, L. F. Allard, Z. Jiang, Y. Cui, J. Liu, J. Li and T. Zhang, Single-atom catalysis of CO oxidation using $Pt_1/FeO_x$, *Nat. Chem.*, 2011, **3**, 634-641.
49. Y. Wang, J. Mao, X. Meng, L. Yu, D. Deng and X. Bao, Catalysis with Two-Dimensional Materials Confining Single Atoms: Concept, Design, and Applications, *Chem. Rev.*, 2019, **119**, 1806-1854.
50. C. Gao, J. Low, R. Long, T. Kong, J. Zhu and Y. Xiong, Heterogeneous Single-Atom Photocatalysts: Fundamentals and Applications, *Chem. Rev.*, 2020, **120**, 12175-12216.
51. F. Kraushofer and G. S. Parkinson, Single-Atom Catalysis: Insights from Model Systems, *Chem. Rev.*, 2022, **122**, 14911-14939.
52. Z. Zhang, Z. Zhang, C. Chen, R. Wang, M. Xie, S. Wan, R. Zhang, L. Cong, H. Lu, Y. Han, W. Xing, Z. Shi and S. Feng, Single-atom platinum with asymmetric coordination environment on fully conjugated covalent organic framework for efficient electrocatalysis, *Nat. Commun.*, 2024, **15**, 2556.
53. S. Masuda, K. Sakamoto and T. Tsukuda, Atomically precise Au and Ag nanoclusters doped with a single atom as model alloy catalysts, *Nanoscale*, 2024, **16**, 4514-4528.
54. J. Yan, L. Kong, Y. Ji, J. White, Y. Li, J. Zhang, P. An, S. Liu, S.-T. Lee and T. Ma, Single atom tungsten doped ultrathin α-$Ni(OH)_2$ for enhanced electrocatalytic water oxidation, *Nat. Commun.*, 2019, **10**, 2149.
55. Y. Li, Z. Wang, T. Xia, H. Ju, K. Zhang, R. Long, Q. Xu, C. Wang, L. Song, J. Zhu, J. Jiang and Y. Xiong, Implementing Metal-to-Ligand Charge Transfer in Organic Semiconductor for Improved Visible-Near-Infrared Photocatalysis, *Adv. Mater.*, 2016,

**28**, 6959-6965.

56. T. Tong, B. Zhu, C. Jiang, B. Cheng and J. Yu, Mechanistic insight into the enhanced photocatalytic activity of single-atom Pt, Pd or Au-embedded g-$C_3N_4$, *Appl. Surf. Sci.*, 2018, **433**, 1175-1183.
57. W. Liu, L. Cao, W. Cheng, Y. Cao, X. Liu, W. Zhang, X. Mou, L. Jin, X. Zheng, W. Che, Q. Liu, T. Yao and S. Wei, Single-Site Active Cobalt-Based Photocatalyst with a Long Carrier Lifetime for Spontaneous Overall Water Splitting, *Angew. Chem. Int. Ed.*, 2017, **56**, 9312-9317.
58. S. Cao, H. Li, T. Tong, H.-C. Chen, A. Yu, J. Yu and H. M. Chen, Single-Atom Engineering of Directional Charge Transfer Channels and Active Sites for Photocatalytic Hydrogen Evolution, *Adv. Funct. Mater.*, 2018, **28**, 1802169.
59. J. Yu, X. Zhao and Q. Zhao, Effect of surface structure on photocatalytic activity of $TiO_2$ thin films prepared by sol-gel method, *Thin Solid Films*, 2000, **379**, 7-14.
60. W. Lei, T. Zhang, L. Gu, P. Liu, J. A. Rodriguez, G. Liu and M. Liu, Surface-Structure Sensitivity of $CeO_2$ Nanocrystals in Photocatalysis and Enhancing the Reactivity with Nanogold, *ACS Catal.*, 2015, **5**, 4385-4393.
61. C. Ban, Y. Wang, Y. Feng, Z. Zhu, Y. Duan, J. Ma, X. Zhang, X. Liu, K. Zhou, H. Zou, D. Yu, X. Tao, L. Gan, G. Han and X. Zhou, Photochromic single atom Ag/$TiO_2$ catalysts for selective $CO_2$ reduction to $CH_4$, *Energy Environ. Sci.*, 2024, **17**, 518-530.
62. J. Di, C. Chen, S.-Z. Yang, S. Chen, M. Duan, J. Xiong, C. Zhu, R. Long, W. Hao, Z. Chi, H. Chen, Y.-X. Weng, J. Xia, L. Song, S. Li, H. Li and Z. Liu, Isolated single atom cobalt in $Bi_3O_4Br$ atomic layers to trigger efficient $CO_2$ photoreduction, *Nat. Commun.*, 2019, **10**, 2840.
63. Y. Tachibana, L. Vayssieres and J. R. Durrant, Artificial photosynthesis for solar water-splitting, *Nat. Photonics*, 2012, **6**, 511-518.
64. T. L. Wakjira, A. B. Gemta, G. B. Kassahun, D. M. Andoshe and K. Tadele, Bismuth-Based Z-Scheme Heterojunction Photocatalysts for Remediation of Contaminated Water, *ACS Omega*, 2024, **9**, 8709-8729.
65. J. Zhang, M. Zhang, R.-Q. Sun and X. Wang, A Facile Band Alignment of Polymeric

Carbon Nitride Semiconductors to Construct Isotype Heterojunctions, *Angew. Chem. Int. Ed.*, 2012, **51**, 10145-10149.

66. J. Low, J. Yu, M. Jaroniec, S. Wageh and A. A. Al-Ghamdi, Heterojunction Photocatalysts, *Adv. Mater.*, 2017, **29**, 1601694.
67. S. J. Hong, S. Lee, J. S. Jang and J. S. Lee, Heterojunction $BiVO_4/WO_3$ electrodes for enhanced photoactivity of water oxidation, *Energy Environ. Sci.*, 2011, **4**, 1781-1787.
68. X. Guo, Y. Peng, G. Liu, G. Xie, Y. Guo, Y. Zhang and J. Yu, An Efficient $ZnIn_2S_4$@$CuInS_2$ Core–Shell p–n Heterojunction to Boost Visible-Light Photocatalytic Hydrogen Evolution, *J. Phys. Chem. C*, 2020, **124**, 5934-5943.
69. S. Li, C. Wang, Y. Liu, B. Xue, W. Jiang, Y. Liu, L. Mo and X. Chen, Photocatalytic degradation of antibiotics using a novel $Ag/Ag_2S/Bi_2MoO_6$ plasmonic p-n heterojunction photocatalyst: Mineralization activity, degradation pathways and boosted charge separation mechanism, *Chem. Eng. J.*, 2021, **415**, 128991.
70. J. Yu, S. Wang, J. Low and W. Xiao, Enhanced photocatalytic performance of direct Z-scheme g-$C_3N_4$–$TiO_2$ photocatalysts for the decomposition of formaldehyde in air, *Phys. Chem. Chem. Phys.*, 2013, **15**, 16883-16890.
71. L. Zhang, J. Zhang, H. Yu and J. Yu, Emerging S-Scheme Photocatalyst, *Adv. Mater.*, 2022, **34**, 2107668.
72. Q. Xu, L. Zhang, B. Cheng, J. Fan and J. Yu, S-Scheme Heterojunction Photocatalyst, *Chem*, 2020, **6**, 1543-1559.
73. J. Fu, Q. Xu, J. Low, C. Jiang and J. Yu, Ultrathin 2D/2D $WO_3$/g-$C_3N_4$ step-scheme $H_2$-production photocatalyst, *Appl. Catal., B*, 2019, **243**, 556-565.
74. P. Xia, S. Cao, B. Zhu, M. Liu, M. Shi, J. Yu and Y. Zhang, Designing a 0D/2D S-Scheme Heterojunction over Polymeric Carbon Nitride for Visible-Light Photocatalytic Inactivation of Bacteria, *Angew. Chem. Int. Ed.*, 2020, **59**, 5218-5225.
75. H. Wang, L. Zhang, Z. Chen, J. Hu, S. Li, Z. Wang, J. Liu and X. Wang, Semiconductor heterojunction photocatalysts: design, construction, and photocatalytic performances, *Chem. Soc. Rev.*, 2014, **43**, 5234-5244.
76. S. K. Dutta, S. K. Mehetor and N. Pradhan, Metal Semiconductor Heterostructures for

Photocatalytic Conversion of Light Energy, *J. Phys. Chem. Lett.*, 2015, **6**, 936-944.

77. X. Li, R. Shen, S. Ma, X. Chen and J. Xie, Graphene-based heterojunction photocatalysts, *Appl. Surf. Sci.*, 2018, **430**, 53-107.
78. K. Woan, G. Pyrgiotakis and W. Sigmund, Photocatalytic Carbon-Nanotube–$TiO_2$ Composites, *Adv. Mater.*, 2009, **21**, 2233-2239.
79. R. Yang, Y. Fan, Y. Zhang, L. Mei, R. Zhu, J. Qin, J. Hu, Z. Chen, Y. Hau Ng, D. Voiry, S. Li, Q. Lu, Q. Wang, J. C. Yu and Z. Zeng, 2D Transition Metal Dichalcogenides for Photocatalysis, *Angew. Chem. Int. Ed.*, 2023, **62**, e202218016.
80. X. Chia and M. Pumera, Layered transition metal dichalcogenide electrochemistry: journey across the periodic table, *Chem. Soc. Rev.*, 2018, **47**, 5602-5613.
81. C. Tan, X. Cao, X.-J. Wu, Q. He, J. Yang, X. Zhang, J. Chen, W. Zhao, S. Han, G.-H. Nam, M. Sindoro and H. Zhang, Recent Advances in Ultrathin Two-Dimensional Nanomaterials, *Chem. Rev.*, 2017, **117**, 6225-6331.
82. J. Li, G. Zhan, Y. Yu and L. Zhang, Superior visible light hydrogen evolution of Janus bilayer junctions via atomic-level charge flow steering, *Nat. Commun.*, 2016, **7**, 11480.
83. L. Li, Y. Xia, M. Zeng and L. Fu, Facet engineering of ultrathin two-dimensional materials, *Chem. Soc. Rev.*, 2022, **51**, 7327-7343.
84. C. Xiao, B.-A. Lu, P. Xue, N. Tian, Z.-Y. Zhou, X. Lin, W.-F. Lin and S.-G. Sun, High-Index-Facet- and High-Surface-Energy Nanocrystals of Metals and Metal Oxides as Highly Efficient Catalysts, *Joule*, 2020, **4**, 2562-2598.
85. S. Wu, Y.-K. Peng, T.-Y. Chen, J. Mo, A. Large, I. McPherson, H.-L. Chou, I. Wilkinson, F. Venturini, D. Grinter, P. Ferrer Escorihuela, G. Held and S. C. E. Tsang, Removal of Hydrogen Poisoning by Electrostatically Polar MgO Support for Low-Pressure $NH_3$ Synthesis at a High Rate over the Ru Catalyst, *ACS Catal.*, 2020, **10**, 5614-5622.
86. Z. Zhao, Z. Li and Z. Zou, A Theoretical Study of Water Adsorption and Decomposition on the Low-Index Stoichiometric Anatase $TiO_2$ Surfaces, *J. Phys. Chem. C*, 2012, **116**, 7430-7441.
87. G. Liu, J. C. Yu, G. Q. Lu and H.-M. Cheng, Crystal facet engineering of

semiconductor photocatalysts: motivations, advances and unique properties, *Chem. Commun.*, 2011, **47**, 6763-6783.

88. H. Xu, P. Reunchan, S. Ouyang, H. Tong, N. Umezawa, T. Kako and J. Ye, Anatase $TiO_2$ Single Crystals Exposed with High-Reactive {111} Facets Toward Efficient $H_2$ Evolution, *Chem. Mater.*, 2013, **25**, 405-411.
89. M. Maisano, M. V. Dozzi and E. Selli, Searching for facet-dependent photoactivity of shape-controlled anatase $TiO_2$, *J. Photochem. Photobiol. C Photochem. Rev.*, 2016, **28**, 29-43.
90. S. Sun, L. He, M. Yang, J. Cui and S. Liang, Facet Junction Engineering for Photocatalysis: A Comprehensive Review on Elementary Knowledge, Facet-Synergistic Mechanisms, Functional Modifications, and Future Perspectives, *Adv. Funct. Mater.*, 2022, **32**, 2106982.
91. T. Ohno, K. Sarukawa and M. Matsumura, Crystal faces of rutile and anatase $TiO_2$ particles and their roles in photocatalytic reactions, *New J. Chem.*, 2002, **26**, 1167-1170.
92. J. B. Sambur, T.-Y. Chen, E. Choudhary, G. Chen, E. J. Nissen, E. M. Thomas, N. Zou and P. Chen, Sub-particle reaction and photocurrent mapping to optimize catalyst-modified photoanodes, *Nature*, 2016, **530**, 77-80.
93. T. Tachikawa, S. Yamashita and T. Majima, Evidence for Crystal-Face-Dependent $TiO_2$ Photocatalysis from Single-Molecule Imaging and Kinetic Analysis, *J. Am. Chem. Soc.*, 2011, **133**, 7197-7204.
94. J. Yu, J. Low, W. Xiao, P. Zhou and M. Jaroniec, Enhanced Photocatalytic $CO_2$-Reduction Activity of Anatase $TiO_2$ by Coexposed {001} and {101} Facets, *J. Am. Chem. Soc.*, 2014, **136**, 8839-8842.
95. T. Takata, J. Jiang, Y. Sakata, M. Nakabayashi, N. Shibata, V. Nandal, K. Seki, T. Hisatomi and K. Domen, Photocatalytic water splitting with a quantum efficiency of almost unity, *Nature*, 2020, **581**, 411-414.
96. H. Nishiyama, T. Yamada, M. Nakabayashi, Y. Maehara, M. Yamaguchi, Y. Kuromiya, Y. Nagatsuma, H. Tokudome, S. Akiyama, T. Watanabe, R. Narushima, S. Okunaka, N.

Shibata, T. Takata, T. Hisatomi and K. Domen, Photocatalytic solar hydrogen production from water on a 100-$m^2$ scale, *Nature*, 2021, **598**, 304-307.

97. Y. Liu, S. Ye, H. Xie, J. Zhu, Q. Shi, N. Ta, R. Chen, Y. Gao, H. An, W. Nie, H. Jing, F. Fan and C. Li, Internal-Field-Enhanced Charge Separation in a Single-Domain Ferroelectric $PbTiO_3$ Photocatalyst, *Adv. Mater.*, 2020, **32**, 1906513.
98. R. Chen, F. Fan and C. Li, Unraveling Charge-Separation Mechanisms in Photocatalyst Particles by Spatially Resolved Surface Photovoltage Techniques, *Angew. Chem. Int. Ed.*, 2022, **61**, e202117567.
99. R. Li, H. Han, F. Zhang, D. Wang and C. Li, Highly efficient photocatalysts constructed by rational assembly of dual-cocatalysts separately on different facets of $BiVO_4$, *Energy Environ. Sci.*, 2014, **7**, 1369-1376.
100. R. Li, F. Zhang, D. Wang, J. Yang, M. Li, J. Zhu, X. Zhou, H. Han and C. Li, Spatial separation of photogenerated electrons and holes among {010} and {110} crystal facets of $BiVO_4$, *Nat. Commun.*, 2013, **4**, 1432.
101. R. Chen, S. Pang, H. An, J. Zhu, S. Ye, Y. Gao, F. Fan and C. Li, Charge separation via asymmetric illumination in photocatalytic $Cu_2O$ particles, *Nat. Energy*, 2018, **3**, 655-663.
102. R. Chen, Z. Ren, Y. Liang, G. Zhang, T. Dittrich, R. Liu, Y. Liu, Y. Zhao, S. Pang, H. An, C. Ni, P. Zhou, K. Han, F. Fan and C. Li, Spatiotemporal imaging of charge transfer in photocatalyst particles, *Nature*, 2022, **610**, 296-301.

# Chapter 2 Characterisation Techniques and Experimental Methods

## 2.1 Introduction

Characterisation techniques play a crucial role in the understanding of solid-state materials and reaction systems. Recent advances in state-of-the-art characterisation methods have significantly expanded the scope of materials research, offering deeper insights into structure-activity correlations and providing valuable guidelines for the rational design of next-generation catalysts. In this chapter, both *ex-situ* and *in-situ* techniques included in this thesis are introduced, with a focus on their relevance to the study of photocatalysis.

The chapter starts by presenting the fundamental principles and operational conditions of these characterisation techniques, aiming to enhance comprehension of how these techniques contribute to research on materials. Emphasis is placed on the ability of these techniques to unravel complex material properties, such as surface morphology, electronic structure, and charge carrier dynamics, which are critical for photocatalytic applications. Additionally, the chemicals used in the experiments are outlined, along with detailed synthetic procedures for fabricating the photocatalysts. This includes step-by-step methodologies, reaction conditions, and any modifications applied to optimise material properties for improved photocatalytic efficiency.

## 2.2 Characterisation Techniques

### 2.2.1 Powder X-ray Diffraction (PXRD)

PXRD is widely used as a non-destructive characterisation method for structural analysis of solid-state materials.[1] Generally, for heterogeneous catalysts, it is essential to apply PXRD to identify the crystal phases present in the powders at early stages, revealing if the measured

sample has mixed components or is a single-crystal. When measuring the composite materials, the PXRD peaks can also indicate the content increase or decrease of a species of interest. Then, by combining it with other characterisation techniques such as electron microscopy, it is possible to generate theoretical models of local structures which are responsible for the high catalytic reactivity.

The PXRD method takes advantage of the diffraction of an X-ray beam in a crystalline material with similar interatomic distances compared to the beam wavelength. The X-ray emission is normally generated by the inner-shell ionisation of metals (*e.g.* Cu) which are firstly bombarded by high energy electrons. Then the generated X-ray is directed toward the sample. It is assumed that every orientation of the isotropic particle has been sampled with equal probability for X-ray diffraction. Under X-ray illumination, the crystallographic planes of the prepared particle can work as gratings for the monochromatic X-rays and the discretely diffracted beams are collected by the detector at different angles for the further analysis of crystal structures (**Fig. 2.1**). Notably, only signals from constructive interference between X-ray beams can be detected, as the diffracted X-rays that have suffered destructive interference have been cancelled out with each other. The positions of the PXRD peaks are determined by the following equation known as Bragg's Law:

$$n\lambda = 2d\ sin\theta \qquad \textbf{Equation 2.1}$$

where n is the order of diffraction; λ is the wavelength of the beam; d is the lattice spacing of a set of well-defined crystal planes and θ is the diffraction angle.[2]

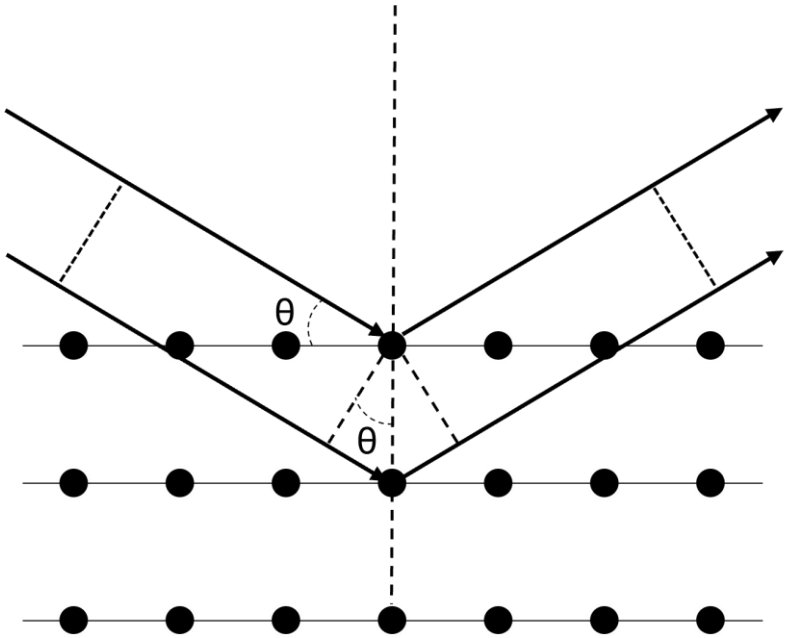



**Figure 2.1** Illustration of simplified Bragg's law, showing X-ray diffraction at crystal planes of the sample with the diffraction angle of θ. Reproduced from ref. 2. Copyright 2021 Springer Nature.

The Bragg peaks normally show at discrete 2θ angles for different crystallographic planes in the lattice. Each peak is labelled with three integers (hkl) known as Miller indices to represent various crystallographic planes.[3] The lattice parameters such as the spacing of each set of planes can be calculated depending on the crystal structure. For instance, the relationship of a cubic crystal system can be expressed as:

$$d_{hkl} = \frac{a}{\sqrt{h^2 + k^2 + l^2}} \qquad \textbf{Equation 2.2}$$

while for hexagonal crystal structure the equation becomes:

$$d_{hkl} = \frac{a}{\sqrt{\frac{4}{3}(h^2 + k^2 + hk) + \frac{a^2}{c^2}l^2}} \qquad \textbf{Equation 2.3}$$

where a and c are lattice parameters; d is the lattice spacing; h, k and l are Miller indices.

In addition to peak positions, the PXRD signals can be obtained in varied widths and shapes, which are highly dependent on the size, shape and strain state of the measured samples. For

example, the defects and reduced particle sizes destroying particles' crystallinity can result in peak broadening due to wider distribution of interlayer spacing. This peak broadening from the PXRD measurements can be determined by the Scherrer equation:

$$\tau = \frac{K\lambda}{\beta \cos\theta} \qquad \textbf{Equation 2.4}$$

where τ is the particle size; K is a dimensionless shape factor; λ is the wavelength of the beam; β is the width of the peak at full width half maximum in radians and θ is the diffraction angle.[4]

In this thesis, PXRD measurements were performed on a Bruker D8 Advance diffractometer with LynxEye detector and Cu Kα1 radiation (λ = 1.5406 Å). Measurements were conducted at 2θ angles of 5° to 90°. For sample preparation, powders for XRD measurement were dispersed in ethanol using sonication, and then the suspensions were dropped on the cover glasses. After drying on a hot plate at 80 °C in air, the cover glasses were mounted on the Bruker XRD sample holders for measurement.

### 2.2.2 Transmission Electron Microscopy (TEM)

The fundamental working principle of electron microscopy is that electrons can be used as 'light' owing to their wave-particle duality. The short wavelength of the high-energy electron beam (80 - 300 keV) gives much higher resolution (in nm scale of smaller) compared to traditional optical microscopy (in μm scale).[5] The TEM images are generated by transmitting electron beams through a thin sample and collecting the transmitted electrons by detectors. Additionally, an electron microscope is normally equipped with other spectroscopy techniques including energy-dispersive X-ray spectroscopy (EDX) and electron energy-loss spectroscopy (EELS). Combining these characterisation methods allows studying the

structure, the morphology and elemental composition of the materials of interest in atomic scales, which can assist in gaining an in-depth understanding of the structure-activity correlation. Consequently, TEM has become a vital technique for studying the fine structure of the material. The resolution can be described by the Abbe's diffraction limit as the following equation:

$$d = \frac{\lambda}{2nsin\theta} \quad \textbf{Equation 2.5}$$

where d is the resolvable distance; λ is the wavelength; n is the refraction index and θ is the half-angle subtended by the objective lens. Theoretically, since the wavelength is determined by the electron's speed, which in turn depends on its energy, higher energy can potentially lead to better resolution.[6] However, it should be noted that the samples can be damaged under the high energy electron beam, so the practical resolution correlates to both the sample stability and the electron microscope.

The structure of a typical electron microscope is shown in **Fig. 2.2**. It is typically composed of an electron beam source, multiple lens for different purposes (*e.g.* focus and magnification) and detectors for data collection.[5] It is operated under high vacuum conditions ($10^{-6}$ mbar) to avoid scattering of electrons by the gas molecules. Generally, the electrons are firstly generated by the electron gun and focused into a fine spot using the electromagnetic lenses. Then, the focused electron beam passes through the prepared sample which is normally supported by the Cu grids with carbon films. Following that, the electrons can interact with the sample differently, which can further lead to generation of emitted X-rays, backscattered electrons, secondary electrons, Auger electrons, elastically scattered electrons, inelastically scattered electrons and transmitted electrons. The emitted X-rays can be collected for EDX

measurement and the inelastically scattered electrons can be used to generate EELS results. The transmitted and elastically scattered electrons are collected and further focused by a series of lenses to generate a highly magnified image of the measured sample on a screen or a detector.

Two operational modes (dark field and bright field) are normally used depending on the experimental requirements, which are classified based on the type of electrons collected by the lenses and detectors as discussed previously to generate the TEM images. The dark field mode collects scattered electrons by the aperture, where heavier atoms have higher chance for electron scattering, thus these atoms are brighter in the TEM image compared to the light elements. As for the bright field mode, the electron beams transmitted through the sample are captured by the aperture and the scattered electrons are not collected. Consequently, heavier atoms appear darker in the image due to the lower probability for electron transmission compared to lighter atoms.

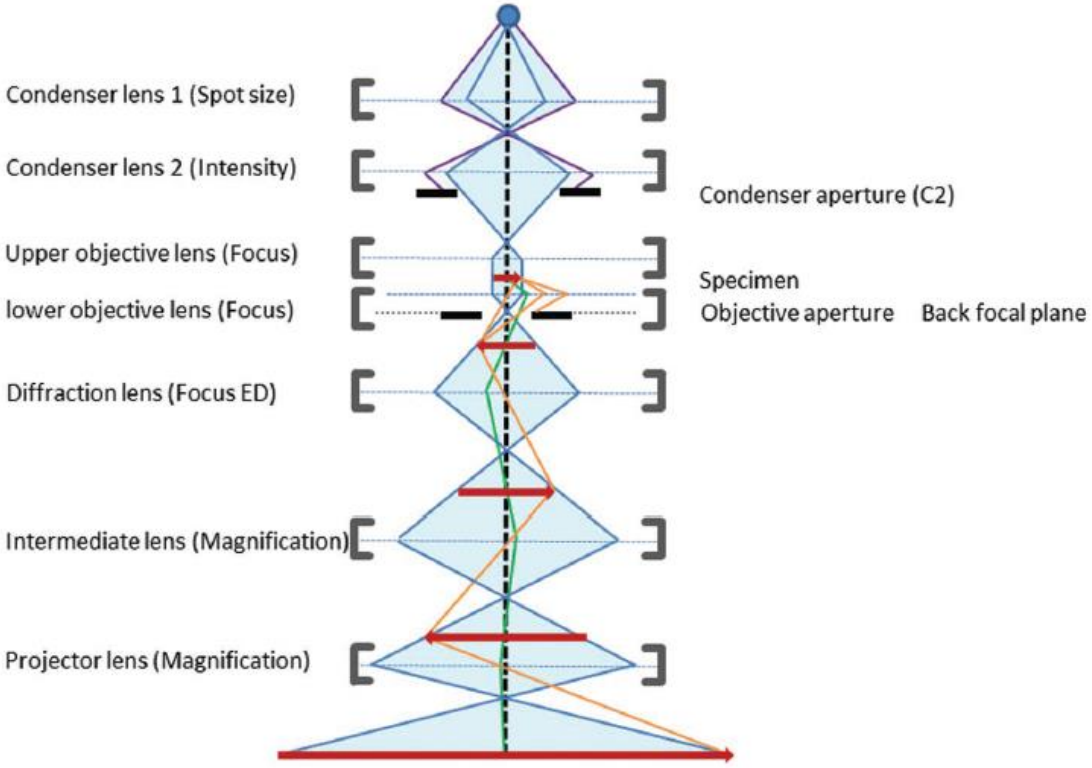



**Figure 2.2** Illustration of structure of a typical electron microscope. Reproduced from ref 5. Copyright 2020 John Wiley and Sons.

In this thesis, most of the high resolution TEM images were captured using a double spherical aberration-corrected electron microscope (S/TEM FEI Titan G2 60-300) operated at 300 kV. The probe convergence angle on the Titan electron microscope was 24.5 mrad, and the angular range of the HAADF detector was from 79.5 mrad to 200 mrad. For sample preparation, *ca.* 5 mg powders for TEM measurements were firstly dispersed in 10 mL ethanol by using ultrasonication for at least 15 minutes. Then the suspensions were dropped onto the Cu grids and then dried naturally before the TEM measurement.

### 2.2.3 X-ray Photoelectron Spectroscopy (XPS)

XPS is a powerful characterisation technique for studying the elemental composition, chemical state and electronic structure of materials. It uses a soft X-ray beam source to excite

core electrons, generating photoelectrons from the sample. The escape depth of electrons is relatively short, so this technique is more surface-sensitive compared to the characterisation methods using hard X-ray beams, such as XRD. The XPS signals are typically averaged from a few atomic layers near the sample surface, and the positions of the XPS peaks are sensitive to the electron density of the measured elements. The binding energy of the photoelectrons ejected from the surface is analysed by the XPS instrument and can be used for differentiating elements. Theoretically, the calculation for the binding energy uses the following equation:

$$E_{binding} = h\nu - E_{kinetic} - \varphi \qquad \textbf{Equation 2.6}$$

where h is the Plank constant; ν is the X-ray frequency; φ is the work function correction of the XPS instrument derived from the contact potential; $E_{binding}$ and $E_{kinetic}$ are the binding energy of the excited core electron and the kinetic energy of the photoelectron collected by the detector.[7]

For a typical XPS experiment (**Fig. 2.3**), samples are mounted on a conductive support (*e.g.* carbon tape or gold coated silicon wafer) at an initial stage to avoid the accumulation of electrons on the sample. Then the prepared sample is transferred into an experimental chamber under high vacuum to avoid the loss of the kinetic energy of photoelectrons due to collisions with gas molecules.[8] Following that, during the measurement, the generated photoelectrons with different kinetic energies are separated by an energy analyser equipped with a strong magnetic field, and are collected by the detector to obtain the XPS spectra.

Normally, a survey scan from 0 eV to 1400 eV is first conducted to determine the chemical composition of the sample. Each characteristic peak of an element of interest has a certain

relative sensitivity factor, which can be used for calculating the chemical formula of the sample. High resolution scans in the region of the Fermi level or C 1s are then typically recorded for calibration of the XPS peaks to eliminate peak shift originating from charging effects in the sample. Following that, the XPS measurements on elements of interest are also conducted in high resolution scan mode. The XPS spectra generated from high resolution scans are calibrated based on the C 1s spectra or Fermi level and can then be used for deconvolution of the XPS peaks to investigate their oxidation states and concentrations in the sample.

One of the shortcomings of XPS is that the analyser and the detector require high-vacuum conditions to work, which makes it difficult to track changes in the sample during the catalytic process. For instance, in thermal catalysis, catalysts are explored in gas environments for chemical reactions, and these gases can make it impossible to accurately measure the kinetic energy of photoelectrons in normal XPS due to the collision with gas molecules. To accommodate the need for *in-situ* XPS analysis, the near ambient pressure XPS (NAP-XPS) method has been developed, which allows XPS measurements on heterogeneous catalysts under experimental conditions.[9] Differential pumping stages are introduced between the sample chamber and the energy analyser. This enables a gaseous environment near the sample region while maintaining high-vacuum conditions in the energy analyser. Consequently, it is possible to conduct *in-situ* experiments on the chemical composition changes of catalysts used for thermal, electrochemical and photo-catalysis.

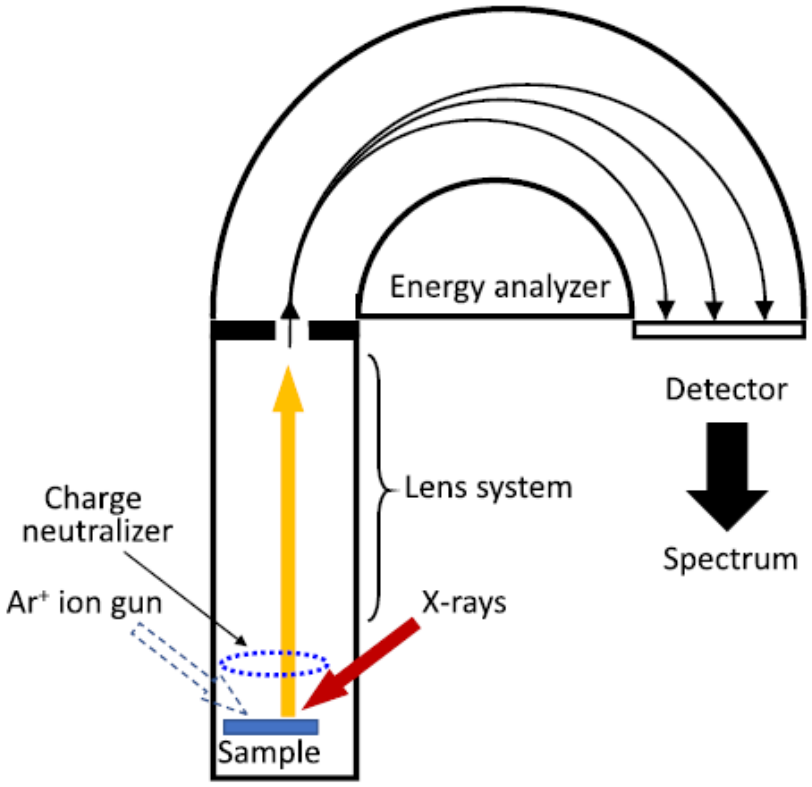



**Figure 2.3** Schematic view of a photoelectron spectrometer equipped with a hemispherical energy analyser for separation and detection of photoelectrons. Reproduced from ref. 8. Copyright 2020 Elsevier.

In this thesis, the *ex-situ* XPS experiments were conducted on a PHI Quantum-2000 photoelectron spectrometer (Al Kα with 1486.7 eV operating at 15kV, 35 W and 200 μm spot size) and an Omicron Sphera II hemispherical electron energy analyser with a Thermo Scientific model Nexsa analysis system. The Al anode tube was operated under 12 kV for X-ray emission. The survey scans were obtained with a pass energy of 200 eV with a 1 eV measuring step, repeated for 5 times. For high resolution scans, the pass energy was set to 50 eV with a 0.1 eV measuring step, and measurements were repeated at least 10 times. The XPS spectra were calibrated by C 1s peak at 284.8 eV.

For *in-situ* XPS experiments, samples were measured in the Diamond Light Source where the

XPS instrument was equipped with a UV laser of 365 nm (0.15 mW $cm^{-2}$). The powdered samples were dispersed in ethanol and deposited on a 1 cm × 1 cm piece of silicon wafer. Subsequently, the silicon wafer was heated on a hot plate at 100 ℃ to remove the solvent. Then the silicon wafer was mounted onto the XPS sample holder and transferred into the XPS experimental chamber. The sample was left at room temperature (20 ℃) under vacuum for at least 15 mins for gas desorption, followed by introducing 0.2 mbar of trimethylphosphine (TMP) vapour into the chamber. The vapour pressure was monitored by a gauge controller assembled on the experiment apparatus rack, and the gas composition was monitored by online mass spectrometry (MS). For the high resolution scans, if not specified, the photon energy was set to 1300 eV (930 eV for $TiO_2$ and 1600 eV for MgO), and the pass energy was set to 20 eV with a 600 l/mm grating and a 0.05 eV measuring step.

### 2.2.4 X-ray Absorption Spectroscopy (XAS)

XAS is another widely applied characterisation method using X-rays as the excitation source for core electrons. However, different from XPS, it uses tuneable X-ray photon energies within a certain range instead of using a fixed X-ray photon energy during measurement.[10] Depending on the energy region, X-rays can be divided into two categories: soft (100 - 2000 eV) and hard (2 - 100 keV) X-ray ranges. The soft X-ray range is normally used for studying light elements such as C, N and O, and can be used for surface studies due to the low penetration depth of soft X-rays. In comparison, hard X-rays are used for investigating heavy elements like transition metals. Additionally, as the hard X-ray beam is more widely used which can penetrate samples, XAS measurements are typically bulk-sensitive rather than surface-sensitive.

During XAS measurements, when the X-ray energy matches the binding energy of core electrons, a sharp increase in absorption occurs, which can be detected, which is known as the absorption edge. Depending on the principal quantum numbers (n=1, 2, 3), K-, L- and M-edges are used to name the absorption edge. A typical XAS measurement set-up is illustrated in **Fig. 2.4**. The incident X-rays with varied photon energies, noted as $I_0$, can pass through or be absorbed by the measured samples.[10] Then, the transmitted X-ray can be monitored by the detectors, which is noted as $I_T$. A reference sample (normally metal foils with an oxidation state of zero) is placed behind the transmission detector. The X-rays transmitted from the sample can further transmit through the reference and can be measured by another detector behind the reference sample. The transmitted X-rays from the reference sample are normally noted as $I_{ref}$ and can be used for calibrating XAS signals of measured samples. This method is called transmission mode, and it is suitable for studying elements that are abundant in the sample. For investigation of elements that are low in concentration (normally less than 10wt%) such as dopants, fluorescence mode is then applied, where the fluorescence detector is placed beside the measured sample for signal collection. The fluorescence mode collects the X-ray emitted by the electron relaxation to the unoccupied states created by the previous excitation step. The fluorescent X-rays are also characteristic of the measured elements and related to the local environment and oxidation state of the absorbing atoms.

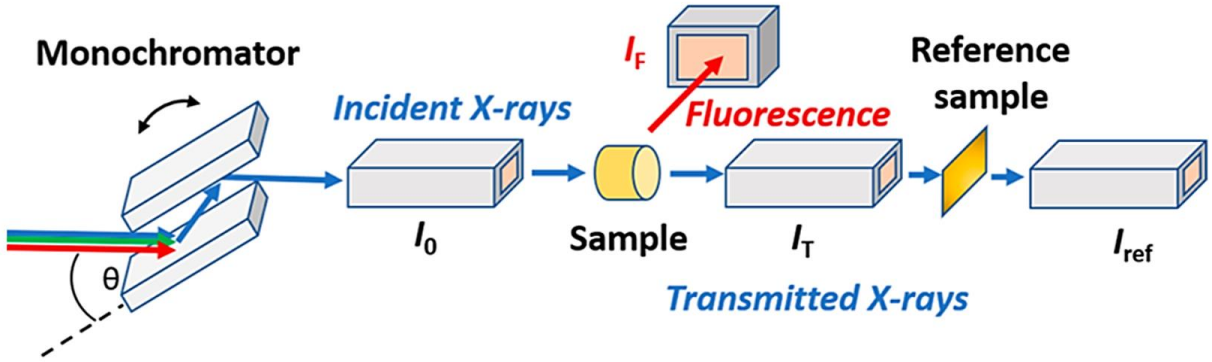



**Figure 2.4** Schematic view of XAS set-up. Reproduced from ref. 10. Copyright 2021 American Chemical Society.

Analysis of XAS results can generally be divided into three parts: the pre-edge region, the X-ray absorption near-edge structure (XANES), and the extended X-ray absorption fine structure (EXAFS).[11] The pre-edge region corresponds to the part before the main absorption peak. A shoulder peak can appear in this region when the electrons are excited to a vacant orbital with higher energy. Notably, this region is highly sensitive to the local symmetry of the absorbing atom, and the probability of the transition is controlled by the dipole selection rules. In many cases, the intensity is too weak to be observed due to selection rules that forbid the relevant transitions. For example, the 1s to 3d transitions are forbidden in highly symmetric pure octahedral case, leading to weak pre-edge intensity.[12] The peak intensity can be enhanced when the symmetry is distorted. For absorbing atoms with a pure tetrahedral structure, the pre-edge peak normally has the highest intensity owing to allowed p-d mixing.

Different from the pre-edge region, XANES corresponds to the quasi-bound states from core electron excitation to the continuum, which gives a sharp absorption edge known as the white line. It can be used to determine the oxidation state and electronic structures of the measured element. The EXAFS region is responsible for photoelectrons with high kinetic energy

ejected from the absorbing atoms, which can interact with the neighbouring atoms by scattering. Consequently, the local environment of absorbing atoms, such as bond length and coordination number, can also be derived from the EXAFS region by proper fitting procedures.

In heterogeneous catalysis, particularly, it is vital to understand the local structure of the active sites and how the structure changes during the catalytic process, which makes *ex-situ* and *in-situ* XAS vital for investigating the reaction mechanism and material properties. Unlike XPS, as the XAS measurement does not require an ultra-high vacuum condition, it allows more flexibility in designing the *in-situ* XAS testing cells. For instance, by using the fluorescence mode, it is possible to track the change of oxidation state and coordination environment of an element of interest from samples deposited on electrodes and placed in electrolyte. This makes it a very powerful and vital technique for providing information on the actual catalysis process.

In this thesis, the XAS experiments were conducted at BL01C of the Synchrotron Radiation Research Centre (SRRC) in Taiwan and BL05U of Shanghai Synchrotron Radiation Facility (SSRF) in Shanghai. Fluorescence mode was applied for data collection of the dopants in the sample.

### 2.2.5 Electron Paramagnetic Resonance (EPR) Spectroscopy

EPR can be used for measuring unpaired electrons in a sample. In the presence of an external magnetic field, the original energy level of electrons with different spin quantum numbers ($m_s$=1/2 or -1/2) splits into two different energy states, known as the Zeeman effect (**Fig. 2.5**).[13] The energy difference between the two energy states can be determined by the

following equation:

$$\Delta E = g_e \mu_B B_0 \qquad \textbf{Equation 2.7}$$

where $g_e$ is the g factor (Landé g-factor) of the electron; $\mu_B$ is the Bohr magneton and $B_0$ is the strength of the external magnetic field.[13]

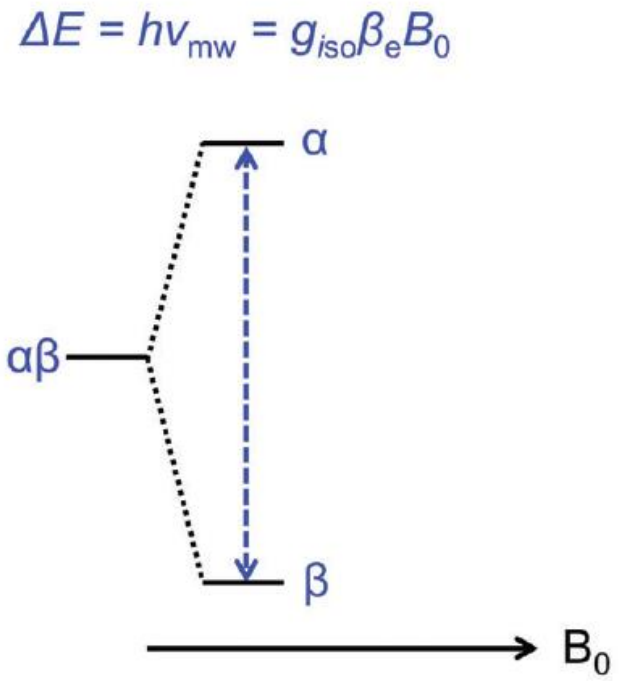



**Figure 2.5** Zeeman effect under an external magnetic field $B_0$. Reproduced from ref 13. Copyright 2018 Royal Society of Chemistry.

Based on the above equation, the energy level difference is dependent on the strength of the applied magnetic field. Consequently, the unpaired electrons can be excited by electromagnetic radiation with an appropriate wavelength under a certain magnetic field strength. For EPR measurements, microwaves (9 - 10 GHz) are used for electron excitation and are kept at a fixed value during measurement. The magnetic field strength is around 3500 Gauss, which is changed from low to high until the energy level difference matches the energy of microwaves, and the absorption of the microwave can be detected by the spectrometer.

In heterogeneous catalysis, EPR can be used for different purposes. Detection of oxygen vacancies ($O_v$) in solid-state materials is one of the most common applications of EPR, as $O_v$ can serve as reactive sites and modify the electronic properties of materials, which is important for catalytic reactivity interpretation. Furthermore, EPR can be also applied for detection of radicals produced during the reaction process, which makes EPR very useful for studying the reaction mechanism.

In this thesis, the EPR spectra were recorded using an X-band (9.4 GHz) Bruker EMX spectrometer at room temperature. Around 40 mg samples were placed into a 3 mm diameter EPR tube. Each spectrum was average from at least 5 scans.

### 2.2.6 Gas Chromatography (GC)

GC is widely used for determining the composition of the gas mixture from catalytic reactions. The gas for analysis is first injected into carrier gases (mobile phase) before entering the columns (stationary phase).[14] For different gas molecules, they normally have various progression rates originating from the varied interaction strengths between the mobile and the stationary phase. As a result, it is possible to differentiate them by the retention times and the different stationary phases can be selected based on the composition of the sample gases. Detectors are normally placed at the end of the columns to monitor the retention time of each species. Thermal conductivity detector (TCD, measurement on changes in thermal conductivity), flame ionisation detector (FID, measurement on ions produced from the sample burning in a hydrogen-air flame) and photo-ionisation detector (PID, measurement on ions produced from ionising the sample with ultraviolet light) are three types of commonly used detectors. Furthermore, mass spectrometer (MS) can be coupled with GC to construct

GC-MS instruments. An important feature of GC-MS is that it can provide structural information for compound identification with high sensitivity and selectivity. Consequently, it is very useful for measuring complicated reaction systems, such as plastic decomposition, to identify the actual products after catalysis.

Practically, besides the selection of columns and detectors, other parameters can be optimised in different aspects to achieve better separation of the sample gases. For instance, the column length can be varied depending on the experimental requirements. Longer columns normally provide better separation of molecules, but the analysis time will be also extended due to increased resistance from the stationary phase. Additionally, the selection of carrier gases is vital for the successful detection of the sample gases of interest. For example, for $H_2$ detection, $N_2$ gas is a better choice compared to He gas, as a He and $H_2$ mixture cannot generate a monotonic signal increase in the $H_2$ concentration in TCD, whilst a linear correlation can be found using $N_2$ as the carrier gas.[15]

In this thesis, the GC (Agilent) was equipped with thermal conductivity detectors (TCD) using He and $N_2$ as the carrier gases. The amount of product (e.g. $H_2$, $CO_2$) was quantified by integrating the peak area, with calibration of gases of interest conducted prior to measuring the experimental products. The columns were kept at a fixed temperature for the gas separation process.

### 2.2.7 Time-Resolved Photoluminescence (TRPL)

TRPL studies the photoluminescence properties of materials by detecting the light emission as a function of time after photoexcitation. It uses a very short pulse (ps to ns) from a laser for photoexcitation, where the electrons in a semiconductor's valence band are promoted to the

conduction band. After the photoexcitation, photoluminescence can be emitted owing to the relaxation of the excited electrons to their ground state. A high-speed detection unit is used for collecting and analysing the emitted light as a function of time, and the decay curve can be generated as shown in **Fig. 2.6**.[16]

The lifetime of the photo-generated charge carriers can be obtained by fitting the background-corrected PL spectrum using a decay function, where mono- or bi- exponential decay function is applied depending on the types of recombination rate. The correlation can be expressed as the following equations:

$$y = A_1 e^{-t/\tau_1} + y_0 \qquad \textbf{Equation 2.8}$$

$$y = A_1 e^{-t/\tau_1} + A_2 e^{-t/\tau_2} + y_0 \qquad \textbf{Equation 2.9}$$

where $A_1$, $A_2$, $\tau_1$ and $\tau_2$ are the parameters for lifetime fitting and $y_0$ is a constant.[17]

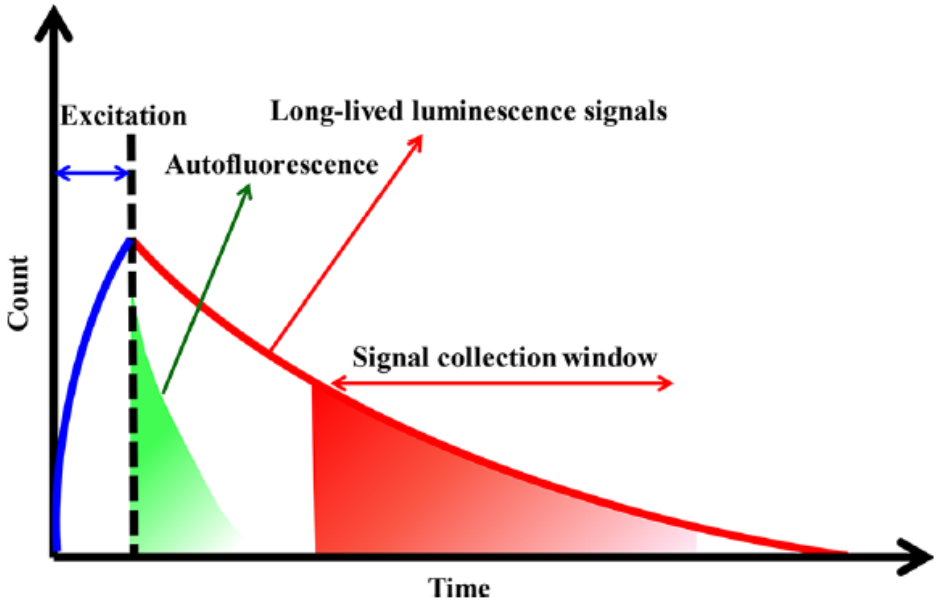



**Figure 2.6** A typical spectrum obtained from the TRPL measurement. Reproduced from ref 16. Copyright 2018 American Chemical Society.

In photocatalysis, TRPL is particularly powerful for studying the charge separation process. By measuring the lifetime of excited electrons, it is possible to evaluate how effective a material is at separating and utilising the photo-generated charges. Additionally, *in-situ* TRPL measurement is also possible, where photocatalysts can be exposed to different gas atmospheres or electrolytes and the change of lifetime can be detected. The TRPL results are often used to interpret the photocatalytic activity. Normally, a longer lifetime contributes to higher photocatalytic activity, as the charge recombination is suppressed, and photon energy loss is minimised.

In this thesis, the TRPL measurements were conducted on a bespoke micro-photoluminescence set-up. A Ti-Sapphire laser (λ=266 nm, pulse duration = 150 fs, repetition rate = 76 MHz) was used with a laser spot diameter of *ca.* 200 micron and an output power of 2 mW. The spectrometer was used as a monochromator before passing signals to a photomultiplier tube detector and the instrument response function width was *ca.* 150 ps. A pulse-picking mode was used for collecting the consecutive signals with enough delay for samples to return to the ground state.

### 2.2.8 Ultraviolet-Visible Diffuse Reflectance Spectroscopy (UV-Vis DRS)

UV-Vis DRS is applied to study the electronic structure and band gap of powdered materials. Instead of measuring the light absorption, it focuses on the diffuse reflectance of a sample, which can also provide information on the light absorption properties. The Kubelka-Munk theory is applied to describe and interpret the UV-Vis DRS data:

$$F(R_\infty) = \frac{(1-R_\infty)^2}{2R_\infty} = \frac{K}{S} \qquad \textbf{Equation 2.10}$$

where $R_\infty$ is the reflectance of an infinitely thick layer; K is the absorption coefficient, and S

is the scattering coefficient.[18]

The UV-Vis DRS results are normally used to generate Tauc plots which correspond to the band gap of the measured sample. It assumes that the absorption coefficient can be described by the following equation:

$$(\alpha h\nu)^{1/\gamma} = B(h\nu - E_g) \qquad \textbf{Equation 2.11}$$

where α is the absorption coefficient; $h$ is the Plank constant; ν is the frequency of photons; γ is dependent on the electron transition in a material which equals to 1/2 or 2 for direct allowed transition or indirect allowed transitions; B is a constant; $E_g$ is the band gap energy of the measured sample. For semiconductors, $F(R_\infty)$ is used instead of α and $(F(R_\infty)h\nu)^{1/\gamma}$ versus hν is plotted, where the band gap is determined at the x-intersection point of the linear fitting curve from the Tauc plot, as shown in **Fig. 2.7**.[19]

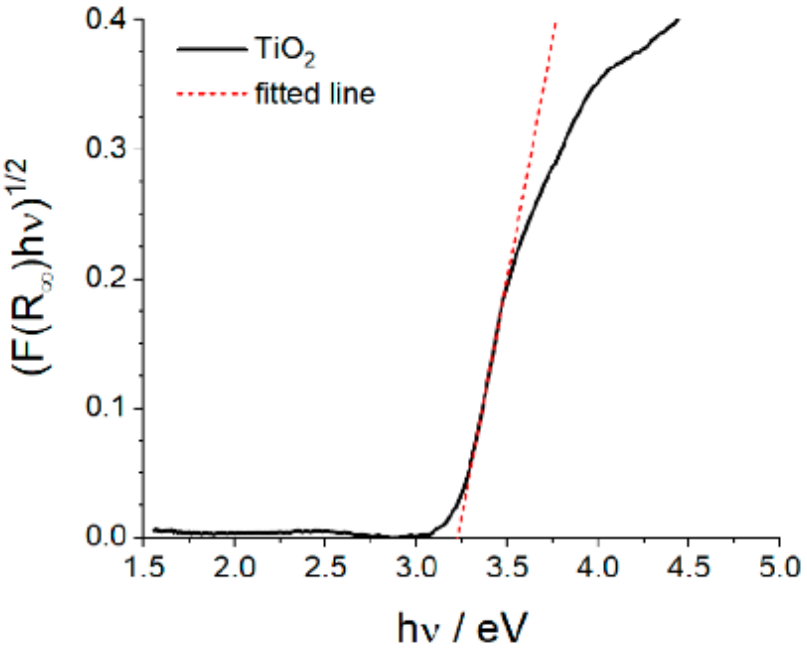



**Figure 2.7** Tauc plot for determination of the band gap energy generated from UV-Vis DRS spectra. Reproduced from ref. 19. Copyright 2018 American Chemical Society.

In this thesis, the UV-Vis DRS measurements were conducted on a SHIMADZU UV-Vis-NIR

(UV-2600) instrument. Around 80 mg samples were used and pressed into a sample holder and the signals were recorded in the range of 200 nm to 1000 nm in reflectance mode.

### 2.2.9 Electrochemical Impedance Spectroscopy (EIS)

EIS uses a small amplitude sinusoidal AC voltage for measuring the amplitude and phase angle of the resulting current, where the impedance can be determined as the following equation:

$$Z = \frac{V_{(t)}}{I_{(t)}} = Z' + jZ'' \qquad \textbf{Equation 2.12}$$

where Z is the impedance; $V_{(t)}$ and $I_{(t)}$ are the applied voltage and the measured current; Z' and Z'' are the real and imaginary parts of the impedance and the imaginary number $j = \sqrt{-1}$.[20] Multiple steps, including charge transfer, mass transport, adsorption, and desorption, can occur at different timescales for an electrochemical process. The EIS can be used to differentiate these steps based on the change in behaviour to the variation of AC frequency. For the application in photocatalysis, the EIS results are typically plotted in the form of Nyquist plot (Z' versus Z''). By using an appropriate equivalent circuit model, the charge transfer resistance at the interface of semiconductor and electrolyte can be obtained.[21] For instance, the Randles circuit (**Fig. 2.8**) is widely used for comparing charge transfer resistance between samples, where $R_s$ is the solution resistance; $R_{ct}$ is the charge transfer resistance, and $C_{int}$ is the interfacial capacitance.[22] Samples with a lower value of $R_{ct}$ are generally believed to have lower charge transfer resistance.

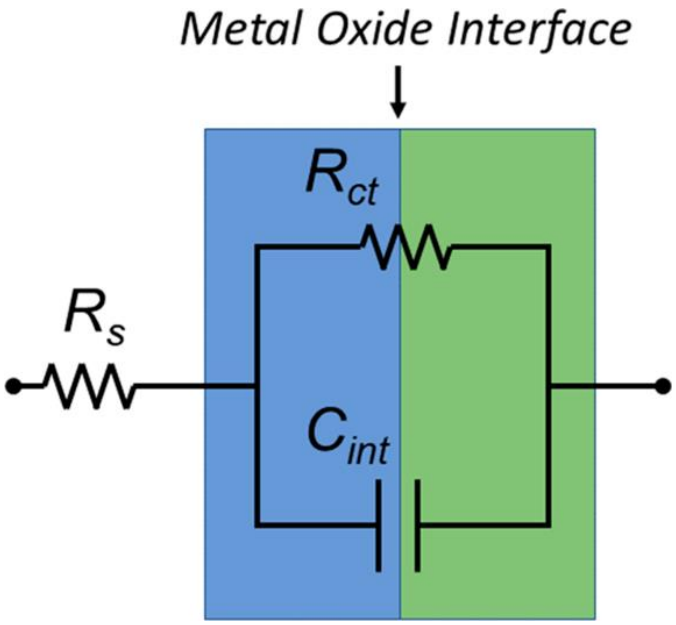



**Figure 2.8** Randles circuit for measurement of interfacial charge transfer resistance $R_{ct}$. Reproduced from ref. 22. Copyright 2020 American Chemical Society.

In this thesis, the EIS measurements were conducted on an electrochemical workstation (Autolab PGSTAT302N) using measuring frequency range from 10000 Hz to 1 Hz under open-circuit potential mode in 0.5 M $Na_2SO_4$ aqueous solution. For the ink preparation, 10 mg sample was dispersed in a mixed solution of 2 mL ethanol, 67 µL deionised (DI) water and 13 µL Nafion®, followed by 30 minutes sonication. 2 µL of the prepared ink was coated on a glassy carbon electrode with a diameter of 0.07 $cm^2$. A graphene counter electrode with 4 $cm^2$ effective working area was used to obtain more uniform current/potential distribution on the working electrode.

### 2.2.10 Atomic Force Microscopy (AFM)

AFM is a powerful technique used to study surface morphology and properties. It measures the interaction forces between a sharp tip (attached to a microcantilever) and the sample surface to obtain surface information.[23, 24] Various surface characteristics including morphology, hardness, roughness, and elasticity, can be measured, making it very useful in

material investigations. A schematic illustration of a typical AFM set-up is shown in **Fig. 2.9**.[23] Besides the tip and microcantilever, the AFM instrument also consists of a cantilever deflection sensor and a piezoelectric positioner to monitor the deflection feedback of the cantilever during AFM measurement. When the tip scans the contour of the surface, the motion of the tip is monitored by the photodiode, which records the light intensity difference of the deflected laser beam (the laser is focused on the tip). The photodiode signal difference is further analysed by a software to generate the AFM results. The tip can be maintained at a constant force or constant height above the surface of the sample, depending on the applied operation mode. Typically, there are three operation modes: non-contact mode, contact mode, and tapping mode.[23] In non-contact mode, the cantilever is placed slightly away from the sample surface and oscillates at its natural resonance frequency. During measurement, shifts from the natural resonance frequency can be caused by the interactions between the sample and the tip, from which surface information can be extracted. This mode is applied for soft and sensitive samples to avoid sample destruction, but the resolution is lower than the contact mode. When using contact mode, continuous contact between the tip and the sample surface is programmed in the software. It is suitable for generating high resolution images and determining the mechanical properties of the measured material. However, it may cause sample damage and tip wear during measurement. The tapping mode combines the advantages of non-contact and contact modes, where the tip is allowed to contact the surface during oscillation. It can minimise contact time and the damage on the sample while retaining promising resolution. By selecting the most appropriate AFM mode, imaging quality, measurement accuracy, and sample preservation can be optimised depending on the specific

experimental goals.

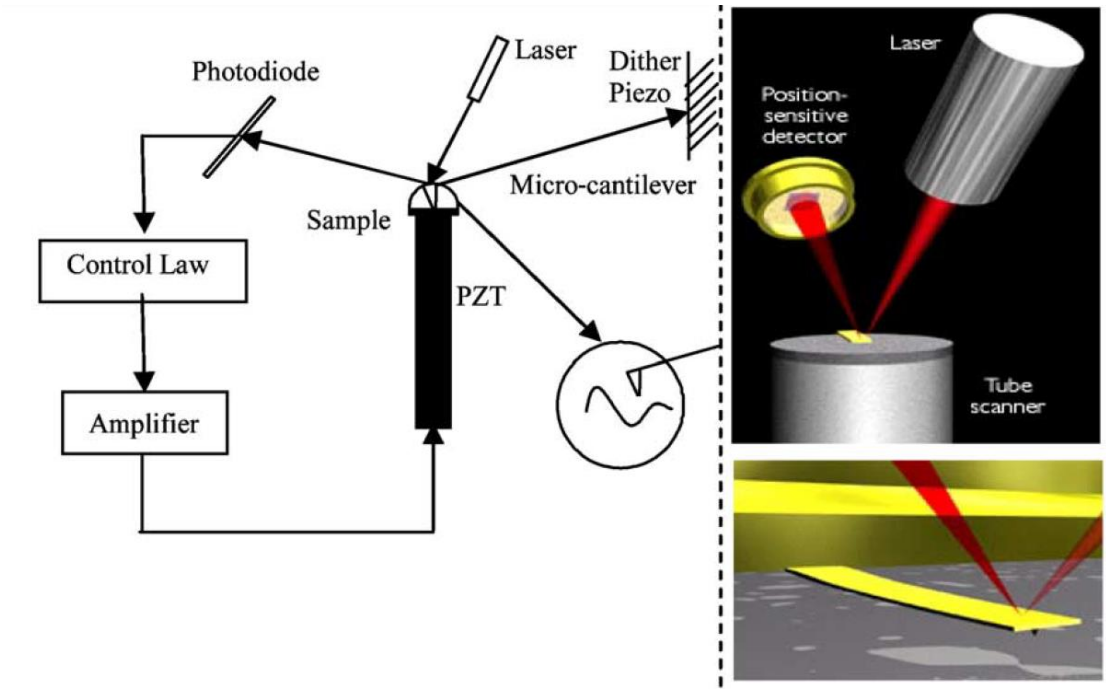



**Figure 2.9** Schematic illustration of a typical AFM set-up. Reproduced from ref. 23. Copyright 2004 Elsevier.

In this thesis, AFM measurements were conducted on Bruker MM-8 high resolution AFM equipped with SNL-10 cantilever. PeakForce tapping mode was applied and the voltage setpoint was 0.3 V to maintain constant height accuracy. For sample preparation, solid particles were dispersed in isopropanol by 3-hour sonication. Then the suspension was centrifuged at 1500 rpm for 5 minutes. The supernatant (2.5 μL) was collected and drop-cast onto ultra-flat mica. Following that, the prepared sample was dried at room temperature before the AFM measurement.

## 2.3 Experimental Methods

### 2.3.1 Chemicals

The reagents used in this thesis were as listed below without further purification: Potassium iodate (purity ≥ 98.0%, Fluka); Tungsten sulphide (99.8% metals basis, Alfa Aesar);

Hydrochloric acid S. G. (reagent grade, ~37%, Fisher Scientific); Triethanolamine (reagent grade, 98%, Sigma-Aldrich); Methanol (for HPLC, ≥99.9%, Sigma-Aldrich); Ethanol (for GC, ≥99.8%, Sigma-Aldrich); 2-Propanol (for GC, ≥99.5%, Sigma-Aldrich); Cyclohexane (ACS reagent, ≥99.5%, Sigma-Aldrich); Hexane (for HPLC, ≥97.0%, Sigma-Aldrich); Nafion® D-520 dispersion (5% w/w in water and 1-propanol, ≥1.00 meq/g exchange capacity, Alfa Aesar); n-Butyllithium (1.6M solution in hexanes, AcroSeal®, ACROS ORGANICS); Cyclohexane (ACS reagent, ≥99.5%, Sigma-Aldrich); 2-Phenylethanol (95+%, Alfa Aesar); Octylamine (99%, Sigma-Aldrich); Formamide (Analytical reagent grade, ≥99.5%, Fisher Scientific); Titanium (IV) isopropoixde (97%, Aldrich); Thiourea (ReagentPlus™, ≥99.0%, Sigma); Polyvinylpyrrolidone (average mol wt 360000, Sigma-Aldrich); Chloroplatinic acid hexahydrate (ACS reagent, ≥37.5% Pt basis, Sigma-Aldrich); Ruthenium (III) chloride hydrate (Fluorochem); Nickel (II) chloride hexahydrate (reagent grade, ≥98.0%, Sigma-Aldrich); Cobalt (II) nitrate hexahydrate (ACS reagent, ≥98.0%, Sigma-Aldrich); Palladium (II) nitrate dihydrate (40%Pd, Sigma-Aldrich); Silver nitrate (ACS reagent, ≥99.0%, Sigma-Aldrich); Iron (III) chloride (reagent grade, 97%, Sigma-Aldrich); Cerium (III) nitrate hexahydrate (99% trace metals basis, Aldrich); Sodium hydroxide anhydrous pellets (reagent grade, ≥98%, Sigma-Aldrich); Hexamethylenetetramine (ReagentPlus®, 99%, Sigma-Aldrich); Zinc (II) acetate dihydrate (ACS reagent, ≥99.0% (KT), Sigma-Aldrich); Zinc (II) nitrate hexahydrate (reagent grade, 98%, Sigma-Aldrich); Titanium (IV) butoxide (99.999% trace metal basis, Sigma-Aldrich); Hydrofluoric acid (ACS reagent, 48%, Sigma-Aldrich), Trimethylphosphine (97%, Sigma-Aldrich). DI water used for experiments was obtained from a Purite Select Water Purification System.

### 2.3.2 Synthesis of Few-Layer $WS_2$ (FL-$WS_2$) and Metal-Doped $WS_2$

2.5 g $WS_2$ powder was placed in a 100 mL round-bottom flask under $N_2$ flush for 15 mins before adding 12.5 mL 1.6M n-Butyllithium (n-BuLi). Then the system was sealed and stirred at 65 °C for 24 hours. After cooling down to room temperature, the lithium intercalated $WS_2$ was washed with 50 mL hexane to remove excessive n-BuLi. Following that, the washed sample was centrifuged and dried under vacuum at 60 °C for 15 minutes. The dried sample was dispersed in 400 mL DI water and sonicated for 6 hours. The $WS_2$ suspension was centrifuged at 5000 rpm for 15 minutes and the supernatant was collected. 15 mL of diluted HCl (1 : 10 in DI water) was added to the supernatant followed by centrifugation at 5000 rpm for 5 minutes to obtain FL-$WS_2$. The FL-$WS_2$ was then dried under vacuum overnight.

For the synthesis of metal-doped $WS_2$, 75 mg thiourea and certain amount of metal precursors (5wt%) were mixed in 10 mL DI water and left overnight. Then the metal complex solution was added into a $WS_2$ suspension where 60 mg FL-$WS_2$ and 60 mg polyvinylpyrrolidone were dispersed in a mixture of 35 mL DI water and 15 mL isopropanol. The mixture was sonicated for 1 hour and transferred to an autoclave, followed by hydrothermal treatment at 160 °C for 24 hours. After cooling down to room temperature, the precipitate was washed three times using DI water and dried under vacuum overnight. The metal-doped $WS_2$ was reduced under 5% $H_2$ in $N_2$ at 300 °C (ramp rate 2 °C/minute) for 2 hours. For calcined $WS_2$ at different temperatures for heterojunction study, the gas was changed to pure $N_2$.

### 2.3.3 Synthesis of $TiO_2$ Flake (f-$TiO_2$)

2 mL $Ti[OCH(CH_3)_2]_4$ was added into 36 mL 2-phenyl ethanol in a 100 mL Teflon-lined

stainless-steel autoclave and stirred for 5 minutes. Then 2 mL octylamine was slowly added in dropwise manner and further stirred for 10 minutes. Then the autoclave was transferred to an oven at 200 °C for 36 hours. After cooling down to room temperature, the pale-yellow powder was washed with 75%/25% ethanol and cyclohexane for three times and dried overnight under vacuum. 0.5 g of the dried powder was dispersed in 10 mL formamide and sonicated for 24 hours, followed by washing with 75%/25% ethanol and cyclohexane mixture for three times. After centrifugation, the white powder was dried under vacuum overnight.

### 2.3.4 Synthesis of $WS_2$-$TiO_2$ and W-$TiO_2$

8 mg of FL-$WS_2$ (*ca.* 12wt%) and 64 mg $TiO_2$ flake were dispersed in 40 mL and 160 mL DI water respectively by 2 hours sonication. The $WS_2$ suspension was centrifuged at 3000 rpm for 1 minute to remove the undissolved FL-$WS_2$. Then the $TiO_2$ suspension was stirred at 1000 rpm with $N_2$ bubbling. The supernatant of $WS_2$ suspension was slowly added into the $TiO_2$ suspension and stirring at room temperature for 15 minutes followed by 80 °C heating in oil bath under reflux for 2 hours to obtain $WS_2$-$TiO_2$ (black powder, Chapter 3). For the synthesis of W-$TiO_2$ (dark-grey powder, Chapter 4), the stirring was extended to 24 hours at 80 °C under reflux. The obtained powders were dried under vacuum overnight. For the $WS_2$-$TiO_2$ sample (Chapter 4) with 0 h fabrication time, the $WS_2$ and $TiO_2$ suspension were mixed and stirred at room temperature for 15 minutes without any further treatment.

### 2.3.5 Synthesis of Faceted $CeO_2$ Samples

**c-$CeO_2$** Cerium (III) nitrate hexahydrate (0.868 g) and sodium hydroxide (9.6 g) were dissolved in 5 mL and 35 mL DI water, respectively. Then, two solutions were mixed in a Teflon liner and kept stirring for 30 minutes. A milky slurry was formed after stirring and was

then sealed in a stainless-steel autoclave. The autoclave was then transferred into an electric oven for hydrothermal treatment at 180 ℃ for 24 hours. After naturally cooling down to room temperature, the sample was washed with DI water and ethanol for three times.

**o-$CeO_2$** Cerium (III) nitrate hexahydrate (0.434 g) and hexamethylenetetramine (HMT) (3.5 g) were dissolved in 50 mL DI water with stirring for 30 minutes. Then, it was heated at 75 ℃ for 3 hours. The obtained samples were washed with DI water and ethanol for at least three times. It was dried in vacuum oven at 60 ℃ overnight and calcined at 200 ℃ in air flow to remove HMT.

**s-$CeO_2$** Cerium (III) nitrate hexahydrate (0.868 g) and sodium hydroxide (9.6 g) were dissolved in 5 mL and 35 mL DI water, respectively. Then, two solutions were mixed in a flask and kept stirring for 24 hours at room temperature. The sample was washed with DI water and ethanol for three times.

### 2.3.6 Synthesis of Faceted $TiO_2$ Samples

**p-$TiO_2$** 48% hydrofluoric acid (0.6 mL) was added into titanium (IV) butoxide (5 mL) in a 40 mL Teflon liner with stirring. Then it was sealed in a stainless-steel vessel autoclave and transferred into an electric oven for hydrothermal treatment at 180 ℃ for 24 hours. After naturally cooling down to room temperature, the white precipitate was washed with DI water and ethanol three times. Then it was dried overnight in a vacuum oven at 60 ℃ overnight. To remove the fluorine atoms on the sample surface, it was calcined at 600 ℃ for 90 minutes before the NAP-XPS measurement.

**b-$TiO_2$** DI water (0.6 mL) was added into titanium (IV) butoxide (5 mL) in a 40 mL Teflon liner with stirring. Then it was sealed in a stainless-steel autoclave and transferred into an

electric oven for hydrothermal treatment at 180 ℃ for 24 hours. After naturally cooling down to room temperature, the white precipitate was washed with DI water and ethanol for three times. Then it was dried overnight in a vacuum oven at 60 ℃ overnight.

### 2.3.7 Synthesis of Faceted ZnO Samples

**p-ZnO** Zinc (II) acetate dihydrate (6.0 g) and HMT (3.84 g) were dissolved in 48 mL DI water and kept stirring for 10 minutes. Then the mixture was transferred into a Teflon liner and sealed in a stainless-steel autoclave. It was transferred into an electric oven for hydrothermal treatment at 99 ℃ for 24 hours. After naturally cooling to room temperature, the sample was washed with DI water and ethanol for three times. It was dried in vacuum oven at 60 ℃ overnight and calcined at 450 ℃ in air flow for 2 hours to remove HMT.

**r-ZnO** Zinc (II) nitrate hexahydrate (1.487 g) and sodium hydroxide (6 g) were dissolved in 10 mL of DI water. Then 100 mL of ethanol was added into the Zn precursor solution. Following that, 1,2-ethanediamine (EDA) (5 mL) was added into the mixture. The mixture was transferred to a 250 mL covered plastic container and kept stirring for 3 days at room temperature. The white precipitate was washed with DI water and ethanol for three times. It was dried in vacuum oven at 60 ℃ overnight and calcined at 450 ℃ in air flow for 2 hours to remove EDA.

### 2.3.8 Photocatalytic Testing

The photocatalytic testing for metal-doped $WS_2$ was conducted in a flow cell where $N_2$ was used as a carrier gas with a flow rate of 100 mL/minute and 15 mg sample was dispersed in 100 mL 10% methanol aqueous solution. The light source was a mercury UV lamp (helios quartz) with a 365 nm wavelength.

The photocatalytic testing for $WS_2$-$TiO_2$, W-$TiO_2$ and faceted metal oxides, an overhead-irradiation-type batch reactor was used. Argon gas was used as the carrier gas for hydrogen evolution reactions and helium gas was used for oxygen evolution. Typically, 5 mg of catalyst was dispersed in 10 mL aqueous solution with certain percentage of sacrificial reagents (if not specified, 0.01M $KIO_3$ for OER and 10% methanol for HER) with stirring. 300 W Xe Arc lamp (Photonic Solutions) was used as a light source. All the evolved gases were analysed by gas chromatography with TCD detectors. Oxalydihydrazide was used to detect the HCHO for which the hydrazone bonds (-NH-N=CH-) formed by the chemical reaction between the hydrazine group and aldehyde could be monitored by UV-Vis spectroscopy. HCOOH and $CH_3OH$ was detected by NMR (Bruker Hg400) and CO, $CO_2$, $H_2$ and $O_2$ were measured by GC. The $CO_2$ evolution rate was determined based on the following equation:

$$Rate_{CO_2} = \frac{n_{CO_2}\ (mol)}{m_{catalyst}\ (g) \times t\ (s)}$$

where n is the amount of $CO_2$ produced; m is the mass of photocatalysts used for catalytic reactions; and t is the reaction time.

## 2.4 Conclusion

In summary, this chapter introduced the fundamental principles of the characterisation techniques applied in this thesis and explained their contributions to the investigation of materials. Additionally, the experimental methods and chemicals used in DPhil projects were described.

In the next chapter, the structure of surface-engineered $WS_2$-based materials and their application in photocatalytic HER will be explored. Detailed examples of the application of characterisation techniques such as AFM, XPS, XAS, XRD, and TEM will be presented.

## 2.5 References


1. C. F. Holder and R. E. Schaak, Tutorial on Powder X-ray Diffraction for Characterizing Nanoscale Materials, *ACS Nano*, 2019, **13**, 7359-7365.
2. J. A. Kaduk, S. J. L. Billinge, R. E. Dinnebier, N. Henderson, I. Madsen, R. Černý, M. Leoni, L. Lutterotti, S. Thakral and D. Chateigner, Powder diffraction, *Nat. Rev. Methods Primers*, 2021, **1**, 77.
3. S. Sun, X. Zhang, J. Cui and S. Liang, Identification of the Miller indices of a crystallographic plane: a tutorial and a comprehensive review on fundamental theory, universal methods based on different case studies and matters needing attention, *Nanoscale*, 2020, **12**, 16657-16677.
4. F. Xu, Y.-C. Shi and D. Wang, X-ray scattering studies of lignocellulosic biomass: A review, *Carbohydr. Polym.*, 2013, **94**, 904-917.
5. L. E. Franken, K. Grünewald, E. J. Boekema and M. C. A. Stuart, A Technical Introduction to Transmission Electron Microscopy for Soft-Matter: Imaging, Possibilities, Choices, and Technical Developments, *Small*, 2020, **16**, 1906198.
6. M. A. Lauterbach, Finding, defining and breaking the diffraction barrier in microscopy – a historical perspective, *Opt. Nanoscopy*, 2012, **1**, 8.
7. D. N. G. Krishna and J. Philip, Review on surface-characterization applications of X-ray photoelectron spectroscopy (XPS): Recent developments and challenges, *Appl. Surf. Sci. Adv.*, 2022, **12**, 100332.
8. G. Greczynski and L. Hultman, X-ray photoelectron spectroscopy: Towards reliable binding energy referencing, *Prog. Mater. Sci.*, 2020, **107**, 100591.
9. D. E. Starr, in *Ambient Pressure Spectroscopy in Complex Chemical Environments*, American Chemical Society, 2021, vol. 1396, ch. 1, pp. 1-17.
10. J. Timoshenko and B. Roldan Cuenya, In Situ/Operando Electrocatalyst Characterization by X-ray Absorption Spectroscopy, *Chem. Rev.*, 2021, **121**, 882-961.
11. A. Iglesias-Juez, G. L. Chiarello, G. S. Patience and M. O. Guerrero-Pérez, Experimental methods in chemical engineering: X-ray absorption spectroscopy—

XAS, XANES, EXAFS, *Can. J. Chem. Eng.*, 2022, **100**, 3-22.

12. P. Zimmermann, M. O. J. Y. Hunault and F. M. F. de Groot, 1s2p RIXS Calculations for 3d Transition Metal Ions in Octahedral Symmetry, *J. Spectrosc.*, 2018, **2018**, 3618463.
13. M. M. Roessler and E. Salvadori, Principles and applications of EPR spectroscopy in the chemical sciences, *Chem. Soc. Rev.*, 2018, **47**, 2534-2553.
14. G. A. Eiceman, J. Gardea-Torresdey, E. Overton, K. Carney and F. Dorman, Gas Chromatography, *Anal. Chem.*, 2002, **74**, 2771-2780.
15. K. Snavely and B. Subramaniam, Thermal Conductivity Detector Analysis of Hydrogen Using Helium Carrier Gas and HayeSep® D Columns, *J. Chromatogr. Sci.*, 1998, **36**, 191-196.
16. K. Y. Zhang, Q. Yu, H. Wei, S. Liu, Q. Zhao and W. Huang, Long-Lived Emissive Probes for Time-Resolved Photoluminescence Bioimaging and Biosensing, *Chem. Rev.*, 2018, **118**, 1770-1839.
17. Y. Li, H. Zhou, S. Cai, D. Prabhakaran, W. Niu, A. Large, G. Held, R. A. Taylor, X.-P. Wu and S. C. E. Tsang, Electrolyte-assisted polarization leading to enhanced charge separation and solar-to-hydrogen conversion efficiency of seawater splitting, *Nat. Catal.*, 2024, **7**, 77-88.
18. R. A. Schoonheydt, UV-VIS-NIR spectroscopy and microscopy of heterogeneous catalysts, *Chem. Soc. Rev.*, 2010, **39**, 5051-5066.
19. P. Makuła, M. Pacia and W. Macyk, How To Correctly Determine the Band Gap Energy of Modified Semiconductor Photocatalysts Based on UV–Vis Spectra, *J. Phys. Chem. Lett.*, 2018, **9**, 6814-6817.
20. S. Wang, J. Zhang, O. Gharbi, V. Vivier, M. Gao and M. E. Orazem, Electrochemical impedance spectroscopy, *Nat. Rev. Methods Primers*, 2021, **1**, 41.
21. S. J. A. Moniz, S. A. Shevlin, D. J. Martin, Z.-X. Guo and J. Tang, Visible-light driven heterojunction photocatalysts for water splitting – a critical review, *Energy Environ. Sci.*, 2015, **8**, 731-759.
22. A. R. C. Bredar, A. L. Chown, A. R. Burton and B. H. Farnum, Electrochemical

Impedance Spectroscopy of Metal Oxide Electrodes for Energy Applications, *ACS Appl. Energy Mater.*, 2020, **3**, 66-98.

23. N. Jalili and K. Laxminarayana, A review of atomic force microscopy imaging systems: application to molecular metrology and biological sciences, *Mechatronics*, 2004, **14**, 907-945.

24. D. J. Müller, A. C. Dumitru, C. Lo Giudice, H. E. Gaub, P. Hinterdorfer, G. Hummer, J. J. De Yoreo, Y. F. Dufrêne and D. Alsteens, Atomic Force Microscopy-Based Force Spectroscopy and Multiparametric Imaging of Biomolecular and Cellular Systems, *Chem. Rev.*, 2021, **121**, 11701-11725.

# Chapter 3 Surface Engineering of Ultrathin $WS_2$ as Photocatalysts

## 3.1 Introduction

In heterogeneous catalysis, surface engineering plays an important role in catalytic reactions such as the formation and breakage of chemical bonds are highly dependent on surface properties.[1] Ultrathin 2D materials are believed to be the ideal platforms for surface functionalisation, as the majority of atoms in their layered structures are exposed for catalytic reactions.[2] Among various 2D materials, TMDs are regarded as an important class of layered materials in photocatalysis due to their unique chemical and physical properties after exfoliation. TMDs usually have the chemical formula of $MX_2$, where M represents a d-block metal element (groups IV-VI for layered TMDs), and X represents a chalcogen element (S, Se or Te).[3] Each layer of a TMD generally follows an atomic sequence of X-M-X in the out-of-plane direction, and layers are stacked via weak van der Waals interactions.[4] This unique structure makes the exfoliation of TMDs by various feasible approaches (mechanical/chemical exfoliation or physical/chemical vapour deposition) cost-effective.[5, 6] Compared with their bulk counterparts, ultrathin TMD layers enable photo-generated charge carriers to migrate to the surface reactive sites with shorter distances, which can potentially minimise charge recombination and increase quantum efficiency.[7] Additionally, their strong in-plane covalent bonds allow exfoliated ultrathin TMDs to achieve relatively large lateral sizes while maintaining atomic thickness, which can contribute to high specific surface for catalytic reactions.[8] Furthermore, their electronic properties such as band structure and charge carrier mobility are dependent on thickness and phase (*e.g.* 1T and 2H) and can be tuned through appropriate synthetic methods.[2, 9] These advantages can lead to enhanced

photocatalytic activity by optimisation of the corresponding properties.

Among TMDs, molybdenum disulphide ($MoS_2$) is one of the most widely used materials due to its outstanding catalytic performance in both photocatalytic and electrochemical HER from water-splitting.[10, 11] In photocatalysis, the formation of heterojunctions with other semiconductor materials and its role as a cocatalyst make $MoS_2$ a promising noble-metal-free alternative to reduce overall costs for large-scale production.[12] For example, Li *et al.* reported a novel Janus bilayer junction photocatalyst ($MoS_2$-$Bi_{12}O_{17}Cl_{l2}$).[13] This study suggested that $MoS_2$ not only provided reactive sites, but also prolonged the lifetime of photo-generated charge carriers via the efficient electron transfer channel at the interface between the two materials. It was found that the photocatalytic HER rate of $MoS_2$-$Bi_{12}O_{17}Cl_{l2}$ increased by 38 times after forming the heterojunction compared with pristine $Bi_{12}O_{17}Cl_{l2}$. In addition to forming heterojunctions, Li *et al.* also successfully demonstrated the potential of using d-block metal-doped ultrathin $MoS_2$ alone as an efficient photocatalyst when combined with appropriate surface engineering strategies.[14]

Tungsten disulphide ($WS_2$), which possesses the same crystal structure as $MoS_2$, is currently less widely used compared to $MoS_2$. In electrocatalysis, studies conducted by Manish's group have demonstrated significantly low overpotentials using 1T-$WS_2$ monolayer for electrochemical HER.[15] However, relatively few studies have focused on its application in photocatalysis. Theoretically, it has been shown by DFT studies that $WS_2$ has a more negative conduction band potential compared to $MoS_2$, which may make ultrathin $WS_2$ nanosheet a better candidate for photocatalytic HER.[16] Additionally, although previous studies have suggested that $WS_2$ can enhance the rate of photocatalysis like $MoS_2$ when forming

heterojunctions with traditional particulate photocatalysts (*e.g.* $TiO_2$), the interaction between two materials has not been systematically studied.[17, 18] Moreover, the $WS_2$ nanosheets used in these studies often suffered from significant layer restacking, which might result in poor contact between two materials. Consequently, further investigation into the use of ultrathin $WS_2$ nanosheets as both the main catalyst and cocatalyst in photocatalysis remains necessary.

In this chapter, the possibility using ultrathin $WS_2$ nanosheets as the support for photocatalysis is firstly explored. Surface modification through doping with d-block metals including Fe, Ru, Co, Pt, Pd Ni and Ag was applied to ultrathin few-layer $WS_2$ (FL-$WS_2$). It was found that Ru doped FL-$WS_2$ (Ru-$WS_2$) exhibited the highest activity for photocatalytic HER. Following that, its structure and corresponding effects were investigated using a range of cutting-edge techniques. Then, the study of 2D-2D heterojunctions between thin $TiO_2$ flake (f-$TiO_2$) and FL-$WS_2$ was carefully conducted to explore the effect of introducing FL-$WS_2$ as a cocatalyst. It was found that the intimate contact between two materials after heterojunction formation enabled the development of a built-in electric field at the interface, which led to increased charge transfer efficiency and enhanced photocatalytic activity.

## 3.2 Results and Discussion

### 3.2.1 Bulk $WS_2$ Exfoliation to FL-$WS_2$

The FL-$WS_2$ nanosheets were synthesised from commercial bulk $WS_2$ (2H phase) by chemical exfoliation. **Fig. 3.1a** illustrates the XRD patterns of bulk and FL-$WS_2$, confirming its 2H crystal structure. Notably, the peak intensity was significantly decreased after exfoliation, while the (002) peak could still be observed. The reduction in peak intensity indicates the loss of crystallinity originating from the reduced thickness of FL-$WS_2$.

Additionally, the presence of the (002) peak implies that the overall crystal structure of FL-$WS_2$ was still preserved after chemical exfoliation. Then, the AFM results reveal that the thickness of FL-$WS_2$ can reach up to a monolayer thickness of 0.95 ± 0.04 nm as illustrated in **Fig. 3.1b, c**, which is consistent with the XRD results.[19]

To further study the morphology and phase of FL-$WS_2$ after exfoliation, high resolution TEM measurements were performed. The ultrathin 2D morphology of FL-$WS_2$ can be confirmed by the TEM images as shown in **Fig. 3.2a**, which further supports the XRD and AFM results. Interestingly, a mixed phase of 1T and 2H $WS_2$ can be observed, as revealed by high resolution TEM in **Fig. 3.2b, c**. The 2H phase can be attributed to the original structure of bulk $WS_2$ before exfoliation, while the 1T phase may be produced from the phase transition of the original 2H phase during the exfoliation process. The 2H to 1T phase transition was reported by previous studies on $MoS_2$ nanosheets after chemical exfoliation, which was considered to be caused by lithium intercalation during the chemical exfoliation process.[20]

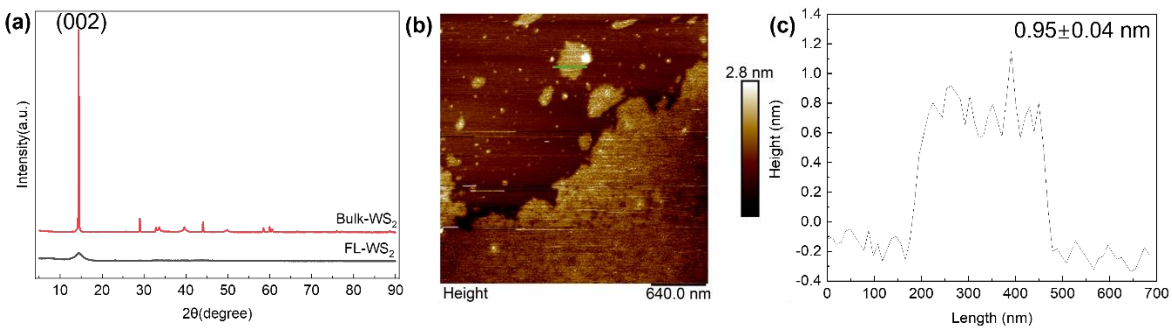



**Figure 3.1 (a)** XRD patterns of $WS_2$ before (bulk $WS_2$) and after (FL-$WS_2$) exfoliation; **(b, c)** AFM measurement showing the thinness of FL-$WS_2$ of 0.95 ± 0.04 nm. AFM measurements in this figure were conducted by Dr. Weiran Zheng (PolyU).

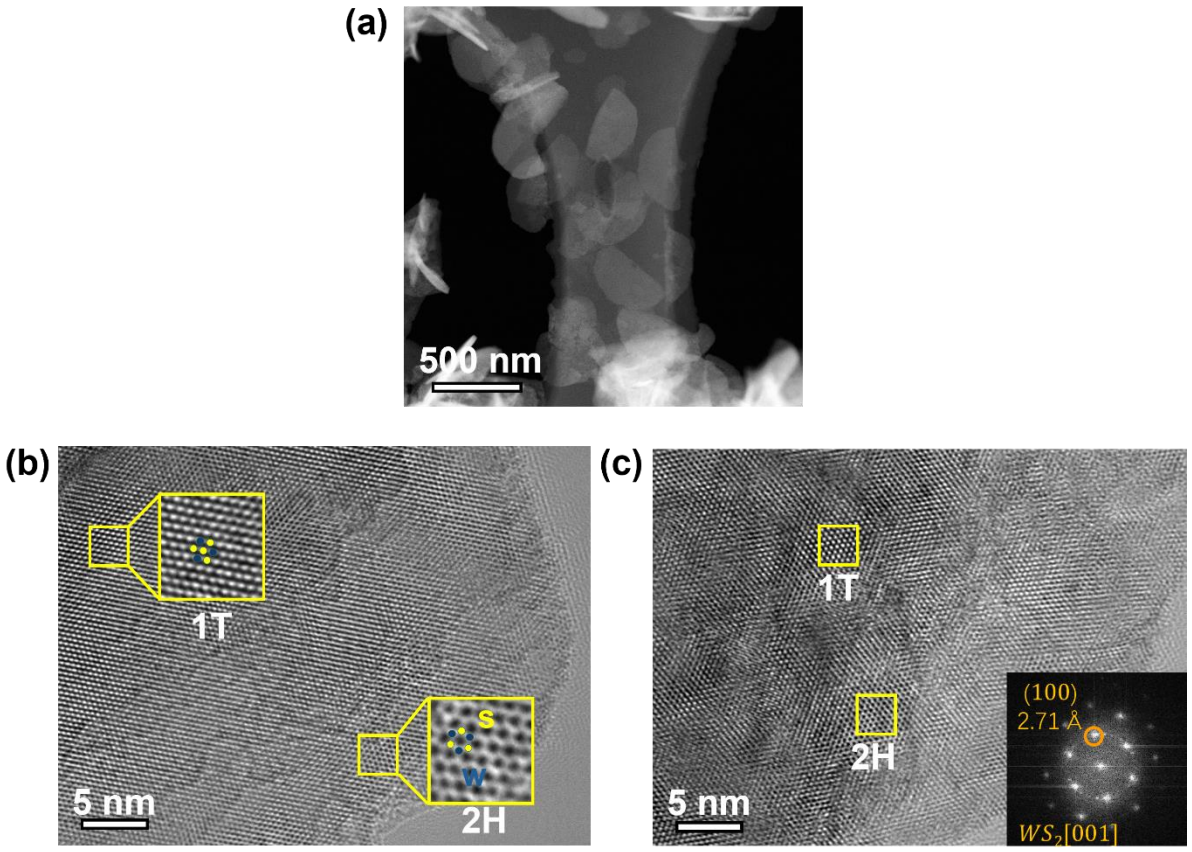



**Figure 3.2 (a)** TEM image of FL-$WS_2$; **(b, c)** High resolution TEM images of FL-$WS_2$ revealing the mixture of 1T and 2H phases. TEM images in this figure were acquired and analysed by Dr. Zhihang Xu (PolyU).

### 3.2.2 FL-$WS_2$ Modification by d-Block Metal Doping

After confirming its ultrathin 2D morphology, FL-$WS_2$ nanosheets were then doped with various transition metals (calculated to be 5% by weight) as cocatalysts by hydrothermal methods and followed by thermal reduction in a $H_2$ atmosphere (in 5% $H_2/N_2$ atmosphere, 300 ℃, ramp rate 2 ℃/minute, 2 hours). The corresponding photocatalytic HER activities using methanol as sacrificial reagents are summarised in **Fig. 3.3a**. The photocatalytic $H_2$ evolution rate of FL-$WS_2$ increased up to 8.86 times compared to the commercial bulk $WS_2$. Despite the higher surface area after exfoliation, the activity enhancement may also be

attributed to the formation of a Schottky junction in the mixture of 2H and 1T phases, as 2H-$WS_2$ is a semiconductor material, whereas 1T-$WS_2$ is metallic.[21] The Schottky barrier could assist charge separation upon photoexcitation, promoting the electron migration to the conductive sites, resulting in the prolonged lifetime of photo-generated charge carriers and higher catalytic activity, as previously reported.[22]

Notably, most of the d-block metal-doped FL-$WS_2$ did not show significant enhancement in catalytic activity (Co, Ni and Ag doped FL-$WS_2$), and FL-$WS_2$ nanosheets doped with Fe, Pt and Pd even showed suppressed catalytic activity. Only Ru doped $WS_2$ (Ru-$WS_2$) showed a 2.14-fold increase in activity compared to FL-$WS_2$. Unfortunately, the overall photocatalytic HER activity of Ru-$WS_2$ is lower than that in previous studies using other photocatalysts (e.g. $TiO_2$) as the supports for single atoms under similar catalytic conditions as shown in **Table A1**. Consequently, this indicates $WS_2$ may not be a promising choice when used alone as the primary photocatalyst.

Interestingly, compared to previous studies on anchoring d-block metals on the $MoS_2$ surface by the same synthesis approach, a clear volcano activity curve could be found, which was attributed to the strength of metal-hydrogen bonding for HER reactions.[14] Although the Ru atom was also the most promising dopant for $MoS_2$ nanosheets, the trend in catalytic activity suggests a different reaction mechanism between metal-doped $WS_2$ and $MoS_2$, which might be caused by the structural differences of the synthesised samples. Consequently, it is important to investigate the actual position and coordination environment of the transition meal dopants in FL-$WS_2$. Since Ru-$WS_2$ exhibits the highest activity for photocatalytic HER, further investigations have focused on these samples by applying various characterisation

techniques to understand their structure and the corresponding contribution to the increased activity. Before conducting further characterisation, the activity was first investigated and optimised by varying the amount of doped Ru, and it was found that 5wt% Ru-$WS_2$ (4.49% in weight percentage from the ICP test) showed the highest activity in photocatalytic HER as illustrated in **Fig. 3.3b**.

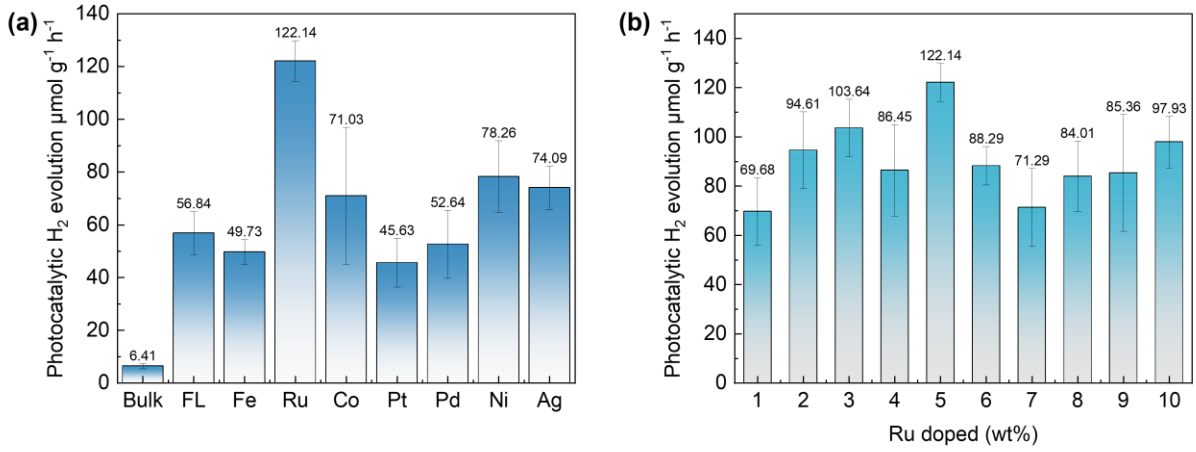



**Figure 3.3 (a)** Photocatalytic HER performance of FL-$WS_2$ with different d-block metal dopants; **(b)** Photocatalytic HER performance of Ru doped FL-$WS_2$ with different weight percentages of Ru atoms loaded for catalytic activity optimisation.

### 3.2.3 Structural Characterisation on Ru-$WS_2$

Among all the Ru doped samples, no additional phases, except the FL-$WS_2$ phase, can be identified from the XRD pattern as shown in **Fig. 3.4a**. This indicates that the Ru dopant did not suffer from significant aggregation into large Ru nanoparticles or other Ru-containing crystalised bulk species. High resolution TEM images in **Fig. 3.4b** reveal that the atomic dots exhibiting higher contrast could be attributed to Ru atoms, which were mainly adapted into the structure in the form of single atoms and nanoclusters (labelled in yellow circles), consistent with the previous XRD results. Following that, EELS studies on the Ru edge

further confirm the existence of Ru atoms in the sample, as shown in **Fig. 3.4c**, which is in agreement with the TEM results. Additionally, it should be noted that both 2H and 1T phases are retained in Ru-$WS_2$, as shown in **Fig. 3.4b**, indicating the stability of this mixed-phase structure under the synthetic conditions.

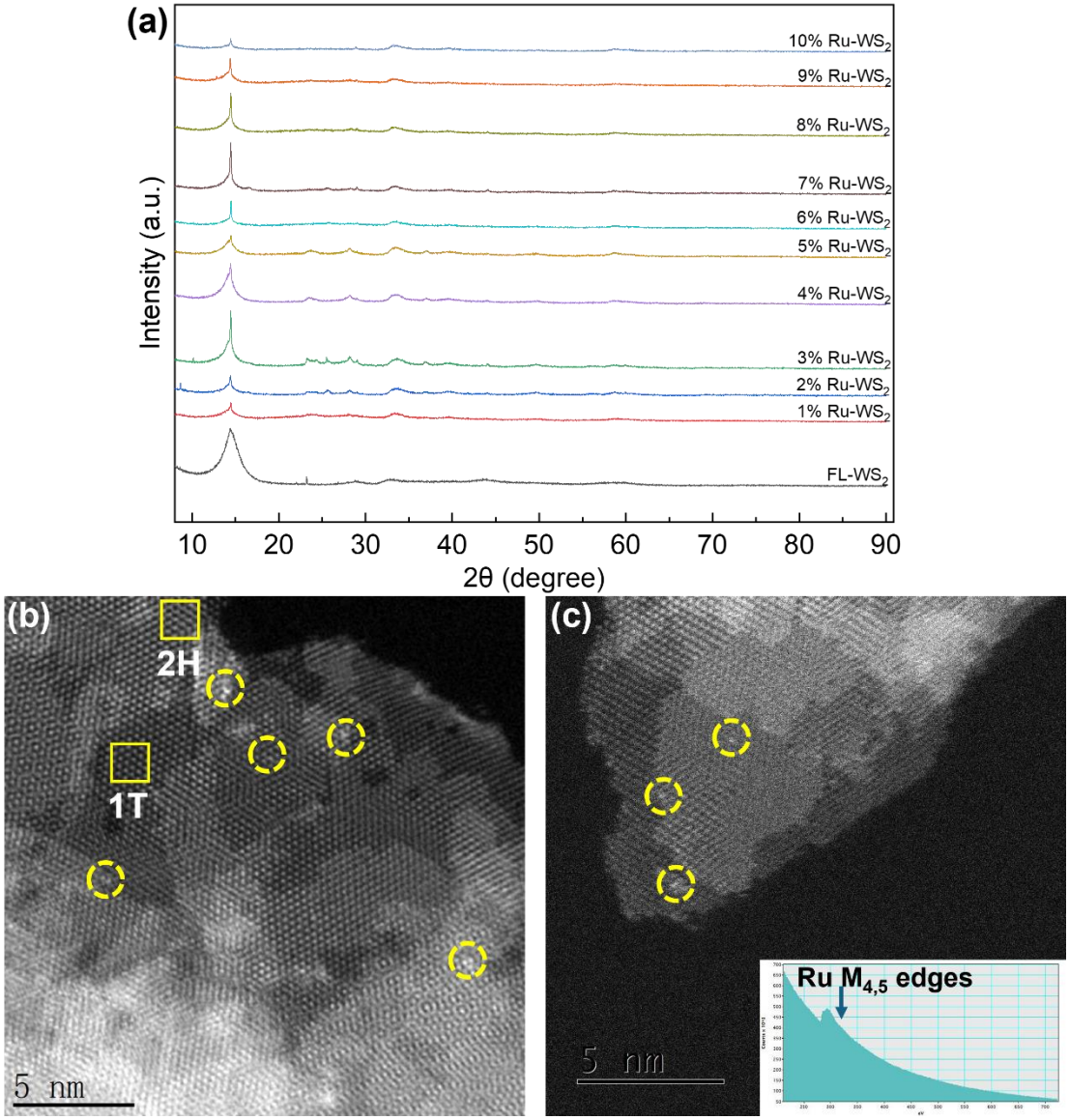



**Figure 3.4 (a)** XRD patterns of FL-$WS_2$ with different amounts of Ru atoms doped; **(b)** High resolution TEM image of Ru-$WS_2$; **(c)** High resolution TEM and EELS results of Ru-$WS_2$ at Ru edge. TEM images in this figure were acquired by Dr. Ping-Luen Ho.

The chemical state and coordination environment of Ru atoms were then investigated by

XANES (**Fig. 3.5a**) and EXAFS (**Fig. 3.5b**) measurements. The XANES results generated from Ru K-edge measurements illustrate that the Ru atoms in Ru-$WS_2$ nanosheets have almost the same absorption edge as the elemental Ru foil reference, indicating a chemical state of zero for the doped Ru atoms in $WS_2$ nanosheets. Furthermore, the corresponding Fourier-transformed EXAFS (FT-EXAFS) of Ru-$WS_2$ shows no Ru-Ru scattering peak compared to the Ru foil. This is consistent with the XRD and TEM results, confirming that the Ru atoms are mainly in the form of single atoms and nanoclusters without forming large Ru nanoparticles. The peak at 2.391 ± 0.004 Å can be assigned to Ru-S scattering with a coordination number of 6.17 ± 0.32 and the EXAFS fitting results are summarised in **Table 3.1**. Given that Ru atoms are in the chemical state of zero, it is possible that the doped Ru atoms weakly interact with the surrounding sulphur atoms. The similar electronegativities of these two elements may also contribute to the chemical state of zero.

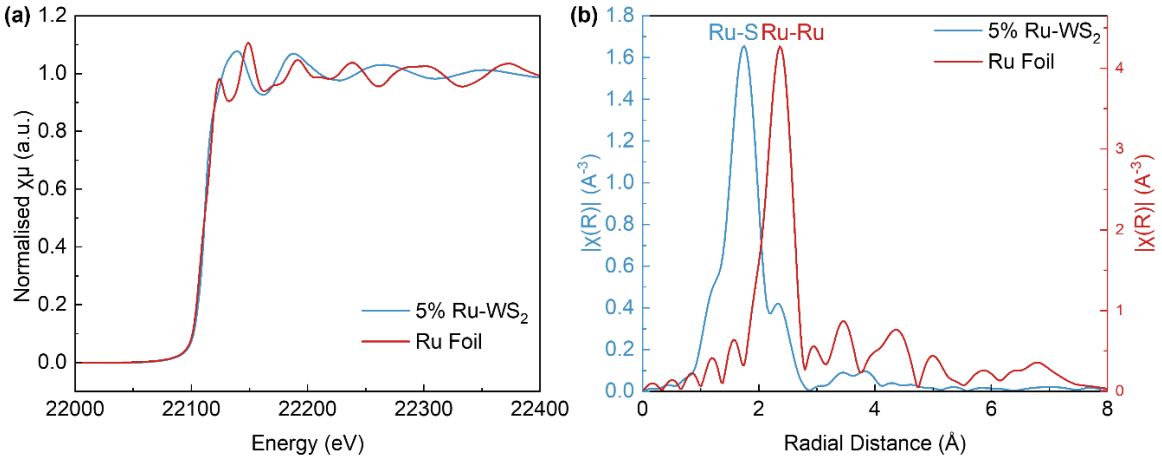



**Figure 3.5 (a)** XANES spectra of 5wt% Ru-$WS_2$ (Ru K-edge), showing a similar absorption edge to elemental Ru foil; **(b)** FT-EXAFS spectra of 5wt% Ru-$WS_2$. No Ru-Ru scattering peak can be observed in the Ru doped samples compared to the Ru foil, suggesting that the Ru atoms are doped in the form of single atoms/nanoclusters. The XAS measurement was conducted by Dr. Tai-Sing Wu (NSRRC).

**Table 3.1** EXAFS fitting parameters at the Ru-K edge of 5wt% Ru-$WS_2$.

| Composition | Shell | Coordination Number | R (Å) | $\sigma^2$ | R factor |
|---|---|---|---|---|---|
| 5wt% Ru-$WS_2$ | Ru-S | 6.17 ± 0.32 | 2.391 ± 0.004 | 0.005 | 2.8% |

Different from Ru doped $MoS_2$ from previous studies, which has a coordination number of 2.8 ± 0.3 and a bond length of 1.98 ± 0.03 Å for Ru-S bonds, the high coordination number and long bond length of Ru-S in Ru doped $WS_2$ may exclude the possibility of Ru atoms existing as surface exposed catalytic sites.[12] Instead, it is more probable that the Ru atoms replaced W atoms in the $WS_2$ crystal structure, or were accommodated in the interlayer region during synthesis. If the Ru atoms had replaced W atoms in the structure, it would not be possible to observe the bright single atom sites from the high resolution TEM image (**Fig. 3.2b, c**), as tungsten atoms normally have higher contrast compared to Ru atoms in the dark field TEM images due to their higher atomic number. Therefore, it is possible that the introduced Ru atoms were accommodated between the $WS_2$ layers, coordinated to the sulphur atoms in the $WS_2$ layers above and below the Ru atoms. Additionally, since the shortest distance between sulphur atoms in adjacent $WS_2$ layers is *ca.* 4.636 Å, the large interlayer distance makes it possible to accommodate the introduced Ru atoms.

Following the identification of Ru atoms in the FL-$WS_2$ nanosheets, their role in promoting photocatalytic reactions needs to be verified. It is well-established that the conductivity of TMDs in the in-plane direction is much higher than the out-of-plane direction (up to 2200 times higher), as the weak van der Waals interaction cannot serve as an ideal channel for charge transfer in the interlayer region.[23] However, with the intercalation of Ru atoms, the large interlayer charge transfer resistance could be minimised. To verify this assumption, EIS

testing was conducted both under dark and light conditions, comparing it with thermally reduced FL-$WS_2$ without Ru dopant. As implied by the Nyquist plots from the EIS testing as shown in **Fig. 3.6**, the samples with Ru atoms doped showed lower impedance radii both under dark and light conditions. This indicates a more effective charge transfer process after the introduction of Ru atoms, which facilitates the catalytic reaction and reduces the possibility of charge recombination.

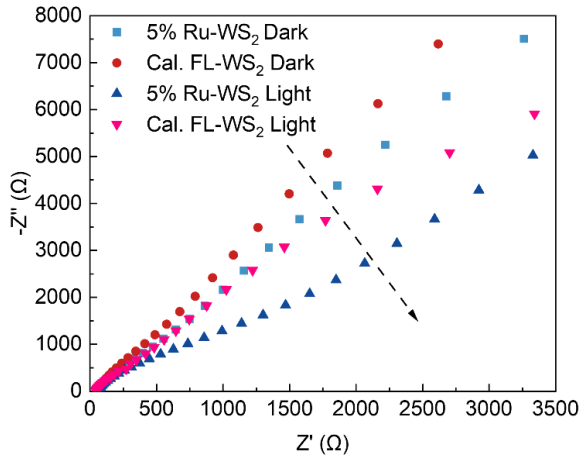



**Figure 3.6** Nyquist plots from EIS testing of thermally reduced FL-$WS_2$ with Ru and without under dark and light conditions. Introducing Ru atoms reduced the charge transfer resistance under both dark and light conditions. EIS testing was conducted under assistance of Dr. Yifei Wang.

However, in this study, as the Ru atoms might not be exposed on the surface, theoretical evidence on how introduced Ru atoms change the electronic structure of $WS_2$ is still lacking to explain why Ru doped samples exhibit higher activity than other d-block metal dopants. Moreover, although the $H_2$ evolution rate of Ru-$WS_2$ has significantly improved compared to commercial bulk $WS_2$, the overall photocatalytic activity is still lower compared to previous studies.[13] This implies that $WS_2$ may not be suitable to be used as a reactive photocatalyst on

its own.

### 3.2.4 $WS_2$ -$TiO_2$ Assembly for 2D-2D Heterojunctions

The investigation of applying FL-$WS_2$ as a cocatalyst to traditional anatase $TiO_2$ photocatalysts was then conducted. To maximise the contact when forming the heterojunction, $TiO_2$ with thin flake morphology (**Fig. 3.7a, b**) was prepared to fabricate the $WS_2$-$TiO_2$ 2D-2D heterojunctions. The anatase crystal structure of f-$TiO_2$ is revealed by XRD as shown in **Fig. 3.7c**. Notably, after forming $WS_2$-$TiO_2$ with the weight ratio of 1 : 8, the XRD patterns are almost identical to those of the pristine f-$TiO_2$, with the absence of characteristic $WS_2$ XRD peaks. As seen in **Fig. 3.1a**, the exfoliated $WS_2$ layers exhibited weak XRD peaks compared to the bulk sample. The absence of $WS_2$ XRD patterns in the composite material may indicate that the FL-$WS_2$ nanosheets were well-dispersed on the $TiO_2$ support rather than aggregating.

However, it should be noted that, if the FL-$WS_2$ nanosheets were not successfully attached to the $TiO_2$ support, or suffered from decomposition, similar XRD patterns of $WS_2$-$TiO_2$ could also be obtained. Furthermore, it is possible that the absence of the $WS_2$ XRD patterns could be due to the resolution limitations of the applied XRD instrument at low $WS_2$ loading levels. Therefore, to further confirm the existence of $WS_2$, Raman spectroscopy was applied to the $WS_2$-$TiO_2$ composite, along with FL-$WS_2$ and f-$TiO_2$ for comparison. As shown in **Fig. 3.8**, the $E^1_{2g}$ and $A^1_{1g}$ peaks are the characteristic Raman peaks of $WS_2$ which cannot be seen in f-$TiO_2$.[24] For $WS_2$-$TiO_2$, the $E^1_{2g}$ and $A^1_{1g}$ peaks are evident in the Raman spectra. The Raman and XRD results imply that FL-$WS_2$ has successfully assembled with f-$TiO_2$ without significant layer restacking.

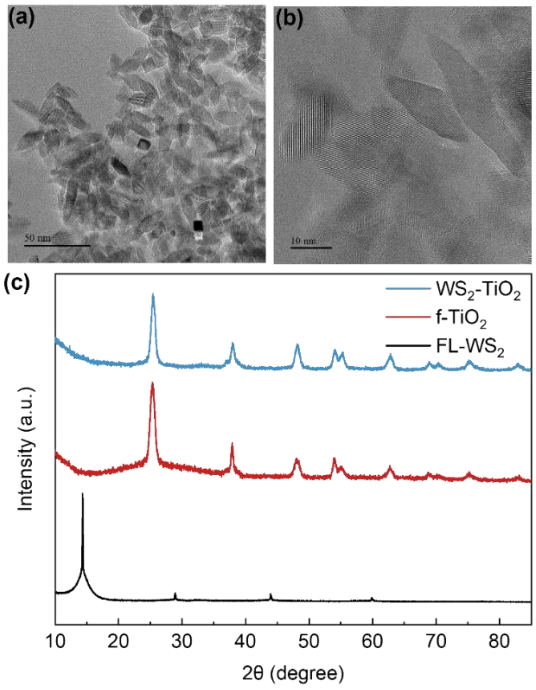



**Figure 3.7 (a, b)** TEM images of f-$TiO_2$ showing its flake morphology; **(c)** XRD patterns of $WS_2$-$TiO_2$, f-$TiO_2$ and FL-$WS_2$. No $WS_2$ XRD pattern can be observed after forming the heterojunction. TEM images were acquired by Prof. Huihuang Fang.

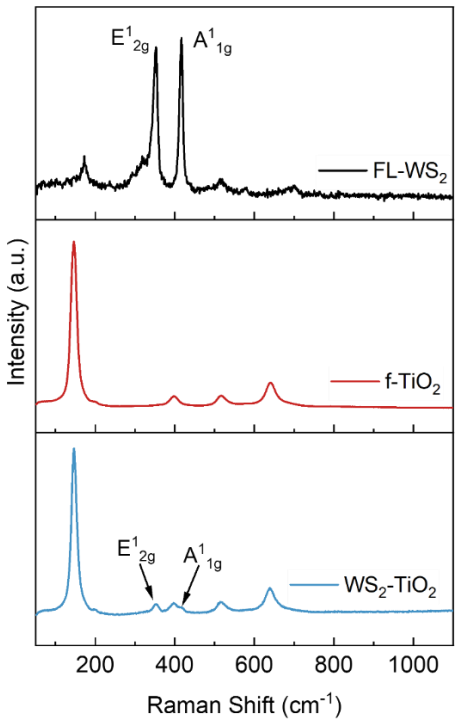



**Figure 3.8** Raman results of FL-$WS_2$, f-$TiO_2$ and $WS_2$-$TiO_2$, confirming the existence of FL-$WS_2$ in $WS_2$-$TiO_2$. Raman testing was conducted by Dr. Xuelei Pan.

The intimate contact between the two materials was further supported by the TEM results as illustrated in **Fig. 3.9**. No clear isolated $WS_2$ phase can be observed on top of f-$TiO_2$, as shown in **Fig. 3.9a**. However, the $WS_2$ nanosheets become evident under atomic resolution with a clear $WS_2$-$TiO_2$ interface in **Fig. 3.9b**. It is worth noting that some of the $WS_2$ nanosheets have been transformed into nanoclusters and a single-atom-like morphology on the f-$TiO_2$ support, which will be analysed and discussed in Chapter 4.

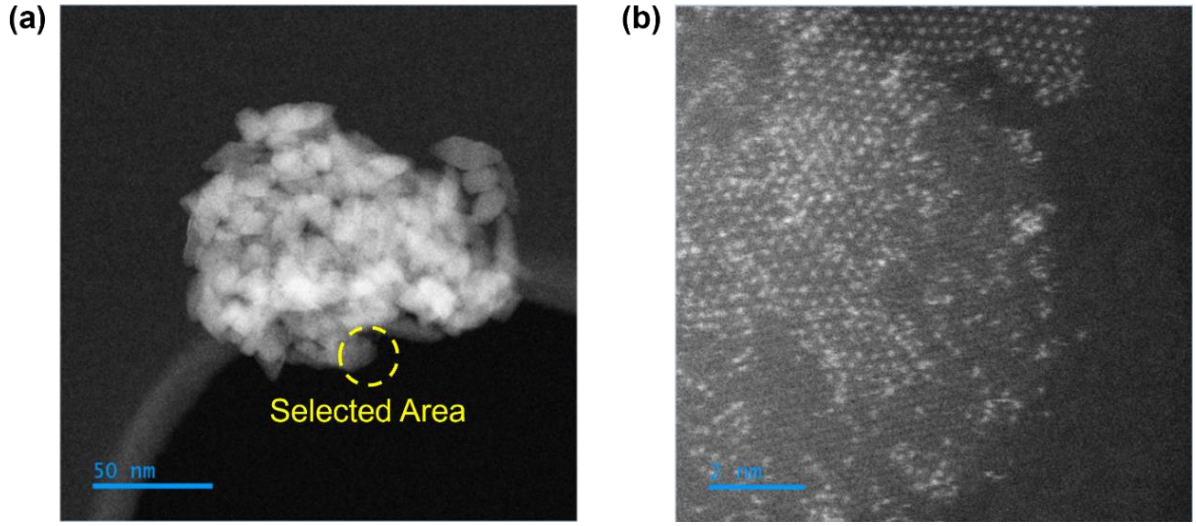



**Figure 3.9** High resolution TEM images of $WS_2$-$TiO_2$. The $WS_2$ nanosheets are closely in contact with the $TiO_2$ support, with part of $WS_2$ dissociated into single atoms and clusters. TEM images were acquired by Dr. Ping-Luen Ho.

The effect of the close contact between the two materials was then studied by XPS. As demonstrated in **Fig. 3.10a, b**, the Ti 2p and O 1s both show a positive shift by 0.34 eV and 0.31 eV, respectively, after the formation of the heterojunction, whilst W 4f and S 2p both exhibit a negative shift by 0.56 eV and 0.83 eV in $WS_2$-$TiO_2$ compared to pristine FL-$WS_2$. This indicates that an internal electric field was created at the interface, with a decrease in electron density on f-$TiO_2$ and an increase on FL-$WS_2$. In the presence of this internal electric field, the separation of photo-generated electrons and holes can be more efficient, as the

electric field provides an extra driving force for the migration of electrons and holes to different sites.[25]

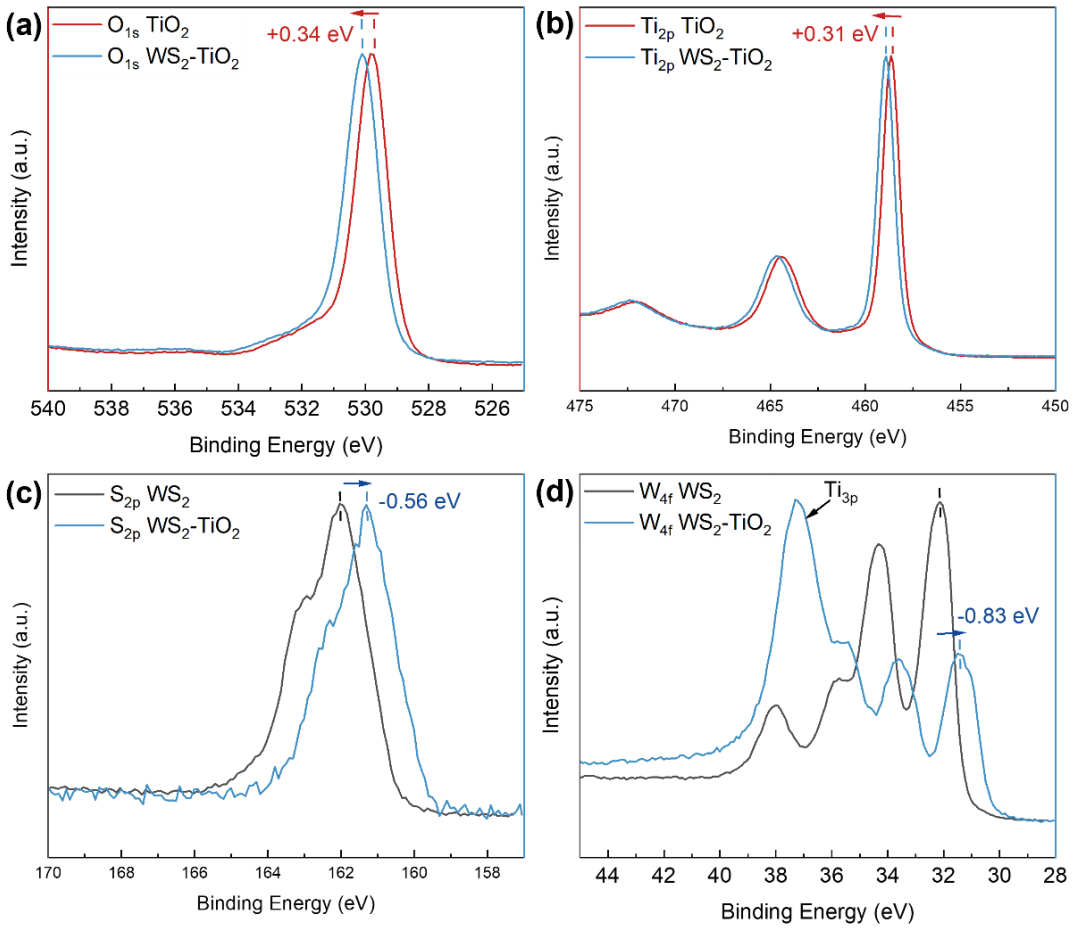



**Figure 3.10** XPS spectra of $WS_2$ and $TiO_2$ based samples. **(a)** O 1s, **(b)** Ti 2p, **(c)** S 2p and **(d)** W 4f. The positive shift in $TiO_2$ peaks and the negative shift in $WS_2$ peaks indicate a built-in electric field formed with electrons transferring from $TiO_2$ into $WS_2$. XPS measurement was performed by Dr. Shaoliang Guan (HarwellXPS).

As FL-$WS_2$ contains both the conducting 1T phase and the semiconducting 2H phase, there are several possible charge migration mechanisms. For the electrons generated from f-$TiO_2$, they can preferably migrate to the 1T-$WS_2$ side due to the formation of a Schottky barrier between f-$TiO_2$ and 1T-$WS_2$, which traps electrons on 1T-$WS_2$ (metallic), separating them

from photogenerated holes. At the 2H-$WS_2$ and f-$TiO_2$ interface, as $TiO_2$ is more positively charged, photo-generated electrons from 2H-$WS_2$ may preferentially migrate to the $TiO_2$ side, with holes attaching to 2H-$WS_2$. In both cases, the electrons and holes can be effectively separated, thereby suppressing the recombination process and enhancing the photocatalytic activity.

### 3.2.5 $WS_2$-$TiO_2$ Heterojunctions for Photocatalytic HER

As seen in **Fig. 3.2**, chemical exfoliation can result in partial phase transformation from 2H to 1T phase. According to previous reports, this process may also be reversible when treating the as-exfoliated TMD nanosheets with calcination.[26] As discussed, the charge migration mechanism under illumination can vary depending on the phase of $WS_2$. This may make it complicate to identify the actual contributions from each phase for the increased catalytic performance.

To investigate the influence of phase change in $WS_2$ on photocatalysis, the FL-$WS_2$ nanosheets were calcined at different temperatures in $N_2$ atmosphere to obtain varying proportions of 1T-$WS_2$ and 2H-$WS_2$ in the $WS_2$ sample as the starting materials for fabrication of 2D-2D heterojunctions. The composition of $WS_2$-$TiO_2$ was first optimised as shown in **Fig. 3.11a**. The photocatalytic activity of $WS_2$-$TiO_2$ with a ratio of 1 : 8 can be enhanced up to 4.60-fold compared to pristine f-$TiO_2$, which may be due to the formation of internal electric field as discussed earlier. The photocatalytic HER activity of $WS_2$-$TiO_2$ is comparable to that reported in previous heterojunction studies, as shown in **Table A2**, highlighting the potential of $WS_2$ as a promising cocatalyst.

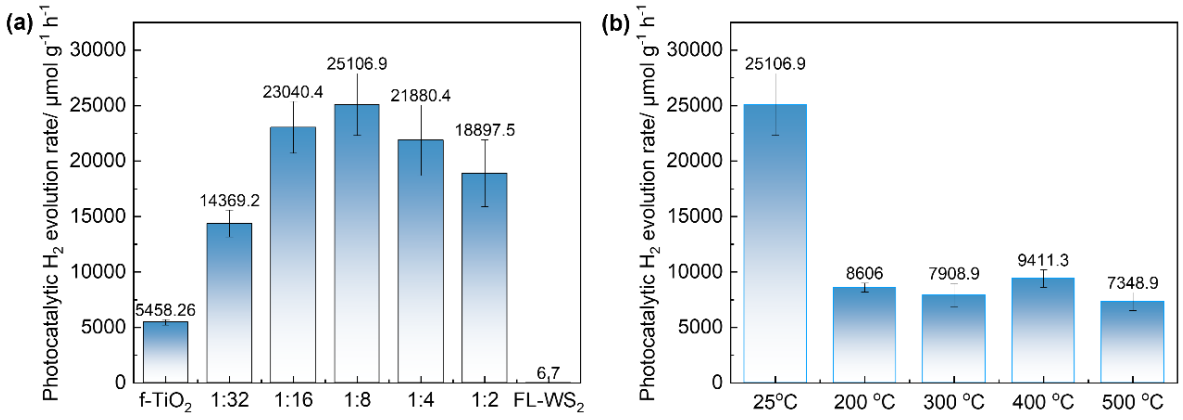



**Figure 3.11** Photocatalytic HER tests on **(a)** different proportions of FL-$WS_2$ in $WS_2$-$TiO_2$ heterojunctions and **(b)** calcined FL-$WS_2$ at different temperatures before forming the heterojunction with a weight ratio of 1 : 8 for $WS_2$ : $TiO_2$. Triethanolamine (TEOA) was used as the sacrificial reagent in an aqueous solution (10%).

Then, the $WS_2$ : $TiO_2$ ratio was kept the same (1 : 8 in weight ratio), while the calcination temperature of FL-$WS_2$ was varied before forming the $WS_2$-$TiO_2$ heterojunctions. However, after calcination at temperatures ranging from 200 °C to 500 °C, a significant decrease in activity can be observed in all the samples as shown in **Fig. 3.11b**. From the previous TEM images in **Fig. 3.4**, after thermal reduction at 300 °C ($N_2$ atmosphere, ramp rate 2 °C/minute, 2 hours), 1T-$WS_2$ was still present in the sample. Therefore, to explain the decreased activity, the possibility of a complete loss of the 1T phase after calcination can be excluded. Furthermore, all the samples with calcined $WS_2$ exhibited similar activity, rather than a gradual change in photocatalytic activity as expected. Consequently, the decrease in photocatalytic rate may not be attributed to the phase change of $WS_2$. To understand this phenomenon, TEM accompanied by EDX mapping was used for studying the structure of the samples with calcined $WS_2$. **Fig. 3.11** demonstrates the structure of $WS_2$-$TiO_2$ with $WS_2$

nanosheets calcined at 300 ℃ before forming the heterojunction.

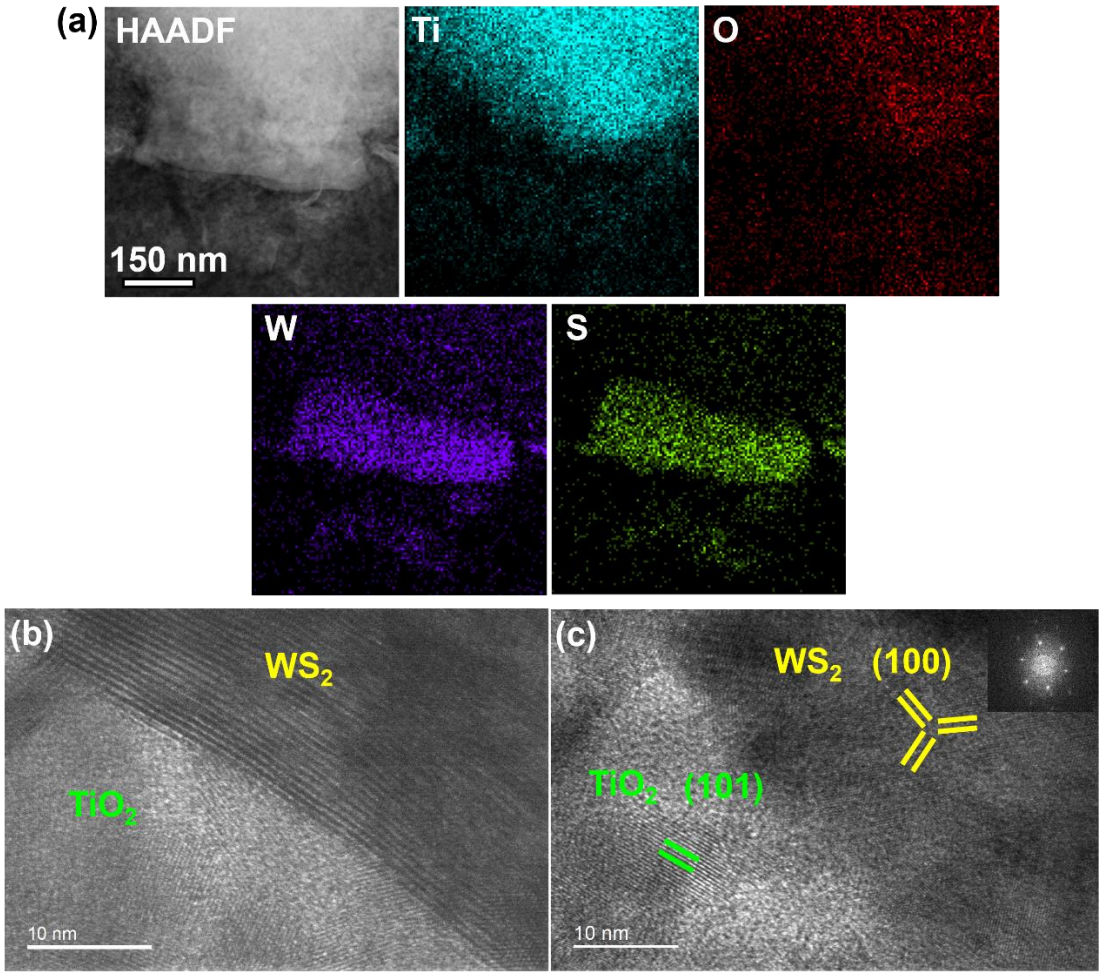



**Figure 3.12** Structural characterisation of $WS_2$-$TiO_2$ with $WS_2$ calcined at 300 ℃ before forming the heterojunction. **(a)** EDX mapping; **(b, c)** TEM images. The calcined $WS_2$ suffered from layer restacking which restricted the contact between $TiO_2$ and $WS_2$. TEM and EDX imaging were acquired by Dr. Zhihang Xu.

In comparison, the same experiment was performed on $WS_2$-$TiO_2$ without calcination of $WS_2$ (**Fig. 3.12**). Comparing the EDX mapping results, the calcined FL-$WS_2$ nanosheets aggregated in a certain area (**Fig. 3.12a**), while uncalcined FL-$WS_2$ nanosheets were well-dispersed on f-$TiO_2$ (**Fig. 3.13a**). Additionally, the calcined FL-$WS_2$ nanosheets clearly suffered from layer restacking as illustrated in **Fig. 3.12b, c**, whereas this effect cannot be seen in uncalcined $WS_2$ (**Fig. 3.13b, c**). The $WS_2$ layer restacking led to poor contact with the

$TiO_2$ support, forming a separated aggregation phase in the TEM images. Therefore, a significant decline in photocatalytic activity was observed, indicating that a different synthesis approach is still required for future studies of the effect of $WS_2$ phase change on catalytic activity.

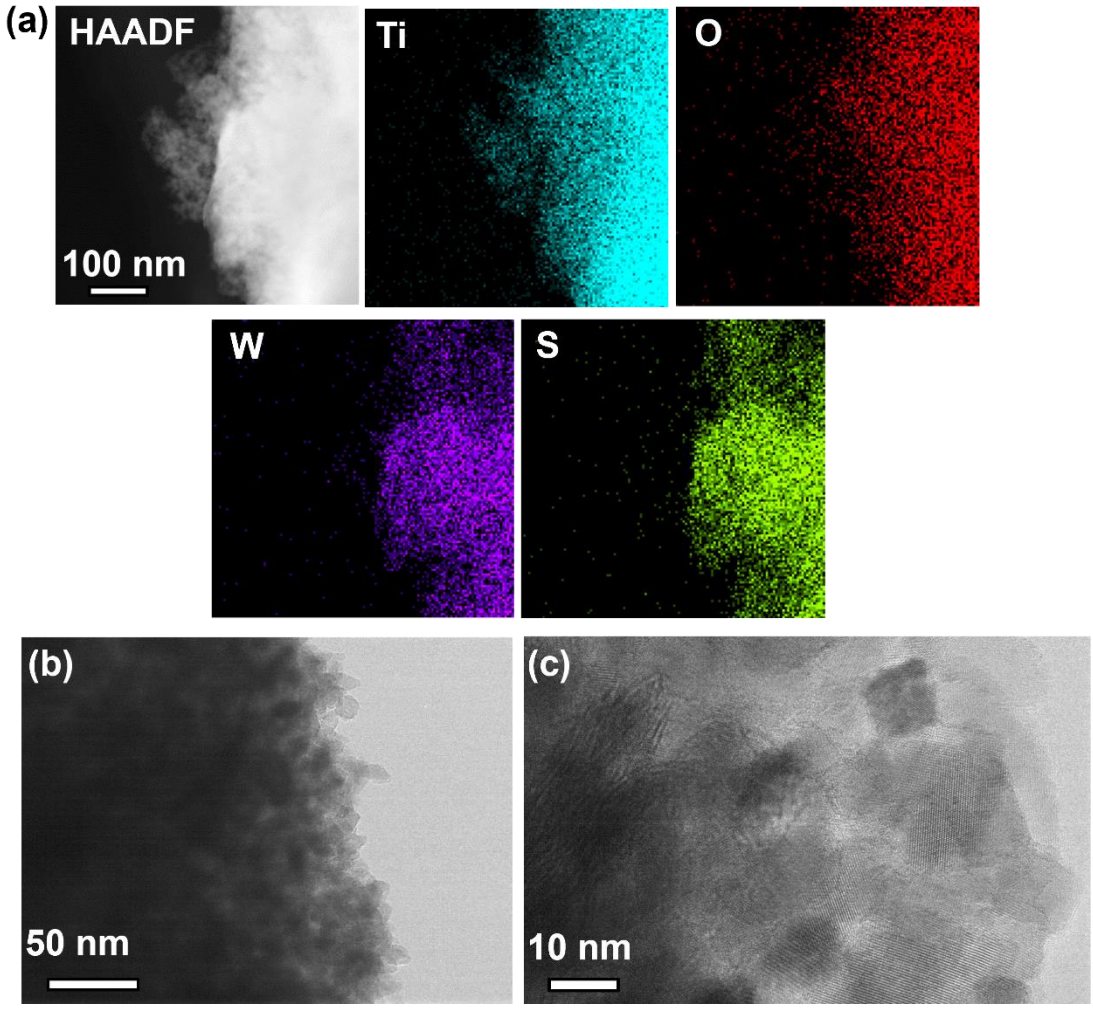



**Figure 3.13** Structural characterisation of $WS_2$-$TiO_2$ without calcination. **(a)** EDX mapping; **(b, c)** TEM images. The $WS_2$ phase is better dispersed on the $TiO_2$ support compared to the calcined $WS_2$ samples. TEM and EDX imaging were acquired by Dr. Zhihang Xu.

### 3.3 Conclusion

In this chapter, the potential use of exfoliated $WS_2$ as the main catalyst and its introduction onto a $TiO_2$ support as a cocatalyst were explored. Ultrathin FL-$WS_2$ nanosheets were

successfully synthesised, as confirmed by XRD, AFM and TEM. Ru-$WS_2$ showed the highest activity compared to other d-block metal-doped FL-$WS_2$. Then the structure of Ru-$WS_2$ was investigated by high resolution TEM, XANES and EXAFS. It was found that, instead of forming exposed Ru sites (single atoms and/or nanoclusters) on the surface, the Ru atoms were inserted into the $WS_2$ layers, facilitating charge transfer in the out-of-plane direction. Following that, thin f-$TiO_2$ was used as a support for fabricating 2D-2D heterojunctions with FL-$WS_2$. The structural characterisation of $WS_2$-$TiO_2$ demonstrated intimate contact between the two materials with a clear interface in the TEM images. This structure benefitted from an internal electric field, as confirmed by XPS, which significantly increased photocatalytic activity. Unfortunately, the contribution from the $WS_2$ phase transformation was unsuccessful due to the significant self-restacking after calcination. For the future work, a different approach should be applied to obtain pure 2H-$WS_2$ with thickness comparable to uncalcined FL-$WS_2$, avoiding the $WS_2$ layer restacking that causes poor contact between the $WS_2$ nanosheets and the $TiO_2$ support.

In the next chapter, the formation of tungsten single atoms and clusters on the $TiO_2$ support, as well as their effects on photocatalytic performance, will be investigated and discussed.

### 3.4 References

1. M. Núñez, J. L. Lansford and D. G. Vlachos, Optimization of the facet structure of transition-metal catalysts applied to the oxygen reduction reaction, *Nat. Chem.*, 2019, **11**, 449-456.
2. C. Tan, X. Cao, X.-J. Wu, Q. He, J. Yang, X. Zhang, J. Chen, W. Zhao, S. Han, G.-H. Nam, M. Sindoro and H. Zhang, Recent Advances in Ultrathin Two-Dimensional Nanomaterials, *Chem. Rev.*, 2017, **117**, 6225-6331.
3. M. Zeng, Y. Xiao, J. Liu, K. Yang and L. Fu, Exploring Two-Dimensional Materials

toward the Next-Generation Circuits: From Monomer Design to Assembly Control, *Chem. Rev.*, 2018, **118**, 6236-6296.

4. X. Duan, C. Wang, A. Pan, R. Yu and X. Duan, Two-dimensional transition metal dichalcogenides as atomically thin semiconductors: opportunities and challenges, *Chem. Soc. Rev.*, 2015, **44**, 8859-8876.
5. H. Li, J. Wu, Z. Yin and H. Zhang, Preparation and Applications of Mechanically Exfoliated Single-Layer and Multilayer $MoS_2$ and $WSe_2$ Nanosheets, *Acc. Chem. Res.*, 2014, **47**, 1067-1075.
6. M. Chhowalla, H. S. Shin, G. Eda, L.-J. Li, K. P. Loh and H. Zhang, The chemistry of two-dimensional layered transition metal dichalcogenide nanosheets, *Nat. Chem.*, 2013, **5**, 263-275.
7. J. Chen, X.-J. Wu, L. Yin, B. Li, X. Hong, Z. Fan, B. Chen, C. Xue and H. Zhang, One-pot Synthesis of CdS Nanocrystals Hybridized with Single-Layer Transition-Metal Dichalcogenide Nanosheets for Efficient Photocatalytic Hydrogen Evolution, *Angew. Chem. Int. Ed.*, 2015, **54**, 1210-1214.
8. M. D. Stoller, S. Park, Y. Zhu, J. An and R. S. Ruoff, Graphene-Based Ultracapacitors, *Nano Lett.*, 2008, **8**, 3498-3502.
9. T. Heine, Transition Metal Chalcogenides: Ultrathin Inorganic Materials with Tunable Electronic Properties, *Acc. Chem. Res.*, 2015, **48**, 65-72.
10. D. Voiry, R. Fullon, J. Yang, C. de Carvalho Castro e Silva, R. Kappera, I. Bozkurt, D. Kaplan, M. J. Lagos, P. E. Batson, G. Gupta, Aditya D. Mohite, L. Dong, D. Er, V. B. Shenoy, T. Asefa and M. Chhowalla, The role of electronic coupling between substrate and 2D $MoS_2$ nanosheets in electrocatalytic production of hydrogen, *Nat. Mater.*, 2016, **15**, 1003-1009.
11. D. Gao, P. Deng, J. Zhang, L. Zhang, X. Wang, H. Yu and J. Yu, Reversing Free-Electron Transfer of $MoS_{2+x}$ Cocatalyst for Optimizing Antibonding-Orbital Occupancy Enables High Photocatalytic H2 Evolution, *Angew. Chem. Int. Ed.*, 2023, **62**, e202304559.
12. Z. Li, X. Meng and Z. Zhang, Recent development on $MoS_2$-based photocatalysis: A

review, *J. Photochem. Photobiol. C Photochem. Rev.*, 2018, **35**, 39-55.

13. J. Li, G. Zhan, Y. Yu and L. Zhang, Superior visible light hydrogen evolution of Janus bilayer junctions via atomic-level charge flow steering, *Nat. Commun.*, 2016, **7**, 11480.
14. Y. Li, S. Wu, J. Zheng, Y.-K. Peng, D. Prabhakaran, R. A. Taylor and S. C. E. Tsang, 2D photocatalysts with tuneable supports for enhanced photocatalytic water splitting, *Mater. Today*, 2020, **41**, 34-43.
15. D. Voiry, H. Yamaguchi, J. Li, R. Silva, D. C. B. Alves, T. Fujita, M. Chen, T. Asefa, V. B. Shenoy, G. Eda and M. Chhowalla, Enhanced catalytic activity in strained chemically exfoliated $WS_2$ nanosheets for hydrogen evolution, *Nat. Mater.*, 2013, **12**, 850-855.
16. H. M. Hill, A. F. Rigosi, K. T. Rim, G. W. Flynn and T. F. Heinz, Band Alignment in $MoS_2/WS_2$ Transition Metal Dichalcogenide Heterostructures Probed by Scanning Tunneling Microscopy and Spectroscopy, *Nano Lett.*, 2016, **16**, 4831-4837.
17. Y. Wu, Z. Liu, Y. Li, J. Chen, X. Zhu and P. Na, Construction of 2D-2D $TiO_2$ nanosheet/layered $WS_2$ heterojunctions with enhanced visible-light-responsive photocatalytic activity, *Chin. J. Catal.*, 2019, **40**, 60-69.
18. E. Rahmanian, C. C. Mayorga-Martinez, R. Malekfar, J. Luxa, Z. Sofer and M. Pumera, 1T-Phase Tungsten Chalcogenides ($WS_2$, $WSe_2$, $WTe_2$) Decorated with TiO2 Nanoplatelets with Enhanced Electron Transfer Activity for Biosensing Applications, *ACS Appl. Nano Mater.*, 2018, **1**, 7006-7015.
19. C. Cong, J. Shang, X. Wu, B. Cao, N. Peimyoo, C. Qiu, L. Sun and T. Yu, Synthesis and Optical Properties of Large-Area Single-Crystalline 2D Semiconductor $WS_2$ Monolayer from Chemical Vapor Deposition, *Adv. Opt. Mater.*, 2014, **2**, 131-136.
20. G. Eda, H. Yamaguchi, D. Voiry, T. Fujita, M. Chen and M. Chhowalla, Photoluminescence from Chemically Exfoliated $MoS_2$, *Nano Lett.*, 2011, **11**, 5111-5116.
21. S. Wang, D. Zhang, B. Li, C. Zhang, Z. Du, H. Yin, X. Bi and S. Yang, Ultrastable In-Plane 1T–2H $MoS_2$ Heterostructures for Enhanced Hydrogen Evolution Reaction, *Adv. Energy Mater.*, 2018, **8**, 1801345.

22. C. Cheng, J. Zhang, R. Zeng, F. Xing and C. Huang, Schottky barrier tuning via surface plasmon and vacancies for enhanced photocatalytic $H_2$ evolution in seawater, *Appl. Catal., B*, 2022, **310**, 121321.

23. H. He, J. Lin, W. Fu, X. Wang, H. Wang, Q. Zeng, Q. Gu, Y. Li, C. Yan, B. K. Tay, C. Xue, X. Hu, S. T. Pantelides, W. Zhou and Z. Liu, $MoS_2/TiO_2$ Edge-On Heterostructure for Efficient Photocatalytic Hydrogen Evolution, *Adv. Energy Mater.*, 2016, **6**, 1600464.

24. L. Liang and V. Meunier, First-principles Raman spectra of $MoS_2$, $WS_2$ and their heterostructures, *Nanoscale*, 2014, **6**, 5394-5401.

25. G. Zhang, S. Huang, X. Li, D. Chen, N. Li, Q. Xu, H. Li and J. Lu, Internal electric field engineering of bifunctional 2D/2D heterojunction photocatalyst for cooperative $H_2$ production and alcohol conversion, *Appl. Catal., B*, 2023, **331**, 122725.

26. D. M. Sim, H. J. Han, S. Yim, M.-J. Choi, J. Jeon and Y. S. Jung, Long-Term Stable 2H-$MoS_2$ Dispersion: Critical Role of Solvent for Simultaneous Phase Restoration and Surface Functionalization of Liquid-Exfoliated $MoS_2$, *ACS Omega*, 2017, **2**, 4678-4687.

# Chapter 4 $WS_2$ to W Single-Atom Transformation on $TiO_2$

## 4.1 Introduction

As discussed in Chapter 3, ultrathin TMDs have been widely investigated for various advantages compared to their bulk counterparts and promising results have been established regarding their application in various research fields, especially in photocatalysis and electrocatalysis.[1] However, it has been found that after exfoliating TMDs into few layers or monolayers by chemical or mechanical methods, the oxidation of ultrathin TMDs becomes more thermodynamically favourable, even under ambient conditions.[2] One reason is that exfoliated TMDs possess an increased number of surface defect sites, which provide additional oxidation sites when exposed to air.[3] Oxidation typically leads to severe deactivation in catalysis, which makes exfoliated TMDs difficult to use in industrial-scale production and applications. Although previous theoretical studies have shown that if a defect-free basal plane can be achieved after exfoliation, ultrathin TMDs can be chemically inert with a high kinetic barrier to oxidation. However, it remains practically challenging to completely avoid the creation of defects during the synthesis process.[4] Consequently, it is still essential to explore other possible solutions for the future application of ultrathin TMDs in catalysis.

To thoroughly investigate the mechanism, the oxidation of TMDs under harsh conditions, such as UV irradiation and high temperature, has been studied previously.[5, 6] These conditions normally lead to the formation of metal oxides ($MoO_3$ and $WO_3$), beginning from the surface region, which destroys the original lattice structure of TMDs. Based on these studies under severe conditions, it was generally believed that TMDs could be relatively stable in ambient

environments, similar to graphene. However, Gao *et al.* demonstrated that when synthesising TMD nanosheets using chemical vapor deposition, oxidation could occur even under ambient exposure, as revealed by electron microscopy.[7] Additionally, they found that moisture in the air could act as an 'ageing catalyst', which significantly accelerated the oxidation process of TMD nanosheets. Following this work, more studies on the oxidation mechanism were conducted by Peto *et al.*, who suggested that under ambient conditions, oxidation began with surface substitution of sulphur atoms by oxygen from the air owing to the higher bond strength of M-O compared to M-S bonds.[8] By employing scanning tunnelling microscopy (STM), oxygen substitution sites at the atomic scale on the $MoS_2$ nanosheet were observed across the basal plane over time, forming a 2D solid-solution-type $MoS_{2-x}O_x$ structure. Further research into the complete decomposition of $MoS_2$ under humid conditions was conducted by Wang *et al.*, who found that $MoS_2$ nanosheets degraded into soluble $MoO_4^{2-}$ and $SO_4^{2-}$ within days in air-saturated water.[9] Moreover, Kotsakidis *et al.* successfully showed that, in addition to air and water molecules, oxidation could also be induced and accelerated by light.[10] It was suggested that even under typical laboratory lighting conditions, the oxidation process initiated at the edge of ultrathin $WS_2$ nanosheet. In contrast, oxidised regions were barely observed in $WS_2$ samples kept in dark conditions.

These studies have successfully identified and summarised the key factors initiating the oxidation process of TMDs, including but not limited to humidity, illumination, and elevated temperature. Such conditions are easily encountered in most of the heterogeneous catalyst synthesis processes and testing environments, which can significantly restrict the potential applications and industrialisation of ultrathin TMDs in heterogeneous catalysis.[11]

Unfortunately, although progress has been made in improving catalytic reactivity and fabricating novel catalytic structures, the ageing issues under these conditions have not been fully addressed or analysed in previous studies. For instance, Li *et al.* used chemically exfoliated $MoS_2$ as a cocatalyst and assembled the $MoS_2$ monolayer with other 2D materials in aqueous solution at 80 ℃ to obtain a Janus bilayer-junction photocatalyst for hydrogen evolution.[12] The structure of the bilayer-junction photocatalyst was evaluated based on the distribution of Mo atoms, while the sulphur atoms that suffered from oxygen substitution were not considered. Furthermore, during photocatalytic testing, the light source inherently provides illumination and increases the temperature of the reaction system, with water molecules also present in water splitting and $CO_2$ reduction reactions.[13, 14] For instance, it was illustrated by Zhou *et al.* that an reaction temperature of 70 ℃ for photocatalytic water splitting could be achieved simply by utilising the infrared portion of the solar spectrum, combined with a heat-insulating layer.[15, 16] Such conditions provide an ideal oxidation environment for TMD nanosheets. Although this process has effectively minimised the presence of air, oxidation of TMDs may still occur with even trace amounts of oxidants, as the key factors for oxidation are present.[17]

Based on studies of the oxidation mechanism, TMDs should be prone to be oxidised during the synthesis and catalytic processes, forming metal oxides ($MoO_3$/$WO_3$) or soluble metal species ($MoO_4^{2-}$/ $WO_4^{2-}$) along with the production of acidic molecules (*e.g.* $H_2SO_4$, $SO_2$), depending on the experimental conditions, reducing their utility and potentially causing environmental pollution. Since the effects of TMD oxidation on the local structure of composite heterogeneous catalysts have not been thoroughly investigated in many catalysis

studies, some interpretations of catalytic testing results may be inaccurate and misleading.

To address the structural changes in TMDs during heterojunction fabrication and their corresponding effects on catalysis, the study following Chapter 3 reveals the structural transformation of FL-$WS_2$ supported by anatase f-$TiO_2$ during the synthetic process, using electron microscopy combined with spectroscopy techniques. As the 2D-2D heterojunction structure can maximise contact between the two materials, the stable heterojunction allows clear observation of the structural changes in FL-$WS_2$ on the $TiO_2$ support, while also increasing the possibility of "capturing" potentially oxidised metal species (generated from FL-$WS_2$ dissociation) at the undercoordinated surface sites of the $TiO_2$ support.

In this study, it was found that FL-$WS_2$ nanosheets underwent complete dissociation when the heterojunction fabrication process was extended to 24 hours with f-$TiO_2$ in DI water at 80 °C. The tungsten atoms from FL-$WS_2$ were oxidised and incorporated as dopants on the f-$TiO_2$ surface (W-$TiO_2$). In contrast, the sulphur content was gradually depleted over time and completely lost after the 24-hour extended synthesis. Moreover, abundant $O_v$ sites on f-$TiO_2$ support were generated during this process, which might be caused by the strong interactions between the two materials. Catalysis studies showed that oxidation of $WS_2$ did not lead to deactivation in the hydrogen evolution reaction; instead, W-$TiO_2$ exhibited even higher catalytic performance than $WS_2$-$TiO_2$. This result might be attributed to the increased number of exposed tungsten atoms on the f-$TiO_2$ surface, providing additional reactive sites for photocatalytic reactions.

## 4.2 Results and Discussion

### 4.2.1 Transformation from $WS_2$ to W Single Atoms on $TiO_2$ Support

In Chapter 3, it was shown that the $WS_2$-$TiO_2$ catalyst exhibited a 2D-2D heterojunction structure, in which FL-$WS_2$ was surrounded by isolated W single atoms and clusters attached on the $TiO_2$ support. To confirm the chemical composition of the observed $WS_2$ nanosheets and W fragments, EELS (**Fig. 4.1b**) and EDX (**Fig. 4.2b**) mapping were applied for elemental analysis. As shown in **Fig. 4.1a**, the co-existence of the $WS_2$ nanosheet region and the W atom region on the $TiO_2$ support can be observed, which is consistent with the TEM results in Chapter 3. Notably, the EELS mapping results in **Fig. 4.1b** reveal that no sulphur atoms region can be detected in the W fragments region, whereas the $WS_2$ sheets region contains both tungsten and sulphur. This excludes the possibility that the isolated tungsten atoms exist in the form of $WS_{2-x}O_x$. Subsequently, EDX measurements further confirm that the W atoms are well dispersed on f-$TiO_2$ with a molar fraction of 0.6 ± 0.07% and no sulphur is detected in the region of the isolated W atoms (**Fig. 4.2**). Moreover, the ratio between titanium and oxygen is not consistent with the theoretical ratio of 1 : 2 but close to 1 : 1.45. This suggests that the oxidation of $WS_2$ attached to the f-$TiO_2$ support may be accompanied by the creation of $O_v$ on the surface of $TiO_2$ support. In addition, at this stage, the chemical state of the W fragments and the form of the lost sulphur atoms remain unclear and require further experimental evidence.

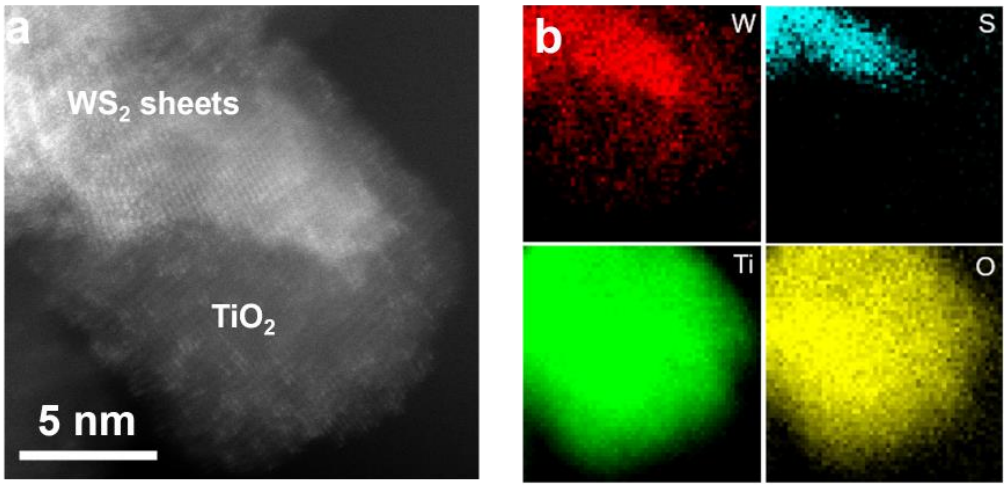



**Figure 4.1 (a)** High resolution TEM image showing both $WS_2$ nanosheets and W single atoms on f-$TiO_2$; **(b)** EELS mapping of the selected area. The TEM and EELS measurements in this figure were conducted by Dr. Zhihang Xu (PolyU).

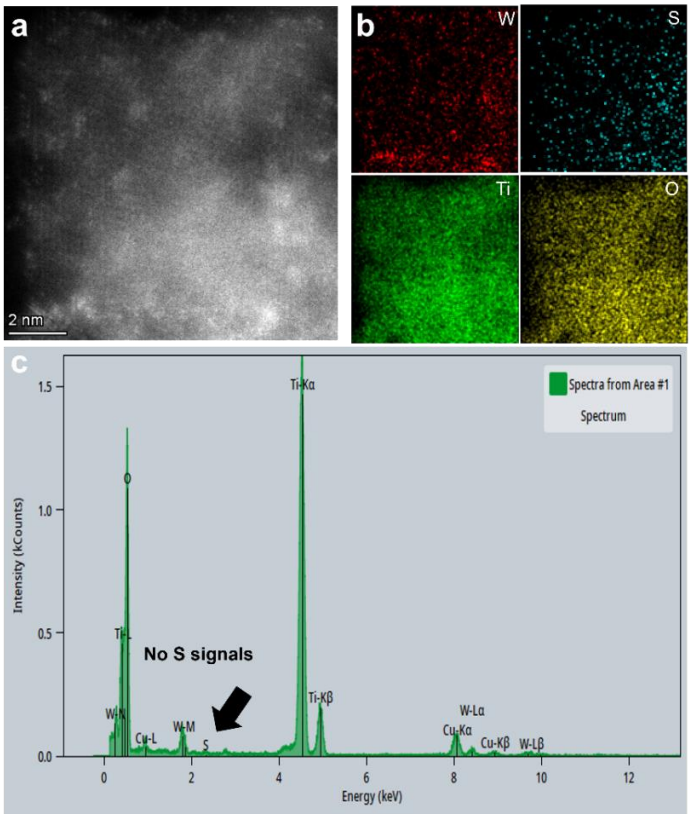



**Figure 4.2 (a)** TEM image showing W single atoms on the $TiO_2$ support; **(b)** EDX elemental mapping of the selected area; **(c)** Elemental analysis from EDX results showing atomic fractions of 40.65 ± 4.08% Ti, 58.74 ± 4.04% O and 0.6 ± 0.07% W. The EDX measurements in this figure were conducted by Dr. Zhihang Xu.

To further demonstrate the overall change in the sample' s chemical composition during the heterojunction fabrication process, XPS measurements were performed on $WS_2$-$TiO_2$ samples (*ca.* 12wt% of $WS_2$) with fabrication durations of 0 h, 2 h and 24 h. XPS high resolution scans of Ti 3p and W 4f are illustrated in **Fig. 4.3a**. The doublet peaks at 31.37 eV (W $4f_{7/2}$) and 33.51 eV (W $4f_{5/2}$) can be attributed to $W^{4+}$ and the molar percentage of W is calculated to be 3.81%, which is comparable with the theoretical value of 3.87% (for 12wt% $WS_2$). However, the tungsten content revealed by EDX is significantly lower than that obtained by XPS. This discrepancy might be caused by the low penetration depth of the soft X-ray beam applied in XPS, making the XPS signal more surface sensitive, where tungsten is more concentrated in the top layers compared with the bulk.

After 2 hours of fabrication, the intensity of the $W^{4+}$ peaks slightly decreased, indicating that the $W^{4+}$ species were partially oxidised due to the decomposition of $WS_2$. Meanwhile, the appearance of a shoulder peak at 35.74 eV can be assigned to $W^{6+}$ $4f_{7/2}$, further suggesting the oxidation of $WS_2$ during the heterojunction fabrication process. After 24 hours, the $W^{4+}$ species were fully oxidised with $W^{6+}$ (2.03%, 35.7 eV for W $4f_{7/2}$) and $W^{5+}$ (1.23%, 33.7 eV for W $4f_{7/2}$) remaining in the sample. Furthermore, XPS high resolution scans of S 2p (**Fig. 4.3b**) reveal a decreasing sulphur concentration with increasing fabrication time. Sulphur was completely depleted at the same time the $W^{4+}$ species were fully oxidised. This loss of sulphur content in XPS is consistent with previous EDX and EELS results, confirming that the oxidation of tungsten was accompanied by sulphur depletion, indicating full decomposition of $WS_2$ into tungsten in higher oxidation states. Based on the previous studies on $WS_2$ oxidation, it is generally believed that oxidation of isolated $WS_2$ results in the

formation of bulk $WO_3$, starting at the sheet edges accompanied by structural destruction.[6] However, when forming the heterojunction with f-$TiO_2$, from the TEM images, it can be seen that the oxidised tungsten species exist as single atoms and clusters attached to the $TiO_2$ surface, with no $WO_3$ phase observed in the high resolution TEM images (**Fig. 4.4**). Consequently, the formation of tungsten single-atom fragments may be more similar to the metal complex ions formed after total dissociation of TMDs as revealed in previous studies, and herein the sample after total $WS_2$ oxidation is referred to as W-$TiO_2$.[9]

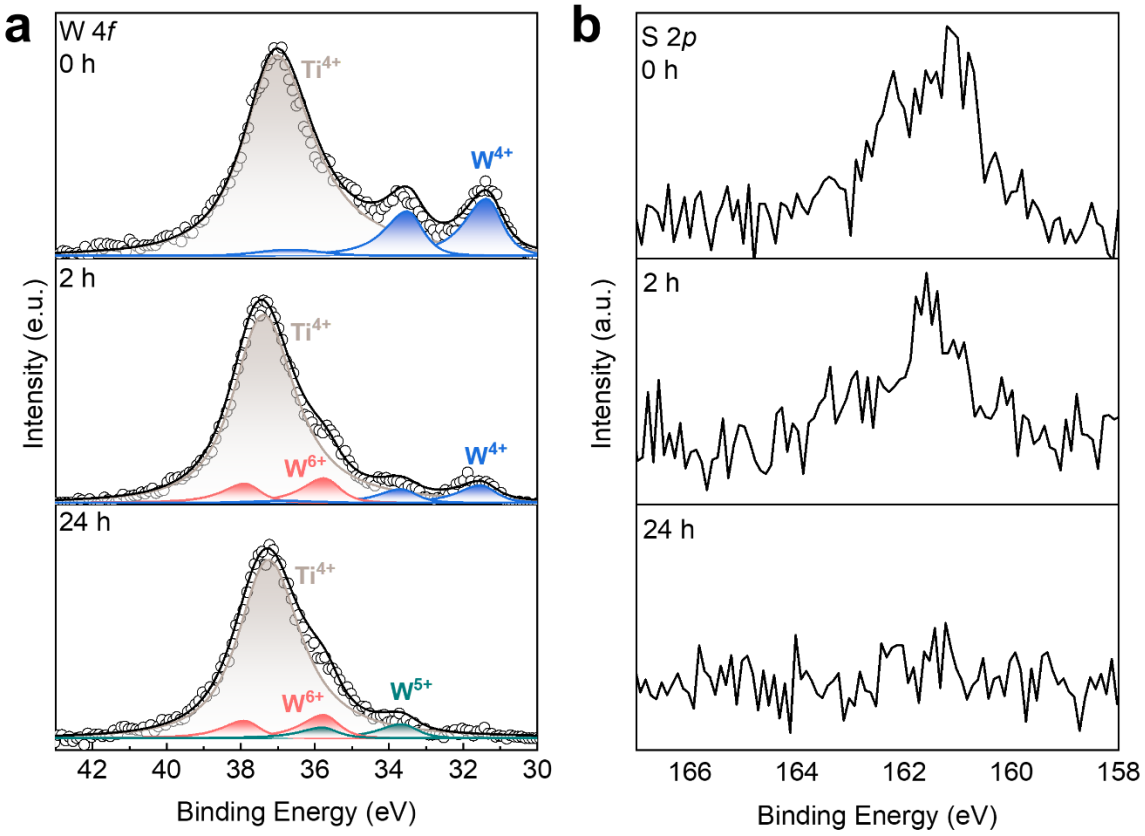



**Figure 4.3** XPS high resolution spectra of **(a)** W 4f and Ti 3p showing that $W^{4+}$ species were being oxidised overtime and **(b)** S 2p with gradually increased fabrication time where the sulphur content was decreasing overtime and was fully depleted after 24 hours. XPS measurements were conducted by Dr. Shaoliang Guan (HarwellXPS).

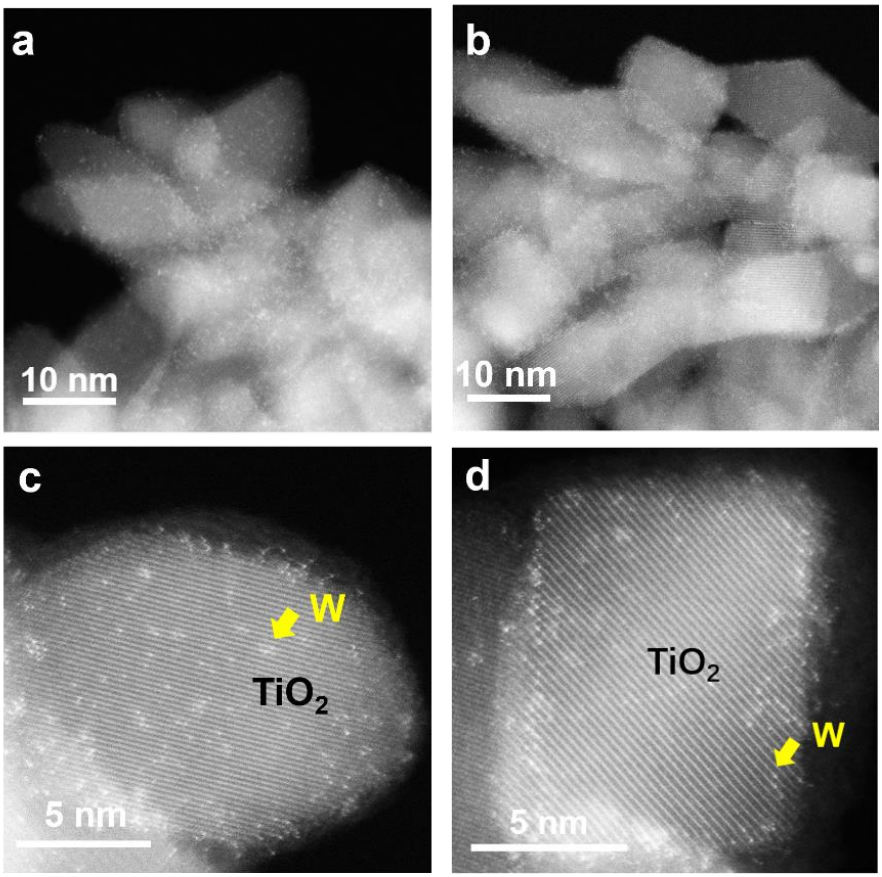



**Figure 4.4** High resolution TEM images of W-$TiO_2$ after complete dissociation of $WS_2$ nanosheets. No $WO_3$ phase can be observed on f-$TiO_2$ but W atoms. TEM images in this figure were acquired by Dr. Zhihang Xu.

### 4.2.2 Structural Characterisations and Analysis of $WS_2$ Decomposition

The positions of W single atoms at atomic resolution are revealed by TEM images taken from the [001] axis, as illustrated in **Fig. 4.5a, b**. The atoms appearing brighter than the surrounding ones represent W single-atom sites attached to the $TiO_2$ surface, which are mostly located directly above the lattice titanium atoms, as suggested by the TEM images. The two-line profiles of contrast shown in **Fig. 4.5c**, originating from the selected areas in **Fig. 4.5b** further confirm that the W atoms are situated directly above Ti atoms, instead of occupying interstitial sites. This implies that the adsorbed W atoms may have undergone a similar adsorption mechanism after complete dissociation of FL-$WS_2$, although it is still

unclear if the tungsten atoms have replaced the exposed Ti atoms on the f-$TiO_2$ (001) facet.

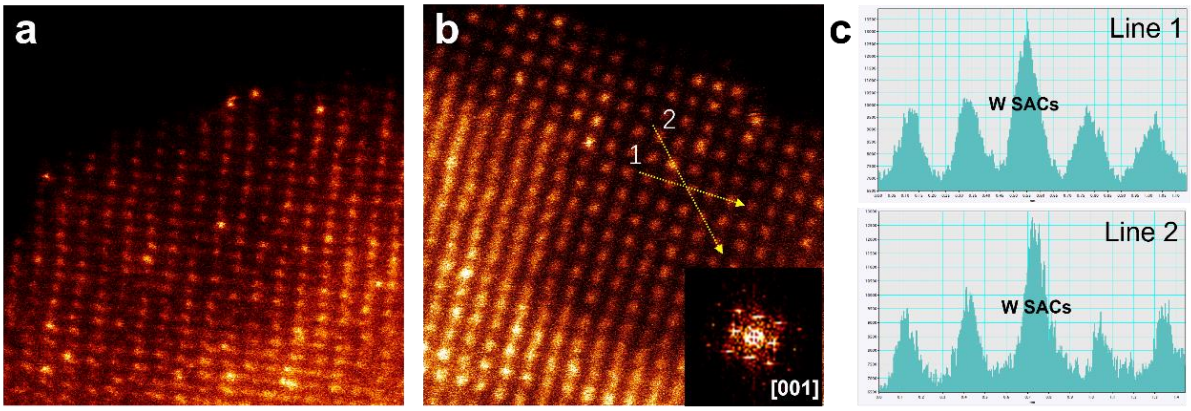



**Figure 4.5 (a, b)** TEM images with atomic resolution of W-$TiO_2$; **(c)** Intensity line profiles of selected area from the TEM image. The TEM results suggest that the tungsten atoms are predominantly located above the titanium atoms on the (001) facet of $TiO_2$. TEM images in this figure were acquired by Dr. Zhihang Xu.

To further investigate the adsorption sites of tungsten on the $TiO_2$ surface, additional TEM experiments were conducted to determine whether tungsten adsorption on the (001) facet could occur on other exposed facets of $TiO_2$. Notably, tungsten single atoms can scarcely be observed in TEM images taken along the [111] axis, as illustrated in **Fig 4.6a**. Similar results can be observed along the [010] axis, where tungsten atoms can be seen on the (001) facet, whilst no tungsten atoms can be seen on the adjacent (010) facet as shown in **Fig. 4.6b**. Theoretically, compared to the (001) facets, the exposed (010) facet is more stable and possesses fewer under-coordinated sites for tungsten adsorption. As for the (111) facet, while it contains more under-coordinated sites, it also has higher surface energy, which may lead to a less stable structure for tungsten adsorption relative to the (001) facets.[18] Consequently, the (001) facet may exhibit a stronger affinity for stabilising tungsten atoms than other facets, causing preferential adsorption on the (001) facet. The subsequent strain analysis (**Fig. 4.6d**)

shows that introducing W atoms induces significant lattice strain on the (001) facet, whereas such strain is absent on the (010) facet without W decoration. A comparison of experimental and simulated TEM results indicates that the introduced tungsten atoms cause a notable change of 12.2% in the d-spacing of (020) facet (**Fig. 4.7**). The strain analysis further corroborates the preferred adsorption of tungsten atoms on the exposed (001) facet, resulting in significant lattice strain to accommodate the structural change on the $TiO_2$ surface.

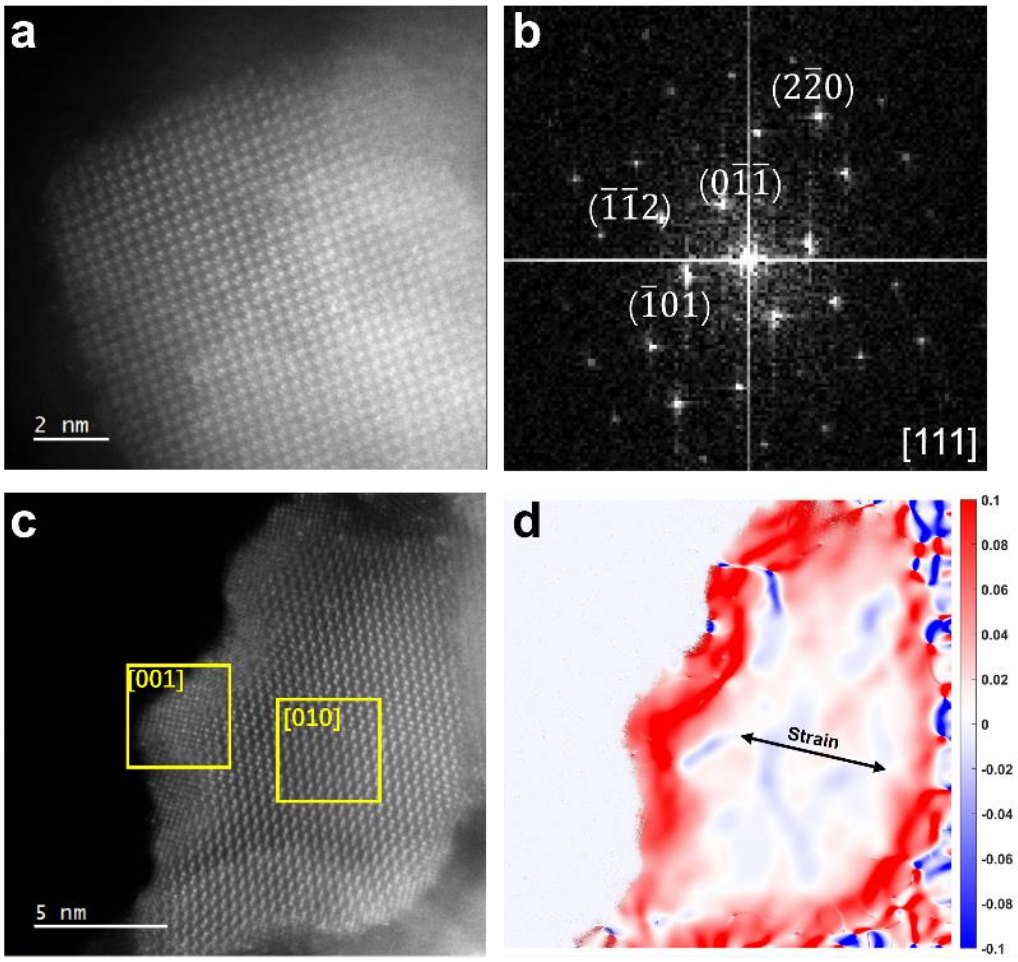



**Figure 4.6 (a)** TEM images W-$TiO_2$ from the [111] axis with no tungsten atoms observed and **(b)** corresponding electron diffraction from [111]; **(c)** TEM images from the [001] and [010] axis and **(d)** corresponding strain analysis showing increased strain on the (001) facet with tungsten decoration compared to the (010) facet without tungsten decoration. TEM images in this figure were acquired by Dr. Zhihang Xu.

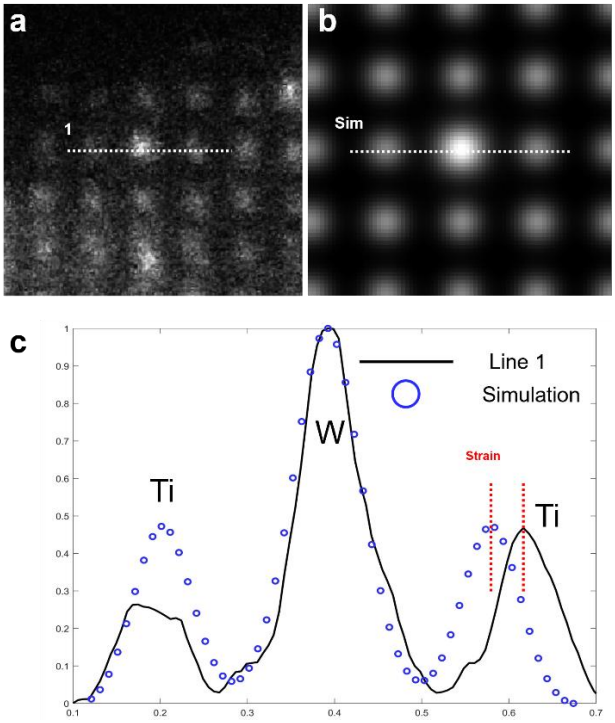



**Figure 4.7 (a)** Experimental and **(b)** simulated TEM images of W-$TiO_2$ from the [001] axis; **(c)** Line profile comparison of selected areas showing lattice strain (intensity on the y-axis and distance in nm on the x-axis). TEM simulations were conducted by Dr. Zhihang Xu using CrystalMaker and SingleCrystal software according to the atomic structures of anatase $TiO_2$.

To study the coordination environment of W atoms, XAS measurements were performed. XANES and Fourier transform extended X-ray absorption fine structure (FT-EXAFS) data at the W-$L_3$ edge are shown in **Fig. 4.8**. Due to the oxidation of $WS_2$, the W absorption edge in the XANES spectra shows a slight positive shift over fabrication time (**Fig. 4.8a**). At t = 0 h, the FT-EXAFS results show a main W-S peak at 2.40 Å with a coordination number of 5.17 ± 0.40, as listed in **Table 4.1**. This number is significantly lower than the theoretical value of 6.00, indicating a typical structure for chemically exfoliated $WS_2$ with abundant sulphur vacancies. Interestingly, with $WS_2$ being oxidised, the bond length gradually increases over time (**Fig. 4.8b**). A W-O bond at 2.41 Å with a coordination number of 4.32 ± 0.33 is observed when $WS_2$ is completely oxidised after 24-hour fabrication time. This provides

further evidence that $WO_3$ did not form during the heterojunction fabrication process, as the characteristic W-O bonding of $WO_3$ at approximately 1.9 Å is absent.[19] Additionally, the 2.41 Å bond length is significantly longer than the typical W-O bond lengths. As previously discussed, W atoms are located above lattice Ti atoms on the anatase (001) facet from the TEM images, and extra lattice strain is observed in this region. The elongated W-O bond may originate from high strain on the (001) facets, where the d-spacing of (020) has increased, thereby increasing the distance between the surface oxygen atoms and the adsorbed tungsten atoms accordingly. Furthermore, the long bond length also indicates that the tungsten atoms are loosely adsorbed onto the surface oxygens of $TiO_2$, instead of substituting lattice titanium atoms, as the Ti-O bond length in the $TiO_2$ lattice is significantly shorter than the measured W-O bond length.

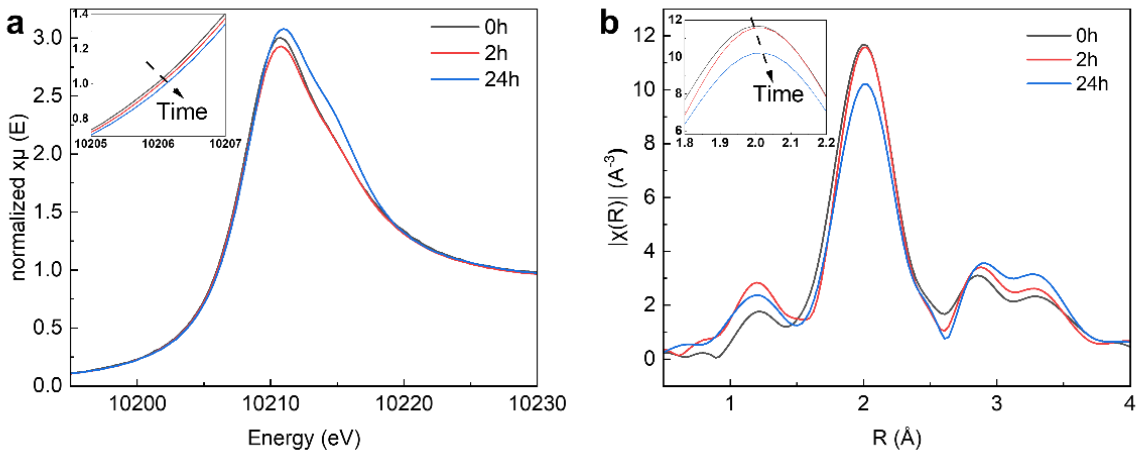



**Figure 4.8 (a)** XANES and **(b)** FT-EXAFS change at the W $L_3$ edge of $WS_2$-$TiO_2$ over fabrication time. The tungsten atoms are oxidised during the fabrication process. Additionally, the W-O bond length from tungsten single atoms is similar to the original bond length of W-S (2.40 Å), rather than decreasing to *ca.* 1.90 Å, which is the W-O bond length in $WO_3$. XAS measurements were performed and analysed by Dr. Xuelei Pan.

**Table 4.1** EXAFS fitting parameters at the W-$L_3$ edge of samples.

| Fabrication Time | Composition | Shell | Coordination Number | R (Å) | $\sigma^2$ | R factor |
|---|---|---|---|---|---|---|
| 0 h | $WS_2$-$TiO_2$ | W-S | 5.17 ± 0.40 | 2.402 ± 0.006 | 0.002 | 2.3% |
| 24 h | W-$TiO_2$ | W-O | 4.32 ± 0.33 | 2.411 ± 0.006 | 0.002 | 2.0% |

The effect on the $TiO_2$ support during the transformation of $WS_2$ into W single atoms was further investigated. From the XRD patterns (**Fig. 4.9**), f-$TiO_2$ retains its anatase crystal structure after forming $WS_2$-$TiO_2$ and W-$TiO_2$, with no additional $WS_2$, $WO_2$, or $WO_3$ crystalline phases observed. It further suggests that the FL-$WS_2$ sample was well-dispersed on the $TiO_2$ surface, without significant layer restacking and the oxidised $WS_2$ did not transform into crystalline metal oxide particles. Although it is still possible that the low $WS_2$ content may result in very weak $WS_2$ peaks under the current resolution of the XRD instrument, neither $WS_2$ phases nor bulk $WO_3$ phases are observed from TEM results for W-$TiO_2$, indicating complete transformation of $WS_2$ into W single atoms or clusters.

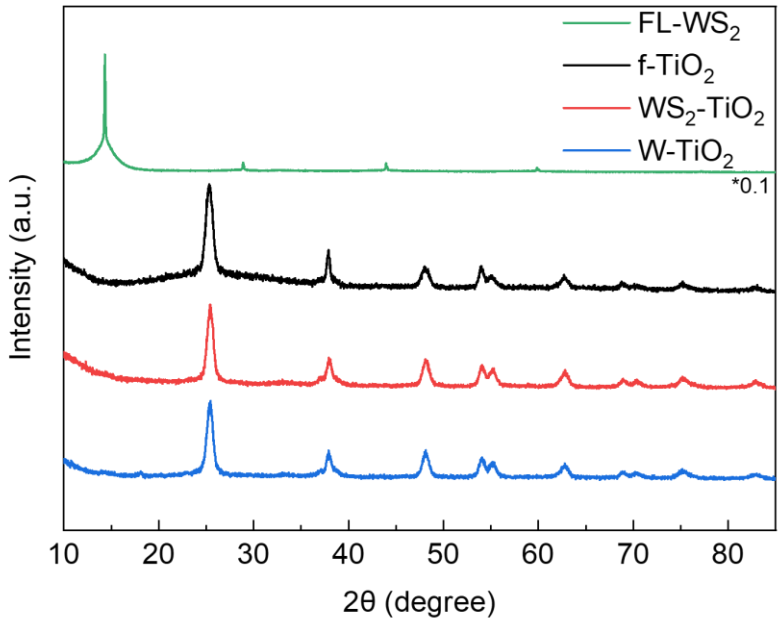



**Figure 4.9** XRD patterns of $WS_2$ and $TiO_2$ samples. After complete $WS_2$ oxidation, no additional $WO_3$ phase can be observed in the W-$TiO_2$ sample.

From the previous EDX results, the ratio of titanium and oxygen was close to 1 : 1.45, indicating the creation of surface $O_v$. Electron paramagnetic resonance (EPR) was applied for samples with different amounts of $WS_2$ added during the synthetic process for the quantification of $O_v$ to confirm if $O_v$ creation correlated with $WS_2$ oxidation. As illustrated in **Fig. 4.10a**, the EPR signal at g = 2.004, corresponding to $O_v$ shows a positive correlation with increasing $WS_2$ content (0wt% to 12wt%) after fabrication time of 24 hours, suggesting that the formation of $O_v$ on the $TiO_2$ support is linked to the oxidation process of $WS_2$. However, further increases in the amount of $WS_2$ did not result in more $O_v$ and sulphur signals in those samples were detected in these samples via the XPS (**Fig. 4.10b**). Presumably, the reactive sites of $TiO_2$ for $WS_2$ dissociation were blocked when excessive $WS_2$ nanosheets were added, resulting in incomplete oxidation.

Notably, the pH values of the suspension from the heterojunction fabrication system follow the same trend as the $O_v$ concentration, reaching a minimum pH value of 4.7 when 12wt% of $WS_2$ was added for the heterojunction fabrication (**Fig. 4.10c**). From previous studies, $SO_2$ and $H_2SO_4$ were the primary products of $WS_2$ oxidation, which could result in acidic environment in the system.[8, 9] Still, other possible sulphur containing products should also be considered. Elemental sulphur is insoluble in water and no sulphur could be detected in W-$TiO_2$, thus can be excluded. Moreover, lead acetate test paper did not detect any $S^{2-}$ species in the suspension, excluding the possibility of $H_2S$ as a product. Additionally, only around $1.34 \times 10^{-6}$ mol of sulfuric acid is required to reach pH=4.7 while 12wt% $WS_2$ contains at least $6.4 \times 10^{-5}$ mol of sulphur, indicating that the $H_2SO_4$ is not the main product of $WS_2$ oxidation, as $SO_3$ is susceptible to hydration and the pH value would have been much lower than 4.7 if

$H_2SO_4$ was the main product during the $WS_2$ oxidation process. Consequently, it is rational to conclude that the primary product left in the water suspension is $HSO_3^-$, which may escape from the synthetic system as $SO_2$, thereby reducing the acidity. Overall, experimental evidence has shown that the $WS_2$ decomposition process on the $TiO_2$ surface involves oxidation of both tungsten ($W^{4+}$ to $W^{5+}$ and $W^{6+}$) and sulphur ($S^{2-}$ to $SO_2$), where abundant surface oxygen from the $TiO_2$ support was depleted alongside sulphur, resulting in adsorbed W single atoms and abundant $O_v$ formation.

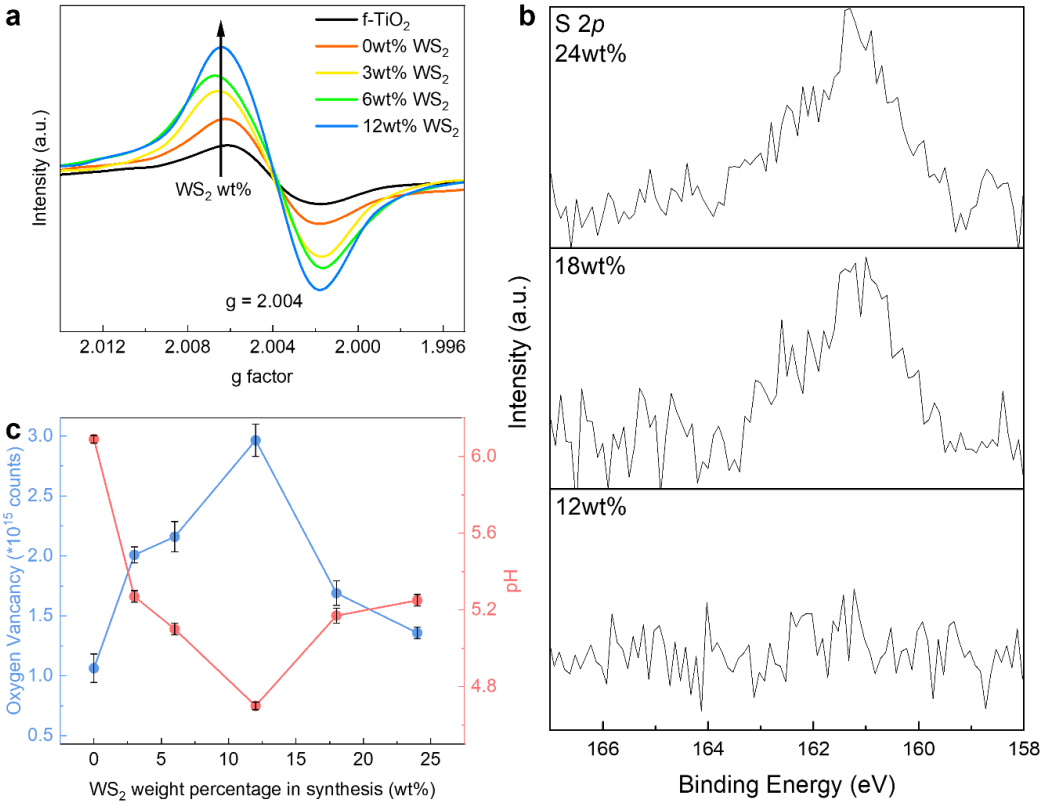



**Figure 4.10 (a)** EPR results at g = 2.004 showing $O_v$ change with different amounts of $WS_2$ introduced on $TiO_2$; **(b)** High resolution S 2p XPS spectra (24 hours fabrication time), showing sulphur presence at increasing $WS_2$ weight percentages; **(c)** Trends of $O_v$ and pH in the fabrication suspension with increasing $WS_2$ proportions. XPS was measured by Dr. Shaoliang Guan.

### 4.2.3 Electronic Properties and Photocatalytic Performance

The influence of $WS_2$ structural transformation into W fragments on the electronic properties and photocatalytic performance of the $TiO_2$-based materials was then investigated. To eliminate the influence from W fragments, herein, $WS_2$-$TiO_2$ refers to the samples being fabricated under room temperature which can be treated as physical mixtures between f-$TiO_2$ and FL-$WS_2$. From the Tauc plot (**Fig. 4.11b**), generated from UV-Vis DRS spectroscopy (**Fig. 4.11a**), the introduction of $WS_2$ into $TiO_2$ enhances visible light absorption, reducing the band gap from 3.20 eV to 2.90 eV. The reduced band gap can be commonly observed following the formation of heterojunctions, which results from band realignment when two materials with different band structures come into contact, leading to a new effective band gap.

Following the complete oxidation of $WS_2$, the band gap of W-$TiO_2$ increases slightly to 2.95 eV but is still significantly lower than that of pristine f-$TiO_2$. Different from the effect of the heterojunction formation in $WS_2$-$TiO_2$, the origin of the decrease in the W-$TiO_2$ band gap can be explained based on the electronic structure change caused by single-atom doping. As discussed previously in Chapter 1, the introduction of single-atom dopant may be attributed to the increase in the density of states in the mid-band region of f-$TiO_2$, providing additional energy levels for photon absorption and charge separation.[20] Additionally, as abundant $O_v$ sites were formed during the heterojunction fabrication process, the defect states might be introduced within the band gap, reducing the effective energy gap between the VB and CB. Typically, a decrease in band gap can facilitate the utilisation of solar energy and promote the rate of photocatalytic reactions.

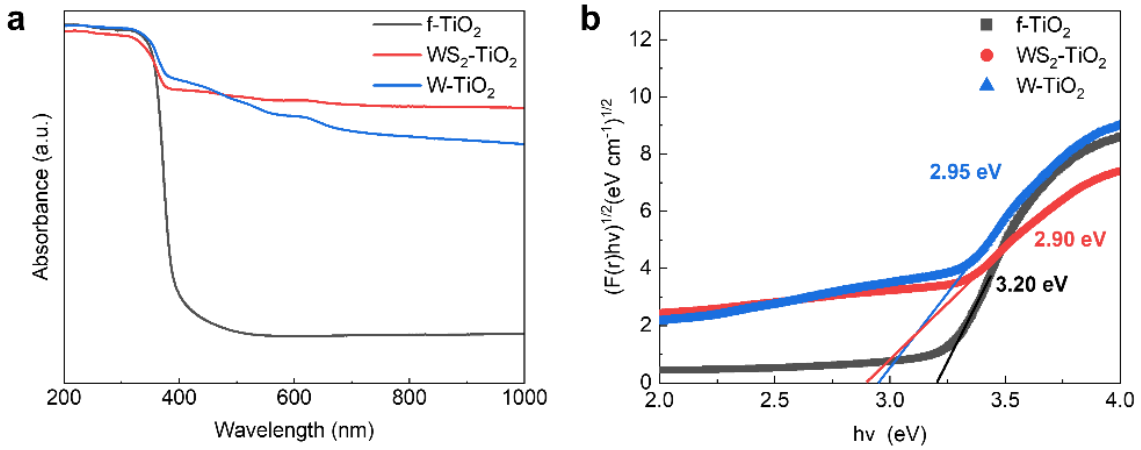



**Figure 4.11 (a)** UV-Vis DRS spectra and **(b)** corresponding Tauc plot. The reduced band gaps of $WS_2$-$TiO_2$ and W-$TiO_2$ compared with pristine f-$TiO_2$ are attributed to the formation of heterojunctions and tungsten atom doping, respectively.

EIS measurements were subsequently conducted on the $TiO_2$-based samples to study charge transfer resistance. The Nyquist plots indicate that W-$TiO_2$ exhibits the smallest impedance radius compared with pristine f-$TiO_2$ and $WS_2$-$TiO_2$, suggesting reduced charge transfer resistance following the introduction of tungsten single atoms onto the $TiO_2$ surface (**Fig 4.12**). The reduced charge transfer resistance after introducing $WS_2$ into $TiO_2$ may be attributed to the intrinsically high conductivity of metallic $WS_2$ and the internal electric field formed at $WS_2$/$TiO_2$ interface, facilitating the charge transfer process as discussed in Chapter 3.[21] However, due to the poor conductivity and low catalytic reactivity along the out-of-plane direction of $WS_2$, charge transfer in this direction may still be restricted. In contrast, this barrier is alleviated in W-$TiO_2$, where W atoms are exposed on the surface instead of S atoms. The introduced tungsten atoms can potentially act as catalytically reactive sites and modify the electronic structure of $TiO_2$ to facilitate more effective charge transfer, thereby lowering charge transfer resistance.

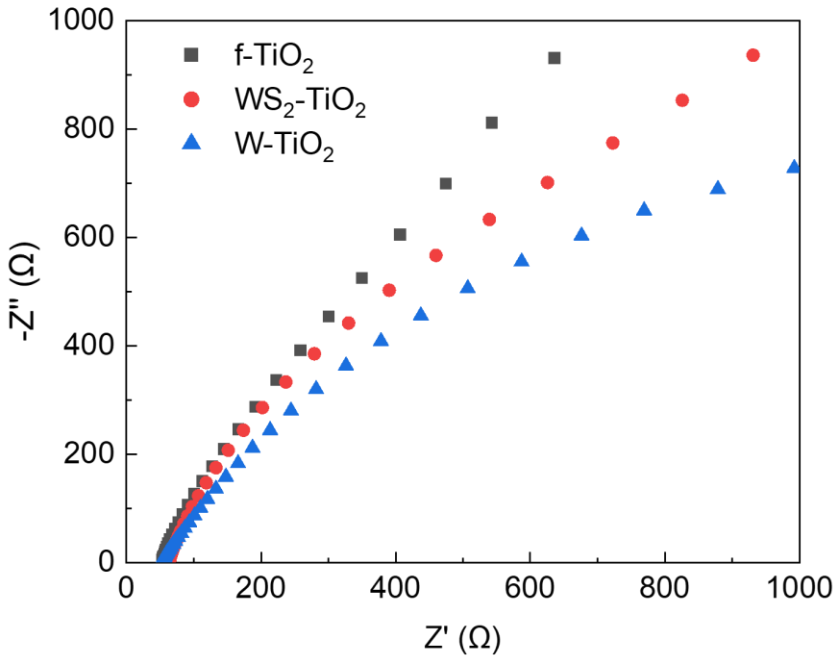



**Figure 4.12** Nyquist plots from EIS tests of $TiO_2$-based samples. W-$TiO_2$ displays the smallest impedance radius, implying the lowest charge transfer resistance among all samples. EIS testing was conducted with the assistance of Dr. Yifei Wang.

TRPL measurements were performed to investigate the lifetime of photo-generated charge carriers. As shown in **Fig. 4.13a**, W-$TiO_2$ exhibits the longest lifetime (2.92 ± 0.031 ns), followed by $WS_2$-$TiO_2$ (2.11 ± 0.023 ns), pristine f-$TiO_2$ (1.36 ± 0.012 ns), and FL-$WS_2$ (1.05 ± 0.011 ns). The prolonged lifetime observed in $WS_2$-$TiO_2$ compared to pristine f-$TiO_2$ may be attributed to the built-in electric field formed upon the heterojunction fabrication, as discussed in Chapter 3, which provides additional driving forces to separate the photo-generated electrons and holes, thus suppressing charge recombination. With the oxidation of $WS_2$, the heterojunction-induced built-in electric field might diminish; however, the tungsten single atoms could still introduce extra energy levels in the mid-gap region that act as trapping centres for photo-generated electrons to achieve the electron-hole separation.

Consequently, it is still possible for W-$TiO_2$ showing the longest lifetime of the photo-generated charge carriers among all the samples. With enhanced light absorption, reduced charge transfer resistance, and extended lifetimes of charge carriers, the photocatalytic $H_2$ evolution rate of W-$TiO_2$ achieves 3148.44 μmol $g^{-1}$ $h^{-1}$, which is comparable to $WS_2$-$TiO_2$, and 9.40 times higher than pristine f-$TiO_2$ (**Fig. 4.13b**).

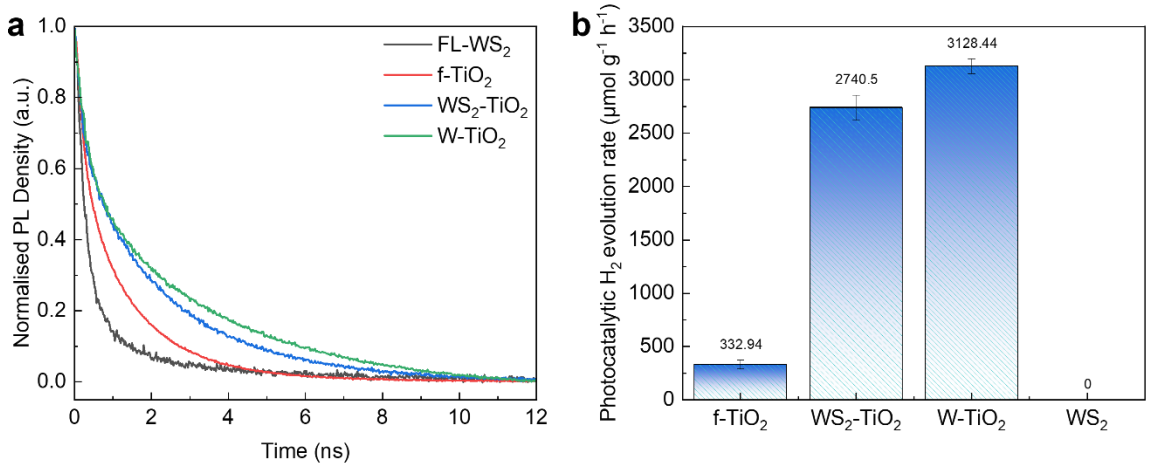



**Figure 4.13 (a)** TRPL results showing the order of W-$TiO_2$ > $WS_2$-$TiO_2$ > f-$TiO_2$ > FL-$WS_2$ in terms of lifetime; **(b)** Photocatalytic $H_2$ evolution rate in 10% methanol ($CH_3OH$) aqueous solution. The photocatalytic performance shows a consistent trend with the TRPL-derived lifetimes. TRPL spectra were acquired and fitted by Dr. Yiyang Li.

To evaluate the consumption rate of methanol as a sacrificial reagent and to study the reaction mechanism of $H_2$ evolution, photocatalytic experiments were conducted by tracking the concentration change of $CH_3OH$ (0.01%) and the reaction products. Typically, formaldehyde (HCHO), formic acid (HCOOH), carbon monoxide (CO) and carbon dioxide ($CO_2$) are the main products of $CH_3OH$ oxidation for $H_2$ evolution.[22] In this study, HCOOH and CO could not be detected from the reaction system, while HCHO and $CO_2$ could be observed during the photocatalytic reaction. As shown in **Fig. 4.14**, HCHO was the primary oxidation product for

$TiO_2$ (f-$TiO_2$) and $WS_2$-$TiO_2$ for $CH_3OH$ oxidation and the turnover frequencies of $CO_2$ production were 3.5 *$10^{-4}$ mol $g^{-1}$ $h^{-1}$ and 4.4 *$10^{-4}$ mol $g^{-1}$ $h^{-1}$, respectively. Notably, the selectivity and the evolution rate of $CO_2$ production significantly increased to 47% and 8.8 *$10^{-4}$ mol $g^{-1}$ $h^{-1}$ for W-$TiO_2$. This enhancement may be attributed to the increased number of exposed tungsten atom sites on the $TiO_2$ surface, which could potentially act as stronger adsorption centres for $CH_3OH$ and reaction intermediates, promoting $CO_2$ generation.

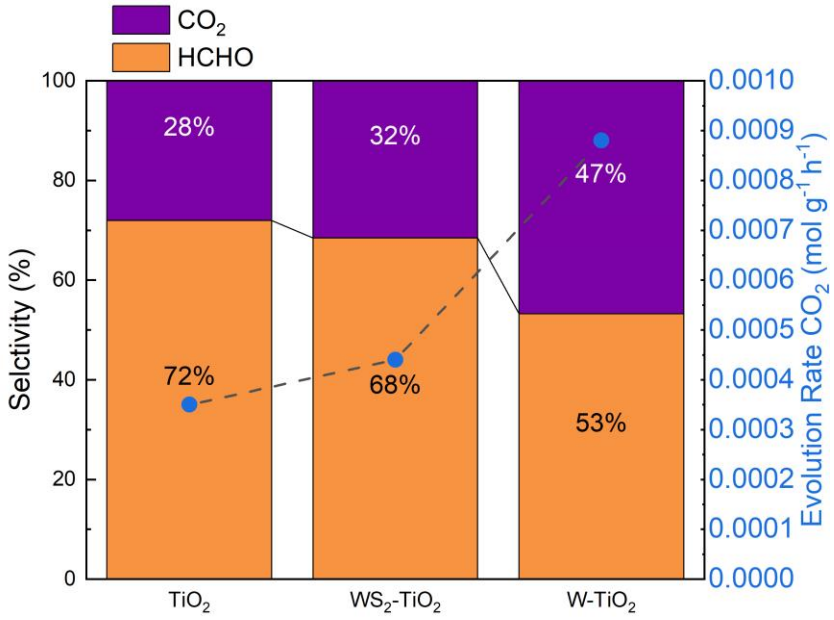



**Figure 4.14** Selectivity and evolution rate of $CO_2$ from photocatalytic $CH_3OH$ oxidation. The selectivity to $CO_2$ was significantly increased with the evolution rate doubled after the formation of tungsten single atoms on the $TiO_2$ surface.

The concentrations (mole percent) of $CH_3OH$, $CO_2$ and HCHO in the reaction system of W-$TiO_2$ were then monitored over an 8-hour period, as illustrated in **Fig. 4.15**. The concentrations of HCHO and $CO_2$ initially increased at a similar rate over the first 2 hours, accompanied by $CH_3OH$ decomposition. Thereafter, the concentration of HCHO started to be stabilised to approximately 18% after 2 hours, while the concentration of $CO_2$ continued to

rise. This implies that the rates of HCHO production from $CH_3OH$ oxidation and the rate of HCHO consumption became comparable. As HCHO and $CO_2$ were the only two products detected during this process, it is likely that the majority of the produced HCHO molecules were further oxidised and desorbed as $CO_2$ from the W-$TiO_2$ surface. $CH_3OH$ molecules were nearly fully consumed after around 6 hours, with the concentration of HCHO subsequently declining, indicating a reduced rate in $CH_3OH$ oxidation and an increased rate in HCHO consumption. Complete oxidation was achieved after 8 hours reaction time, with $CO_2$ as the sole carbon-containing product in the reaction system.

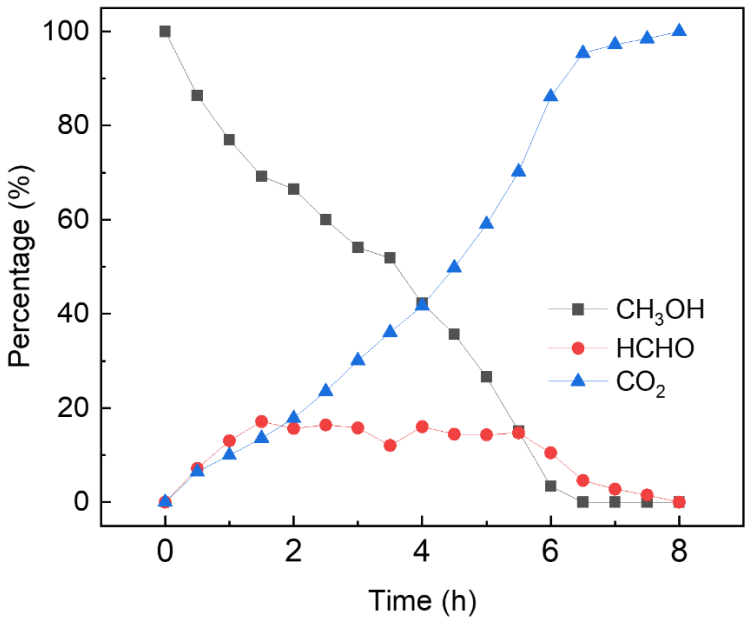



**Figure 4.15** Concentration changes (mole percent) of $CH_3OH$, HCHO and $CO_2$ over reaction time with diluted $CH_3OH$ aqueous solution (0.01%). The concentration of $CH_3OH$ kept decreasing over time indicating its consumption during the catalytic process. The HCHO concentration increased in the first two hours and then stabilised at *ca.* 18% for the next four hours, suggesting the similar rate of production and consumption of HCHO. When $CH_3OH$ was mostly consumed at the 6-hour mark, HCHO concentration was gradually dropped to zero, leaving $CO_2$ as the final product from $CH_3OH$ oxidation.

## 4.3 Conclusion

In conclusion, it has been demonstrated that chemically exfoliated $WS_2$ is susceptible to oxidation when forming the heterojunction in water-rich conditions, even under $N_2$ protection. The oxidation process results in the creation of $O_v$ and formation of tungsten single-atom sites on the surface of $TiO_2$, instead of forming bulk $WO_3$. The structural transformation from $WS_2$-$TiO_2$ to W-$TiO_2$ did not lead to deactivation on photocatalytic $H_2$ evolution rate, as the tungsten-induced electronic structure change and reduced charge transfer resistance could facilitate the photocatalytic reaction. Additionally, the exposed tungsten single atoms might serve as active sites for $CH_3OH$ oxidation, enhancing reactivity and $CO_2$ selectivity. These findings provide further insight into the potential oxidation mechanisms of $WS_2$, highlighting the importance of investigating the structural change of TMDs during the synthetic and catalytic process. Moreover, this study provides a novel approach to simultaneously introduce tungsten single atoms and $O_v$ onto the $TiO_2$ support, which can be potentially applicable to other metal oxide-based materials. For future investigations, theoretical studies can be applied to elucidate how introduced tungsten atoms affect lattice strain, generate $O_v$ on the surface, and promote methanol oxidation.

In the following chapter, surface engineering strategies will be applied to metal oxides, including $TiO_2$, ZnO, and $CeO_2$, to explore the effects of exposed crystal facets on photocatalytic performance. A novel surface-sensitive XPS method will be introduced to investigate facet-dependent surface charge accumulation, offering a deeper understanding of how exposed facets influence photocatalysis.

## 4.4 References

1. S. Manzeli, D. Ovchinnikov, D. Pasquier, O. V. Yazyev and A. Kis, 2D transition metal dichalcogenides, *Nat. Rev. Mater.*, 2017, **2**, 17033.
2. R. C. Longo, R. Addou, S. Kc, J.-Y. Noh, C. M. Smyth, D. Barrera, C. Zhang, J. W. P. Hsu, R. M. Wallace and K. Cho, Intrinsic air stability mechanisms of two-dimensional transition metal dichalcogenide surfaces: basal versus edge oxidation, *2D Mater.*, 2017, **4**, 025050.
3. R. Yang, L. Mei, Q. Zhang, Y. Fan, H. S. Shin, D. Voiry and Z. Zeng, High-yield production of mono- or few-layer transition metal dichalcogenide nanosheets by an electrochemical lithium ion intercalation-based exfoliation method, *Nat. Protoc.*, 2022, **17**, 358-377.
4. S. Kc, R. C. Longo, R. M. Wallace and K. Cho, Surface oxidation energetics and kinetics on $MoS_2$ monolayer, *J. Appl. Phys.*, 2015, **117**, 135301.
5. T. H. Ly, M.-H. Chiu, M.-Y. Li, J. Zhao, D. J. Perello, M. O. Cichocka, H. M. Oh, S. H. Chae, H. Y. Jeong, F. Yao, L.-J. Li and Y. H. Lee, Observing Grain Boundaries in CVD-Grown Monolayer Transition Metal Dichalcogenides, *ACS Nano*, 2014, **8**, 11401-11408.
6. S. Ross and A. Sussman, Surface Oxidation of Molybdenum Disulfide, *J. Phys. Chem.*, 1955, **59**, 889-892.
7. J. Gao, B. Li, J. Tan, P. Chow, T.-M. Lu and N. Koratkar, Aging of Transition Metal Dichalcogenide Monolayers, *ACS Nano*, 2016, **10**, 2628-2635.
8. J. Pető, T. Ollár, P. Vancsó, Z. I. Popov, G. Z. Magda, G. Dobrik, C. Hwang, P. B. Sorokin and L. Tapasztó, Spontaneous doping of the basal plane of $MoS_2$ single layers through oxygen substitution under ambient conditions, *Nat. Chem.*, 2018, **10**, 1246-1251.
9. Z. Wang, A. von dem Bussche, Y. Qiu, T. M. Valentin, K. Gion, A. B. Kane and R. H. Hurt, Chemical Dissolution Pathways of $MoS_2$ Nanosheets in Biological and Environmental Media, *Environ. Sci. Technol.*, 2016, **50**, 7208-7217.
10. J. C. Kotsakidis, Q. Zhang, A. L. Vazquez de Parga, M. Currie, K. Helmerson, D. K. Gaskill and M. S. Fuhrer, Oxidation of Monolayer $WS_2$ in Ambient Is a Photoinduced

Process, *Nano Lett.*, 2019, **19**, 5205-5215.

11. Y. Li, S. Wu, J. Zheng, Y.-K. Peng, D. Prabhakaran, R. A. Taylor and S. C. E. Tsang, 2D photocatalysts with tuneable supports for enhanced photocatalytic water splitting, *Mater. Today*, 2020, **41**, 34-43.
12. J. Li, G. Zhan, Y. Yu and L. Zhang, Superior visible light hydrogen evolution of Janus bilayer junctions via atomic-level charge flow steering, *Nat. Commun.*, 2016, **7**, 11480.
13. S. Singh, A. Modak, K. K. Pant, A. Sinhamahapatra and P. Biswas, MoS2 – Nanosheets-Based Catalysts for Photocatalytic $CO_2$ Reduction: A Review, *ACS Appl. Nano Mater.*, 2021, **4**, 8644-8667.
14. B. Balan, M. M. Xavier and S. Mathew, $MoS_2$-Based Nanocomposites for Photocatalytic Hydrogen Evolution and Carbon Dioxide Reduction, *ACS Omega*, 2023, **8**, 25649-25673.
15. P. Zhou, I. A. Navid, Y. Ma, Y. Xiao, P. Wang, Z. Ye, B. Zhou, K. Sun and Z. Mi, Solar-to-hydrogen efficiency of more than 9% in photocatalytic water splitting, *Nature*, 2023, **613**, 66-70.
16. D. Gao, P. Deng, J. Zhang, L. Zhang, X. Wang, H. Yu and J. Yu, Reversing Free-Electron Transfer of $MoS_{2+x}$ Cocatalyst for Optimizing Antibonding-Orbital Occupancy Enables High Photocatalytic $H_2$ Evolution, *Angew. Chem. Int. Ed.*, 2023, **62**, e202304559.
17. E. Parzinger, B. Miller, B. Blaschke, J. A. Garrido, J. W. Ager, A. Holleitner and U. Wurstbauer, Photocatalytic Stability of Single- and Few-Layer $MoS_2$, *ACS Nano*, 2015, **9**, 11302-11309.
18. H. Xu, P. Reunchan, S. Ouyang, H. Tong, N. Umezawa, T. Kako and J. Ye, Anatase $TiO_2$ Single Crystals Exposed with High-Reactive {111} Facets Toward Efficient $H_2$ Evolution, *Chem. Mater.*, 2013, **25**, 405-411.
19. Y. Feng, C. Wang, P. Cui, C. Li, B. Zhang, L. Gan, S. Zhang, X. Zhang, X. Zhou, Z. Sun, K. Wang, Y. Duan, H. Li, K. Zhou, H. Huang, A. Li, C. Zhuang, L. Wang, Z. Zhang and X. Han, Ultrahigh Photocatalytic $CO_2$ Reduction Efficiency and Selectivity Manipulation by Single-Tungsten-Atom Oxide at the Atomic Step of $TiO_2$,

*Adv. Mater.*, 2022, **34**, 2109074.

20. W. Liu, L. Cao, W. Cheng, Y. Cao, X. Liu, W. Zhang, X. Mou, L. Jin, X. Zheng, W. Che, Q. Liu, T. Yao and S. Wei, Single-Site Active Cobalt-Based Photocatalyst with a Long Carrier Lifetime for Spontaneous Overall Water Splitting, *Angew. Chem. Int. Ed.*, 2017, **56**, 9312-9317.
21. J. Zheng, E. Li, D. Ma, Z. Cui, T. Peng and X. Wang, Effect on Schottky Barrier of Graphene/$WS_2$ Heterostructure With Vertical Electric Field and Biaxial Strain, *Phys. Status Solidi B*, 2019, **256**, 1900161.
22. H. Wang, H. Qi, X. Sun, S. Jia, X. Li, T. J. Miao, L. Xiong, S. Wang, X. Zhang, X. Liu, A. Wang, T. Zhang, W. Huang and J. Tang, High quantum efficiency of hydrogen production from methanol aqueous solution with PtCu−TiO2 photocatalysts, *Nat. Mater.*, 2023, **22**, 619-626.

# Chapter 5 Surface Charge Probing on Faceted Metal Oxides under Illumination

## 5.1 Introduction

Tuning surface properties of heterogeneous catalysts by tailoring exposed facets has been widely explored, as bond formation and breakage are sensitive to the surface chemical environment.[1-3] In photocatalysis, it was first reported by Hotsenpiller *et al.* that altering the exposed facets of rutile $TiO_2$ could strongly influence the rate of photochemical reactions, where the (101), (111) and (001) facets exhibited higher photoreduction reactivity than the (100) and (110) facets.[4, 5] Their subsequent discussions on the properties of rutile $TiO_2$ such as surface chemistry, space charge phenomena, and charge transport suggested that this rate difference originated from more efficient electron-hole utilisation, though no specific model was established to explain the experimental observations.

Then, new evidence from electron microscopy studies revealed that metal ions could be selectively reduced and oxidised on distinct facets during the photo-deposition process, which was regarded as evidence of facet-dependent spatial charge migration.[6, 7] Building on this, the *in-situ* visualisation of the distribution of facet-dependent charge separation was achieved using single-molecule fluorescence spectroscopy.[8, 9] The probe molecules adsorbed on the surface of photocatalysts became highly fluorescent after interacting with photogenerated charges, allowing the spatial distribution of electrons and holes to be observed via fluorescence signals.

Based on these findings, further experimental and theoretical studies conducted by Yu *et al.* suggested that facet-dependent charge separation might originate from variations in the band

structures of exposed facets, leading to differences in band-edge potentials and thereby facilitating charge separation akin to type-II heterojunctions.[10]

However, experimentally quantifying the amount of charge accumulated on a specific facet remains challenging. A significant breakthrough in charge quantification was achieved by Li *et al.*, where Kelvin probe force microscopy was employed for quantitatively mapping the charge distribution via SPV potential differences across exposed facets in a single-crystal $Cu_2O$ particle under illumination.[11, 12] With the help of this technique, it became possible to investigate correlations between photocatalytic performance and surface-accumulated charges on various surface-modified samples. Nevertheless, this technique could only achieve spatiotemporally resolved SPV measurements on the micron-sized single particle level, whilst most of the photocatalysts are nanoparticles and accurate measurement is impossible due to the resolution limitation.[13] Since surface charge density is believed to be one of the key factors in the photocatalytic process, a more accessible method is still required to investigate surface polarisation in nanoscale photocatalysts.[14]

Synchronous illumination X-ray photoelectron spectroscopy (XPS) is a powerful technique for detecting the core-level binding energy (BE) shifts of elements in nanoparticles under different operating conditions.[15] It can reveal chemical information about both heterogeneous catalysts and adsorbates, which makes this technique useful in the reaction mechanism studies.[16, 17] However, due to the long penetration depth of X-rays, even at a very small incidence angle of 0.3°, the resulting XPS signal averages over approximately seven subsurface layers, which limits its suitability for detecting processes occurring on the outermost atomic layers.[18] As a result, simple use of XPS has failed to directly detect charge

separation on intact faceted $TiO_2$, due to inadequate surface sensitivity.[19]

Additionally, as XPS signals are typically averaged across all exposed surfaces, it is difficult to selectively extract information from individual facets. It is well-established in previous studies that introduction of probe molecules can help to extract surface-specific information of materials.[20] For instance, trimethylphosphine (TMP) has been widely used as a surface probe since it was first applied by Lunsford and co-workers to study surface acidity, particularly using nuclear magnetic resonance (NMR).[21] Furthermore, previous works applying TMP-assisted NMR on metal oxides of different morphologies have successfully demonstrated the acquisition of both qualitative and quantitative information on surface features of exposed facets.[22, 23]

Inspired by these studies, if photo-generated electrons and holes are spatially separated across different facets, TMP molecules adsorbed on these facets may reflect the local electron density changes through shifts in P 2p XPS binding energy, towards lower BE for electrons and higher BE for holes. By measuring the BE shifts in XPS spectra, it would be possible to monitor surface charge accumulation on each facet under illumination. To the best of our knowledge, no systematic study on facet-dependent charge separation has been conducted using this approach.

In this work, we demonstrate a TMP-probed XPS technique with high surface sensitivity. This approach is capable of direct measurement on photo-induced electron density change in facet-engineered metal oxides ($CeO_2$, ZnO & $TiO_2$ etc.). The exposed facets of metal oxides were prepared and characterised prior to XPS analysis with the aid of XRD and TEM. It was observed that samples showing BE shifts in both negative and positive directions under

illumination (indicative of facet-dependent charge separation) exhibited higher photocatalytic activity in $O_2$ evolution. Additionally, these samples showed prolonged lifetimes of photo-generated charges carriers compared to other samples lacking such driving force for facet-dependent charge separation. These findings reinforce the facet-dependent charge separation model and provide a novel approach to future investigation of the surface charge in nanoparticulate photocatalysts.

## 5.2 Results and Discussion

### 5.2.1 $CeO_2$: Tuning the Number of Exposed Facets

$CeO_2$ samples with different numbers of exposed facets were prepared with the aid of surface directing reagents and are labelled as c-$CeO_2$, o-$CeO_2$ and s-$CeO_2$, corresponding to their morphologies (cube, octahedron and sphere). All the nanocrystals exhibited a fluorite structure, as indexed from the XRD results illustrated in **Fig. 5.1**, indicating that variation in exposed facets does not alter the overall crystal structure. Notably, samples with well-defined exposed facets (c-$CeO_2$ and o-$CeO_2$) showed higher XRD peak intensities than s-$CeO_2$, which has been reported to possess an amorphous surface. This indicates that c-$CeO_2$ and o-$CeO_2$ are more crystalline compared to s-$CeO_2$.

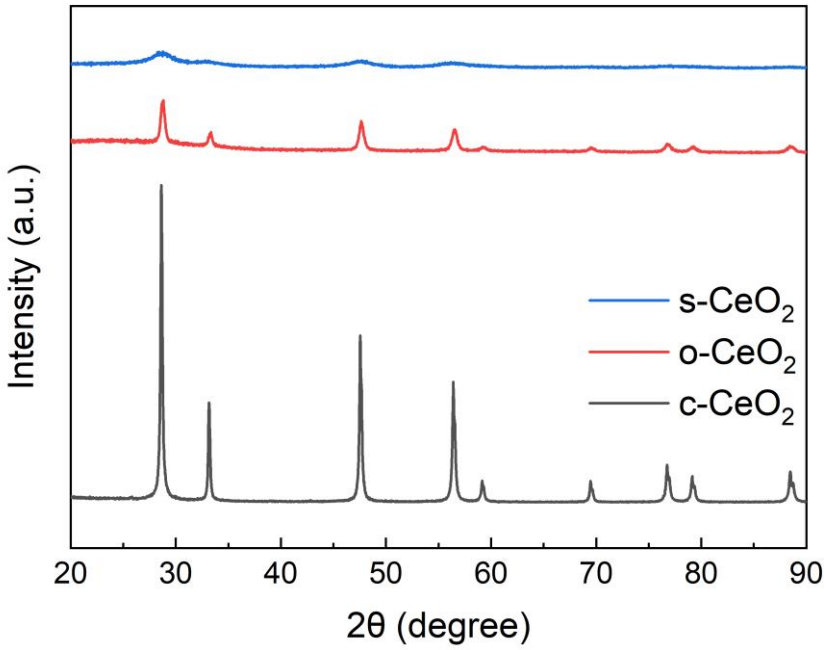



**Figure 5.1** XRD patterns of $CeO_2$ samples with different exposed facets. All the samples show a fluorite crystal structure. Peak intensity suggests s-$CeO_2$ is less crystalline compared to o-$CeO_2$ and c-$CeO_2$.

The morphologies and particle size distributions of the $CeO_2$ samples are revealed by TEM as shown in **Fig. 5.2**. For c-$CeO_2$, the particles are cube-shaped with a size distribution of 40 ± 15 nm (**Fig. 5.2a**). Nanocrystals in the shape of octahedron with a size distribution of 26 ± 7 nm can be seen in the TEM image of o-$CeO_2$ in **Fig. 5.2b**. As for s-$CeO_2$, it is in the shape of nano-sphere and the particle size is generally smaller compared to those of c-$CeO_2$ and o-$CeO_2$, which is *ca.* 10 nm as illustrated in **Fig. 5.2c**. Comparing the three samples, c-$CeO_2$ and o-$CeO_2$ exhibit well-defined morphologies, whilst s-$CeO_2$ is less crystalised with indistinct boundaries between individual particles, which is consistent with the XRD results.

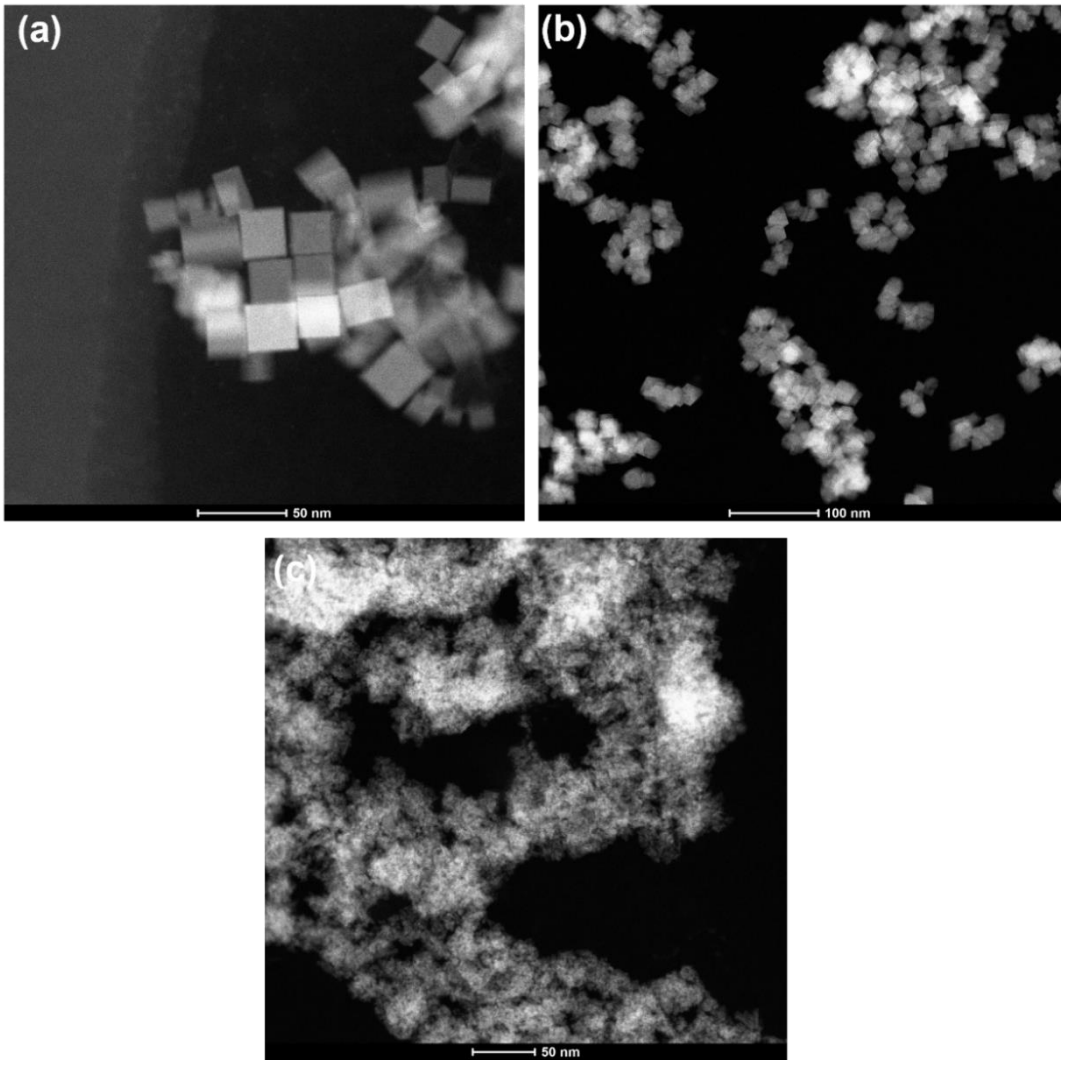



**Figure 5.2** TEM images of **(a)** c-$CeO_2$, **(b)** o-$CeO_2$, and **(c)** s-$CeO_2$. c-$CeO_2$ and o-$CeO_2$ show well-defined structures from the TEM image whilst s-$CeO_2$ is less crystallised and lacks a uniform shape. TEM images in this figure were acquired by Prof. Songhua Cai.

Previous studies suggest that c-$CeO_2$ has a predominately exposed (200) facet with a co-existing (220) facet at the edges of the nano-cubes.[24] The lattice spacings of 0.27 nm and 0.19 nm in high resolution TEM images of c-$CeO_2$ (**Fig. 5.3a, b**) further confirm that the nanocrystals are mainly enclosed by (200) and (220) facets. Different from c-$CeO_2$, o-$CeO_2$ is believed to be exclusively enclosed by (111) facets, evidenced by the lattice spacing of 0.32 nm as shown in **Fig. 5.3c, d**. For s-$CeO_2$ (**Fig. 5.3e, f**), it also has a lattice spacing of 0.32 nm

and the blurry particle boundaries further indicate an amorphous surface.

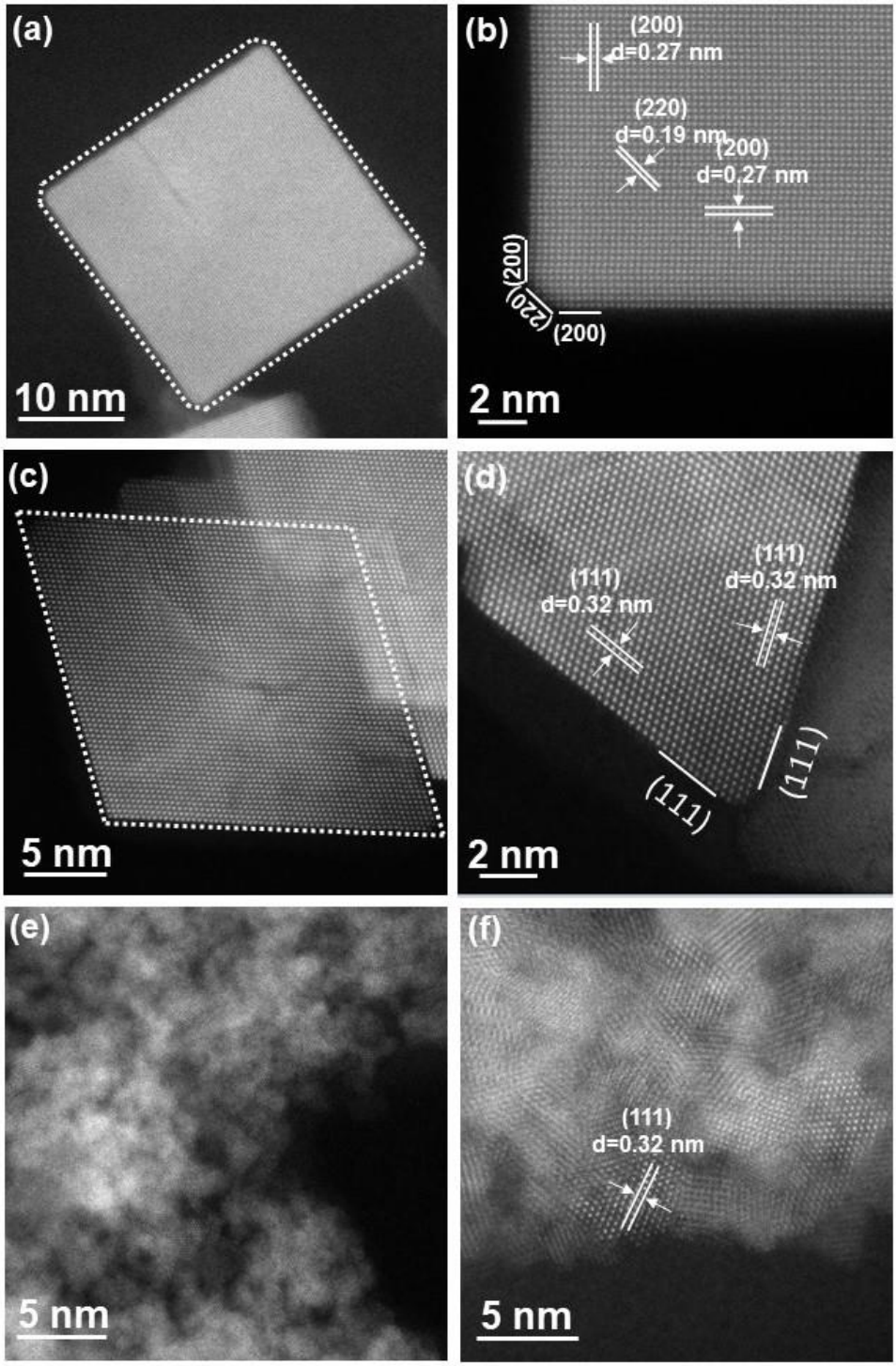



**Figure 5.3** High resolution TEM images of **(a, b)** c-$CeO_2$ enclosed by (220) and (200) facets, **(c, d)** o-$CeO_2$ enclosed by (111) facets and **(e, f)** s-$CeO_2$ with an amorphous surface. TEM images in this figure were acquired by Prof. Songhua Cai.

The corresponding P 2p XPS spectra of TMP molecules adsorbed on c-$CeO_2$ and o-$CeO_2$ samples are shown in **Fig. 5.4**. The P 2p peaks were deconvoluted to quantify the fractions of TMP molecules adsorbed on different facets. For c-$CeO_2$ under dark conditions, two TMP species with P $2p_{3/2}$ BEs at 129.2 eV and 133.2 eV can be differentiated as shown in **Fig. 5.4**. The ratio between the two P species in peak area is 88.6% : 11.4% which correlates well with the (200) : (220) facet ratio revealed by TEM and previous studies.[20] The BE difference between the two TMP species can be attributed to the intrinsic properties of the exposed facets. Theoretically, core-level BEs in XPS are influenced by the redistribution of valence electrons (*i.e.* the shared electron pairs in TMP molecules upon adsorption).[25] Electron shielding and penetration are key factors. Increased shielding, due to a relatively higher local electron density at the TMP adsorption site, reduces the BE of P 2p (negative shift), whereas decreased shielding, caused by a relatively lower local electron density at the TMP adsorption site, increases it (positive shift). Consequently, since the electron density on the (200) facet is higher than that on the (220) facet, it results in greater shielding of the core-level electrons in TMP molecules adsorbed on (200) facets compared to (220) facets, leading to a lower BE in XPS spectra. Therefore, the P $2p_{3/2}$ peaks at 129.2 eV and 133.2 eV are assigned to TMP adsorbed on the Ce sites of the (200) and (220) facets, respectively. Under UV illumination, the P 2p peak assigned to the (200) facet positively shifts by 1.2 eV in BE, whilst a negative shift of -0.5 eV can be observed on the peak assigned to the (220) facet. As previously discussed, a positive/negative shift in BE corresponds to a decrease/increase in electron density on the adsorbed facets. The results indicate that photo-generated holes and electrons can selectively migrate to the (200) facet and the (220) facet of c-$CeO_2$, respectively.

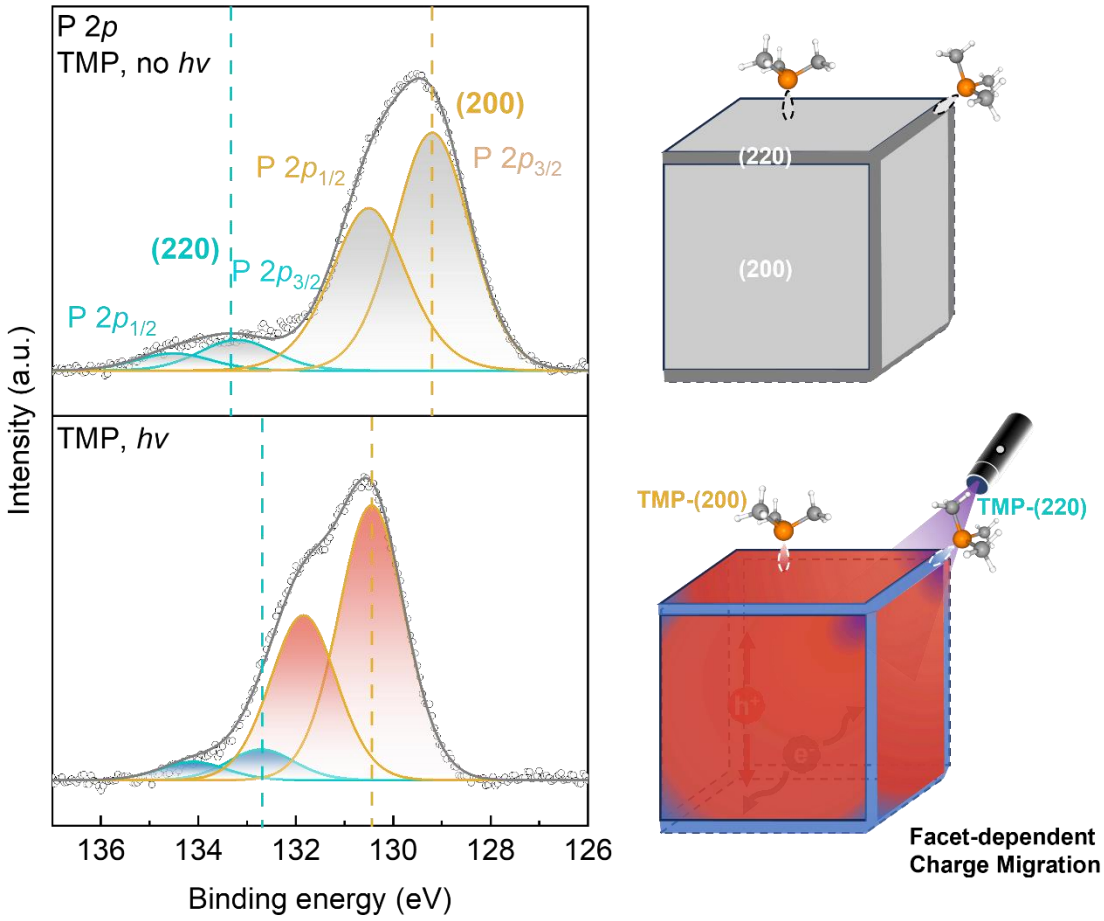



**Figure 5.4** High resolution P 2p spectra of TMP adsorbed on c-$CeO_2$ with and without light. The negative shift can be assigned to TMP molecules adsorbed on (220) facets and the positive shift can be assigned to TMP molecules adsorbed on (200) facets. The red colour indicates an increased hole density, while the blue colour indicates an increased electron density. XPS measurements and data analysis in this figure were conducted by Dr. Yiyang Li.

Different from c-$CeO_2$, only one TMP species with a P $2p_{3/2}$ peak at 133.6 eV can be deconvoluted for o-$CeO_2$ under dark condition (**Fig. 5.5a**). Since o-$CeO_2$ is fully enclosed by the (111) facet, the XPS result agrees with the theoretical model constructed based on the TEM results. Moreover, the XPS BE of P 2p follows the trend of (200) < (220) < (111), inversely related to facet electron densities, aligning with our previous findings.[20] Upon UV

excitation, the P 2p peak shifts negatively with no positively shifted component. A similar result is observed in s-$CeO_2$ with TMP molecules adsorbed on its amorphous surface (**Fig. 5.5b**): only one P 2p peak appears in dark conditions which shifts negatively upon illumination. The absence of a positively shifted component suggests that the TMP adsorption sites (Ce sites) on different facets become more electron-rich under UV light without hole accumulation on specific facets. However, given that the surface of s-$CeO_2$ is amorphous, multiple TMP species should theoretically be distinguishable in the XPS spectra. This may be attributed to the limited resolution of XPS, where the minor differences in electron density at the TMP adsorption sites on the s-$CeO_2$ surface cannot be resolved under current experimental conditions.

To better understand the absence of positive shifts, it is indispensable to investigate the chemical state changes in Ce. **Fig. 5.6** illustrates Ce 3d XPS spectra of all the $CeO_2$ samples under various experimental conditions. Both $Ce^{3+}$ and $Ce^{4+}$ species can be deconvoluted in Ce 3d XPS spectra with higher $Ce^{4+}$ concentration. Upon TMP adsorption, an increase in $Ce^{3+}$ species is observed in all samples, indicating that $CeO_2$ becomes more electron-rich under this condition. Moreover, a further increase in electron density of Ce under UV light is observed, where the $Ce^{3+}$ proportion in c-$CeO_2$ increases from 7.4% to 29.0% with corresponding decreases in $Ce^{4+}$ (**Fig. 5.6a**). Similar electron density increases on Ce as the effect of UV light can also be seen in o-$CeO_2$ and s-$CeO_2$ (**Fig. 5.6b, c**). This result is consistent with the band electron density change upon photoexcitation, where the electrons in the valence band (O 2p orbitals) are excited by light into the conduction band (Ce 4f orbitals), leading to an increased electron population at Ce sites and a decreased electron population at

O sites. Consequently, TMP molecules adsorbed on exposed Ce sites detect increased electron density, resulting in negative P 2p shifts for $CeO_2$ and s-$CeO_2$. Since the O sites are non-Lewis-acidic and are unlikely to serve as TMP adsorption sites, the positive shift in P 2p cannot be observed. In the case of c-$CeO_2$, however, despite the overall increase in $Ce^{3+}$ concentration, the positive shift of TMP on the (200) facet shows the different behaviours of the surface from the bulk, highlighting that exposing different well-defined facets is a crucial factor to provide driving forces for spatially separating electrons and holes on the surface.

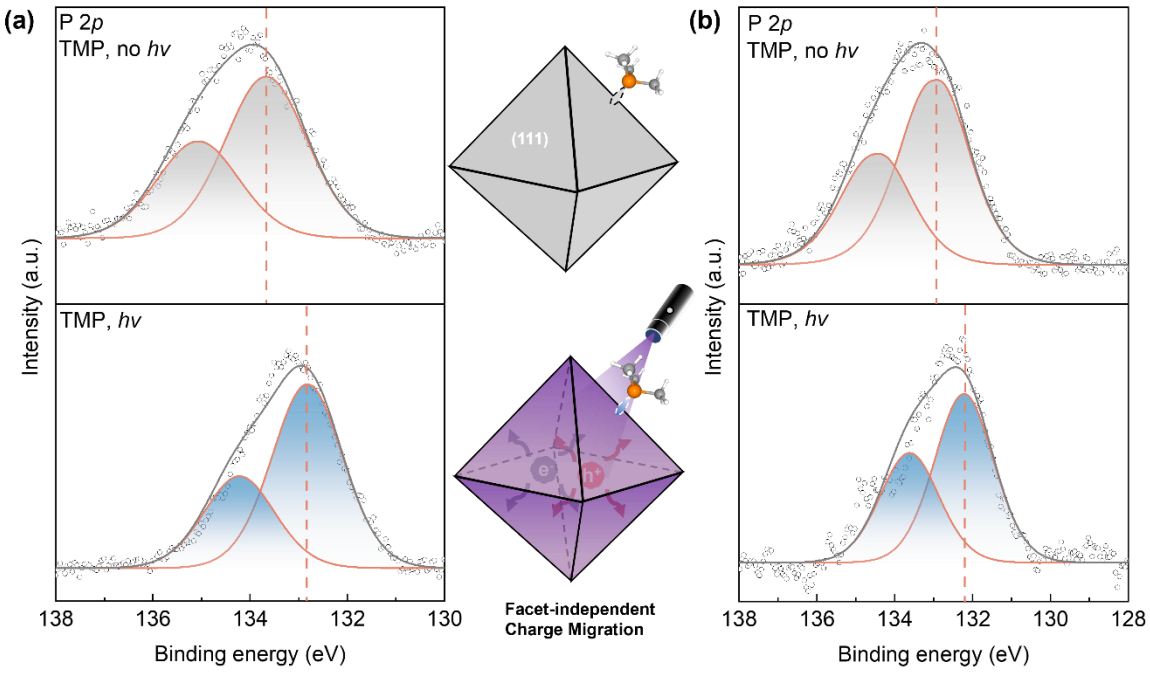



**Figure 5.5** High resolution P 2p spectra of TMP adsorbed on **(a)** o-$CeO_2$ and **(b)** s-$CeO_2$ with and without illumination. Only negative shifts can be found in both samples, potentially caused by the electron density increase in the conduction band (metal binding sites), indicating that the charge migration is not facet-dependent. XPS measurements and data analysis in this figure were conducted by Dr. Yiyang Li.

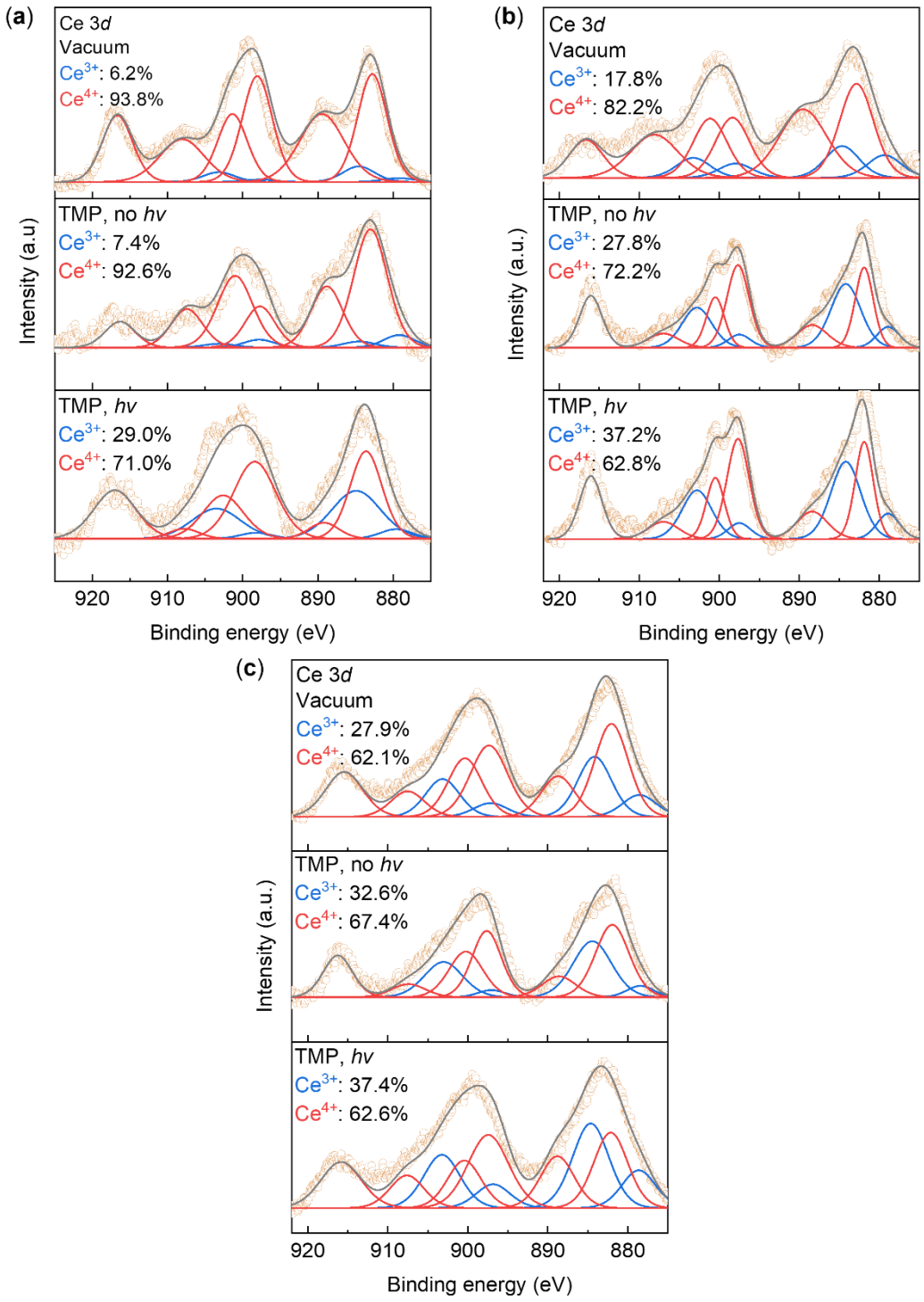



**Figure 5.6** High resolution Ce 3d spectra of **(a)** c-$CeO_2$, **(b)** o-$CeO_2$ and **(c)** s-$CeO_2$ under different experimental conditions. The percentage of $Ce^{3+}$ increased after TMP adsorption and further increased after turning on the light. XPS measurements and data analysis in this figure were conducted by Dr. Yiyang Li.

### 5.2.2 $TiO_2$ and ZnO: Tuning the Ratio of Exposed Facets

The results from $CeO_2$ highlighted the importance of creating an anisotropic surface structure by simultaneously exposing two different facets to achieve spatial charge separation. From previous studies, it has been shown that changing the ratio of co-exposed facets on $TiO_2$ nanocrystals can also result in differences in photocatalytic activity.[4, 10] However, experimental evidence to support this activity difference is still lacking due to limitations of characterisation techniques. Therefore, it is essential to conduct further measurements on the surface charge of nanoparticles upon photoexcitation to gain a more detailed understanding of catalytic performance differences arising from varied proportions of exposed facets.

In light of this, $TiO_2$ nanocrystals with different ratios of (001) and (101) exposed facets were synthesised. Their anatase crystal structure was confirmed by XRD as shown in **Fig. 5.7a**. As seen in **Fig. 5.7b, c**, the two $TiO_2$ nanocrystals exhibit plate-shaped (p-$TiO_2$, diameter *ca.* 50 nm) and bifrustum-shaped (b-$TiO_2$, diameter *ca.*15 nm) morphologies. Both samples have the (001) and (101) facets exposed revealed by the lattice spacings in **Fig. 5.8**, although the ratios of exposed facets are different. Based on the morphology of $TiO_2$ samples observed in TEM images and previous studies using the same synthetic methods, it is estimated that for p-$TiO_2$, the exposed (001) and (101) facets account for approximately 70% and 30%, respectively (**Fig. 5.8a, b**).[23] As for b-$TiO_2$, the exposed (001) facets constitute only 3%, with the exposed (101) facets making up the remaining 97% (**Fig. 5.8c, d**).

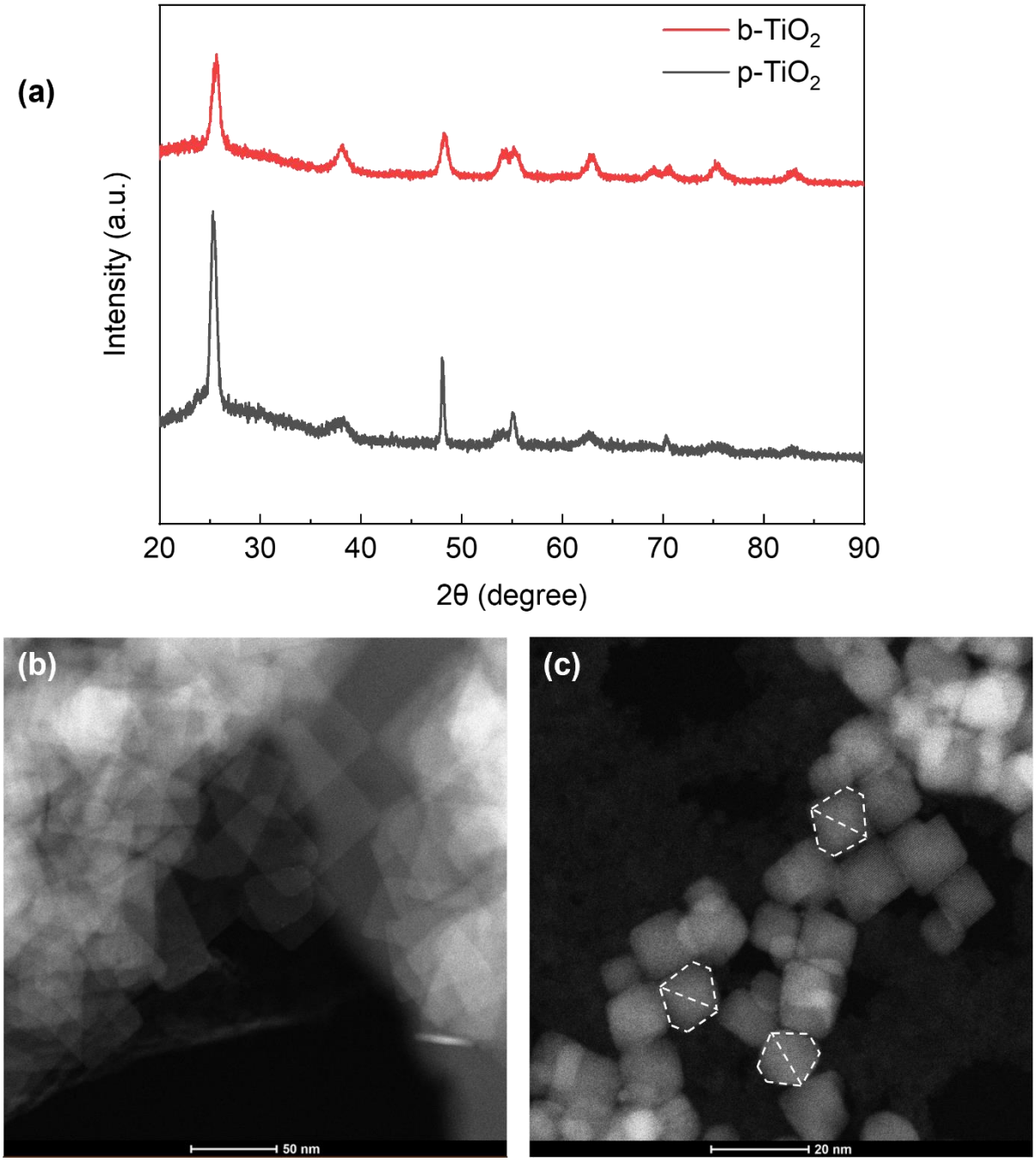



**Figure 5.7 (a)** XRD patterns of $TiO_2$ samples, confirming their anatase crystal structure; TEM images of **(b)** p-$TiO_2$ in the shape of plate and **(c)** b-$TiO_2$ in the shape of bifrustum. TEM images in this figure were acquired by Prof. Songhua Cai.

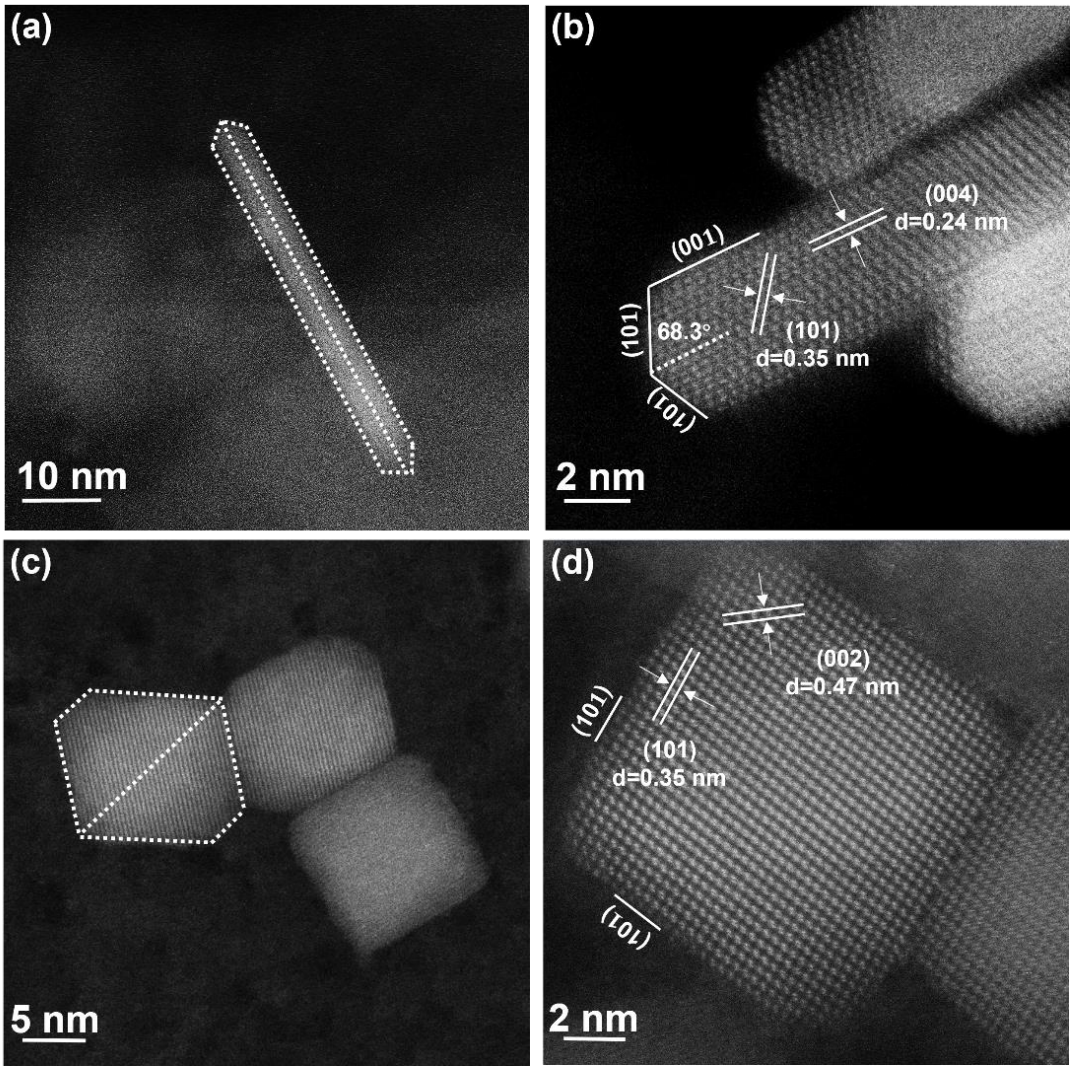



**Figure 5.8** High resolution TEM images of **(a, b)** p-$TiO_2$ and **(c, d)** b-$TiO_2$. Both samples are enclosed by the (101) and (001) facets, where p-$TiO_2$ has more (001) facets exposed and b-$TiO_2$ has more (101) facets exposed. TEM images in this figure were acquired by Prof. Songhua Cai.

Notably, even with co-existing facets, only one TMP species can be deconvoluted from the P 2p spectra of both p-$TiO_2$ and b-$TiO_2$ under dark conditions, with P $2p_{3/2}$ at 130.6 eV (**Fig. 5.9**). In contrast to $CeO_2$, the exposed Ti atoms on the (001) and (101) facets do not exhibit significant differences in electron density at 5-coordinated $Ti^{4+}$ ($Ti_{5c}$) sites (Lewis-acidic), resulting in low surface polarity variation.[23] Therefore, under the current experimental

conditions, the change in electron density of adsorbed TMP molecules may not be significant enough to be differentiated in XPS spectra and only one phosphorus species can be deconvoluted.

However, upon illumination, the P 2p peak of TMP on p-$TiO_2$ splits into two components with opposite shifts, yielding P $2p_{3/2}$ peaks at 131.8 eV and 129.2 eV (**Fig. 5.9a**). More importantly, the integrated area ratio of the positively and negatively shifted components is 62.4% : 37.6%, which closely matches the ratio of (001) : (101) in p-$TiO_2$ based on the previous structural analysis. The positive and negative shifts in BE suggest the accumulation of photo-generated holes and electrons on the (001) and (101) facets, respectively. In contrast, however, only a negatively shifted component is observed for b-$TiO_2$ (**Fig. 5.9b**). As b-$TiO_2$ is mostly enclosed by the (101) facets, the insufficient proportion of (001) facets in b-$TiO_2$ may not be able to establish an effective anisotropic driving force for achieving facet-dependent surface charge accumulation.

Regarding the metal XPS spectra, the Ti 2p peaks exhibit a negative shift under illumination in both $TiO_2$ samples (**Fig. 5.10**), similar to the behaviour seen in Ce 3d. This further supports the previous hypothesis that, in the absence of facet-dependent electron-hole migration, under illumination where electrons are excited into CB (metal orbitals) from VB, only a negative shift on P 2p can be observed due to the increase in electron density at TMP adsorption sites. Moreover, in p-$TiO_2$ and c-$CeO_2$, although hole accumulation on the surface is indicated by P 2p spectra, it is not discernible in the bulk-sensitive metal XPS signals, as the surface signal is averaged out by contributions from sub-surface layers.

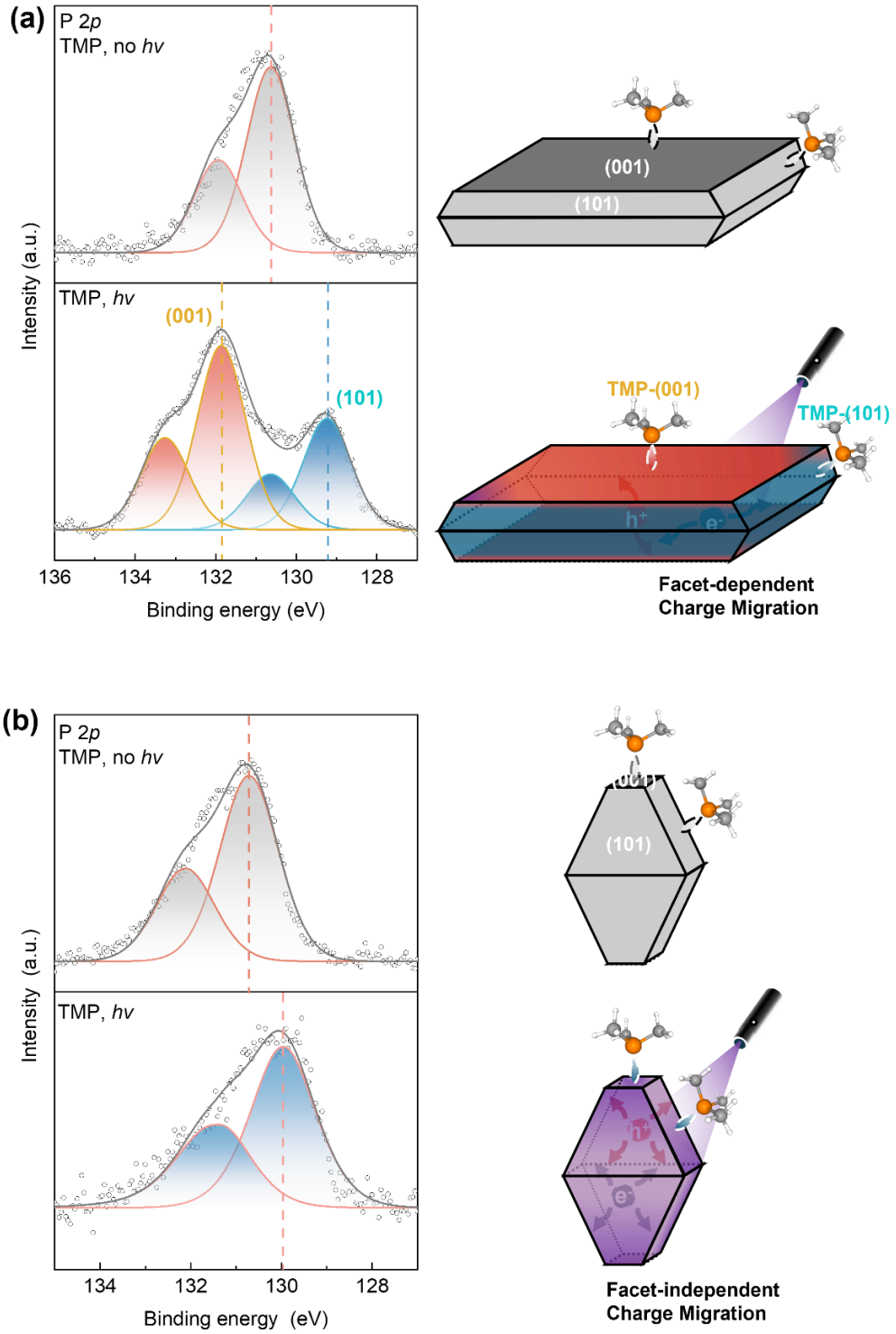



**Figure 5.9** High resolution P 2p spectra of TMP adsorbed on **(a)** p-$TiO_2$ and **(b)** b-$TiO_2$ under dark and illuminated conditions. A positive and a negative shift can be observed in p-$TiO_2$ whilst only a negative shift can be seen in b-$TiO_2$. XPS measurements and data analysis in this figure were conducted by Dr. Yiyang Li.

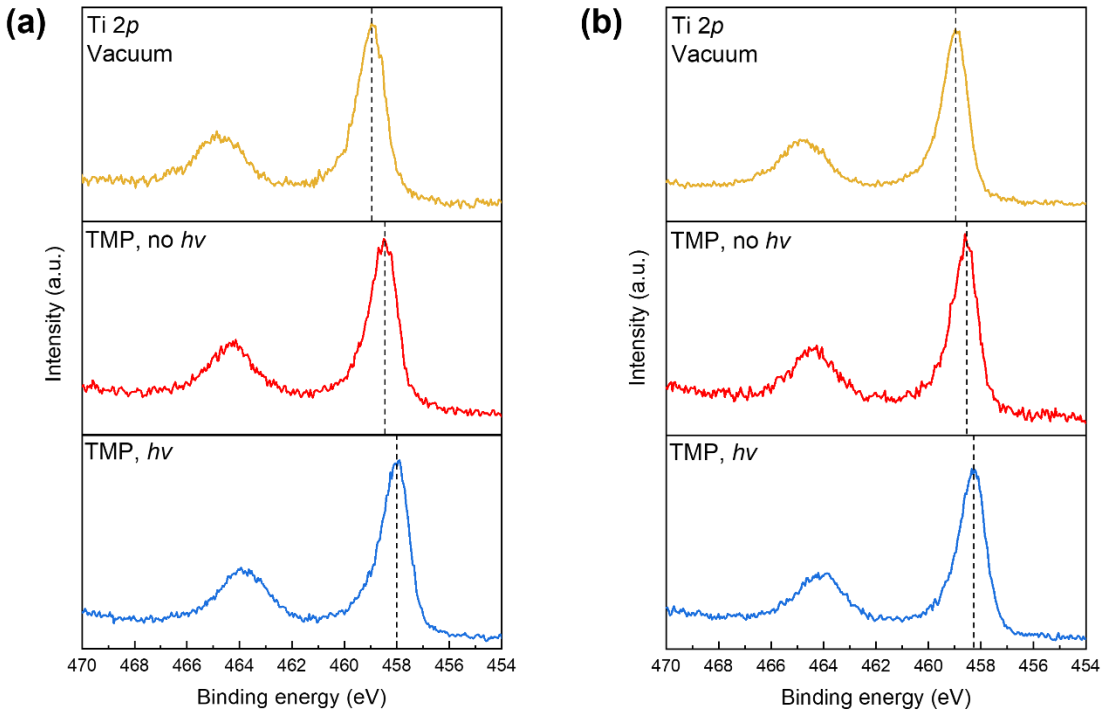



**Figure 5.10** High resolution Ti 2p spectra of **(a)** p-$TiO_2$ and **(b)** b-$TiO_2$ under different experimental conditions. A negative shift can be seen after TMP adsorption and upon illumination, indicating an increase in electron density at metal sites. XPS measurements and data analysis in this figure were conducted by Dr. Yiyang Li.

To further investigate facet-ratio effects on charge migration, wurtzite ZnO nanoparticles were synthesised with plate (p-ZnO, diameter *ca.* 50 nm) and rod (r-ZnO, *ca.* 800-1000 nm in length) morphologies as revealed by XRD (**Fig. 5.11a**) and TEM (**Fig. 5.11b, c** and **Fig. 5.12**). Both p-ZnO and r-ZnO samples have polar (002) and non-polar (100) facets exposed in differing ratios. Due to the unique crystal structure, it is worth noting that the polar (002) facets are terminated by $Zn^{2+}$ and $O^{2-}$ respectively on opposite sides. Consequently, a significant amount of surface OH groups form on the (002) facets to balance surface charge, potentially providing additional Brønsted-acidic sites for TMP molecules in addition to the

Lewis-acidic three-coordinated $Zn^{2+}$ ($Zn_{3c}$) sites.[22] Furthermore, owing to the high polarity of the (002) facet, the $Zn_{3c}$ sites here are more electron-deficient than those on the (100) facet, making it possible to differentiate TMP adsorption sites via XPS.

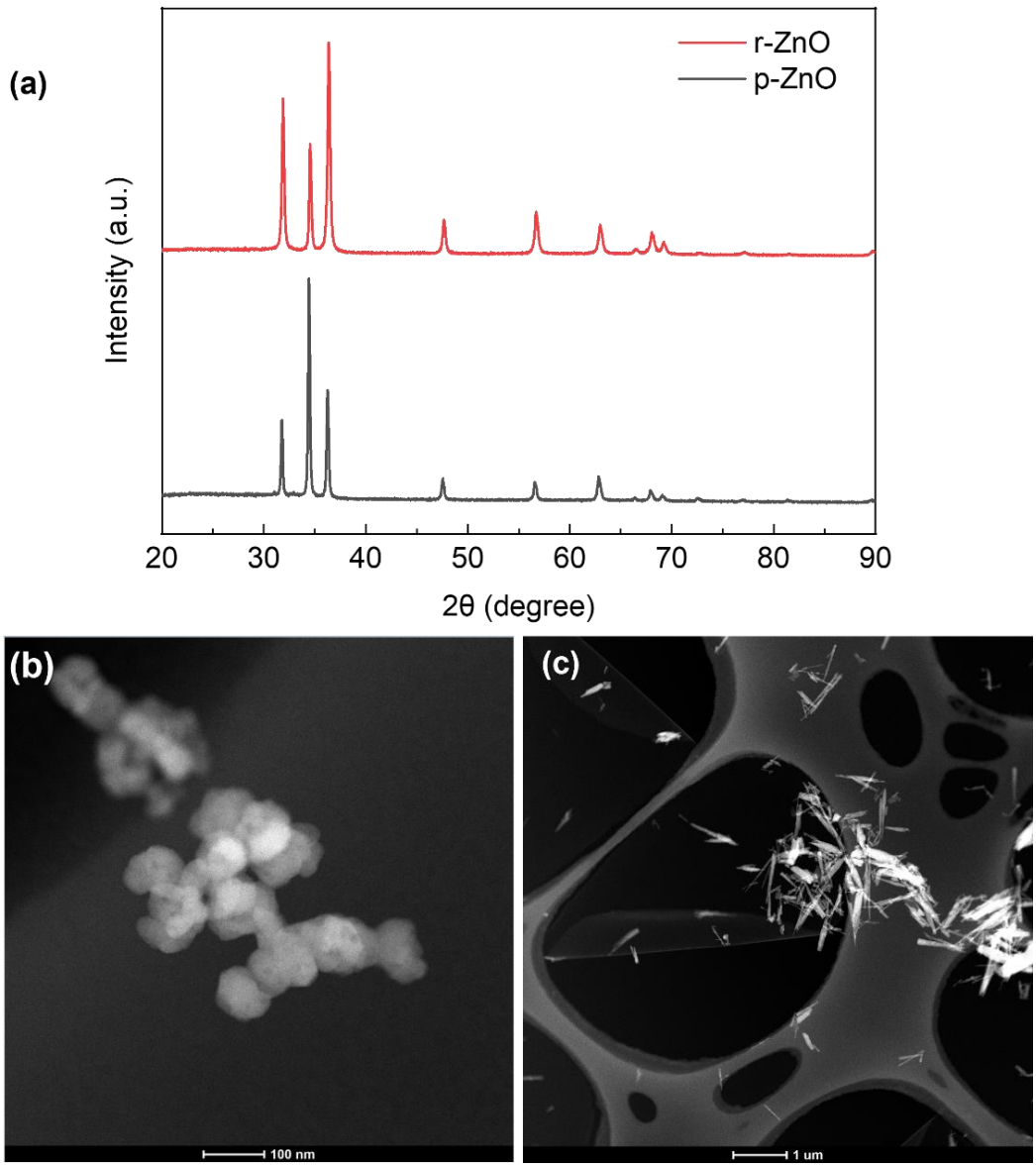



**Figure 5.11 (a)** XRD patterns of ZnO samples, revealing their wurtzite crystal structure, where p-ZnO shows a stronger (002) peak at 34° compared to r-ZnO; TEM images of **(b)** p-ZnO and **(c)** r-ZnO, respectively. TEM images in this figure were acquired by Prof. Songhua Cai.

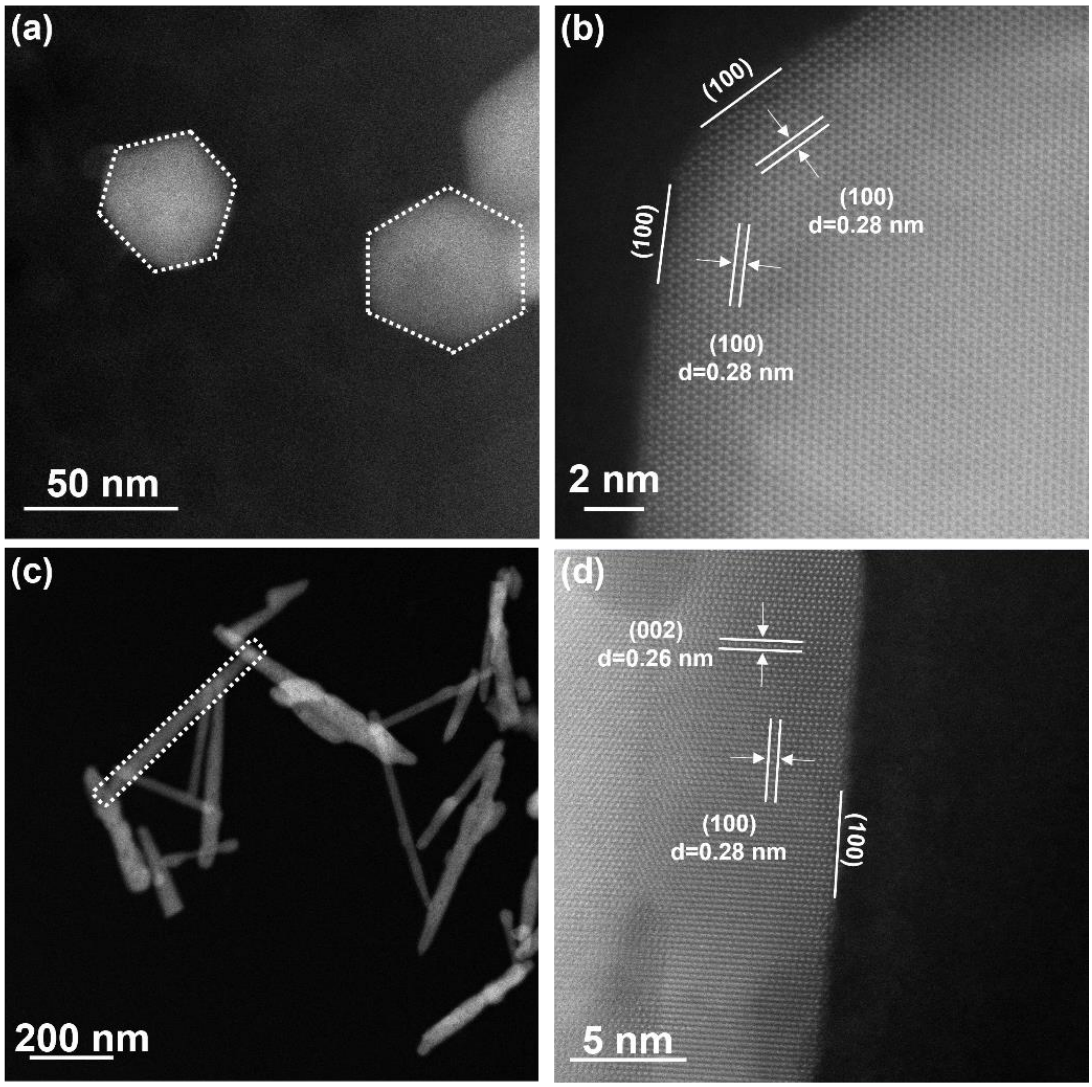



**Figure 5.12** High resolution TEM images of **(a, b)** p-ZnO and **(c, d)** r-ZnO, showing that p-ZnO is mainly enclosed by the (002) facet and r-ZnO is mainly enclosed by the (100) facet. TEM images in this figure were acquired by Prof. Songhua Cai.

The P 2p XPS spectra recorded under TMP atmosphere are presented in **Fig. 5.13**. Under the dark condition, three distinct TMP species can be observed in the P 2p XPS spectra of p-ZnO with P $2p_{3/2}$ at 132.3 eV, 131.4 eV and 130.3 eV (**Fig. 5.13a**). Based on the electron density at the adsorption sites, these species can be identified as TMP adducts formed at $Zn_{3c}$ sites on the (002) facets, $Zn_{3c}$ sites on the (100) facets and OH sites on the (002) facets, respectively. Upon photoexcitation, a positive shift of P 2p peaks from 131.4 eV to 132.7 eV is evident,

with a negative shift from 132.3 eV to 131.8 eV, indicating hole accumulation on the (001) facet of p-ZnO and electron migration to the (002) facet. Moreover, it should be noted that the BE shift of TMP adsorbed at OH group sites is negligible, suggesting insignificant electron density change under light. Interestingly, while similar behaviour can be observed for r-ZnO (**Fig. 5.13b**) that the P 2p peak at 130.3 eV (OH sites) barely responds to light, only negative shifts are seen for the P 2p peak at 132.5 eV ((002)-Zn) and 131.5 eV ((100)-Zn). This further supports that Brønsted-acidic sites are less responsive to the changes of electron density on the surface under illumination. As with b-$TiO_2$, the absence of P 2p positively shifted component in r-ZnO may result from the low (002) facet exposure, insufficient for creating a well-defined long-range driving force to achieve the facet-dependent surface charge accumulation.

Zn 2p spectra were also collected under varying experimental conditions. Under illumination, although a negative shift was expected on the Zn 2p peaks due to the increased electron density, no significant BE shifts can be found in the Zn 2p region after turning on the light (**Fig. 5.14**), likely due to instrumental limitations and the inherent lifetime broadening of the Zn $2p_{3/2}$ core level, where metallic Zn and $Zn^{2+}$ only show a 0.6 eV difference in BE.[26] Nevertheless, the distribution of surface electrons and holes generated from the XPS results is consistent with previous studies, where r-ZnO exhibited electrons accumulation on the (002) facets under illumination, while surface charge accumulation of p-ZnO was not facet-dependent.[27, 28]

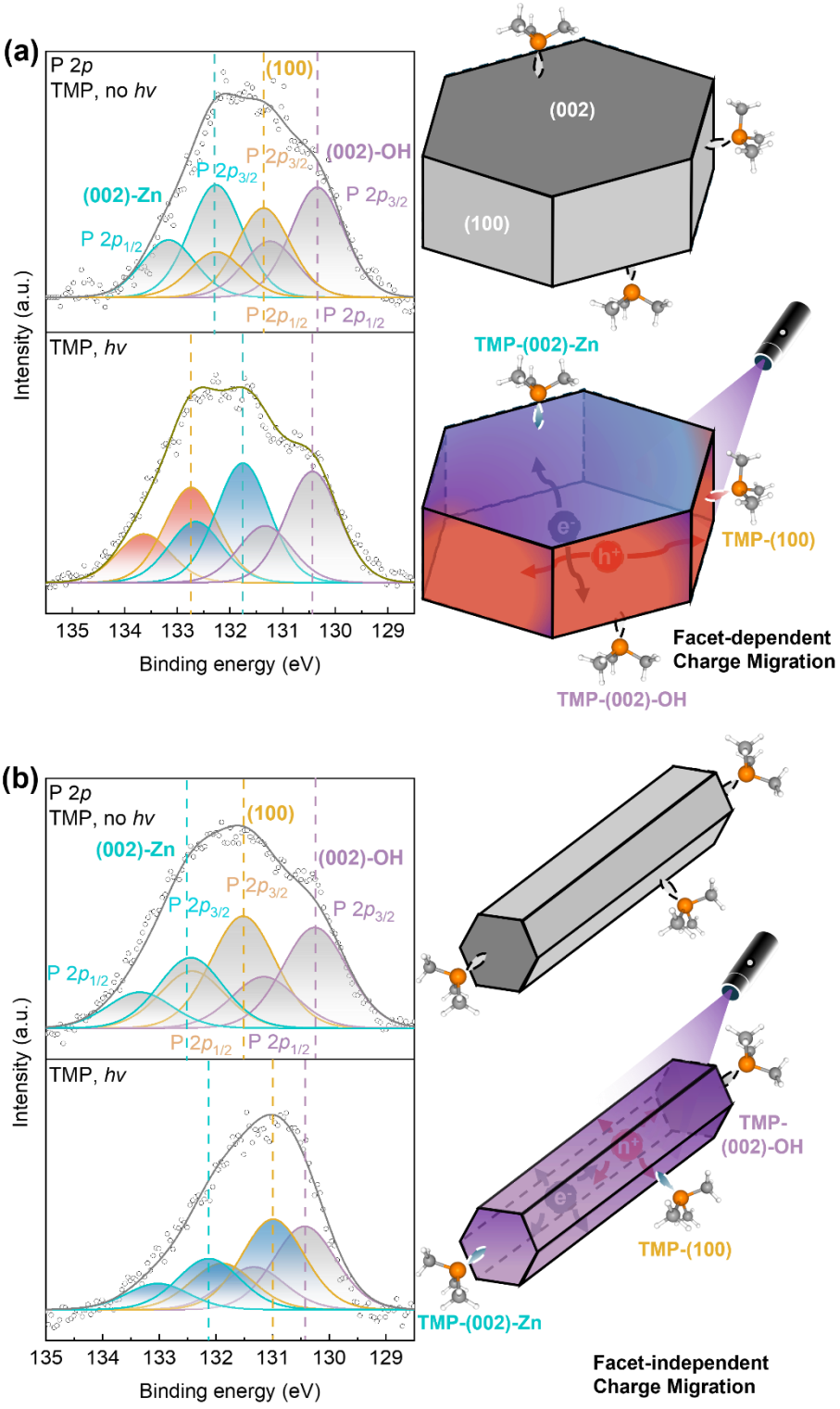



**Figure 5.13** High resolution P 2p spectra of TMP adsorbed on **(a)** p-ZnO and **(b)** r-ZnO under dark and illuminated conditions. Three components can be deconvoluted from the XPS spectra, corresponding to TMP adsorbed on Lewis-acidic (002) Zn sites and (100) Zn sites and Brønsted-acidic (002)-OH sites.

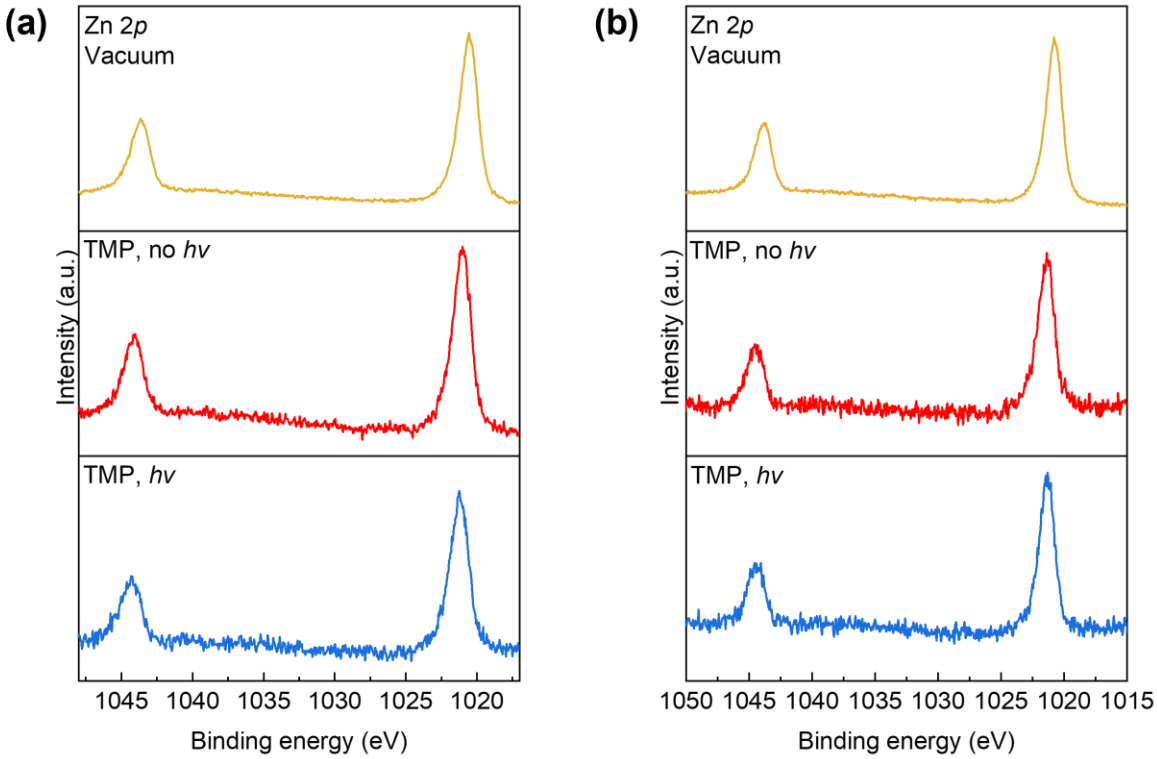



**Figure 5.14** High resolution Zn 2p spectra of **(a)** p-ZnO and **(b)** r-ZnO under different experimental conditions. Peak shifts cannot be resolved under current conditions due to low sensitivity of Zn 2p signals to electron density change.

Control experiments were conducted using MgO (**Fig. 5.15a, b**), which has a large band gap and is theoretically not light responsive. No changes in P 2p or Mg 1s spectra can be observed with and without illumination on MgO samples (**Fig. 5.15c, d**), confirming that the previous shifts of P 2p peaks under light originated from surface charge accumulation on metal oxides rather than the intrinsic light response of the TMP molecules. Furthermore, to rule out the influence of irreversible beam damage and the possibilities of photocatalytic decomposition of TMP molecules, repeat experiments were conducted. As shown in **Fig. 5.16**, it can be seen that the P 2p peaks of both c-$CeO_2$ and p-ZnO reverted fully after light was switched off, confirming that the previously observed peak shifts were not caused by the

surface catalytic reactions or beam damage on the samples, but from reversible surface electron density changes under illumination.

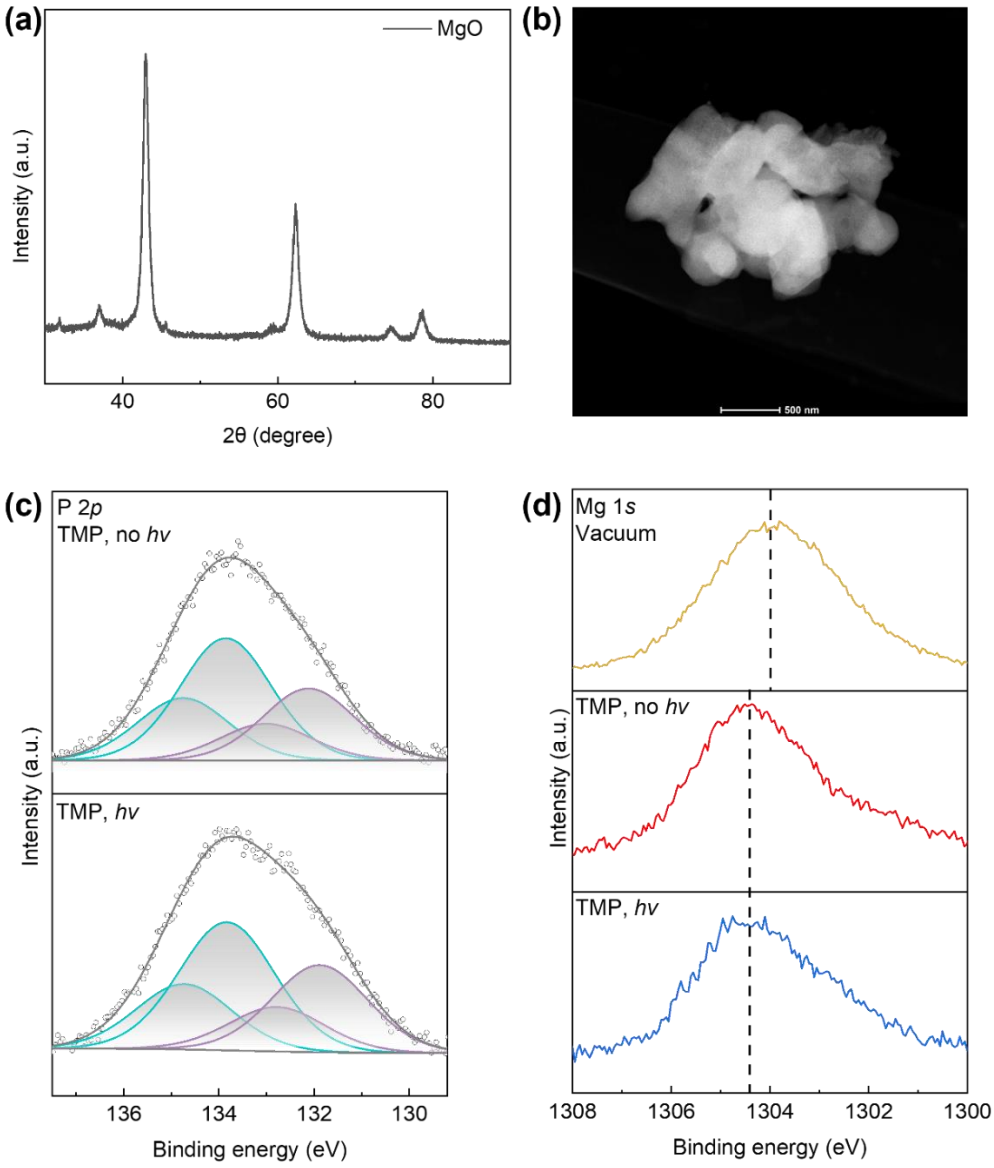



**Figure 5.15 (a)** XRD patterns of MgO; **(b)** TEM images of MgO showing a nanosheet morphology; High resolution XPS spectra of **(c)** P 2p and **(d)** Mg 1s of MgO under different experimental conditions. As MgO is not responsive to the light source, no peak shift can be observed from the spectra under various conditions. The TEM image was acquired by Prof. Songhua Cai.

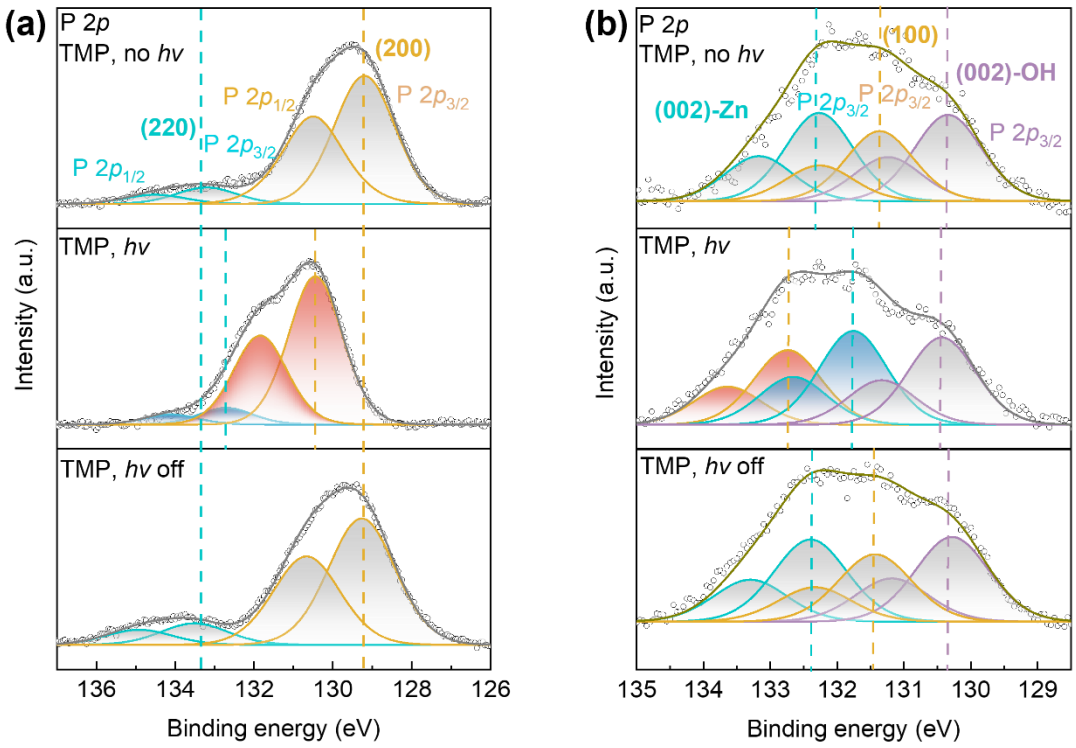



**Figure 5.16** High resolution P 2p spectra of TMP adsorbed on **(a)** c-$CeO_2$ and **(b)** p-ZnO samples in repeated light on/off tests. Peak positions could fully revert after the light was turned off. XPS measurements and data analysis of $CeO_2$ in this figure were conducted by Dr. Yiyang Li.

### 5.2.3 Photocatalytic Study: Effect of Facet-Dependent Charge Accumulation

The probe-assisted XPS study has shown that tailoring the exposed facet plays an important role in the spatial charge separation behaviour. By exposing two facets in an appropriate ratio, photo-generated holes can be detected by TMP molecules at the surface, whereas only electrons are detected in other cases. To understand the contribution of these detected holes, arising from facet-dependent charge accumulation to the photocatalytic performance, photocatalytic $O_2$ evolution tests were conducted as shown in **Fig. 5.17**. It can be observed that the rates of $O_2$ evolution are generally higher for samples exhibiting facet-dependent

surface charge accumulation than for those without. This indicates that the surface holes detected by the TMP molecules may facilitate the photo-oxidation process.

A similar trend can be observed in the lifetimes of charge carriers calculated from TRPL (**Fig. 5.18**), where the lifetime was prolonged in p-$TiO_2$ (5.015 ± 0.028 ns), c-$CeO_2$ (4.602 ± 0.031 ns) and p-ZnO (3.969 ± 0.037 ns). A longer lifetime of charge carriers generally results in better photocatalytic performance. The significant increase in the charge carrier lifetime of p-$TiO_2$, c-$CeO_2$ and p-ZnO can be attributed to efficient spatial charge separation across different facets, which further facilitates the photocatalytic reaction.

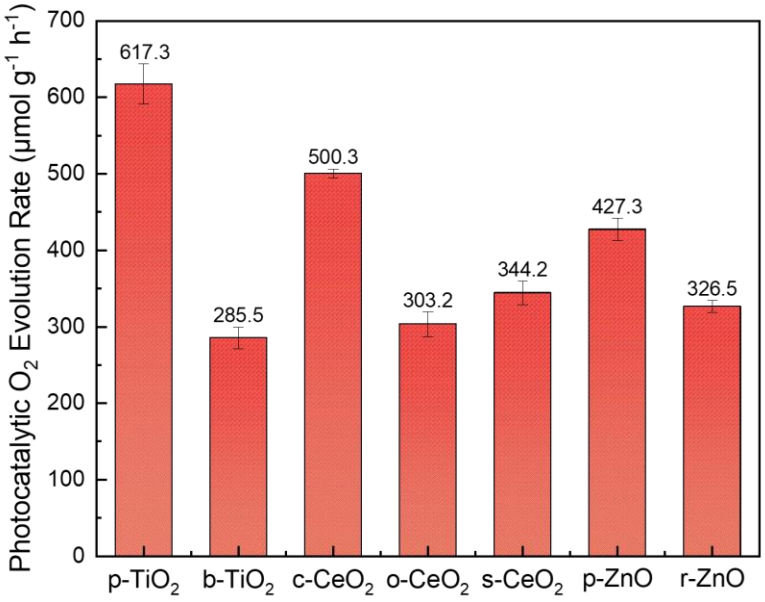



**Figure 5.17** Photocatalytic $O_2$ evolution tests of metal oxides. Samples including p-$TiO_2$, c-$CeO_2$ and p-ZnO exhibited the 'peak-splitting' feature in the P 2p XPS spectra under illumination and showed higher photocatalytic activity in $O_2$ evolution. Other samples, where only a negative shift in P 2p was observed under illumination, generally displayed lower photocatalytic activity.

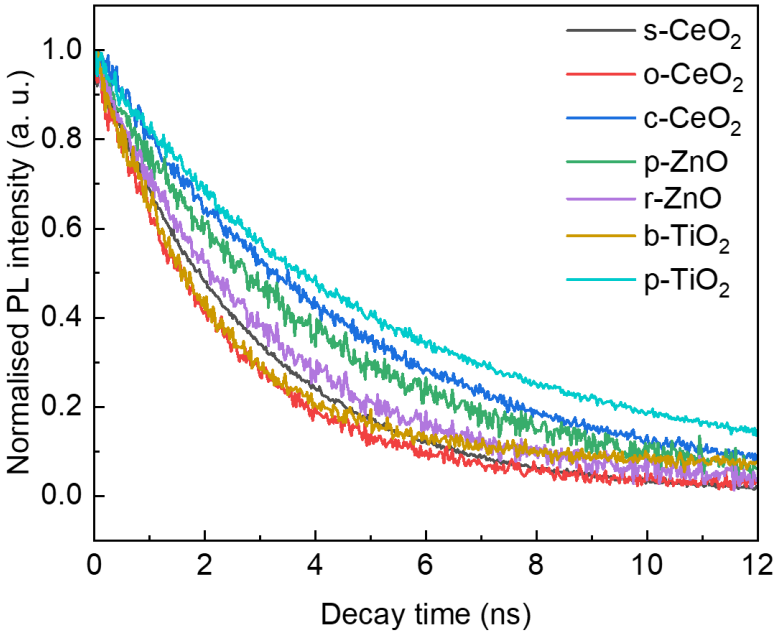



**Figure 5.18** TRPL tests of metal oxides showing the trend of charge carrier lifetimes. The trend is consistent with photocatalytic performance measurements. TRPL was measured and analysed by Dr. Yiyang Li.

However, this analysis can only provide qualitative information. For further advancement, it is essential to study the correlation between changes in BE and electron density in the P 2p signals. This could allow quantitative measurement of electron/hole densities and a better understanding of their contribution to photocatalytic activity.

### 5.2.4 Application of Ammonia as a Surface Probe

It has been shown that TMP molecules can serve as surface probes in XPS in this work for detecting surface-accumulated charges and in NMR for verifying surface acidity, as demonstrated previous studies.[23] To explore the potential of applying other molecules as surface probes for the detection of surface-accumulated charges, $NH_3$ was selected to perform further control experiments under the same conditions (room temperature, 0.2 mbar, p-$TiO_2$)

as TMP.

Similar to the phosphorus atom in TMP, the nitrogen atoms in $NH_3$ molecules also possess lone pairs of electrons, allowing them to serve as Lewis-bases and to form adducts with the acidic sites on the surface of p-$TiO_2$. **Fig. 5.19** illustrates the attempt to use $NH_3$ as a surface probe for p-$TiO_2$ under illumination by monitoring the N 1s signal. For N 1s, it only contains a singlet peak for each nitrogen-containing species. The $NH_3$ peak in the XPS spectrum appears in the shape of a singlet peak, indicating that $NH_3$ adsorption on different facets cannot be distinguished at the current resolution, which is consistent with the TMP experimental observations under dark condition.

However, under illumination, no peak splitting or shifting can be observed in the N 1s spectrum. One explanation could be that the adsorbed $NH_3$ molecules interacting with the photo-generated charges decompose rapidly into $N_2$ and $H_2$ and desorb from the surface of p-$TiO_2$, making them undetectable by XPS. Another possibility is that the interaction between the $NH_3$ molecules and the surface acidic sites is weaker than that of TMP, rendering it less sensitive to changes in surface electron density.

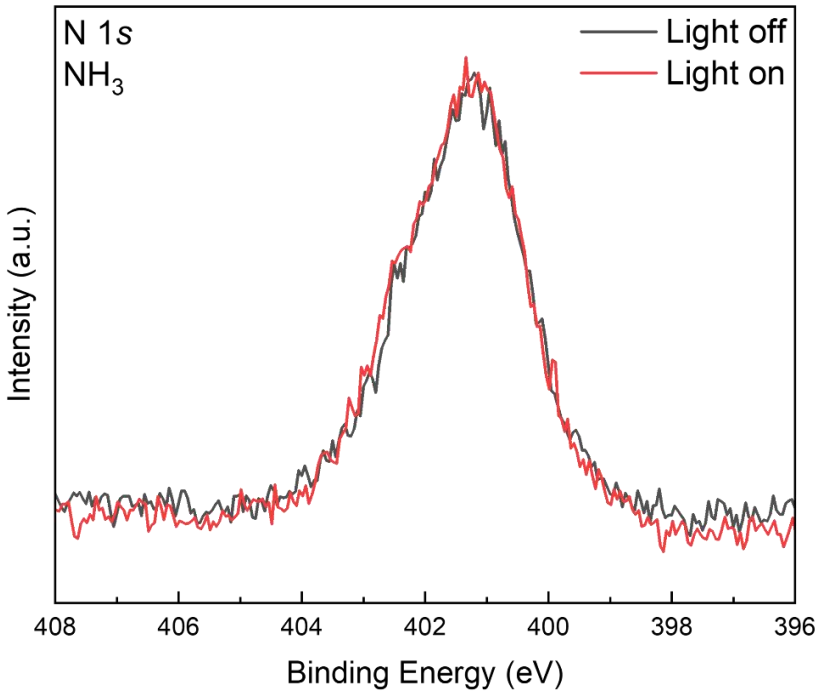



**Figure 5.19** N 1s spectra of $NH_3$ on p-$TiO_2$ with and without illumination. No peak splitting can be observed from the spectra under light.

### 5.2.5 Influence of X-ray Photon Energy on Binding Energy Shifting

As discussed, the penetration depth of X-rays in XPS makes it difficult to extract information solely from the outermost surface, as the signal is averaged over several sublayers. However, the penetration depth is also dependent on the photon energy of incident X-rays, which can be tuned using synchrotron-based XPS instruments. Theoretically, XPS signals can become more surface-sensitive applying lower X-ray photon energy. In contrast, when X-rays with higher photon energy are applied, the XPS signals can become more bulk-sensitive. From the previous investigations on the metal XPS spectra, it was observed that metal peaks shifted negatively under illumination, which might be attributed to the electron excitation into the metal orbitals. Additionally, hole creation in the valence band (oxygen orbitals) should

produce a positive shift in the O 1s spectra. To further verify whether electron density changes are more significant near the surface region under illumination, herein, Ti 2p and O 1s spectra of p-$TiO_2$ were monitored under various photon energies of X-rays. As illustrated in **Fig. 5.20**, measurements were conducted with and without illumination, with varied photon energies from 650 eV to 1300 eV. The spectra collected using the 650 eV photon energy show the highest negative shift under illumination. The negative shift was gradually diminished as photon energy increased. With 1300 eV photon energy applied, the shift under light became almost negligible. A similar trend is observed in O 1s spectra with photon energies varied from 730 eV to 1300 eV (**Fig. 5.21**), where the positive shift is the largest at 650 eV photon energy and this positive BE shift decreases to a minimum using the highest 1300 eV photon energy.

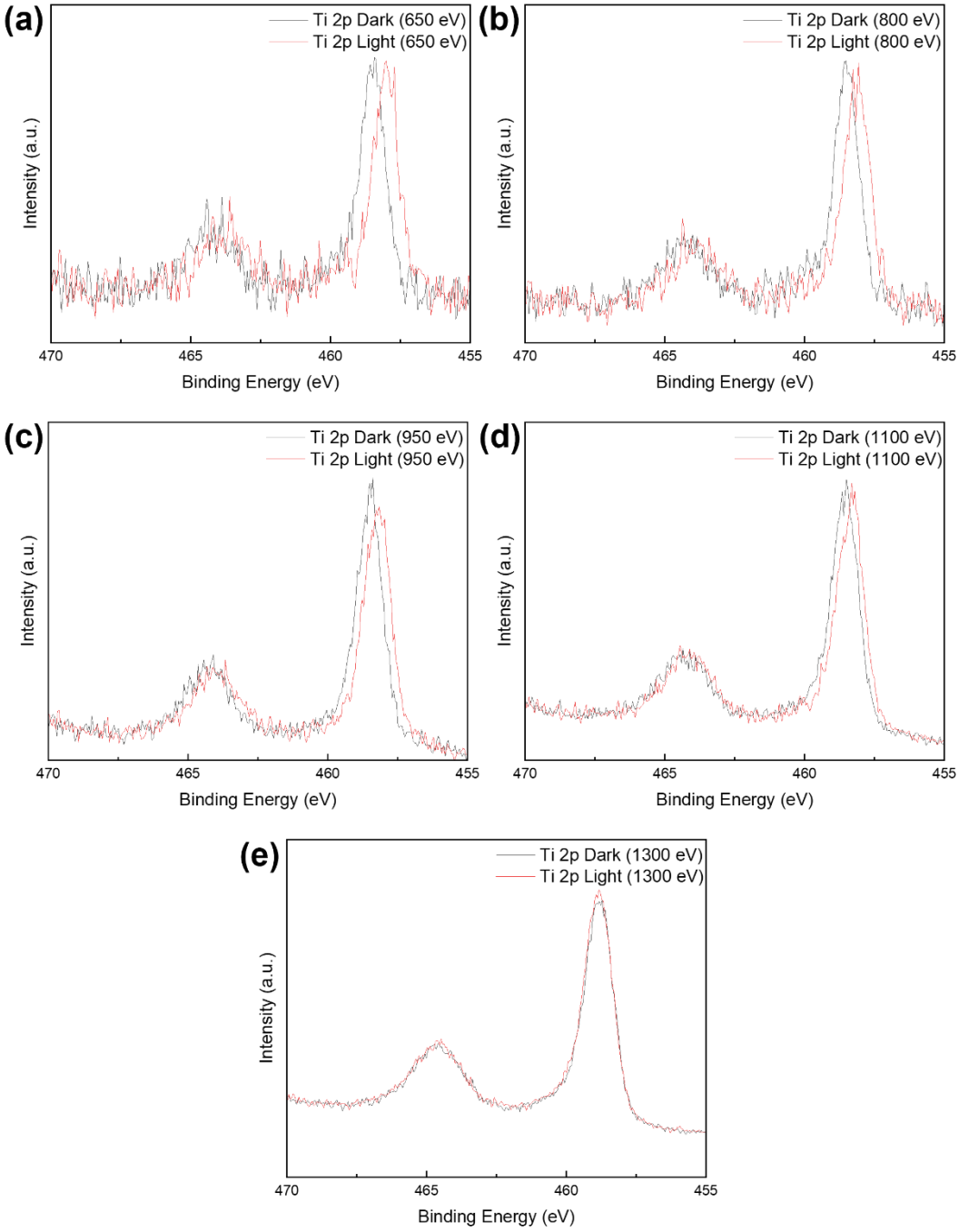



**Figure 5.20** Ti 2p XPS spectra under dark and illuminated conditions at X-ray photon energies of **(a)** 650 eV; **(b)** 800 eV; **(c)** 950 eV; **(d)** 1100 eV and **(e)** 1300 eV. A negative shift in BE can be observed under illumination, decreasing with increasing photon energy.

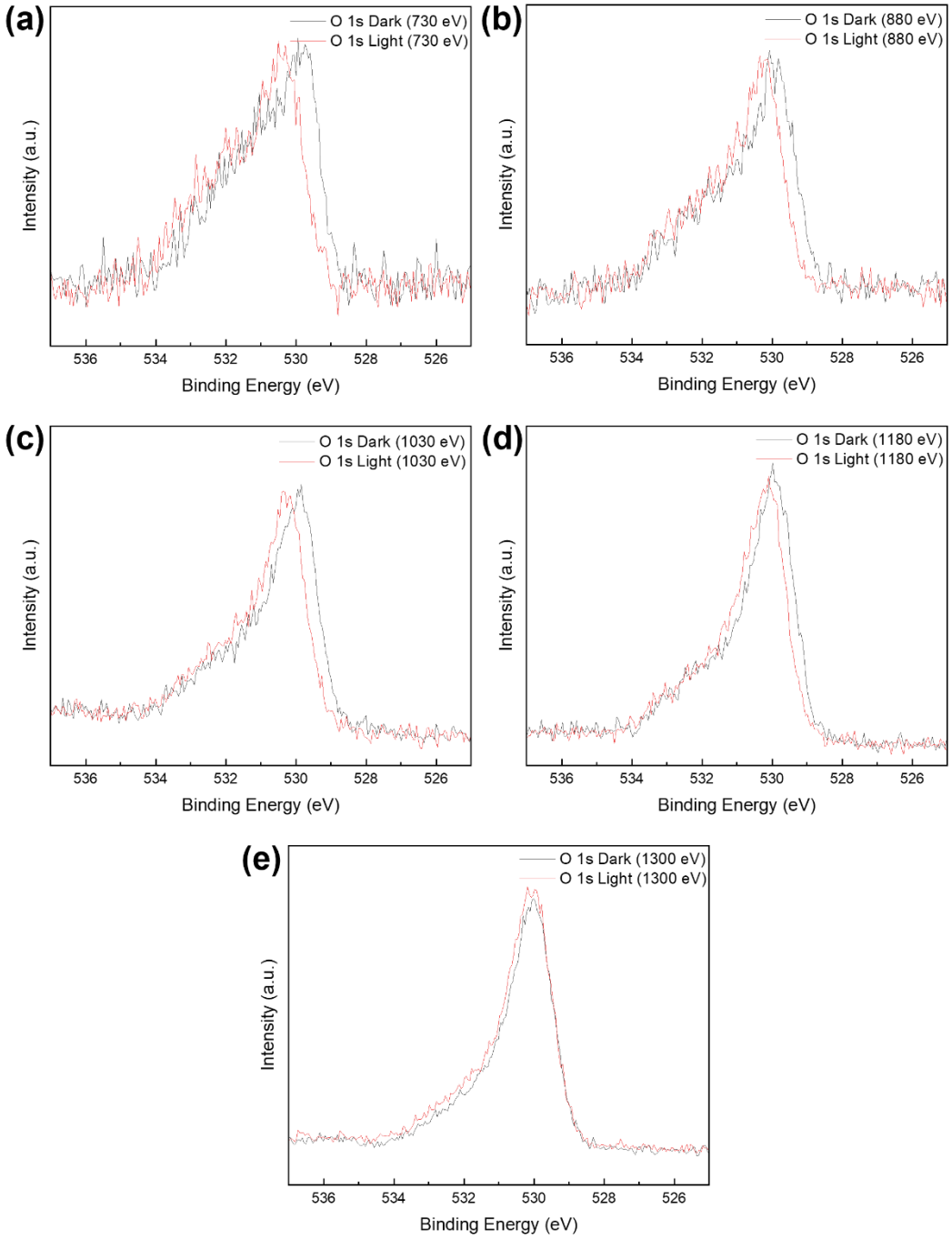



**Figure 5.21** O 1s XPS spectra under dark and illumination at X-ray photon energies of **(a)** 730 eV; **(b)** 880 eV; **(c)** 1030 eV; **(d)** 1180 eV and **(e)** 1300 eV. A positive shift in BE can be observed after turning on the light, with decreasing magnitude at higher photon energies, consistent with the Ti 2p results.

As discussed, XPS signals are more bulk-sensitive at higher photon energies and become more surface-sensitive at lower photon energies. The results from Ti 2p and O 1s suggest that electron density changes upon illumination are more pronounced near the surface than in the bulk. This further underscores the importance of using surface probes with high sensitivity to surface electron density changes.

Additionally, it is worth noting that the signal-to-noise ratio is also affected by the X-ray photon energy. One of the main reasons is that, with lower photon energy, fewer electrons can be collected by the XPS detector, and when the photon energy is too close to the BE of the orbital of interest, the signal-to-noise ratio becomes too poor to determine the precise peak positions.

Interestingly, a near-linear correlation can be found between the X-ray photon energy and the Ti 2p and O 1s peak shifts as shown in **Fig. 5.22**. This suggests that electron density changes from surface to bulk correlate positively with penetration depth. For future research, similar photon energy-dependent XPS studies should be conducted on TMP-adsorbed metal oxide surfaces. Theoretically, as TMP molecules can only exist at the outermost surface, the P 2p signal should remain unaffected by changes in penetration depth, and thus, varying X-ray photon energy should not influence P 2p peak shifts under illumination.

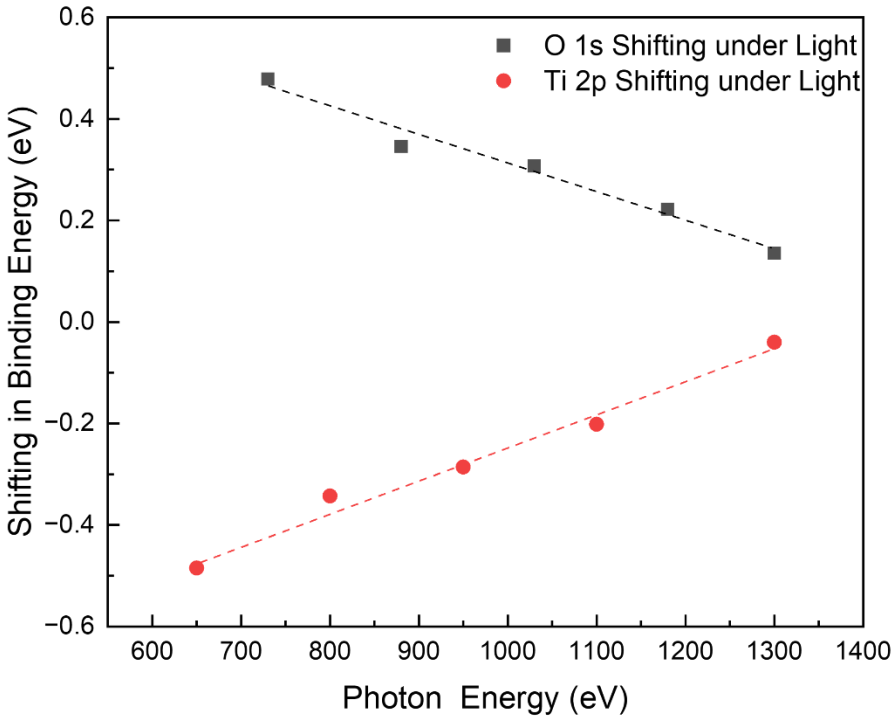



**Figure 5.22** Correlation between XPS peak shift under illumination and X-ray photon energy. A linear-like trend suggests a strong link between surface-to-bulk electron density gradients and X-ray penetration depth which is controlled by the photon energy.

### 5.3 Conclusion

In conclusion, the novel TMP-probed XPS technique enables detection of facet-dependent surface charge accumulation in nano-sized catalysts. The role of anisotropic surface structures, created by co-exposed facets, in facilitating facet-dependent charge accumulation has been investigated. It was demonstrated that the anisotropic surface structure created by exposing two different facets in a suitable ratio could result in facet-dependent charge migration, evidenced by the simultaneous positive and negative shifts of P 2p peaks under illumination. With facet-dependent charge migration, the lifetime of charge carriers was prolonged, resulting in higher photocatalytic activity. The results corroborate the facet-

dependent surface charge accumulation model, and this approach may be applicable to other faceted semiconductors, providing valuable guidance for designing novel photocatalysts for future advanced applications.

In the next chapter, a summary of the thesis will be presented, as well as an outlook on future investigations.

## 5.4 References


1. M. Núñez, J. L. Lansford and D. G. Vlachos, Optimization of the facet structure of transition-metal catalysts applied to the oxygen reduction reaction, *Nat. Chem.*, 2019, **11**, 449-456.
2. C.-Y. Chiu, Y. Li, L. Ruan, X. Ye, C. B. Murray and Y. Huang, Platinum nanocrystals selectively shaped using facet-specific peptide sequences, *Nat. Chem.*, 2011, **3**, 393-399.
3. L. Jiang, K. Liu, S.-F. Hung, L. Zhou, R. Qin, Q. Zhang, P. Liu, L. Gu, H. M. Chen, G. Fu and N. Zheng, Facet engineering accelerates spillover hydrogenation on highly diluted metal nanocatalysts, *Nat. Nanotechnol.*, 2020, **15**, 848-853.
4. P. A. Morris Hotsenpiller, J. D. Bolt, W. E. Farneth, J. B. Lowekamp and G. S. Rohrer, Orientation Dependence of Photochemical Reactions on $TiO_2$ Surfaces, *J. Phys. Chem. B*, 1998, **102**, 3216-3226.
5. J. B. Lowekamp, G. S. Rohrer, P. A. Morris Hotsenpiller, J. D. Bolt and W. E. Farneth, Anisotropic Photochemical Reactivity of Bulk $TiO_2$ Crystals, *J. Phys. Chem. B*, 1998, **102**, 7323-7327.
6. T. Ohno, K. Sarukawa and M. Matsumura, Crystal faces of rutile and anatase $TiO_2$ particles and their roles in photocatalytic reactions, *New J. Chem.*, 2002, **26**, 1167-1170.
7. R. Li, F. Zhang, D. Wang, J. Yang, M. Li, J. Zhu, X. Zhou, H. Han and C. Li, Spatial separation of photogenerated electrons and holes among {010} and {110} crystal facets of $BiVO_4$, *Nat. Commun.*, 2013, **4**, 1432.

8. T. Tachikawa, S. Yamashita and T. Majima, Evidence for Crystal-Face-Dependent $TiO_2$ Photocatalysis from Single-Molecule Imaging and Kinetic Analysis, *J. Am. Chem. Soc.*, 2011, **133**, 7197-7204.
9. J. B. Sambur, T.-Y. Chen, E. Choudhary, G. Chen, E. J. Nissen, E. M. Thomas, N. Zou and P. Chen, Sub-particle reaction and photocurrent mapping to optimize catalyst-modified photoanodes, *Nature*, 2016, **530**, 77-80.
10. J. Yu, J. Low, W. Xiao, P. Zhou and M. Jaroniec, Enhanced Photocatalytic $CO_2$-Reduction Activity of Anatase $TiO_2$ by Coexposed {001} and {101} Facets, *J. Am. Chem. Soc.*, 2014, **136**, 8839-8842.
11. R. Chen, S. Pang, H. An, J. Zhu, S. Ye, Y. Gao, F. Fan and C. Li, Charge separation via asymmetric illumination in photocatalytic $Cu_2O$ particles, *Nat. Energy*, 2018, **3**, 655-663.
12. R. Chen, Z. Ren, Y. Liang, G. Zhang, T. Dittrich, R. Liu, Y. Liu, Y. Zhao, S. Pang, H. An, C. Ni, P. Zhou, K. Han, F. Fan and C. Li, Spatiotemporal imaging of charge transfer in photocatalyst particles, *Nature*, 2022, **610**, 296-301.
13. R. Chen, F. Fan and C. Li, Unraveling Charge-Separation Mechanisms in Photocatalyst Particles by Spatially Resolved Surface Photovoltage Techniques, *Angew. Chem. Int. Ed.*, 2022, **61**, e202117567.
14. C. A. Mesa, L. Francàs, K. R. Yang, P. Garrido-Barros, E. Pastor, Y. Ma, A. Kafizas, T. E. Rosser, M. T. Mayer, E. Reisner, M. Grätzel, V. S. Batista and J. R. Durrant, Multihole water oxidation catalysis on haematite photoanodes revealed by operando spectroelectrochemistry and DFT, *Nat. Chem.*, 2020, **12**, 82-89.
15. M. Salmeron and R. Schlögl, Ambient pressure photoelectron spectroscopy: A new tool for surface science and nanotechnology, *Surf. Sci. Rep.*, 2008, **63**, 169-199.
16. K. A. Stoerzinger, W. T. Hong, E. J. Crumlin, H. Bluhm and Y. Shao-Horn, Insights into Electrochemical Reactions from Ambient Pressure Photoelectron Spectroscopy, *Acc. Chem. Res.*, 2015, **48**, 2976-2983.
17. K. Murugappan, E. M. Anderson, D. Teschner, T. E. Jones, K. Skorupska and Y. Román-Leshkov, Operando NAP-XPS unveils differences in $MoO_3$ and $Mo_2C$ during

hydrodeoxygenation, *Nat. Catal.*, 2018, **1**, 960-967.

18. P. Amann, B. Klötzer, D. Degerman, N. Köpfle, T. Götsch, P. Lömker, C. Rameshan, K. Ploner, D. Bikaljevic, H.-Y. Wang, M. Soldemo, M. Shipilin, C. M. Goodwin, J. Gladh, J. Halldin Stenlid, M. Börner, C. Schlueter and A. Nilsson, The state of zinc in methanol synthesis over a Zn/ZnO/Cu(211) model catalyst, *Science*, 2022, **376**, 603-608.
19. X. Liu, G. Dong, S. Li, G. Lu and Y. Bi, Direct Observation of Charge Separation on Anatase $TiO_2$ Crystals with Selectively Etched {001} Facets, *J. Am. Chem. Soc.*, 2016, **138**, 2917-2920.
20. Z. Tan, G. Li, H.-L. Chou, Y. Li, X. Yi, A. H. Mahadi, A. Zheng, S. C. Edman Tsang and Y.-K. Peng, Differentiating Surface Ce Species among $CeO_2$ Facets by Solid-State NMR for Catalytic Correlation, *ACS Catal.*, 2020, **10**, 4003-4011.
21. J. H. Lunsford, P. N. Tutunjian, P. J. Chu, E. B. Yeh and D. J. Zalewski, Solid-state NMR study using trimethylphosphine as a probe of acid sites in normal and dealuminated zeolite Y, *J. Phys. Chem.*, 1989, **93**, 2590-2595.
22. Y.-K. Peng, L. Ye, J. Qu, L. Zhang, Y. Fu, I. F. Teixeira, I. J. McPherson, H. He and S. C. E. Tsang, Trimethylphosphine-Assisted Surface Fingerprinting of Metal Oxide Nanoparticle by $^{31}P$ Solid-State NMR: A Zinc Oxide Case Study, *J. Am. Chem. Soc.*, 2016, **138**, 2225-2234.
23. Y.-K. Peng, Y. Hu, H.-L. Chou, Y. Fu, I. F. Teixeira, L. Zhang, H. He and S. C. E. Tsang, Mapping surface-modified titania nanoparticles with implications for activity and facet control, *Nat. Commun.*, 2017, **8**, 675.
24. X. Wang, Z. Jiang, B. Zheng, Z. Xie and L. Zheng, Synthesis and shape-dependent catalytic properties of $CeO_2$ nanocubes and truncated octahedra, *CrystEngComm*, 2012, **14**, 7579-7582.
25. J. M. Kahk and J. Lischner, Core electron binding energies of adsorbates on Cu(111) from first-principles calculations, *Phys. Chem. Chem. Phys.*, 2018, **20**, 30403-30411.
26. M. C. Biesinger, B. P. Payne, A. P. Grosvenor, L. W. M. Lau, A. R. Gerson and R. S. C. Smart, Resolving surface chemical states in XPS analysis of first row transition

metals, oxides and hydroxides: Cr, Mn, Fe, Co and Ni, *Appl. Surf. Sci.*, 2011, **257**, 2717-2730.

27. X. Wang, W. Wang, Y. Miao, G. Feng and R. Zhang, Facet-selective photodeposition of gold nanoparticles on faceted ZnO crystals for visible light photocatalysis, *J. Colloid Interface Sci.*, 2016, **475**, 112-118.

28. C. G. Read, E. M. P. Steinmiller and K.-S. Choi, Atomic Plane-Selective Deposition of Gold Nanoparticles on Metal Oxide Crystals Exploiting Preferential Adsorption of Additives, *J. Am. Chem. Soc.*, 2009, **131**, 12040-12041.

# Chapter 6 Conclusions and Outlook

## 6.1 Conclusions

This thesis has explored the application of surface engineering strategies to the transition metal oxides ($TiO_2$, ZnO and $CeO_2$) and the transition metal dichalcogenide ($WS_2$) for photocatalysis. As the current bottleneck in this research field is the poor photocatalytic performance, the goal was to investigate how surface engineering contributes to reactivity, based on structural and property modifications. This may provide guidelines for the future designing of next-generation photocatalysts for industrial-scale applications.

Starting from single-atom doping, the effects of introducing single-atom sites on $WS_2$ nanosheets and fabricating 2D-2D heterojunctions between $WS_2$ and $TiO_2$ photocatalysts were investigated. Subsequently, the structural transformation of $WS_2$ on the $TiO_2$ support was systematically studied to understand the catalytic impact of $WS_2$ nanosheets converting into tungsten single-atom sites. Following that, a surface-tailoring strategy was applied to transition metal oxide samples for the detection of surface-accumulated charges under illumination using a novel probe-assisted XPS technique. Various characterisation methods were employed to study the structure of surface-engineered photocatalysts, thereby enhancing further understanding of the structure-reactivity correlation.

After presenting the research background, current challenges and experimental details in Chapter 1 and 2, Chapter 3 focused on the possibilities of using FL-$WS_2$ for photocatalysis through single-atom doping and heterojunction formation. It was found that FL-$WS_2$ was 8.86 times more reactive than its bulk counterpart in photocatalytic $H_2$ evolution. Then, various d-block metals were introduced into FL-$WS_2$ as single-atom dopants, with Ru doped

FL-$WS_2$ exhibiting the highest reactivity, 2.14 times greater than pristine FL-$WS_2$. Based on the results, structural characterisations were conducted on Ru doped FL-$WS_2$. Structural characterisation via TEM and EXAFS confirmed the presence of single-atom Ru sites at the interlayer region of FL-$WS_2$. This configuration might facilitate interlayer charge transfer, contributing to improved photocatalytic performance. Furthermore, the role of FL-$WS_2$ as a cocatalysts in a 2D-2D heterojunction with $TiO_2$ was investigated. After confirming the structure of $WS_2$- $TiO_2$ by applying electron microscopy, a strong built-in electric field at the interface between $TiO_2$ and $WS_2$ was revealed by XPS, which facilitated the charge separation process. As a result of this strong interaction between $WS_2$ and $TiO_2$, the photocatalytic $H_2$ evolution rate of pristine f-$TiO_2$ was enhanced by a factor of 4.60 when coupled with FL-$WS_2$.

Chapter 4 examined the structural change of $WS_2$ nanosheets attached to the $TiO_2$ support. It was revealed by TEM images that FL-$WS_2$ could transform from 2D nanosheets into tungsten single-atom sites adsorbed onto the $TiO_2$ support. XPS confirmed the loss of sulphur atoms and complete oxidation of $W^{4+}$ (FL-$WS_2$) into $W^{5+}$ and $W^{6+}$ species (tungsten single-atom sites). Further investigation on EPR suggested that abundant $O_v$ sites were created during this process, which might be attributed to the oxidation of $WS_2$ and the concurrent evolution of $SO_2$. Additionally, tungsten atoms were predominantly attached to the exposed (001) facet of anatase of $TiO_2$, causing high lattice strain, whereas tungsten atoms and lattice distortion were absent on other exposed facets including (111) and (010) facets. Besides these structural changes, W atoms increased visible-light absorption and narrowed band gap of W-$TiO_2$ compared to pristine f-$TiO_2$. Furthermore, EIS and TRPL showed decreased charge transfer

resistance and prolonged charge carrier lifetimes, respectively, which might be associated with the high photocatalytic performance, where the $H_2$ evolution rate was increased up to 9.40 times using W-$TiO_2$ compared to f-$TiO_2$.

In Chapter 5, a novel TMP-probe-assisted XPS technique was developed to study facet-dependent charge accumulation under illumination using surface-tailored metal oxides ($CeO_2$, $TiO_2$, and ZnO) as models. $CeO_2$ samples with different types and numbers of exposed facets were used to study the effect of anisotropic surface structures on surface charge accumulation. The results suggested that it was essential to have more than one types of exposed facets to achieve facet-dependant charge accumulation, as observed in c-$CeO_2$ with (220) and (200) facets exposed. In contrast, for samples with a single exposed facet (o-$CeO_2$ with (111)) or an amorphous facet (s-$CeO_2$), charge migration was found to be facet-independent. $TiO_2$ and ZnO samples were used to illustrate how the proportion of exposed facets affects charge migration. It was found that although facet-dependent charge accumulation could be achieved for samples with two exposed facets, the driving force was weakened with an inappropriate ratio between the two exposed facets. Samples with photo-generated electrons and holes accumulated on different facets exhibited longer lifetimes of charge carriers and higher photocatalytic $O_2$ evolution rates, highlighting the contributions from exposed facets on particulate photocatalysis.

Overall, the successful application of appropriate surface engineering strategies generally led to enhanced photocatalytic performance. It is important to conduct systematic studies on the structure of surface-engineered catalysts using edge-cutting characterisation techniques, assisting understanding on how surface modifications influence material properties and

reactivity. In conclusion, the potential application of ultrathin $WS_2$ nanosheets as photocatalysts through single-atom doping, and as cocatalysts via heterojunction formation, has been explored. It was found that the introduced Ru atoms could reside within the interlayer region of $WS_2$ rather than being exposed on the surface, facilitating the charge transfer process. When acting as cocatalysts for $TiO_2$, a built-in electric field was constructed, boosting $H_2$ evolution. The structural change of $WS_2$ on the $TiO_2$ support was also studied, where the formation of tungsten single atoms was found with the decomposition of $WS_2$. Furthermore, a TMP-assisted XPS technique probing the charge distribution on metal oxides was developed which could provide a novel way to understand the charge migration process affected by exposed facets. These findings may guide the future design of next generation photocatalysts for potential large-scale industrial applications.

## 6.2 Outlook

Although 2D transition metal dichalcogenides have been widely used and studied as catalysts, their applications in chemical industry remains controversial due to low stability.[1, 2] Surface modification has been shown to enhance the reactivity of FL-$WS_2$, yet its overall performance was still much poorer than traditional photocatalysts such as $TiO_2$. In heterojunction systems, FL-$WS_2$ demonstrated more promising results as a cocatalyst rather than as a standalone catalyst. However, as discussed, the long-term stability of FL-$WS_2$ as well as other transition metal dichalcogenides remains an open question.[3]

Applying FL-$WS_2$ to synthesise of tungsten single-atom doped $TiO_2$ offers another pathway for the application of transition metal dichalcogenides. This method can simultaneously introduce tungsten single atoms and $O_v$ on the $TiO_2$ surface. The photocatalytic contribution

of this structural change can be further explored through computational modelling. Additionally, this synthesis strategy may be extended to other materials beyond $TiO_2$. Since tungsten sites are generally believed to enhance surface acidity, tungsten-doped materials could be useful in various photocatalytic reactions, such as pollutant degradation and microplastic conversion.[4, 5] Control experiments comparing this method to previously reported techniques for W single-atom doping should be carried out to determine which approach best maximises photocatalytic performance (*e.g.* HER rate and AQY) and to clarify the strengths of each.[6]

Regarding TMP-assisted XPS, current results demonstrate its feasibility for studying the charge distribution. For further development, besides TMP and ammonia, more Lewis-basic probe molecules can be tested to find a cheaper and less toxic substitution. Additionally, more samples with varying proportions of exposed facets, while keeping the facet types unchanged, should be tested to systematically evaluate the effect of anisotropic structure on the charge separation process. The wavelength and intensity of illumination could also be tuned to investigate their correlation with XPS signal changes. Moreover, besides tuning the ratio of exposed facets, other surface modifications such as cocatalyst loading could be introduced to assess their influence on surface charge accumulation.[7] Theoretical modelling would support deeper understanding of the electron density changes in probe molecules in the presence of photo-generated charge carriers. If a relationship between changes in electron density and BE is established, it may become possible to quantitatively determine the number of surface accumulated electrons/holes under illumination. This would enable determining the correlation of surface charge density with photocatalytic activity. Last but not least, as the

current resolution is still limited by the sensitivity of NAP-XPS, combining the probing technique with other characterisation tools, such as nuclear magnetic resonance, could provide improved peak deconvolution and broaden the technique's application to more complex systems.[8]

## 6.3 References


1. S. Park, A. T. Garcia-Esparza, H. Abroshan, B. Abraham, J. Vinson, A. Gallo, D. Nordlund, J. Park, T. R. Kim, L. Vallez, R. Alonso-Mori, D. Sokaras and X. Zheng, Operando Study of Thermal Oxidation of Monolayer $MoS_2$, *Adv. Sci.*, 2021, **8**, 2002768.
2. J. Gao, B. Li, J. Tan, P. Chow, T.-M. Lu and N. Koratkar, Aging of Transition Metal Dichalcogenide Monolayers, *ACS Nano*, 2016, **10**, 2628-2635.
3. J. C. Kotsakidis, Q. Zhang, A. L. Vazquez de Parga, M. Currie, K. Helmerson, D. K. Gaskill and M. S. Fuhrer, Oxidation of Monolayer $WS_2$ in Ambient Is a Photoinduced Process, *Nano Lett.*, 2019, **19**, 5205-5215.
4. C. Wang, S. Yang, H. Chang, Y. Peng and J. Li, Dispersion of tungsten oxide on SCR performance of $V_2O_5WO_3/TiO_2$: Acidity, surface species and catalytic activity, *Chem. Eng. J.*, 2013, **225**, 520-527.
5. G. Zhou, H. Xu, H. Song, J. Yi, X. Wang, Z. Chen and X. Zhu, Photocatalysis toward Microplastics Conversion: A Critical Review, *ACS Catal.*, 2024, **14**, 8694-8719.
6. Y. Wang, X. Li, M. Zhang, J. Zhang, Z. Chen, X. Zheng, Z. Tian, N. Zhao, X. Han, K. Zaghib, Y. Wang, Y. Deng and W. Hu, Highly Active and Durable Single-Atom Tungsten-Doped $NiS_{0.5}Se_{0.5}$ Nanosheet@$NiS_{0.5}Se_{0.5}$ Nanorod Heterostructures for Water Splitting, *Adv. Mater.*, 2022, **34**, 2107053.
7. R. Chen, Z. Ren, Y. Liang, G. Zhang, T. Dittrich, R. Liu, Y. Liu, Y. Zhao, S. Pang, H. An, C. Ni, P. Zhou, K. Han, F. Fan and C. Li, Spatiotemporal imaging of charge transfer in photocatalyst particles, *Nature*, 2022, **610**, 296-301.
8. S.-J. Hwang, C. Petucci and D. Raftery, In Situ Solid-State NMR Studies of Trichloroethylene Photocatalysis: Formation and Characterization of Surface-Bound

Intermediates, *J. Am. Chem. Soc.*, 1998, **120**, 4388-4397.

# Appendix

**Table A1 Summary of recent studies of single-atom engineering**

| Material | Dopant (wt%) | Sacrificial Regent | $H_2$ Evolution Rate (mmol $h^{-1}$ $g^{-1}$) | Light Source | Reference |
|---|---|---|---|---|---|
| g-$C_3N_4$ | 1% Ag | 30% methanol | 0.498 | 300W Xeon lamp | 1 |
| g-$C_3N_4$ | 0.26% Ce | 10% TEOA | 33.5 (AQY = 58.6% at 365 nm) | 300W Xeon lamp (UV-cut-off) | 2 |
| $TiO_2$ | 1.5% Cu | 66% methanol | 101.7 (AQY = 45.5% at 340 nm) | 300W Xeon lamp | 3 |
| $TiO_2$ | 0.2% Pt | 30% methanol | 0.1696 | UV-Vis irradiation | 4 |
| $TiO_2$ | 0.125% Pd | 25% methanol | 24.59 (AQY = 23.4 % at 365 nm) | 300W Xeon lamp | 5 |
| CdS | 0.383% Pd | 15% TEOA | 8.402 (AQY = =33.92% at 420 nm) | 300W Xeon lamp | 6 |
| CdS | 3.18% Co | Lactic acid (pH=5) | 60.10 (AQY = 57.6% at 500 nm) | 300W Xenon lamp (AM 1.5G filter) | 7 |
| CdS | 0.91% Pt | 15% TEOA | 6.35 (AQY = 25.7% at 500 nm) | 300W Xeon lamp | 8 |

**Table A2 Summary of recent studies of heterojunction engineering**

| Material | Type | Sacrificial Regent | $H_2$ Evolution Rate (mmol $h^{-1}$ $g^{-1}$) | Light Source | Reference |
|---|---|---|---|---|---|
| $WS_2/TiO_2$ | Schottky junction | 25% methanol | 2.57 | 300W Xenon lamp (AM 1.5G filter) | 9 |
| CdS-fullerene/graphene | Schottky junction | 25% methanol | 0.1272 (AQY = 7.24% at 420 nm) | LEDs lamps ($\lambda$ = 420 nm) | 10 |
| $SrTiO_3$:Al/$Cd_{0.6}Zn_{0.4}S$ | Type-II | 0.25M $Na_2S$ and 0.35M $Na_2SO_3$ | 3.55 (STH = 2.63%) | 300W Xenon lamp (AM 1.5G filter) | 11 |
| g-$C_3N_4$/P25(N)-Pd | Type-II | 10% TEOA | 6.33 (AQY = 3.98% at 420 nm) | 300W Xenon lamp | 12 |
| CdS/$Cu_9S_5$ | p-n junction | 0.25M $Na_2S$ and 0.35M | 0.0027 (AQY = 4.4% at 1100 nm) | 300W Xenon lamp (UV-Vis | 13 |

| | | $Na_2SO_3$ | | filter, λ > 800 nm) | |
|---|---|---|---|---|---|
| $TiO_2$/NiO | p-n junction | 25% methanol | 0.393 | 350W Xenon light source (λ > 400 nm) | 14 |
| $TiO_2$(rutile)/g-$C_3N_4$/$TiO_2$(anatase) | S-Scheme | 20% methanol | 62.37 (AQY = 45.9% at 365 nm) | 300W Xenon lamp | 15 |
| g-$C_3N_4$/CdS | S-Scheme | 20% lactic acid | 85.66 (AQY = 28.8% at 420 nm) | 300W Xenon light source (λ > 420 nm) | 16 |

**Table A3 Summary of recent studies of facet engineering**

| Material | Exposed Facet | Sacrificial Regent | $H_2$ Evolution Rate (mmol $h^{-1}$ $g^{-1}$) | Light Source | Reference |
|---|---|---|---|---|---|
| $SrTiO_3$:Al | (110), (100) | - | 3.54 (STH = 0.65%) | 300W Xenon lamp | 17 |
| $TiO_2$ | (111) | 18.5% methanol | 0.4052 | 300W Xenon lamp | 18 |
| $TiO_2$ | (101), (001) | 20% methanol | 5.8265 | 300W Xenon lamp | 19 |
| $ZnIn_2S_4$ | (110) | 20% TEOA | 1.94 (AQY = 10.1% at 420 nm) | 300W Xenon lamp | 20 |
| $Cu_2O$ | (111), (001) | 0.5M $Na_2SO_3$ | *ca.* 0.043 (value estimated from the graph) | 300W Xenon lamp | 21 |
| CdS | (101) | 0.35 M $Na_2S$ and 0.35 M $Na_2SO_3$ | 3.42 (AQY = 28.9 % at 450 nm) | 300W Xenon lamp (λ > 420 nm) | 22 |

**References**

1. X. Li, S. Zhao, X. Duan, H. Zhang, S.-z. Yang, P. Zhang, S. P. Jiang, S. Liu, H. Sun and S. Wang, Coupling hydrothermal and photothermal single-atom catalysis toward excellent water splitting to hydrogen, *Appl. Catal., B*, 2021, **283**, 119660.
2. D. Sun, Y. Chen, X. Yu, Y. Yin and G. Tian, Engineering high-coordinated cerium single-atom sites on carbon nitride nanosheets for efficient photocatalytic amine oxidation and water splitting into hydrogen, *Chem. Eng. J.*, 2023, **462**, 142084.
3. Y. Zhang, J. Zhao, H. Wang, B. Xiao, W. Zhang, X. Zhao, T. Lv, M. Thangamuthu, J. Zhang, Y. Guo, J. Ma, L. Lin, J. Tang, R. Huang and Q. Liu, Single-atom Cu anchored catalysts for photocatalytic renewable $H_2$ production with a quantum efficiency of

56%, *Nat. Commun.*, 2022, **13**, 58.

4. J. Xing, J. F. Chen, Y. H. Li, W. T. Yuan, Y. Zhou, L. R. Zheng, H. F. Wang, P. Hu, Y. Wang, H. J. Zhao, Y. Wang and H. G. Yang, Stable Isolated Metal Atoms as Active Sites for Photocatalytic Hydrogen Evolution, *Chem. Eur. J.*, 2014, **20**, 2138-2144.
5. Z.-s. Qiu, T. Zhou, Y.-w. Ma, Y.-x. Ma, T.-p. Lv, J.-h. Zhao, J. Zhang, Y.-m. Zhang and Q.-j. Liu, Single-Atom Pd Supported on $TiO_2$ for the Photocatalytic Production of Hydrogen, *ACS Appl. Nano Mater.*, 2023, **6**, 23524-23531.
6. W. Li, X.-s. Chu, F. Wang, Y.-y. Dang, X.-y. Liu, T.-h. Ma, J.-y. Li and C.-y. Wang, Pd single-atom decorated CdS nanocatalyst for highly efficient overall water splitting under simulated solar light, *Appl. Catal., B*, 2022, **304**, 121000.
7. K. Yang, Y. Huang, T. Wang, Y. Li, Y. Du, J. Ling, Z. Fan, C. Zhang and C. Ma, In-Situ Anchoring of Co Single-Atom Synergistically with Cd Vacancy of Cadmium Sulfide for Boosting Asymmetric Charge Distribution and Photocatalytic Hydrogen Evolution, *Adv. Mater.*, 2024, **36**, 2409832.
8. X.-l. Hao, X.-s. Chu, X.-y. Liu and W. Li, Synergetic metal-semiconductor interaction: Single-atomic Pt decorated CdS nano-photocatalyst for highly water-to-hydrogen conversion, *J. Colloid Interface Sci.*, 2022, **621**, 160-168.
9. B. Mahler, V. Hoepfner, K. Liao and G. A. Ozin, Colloidal Synthesis of 1T-WS2 and 2H-WS2 Nanosheets: Applications for Photocatalytic Hydrogen Evolution, *J. Am. Chem. Soc.*, 2014, **136**, 14121-14127.
10. W. Wang, Y. Tao, J. Fan, Z. Yan, H. Shang, D. L. Phillips, M. Chen and G. Li, Fullerene–Graphene Acceptor Drives Ultrafast Carrier Dynamics for Sustainable CdS Photocatalytic Hydrogen Evolution, *Adv. Funct. Mater.*, 2022, **32**, 2201357.
11. H. Cheng, Z. Bai, R. Cong, Z. Zhou and Z. Zhang, SrTiO3:Al/Cd0.6Zn0.4S Type-II Heterojunction Photocatalysts for Efficient Solar Water Splitting, *J. Phys. Chem. C*, 2024, **128**, 12427-12436.
12. H. Cai, B. Wang, L. Xiong, J. Bi, L. Yuan, G. Yang and S. Yang, Orienting the charge transfer path of type-II heterojunction for photocatalytic hydrogen evolution, *Appl. Catal., B*, 2019, **256**, 117853.

13. Z. Lian, F. Wu, Y. Zhong, J. Zi, Z. Li, X. Wang, T. Nakagawa, H. Li and M. Sakamoto, Tuning plasmonic p – n junction for efficient infrared-light-responsive hydrogen evolution, *Appl. Catal., B*, 2022, **318**, 121860.

14. M. Wang, Y. Hu, J. Han, R. Guo, H. Xiong and Y. Yin, TiO2/NiO hybrid shells: p–n junction photocatalysts with enhanced activity under visible light, *J. Mater. Chem. A*, 2015, **3**, 20727-20735.

15. X. Ruan, C. Huang, H. Cheng, Z. Zhang, Y. Cui, Z. Li, T. Xie, K. Ba, H. Zhang, L. Zhang, X. Zhao, J. Leng, S. Jin, W. Zhang, W. Zheng, S. K. Ravi, Z. Jiang, X. Cui and J. Yu, A Twin S-Scheme Artificial Photosynthetic System with Self-Assembled Heterojunctions Yields Superior Photocatalytic Hydrogen Evolution Rate, *Adv. Mater.*, 2023, **35**, 2209141.

16. R. Li, H. Li, X. Zhang, B. Liu, B. Wu, B. Zhu, J. Yu, G. Liu, L. Zheng and Q. Zeng, S-Scheme g-C3N4/CdS Heterostructures Grafting Single Pd Atoms for Ultrafast Charge Transport and Efficient Visible-Light-Driven H2 Evolution, *Adv. Funct. Mater.*, 2024, **34**, 2402797.

17. T. Takata, J. Jiang, Y. Sakata, M. Nakabayashi, N. Shibata, V. Nandal, K. Seki, T. Hisatomi and K. Domen, Photocatalytic water splitting with a quantum efficiency of almost unity, *Nature*, 2020, **581**, 411-414.

18. H. Xu, P. Reunchan, S. Ouyang, H. Tong, N. Umezawa, T. Kako and J. Ye, Anatase TiO2 Single Crystals Exposed with High-Reactive {111} Facets Toward Efficient H2 Evolution, *Chem. Mater.*, 2013, **25**, 405-411.

19. A.-Y. Zhang, W.-Y. Wang, J.-J. Chen, C. Liu, Q.-X. Li, X. Zhang, W.-W. Li, Y. Si and H.-Q. Yu, Epitaxial facet junctions on TiO2 single crystals for efficient photocatalytic water splitting, *Energy Environ. Sci.*, 2018, **11**, 1444-1448.

20. X. Shi, L. Mao, P. Yang, H. Zheng, M. Fujitsuka, J. Zhang and T. Majima, Ultrathin ZnIn2S4 nanosheets with active (110) facet exposure and efficient charge separation for cocatalyst free photocatalytic hydrogen evolution, *Appl. Catal., B*, 2020, **265**, 118616.

21. R. Chen, Z. Ren, Y. Liang, G. Zhang, T. Dittrich, R. Liu, Y. Liu, Y. Zhao, S. Pang, H.

An, C. Ni, P. Zhou, K. Han, F. Fan and C. Li, Spatiotemporal imaging of charge transfer in photocatalyst particles, *Nature*, 2022, **610**, 296-301.

22. M. Ding, S. Cui, Z. Lin and X. Yang, Crystal facet engineering of hollow cadmium sulfide for efficient photocatalytic hydrogen evolution, *Appl. Catal., B*, 2024, **357**, 124333.